UAB
Universitat Autònoma de Barcelona

HIGH TEMPERATURE SYNTHESIS OF NEW METAL OXYNITRIDE MATERIALS WITH ELECTRONIC PROPERTIES

Jhonatan Ricardo Guarín Romero

Universitat Autònoma de Barcelona

HIGH TEMPERATURE SYNTHESIS OF NEW METAL OXYNITRIDE MATERIALS WITH ELECTRONIC PROPERTIES

Jhonatan Ricardo Guarín Romero

Tesis Doctoral

Programa de doctorado en Ciencia de Materiales

Directora: **Amparo Fuertes Miquel**

Instituto de Ciencia de Materiales de Barcelona

2024

Instituto de Ciencia de Materiales de Barcelona

Consejo Superior de Investigaciones Científicas

Campus de la UAB

08193 Bellaterra (Barcelona)

Memoria presentada para aspirar al grado de doctor por

Jhonatan Ricardo Guarín Romero

Visto bueno de

Amparo Fuertes Miquel

Bellaterra, 12 de septiembre de 2024

La Dr. Amparo Fuertes Miquel, Profesora de Investigación del CSIC en el Instituto de Ciencia de Materiales de Barcelona.

CERTIFICA:

Que Jhonatan Ricardo Guarín Romero, ha realizado bajo su dirección el trabajo que lleva por título **"High temperature synthesis of new metal oxynitride materials with electronic properties"**, que se presenta en esta memoria para optar al grado de Doctor por la Universidad Autónoma de Barcelona.

Y para que así conste, firma el presente certificado en Bellaterra, a 12 de septiembre de 2024

Prof. Amparo Fuertes Miquel

“Las oportunidades no son producto de la casualidad, más bien son resultado del trabajo”

Tonatihu

Acknowledgements

Quisiera agradecer en la Prof. Amparo Fuertes del Instituto de Ciencia de Materiales de Barcelona (ICMAB) por aceptarme en su grupo de investigación, por la dirección del trabajo y su acompañamiento a diario en todas las etapas de este proyecto de investigación; gracias a su amplia experiencia en nitruros metálicos he podido desarrollar la presente tesis.

El presente trabajo es multidisciplinar y las publicaciones realizadas se han llevado a cabo en el seno de colaboraciones imprescindibles del grupo con expertos en el estudio estructural y propiedades físicas de materiales, de entre los que es necesario destacar al Prof. Josep Fontcuberta por la coordinación del estudio e interpretación de las propiedades magnéticas, al Dr. Carlos Frontera por el estudio estructural mediante difracción de rayos X convencionales y de radiación sincrotrón, y por su participación en el estudio por difracción de neutrones y en el estudio de las propiedades magnéticas, y a la Dra. Judith Oró por el estudio mediante difracción de electrones.

También es muy importante destacar mi agradecimiento al Prof. Alejandro Goñi por su contribución en el estudio de las propiedades ópticas realizadas en los oxinitrurosilicatos de tierras raras, así como al Dr. Clemens Ritter (Institut Laue Langevin, Grenoble) por su participación en la adquisición de datos de difracción de neutrones y en el estudio de la estructura nuclear y magnética de los compuestos.

También quisiera agradecer el trabajo de la Dra. Judith Oró y el Dr. Jaume Gàzquez en el estudio de las muestras por STEM en el Joint Electron Microscopy Center de ALBA (Cerdanyola del Vallès, Spain), al Dr. François Fauth (ALBA Synchrotron (Cerdanyola del Vallès, Spain)) por su participación en la adquisición de datos de difracción de rayos X con radiación sincrotrón, y al Dr. Ignasi Fina por el estudio de las propiedades dieléctricas de algunas muestras.

Al Dr. Ashley Black por contribuir en la síntesis de los silicatos y por su ayuda con los hornos de amonolisis durante mis primeros meses del doctorado.

Al Dr. Rafael Trócoli por su ayuda con los hornos de amonolisis en mis primeros meses del doctorado.

Quisiera agradecer a los estudiantes de la Universidad de Rennes Augustin Castets y Bastian Colomel, por su participación en la síntesis de algunas perovsquitas de tántalo descritas en la tesis.

A la Dra. Vega Lloveras por su ayuda en las medidas de reflectancia diffusa de las muestras.

A Xavi Campos, Anna Crespi y Joan Esquius (ICMAB) y a la Dra. Jessica Padilla (ICN2) por la realización de medidas de difracción de rayos X.

Al Dr. Bernat Bozzo (ICMAB) por realizar las medidas de magnetización de las muestras.

A Regina Roca (Universidad de Barcelona) y a Maite Vila (Instituto de Química Avanzada de Cataluña (IQAC-CSIC)) por realizar el análisis elemental para la determinación de nitrógeno de las muestras, y a Roberta Ceravola (ICMAB) por realizar los análisis termogravimétricos.

También quisiera agradecer a mis amigos del ICMAB con los que he compartido en muchos momentos, especialmente a la hora de la comida, algunos viernes y domingos en los que nos encontrábamos para comer en sitios diferentes.

A mi familia por apoyarme en mis estudios y por estar presente en cada etapa de mi vida en especial a mi madre.

Al Ministerio de Ciencia e Innovación por la financiación de esta tesis a través de los siguientes proyectos MAT2017-86616-R, PID2020-113805GB-I00, SEV-2015-0496, CEX2019-000917-S, por la beca de Formación de Personal investigador (FPI) asignada al primer proyecto(PRE2018-08520), y a la Generalitat de Catalunya por su financiación mediante el proyecto 2017SGR581.

Abstract

In this work we have developed a synthetic approach of new perovskite oxynitrides at temperatures between 1200 and 1700 ^{o}C in N_2 or N_2/H_2 (95%/5% V/V) atmospheres, controlling the anion content by the starting stoichiometric ratios of metal nitrides, oxides and oxynitride reactants. New oxynitridosilicates of rare earth and alkaline earth cations have been also prepared, as host structures to produce luminescent materials.

The investigated oxynitrides with perovskite-type structures are formed by rare earth cations in the A position and tantalum in the B site. These perovskites exhibit different structures according to the differences in size of the A and B cations, which are related to the ionic radius of the rare earth metal and the oxidation state of the cations that is tuned by the stoichiometric ratio of oxygen and nitrogen.

We report the synthesis of the pseudocubic perovskite $LaTaON_2$ by a new synthetic approach using solid state reactions between nitrides, oxides and oxynitrides at 1500 ^{o}C under N_2 that produces samples with high crystallinity and sintering degree. Neutron diffraction reveals that the anion order in this oxynitride is different compared with samples prepared by conventional ammonolysis at 950 ^{o}C. This compound exhibits a band gap of 1.9 eV and a dielectric permittivity of 200.

We report the synthesis of the perovskite $EuTaO_{2.37}N_{0.63}$ and the new triple perovskite $Eu_3Ta_3O_{3.66}N_{5.34}$ at 1200°C using N_2 or N_2/H_2 gas and

mixtures of EuN, Ta_3N_5 or TaON and Eu_2O_3 as reactants. The crystal structure of $Eu_3Ta_3O_{3.66}N_{5.34}$ exhibits two different A sites that are occupied by Eu^{3+} and Eu^{2+} with partial order along the c axis. $EuTaO_{2.37}N_{0.63}$ and $Eu_3Ta_3O_{3.66}N_{5.34}$ show ferromagnetism at low temperatures with transition temperatures $T_c \approx 3$ K and 8 K respectively.

We report the new layered perovskites with n=1 Ruddlesden-Popper type structure $R_2TaO_{4-x}N_x$ for R = La, Ce, Nd, Eu and x=2.69, 2.81, 2,54, 1.20 respectively, that were obtained under N_2 at temperatures between 1200°C and 1700°C. They are the first examples of rare earth transition metal oxynitrides with n=1 Ruddlesden-Popper structure, and show different crystal structures and magnetic properties. $Ce_2TaO_{1.19}N_{2.81}$ exhibits anionic ordering with nitrogen preferentially located in the equatorial sites of the Ta octahedron, while the axial sites are occupied by N/O with population 50/50. $Ce_2TaO_{1.19}N_{2.81}$ and $Eu_2TaO_{2.80}N_{1.20}$ display magnetic order at low temperatures, while $Nd_2TaO_{1.46}N_{2.54}$ is paramagnetic down to 2 K.

Finally, the synthesis of the new oxynitridosilicates $NdEuSiO_3N$ and $NdSrSiO_3N$ with β-K_2SO_4 structure is reported. The $Nd^{3+}$and Eu^{2+} cations in $NdEuSiO_3N$ or Nd^{3+} and Sr^{2+} cations in $NdSrSiO_3N$ are partially ordered in the two available crystallographic sites with coordination numbers 10(M1) and 9(M2), with strongly preferred occupancy of the larger divalent cations Eu^{2+} and Sr^2 for the M1 site, whereas the M2 site is preferred by Nd^{3+}. Upon excitation at 405 nm, $NdEuSiO_3N$ and $NdSrSiO_3N$:Eu, with band gaps 2.37 eV and 3.72 eV

respectively, exhibit orange red luminescence with broad emission bands centered between 605 and 639 nm.

Table of contents

Acknowledgements ..... **I**

Abstract ..... **IV**

Table of contents ..... **VII**

I Introduction **1**

1.1 Nitride vs Oxide **2**

1.2 Properties of Nitrides and Oxynitrides **6**

1.2.1 Nitrides **6**

1.2.2 Metal Oxynitrides **9**

1.3 Objectives **18**

1.4 Transition metal perovskite oxynitrides **20**

1.7 References **27**

II Methods **46**

2.1 Synthesis of metal (oxy)nitrides **47**

2.1.1 Thermal Ammonolysis **47**

2.1.2 High temperature solid state synthesis **49**

2.2 Determination of the cationic and anionic stoichiometry ... 51

2.2.1 Combustion analysis ... 51

2.2.2 Thermal analysis ... 51

2.2.3 Energy dispersive X-ray spectroscopy ... 51

2.3 Structural characterization ... 52

2.3.1 Laboratory X-ray powder diffraction ... 52

2.3.2 Synchrotron X-ray powder diffraction ... 52

2.3.3 Neutron powder diffraction ... 52

2.3.4 Electron diffraction ... 53

2.4 Optical characterization ... 54

2.4.1 Diffuse reflectance ... 54

2.4.2 Photoluminescence measurements ... 54

2.5 Electrical and magnetic properties characterization ... 55

2.6 References ... 55

III Perovskite Tantalum Oxynitrides Derived from the Pm-3m Aristotype ... 57

3.1 High Temperature Synthesis and Dielectric Properties of $LaTaON_2$ 58

Abstract 60

3.1.1 Introduction 61

3.1.2 Experimental 64

3.1.3 Results and Discussion 67

3.1.4 Conclusions 82

3.1.5 References 84

3.2 High-Temperature Synthesis of Ferromagnetic $Eu_3Ta_3(O,N)_9$ with a Triple Perovskite Structure 89

Abstract 91

3.2.1 Introduction 92

3.2.2 Experimental Methods 95

3.2.3 Results and Discussion 98

3.2.4 Conclusions 113

3.2.5 References 116

IV Anionic and Magnetic Ordering in Rare Earth Tantalum Oxynitrides with an n = 1 Ruddlesden–Popper Structure 121

Abstract 123

4.1 Introduction 124

4.2 Experimental Methods 126

4.3 Results and Discussion 129

4.4 Conclusions 151

4.5 References 155

V Neodymium Europium Oxynitrido-Silicates of β-K_2SO_4 Type: Structural, Magnetic and Red Luminescence Properties 161

Abstract 163

5.1. Introduction 165

5.2. Experimental 168

5.3. Results and Discussion 171

5.4. Conclusions 184

5.5 References 186

VI. Discussion 190

VII. Conclusions 199

VIII. Appendix..... 204

IX. Publications 215

Chapter I

Introduction

1.1 Nitride vs Oxide

Oxygen can form numerous compounds with different elements, and oxides have been extensively investigated as ferroelectrics, superconductors, catalysts, thermoelectrics, phosphors and battery materials among other applications, as bulk, single crystals, powders, and thin films.[1] Some paradigmatic examples are the high T_c superconductor $YBa_2Cu_3O_7$,[2] piezoelectric $PbZr_xTi_{1-x}O_3$ ($0 \leq x \leq 1$),[3] ferroelectric $LiNbO_3$,[4] colossal magnetoresistive $La_{1-x}Ca_xMnO_6$,[5] electrode material $La_{0.75}Sr_{0.25}Cr_{0.5}Mn_{0.5}O_3$,[6] photoluminescent $SrMoO_4$ [7] or $SrWO_4$,[8] and photocatalyst TiO_2.[9]

Nitrogen and oxygen exhibit similar electronic and crystal chemical properties, such as polarizability, electronegativity, preferred coordination numbers, and anion radii (Table 1.1). These similarities allow for the formation of the same structural types when combined with cations and the occupation of the same crystallographic positions. The nitride anion (N^{3-}) carries a higher charge than oxide (O^{2-}), so introducing nitrogen into an oxidic compound allows the modulation of the oxidation states of the cations because of charge compensation. Nitrogen is more polarizable and less electronegative than oxygen, resulting in the formation of bonds with metals with a stronger covalent character. Due to the higher electronic polarization of nitrogen, the incorporation of nitride anion into an oxide increases the nephelauxetic effect, reducing the interelectronic repulsion, and the crystal field splitting increases due to the higher charge of N^{3-} compared to O^{2-}. These differences affect the energies of the electronic levels, thereby altering the physical properties.

Table 1.1. Properties of nitrogen and oxygen. [10]

	nitrogen	Oxygen
Anion charge (z)	-3	-2
Electronegativity	3.0	3.4
Atomic polarizability ($Å^3$)	1.10	0.80
Electron affinity $A \rightarrow A^{z-}$ ($kJ\ mol^{-1}$)	1736	601
Bond energy A–A ($kJ\ mol^{-1}$)	941	499
Ionic radii (Å) (for CN = IV)	1.46	1.38
Coordination number (CN)	II–VIII	II–VIII

In addition to nitrogen, other elements can be introduced into oxides, such as hydrogen,[11] fluorine,[12] chlorine,[13] bromine,[14] iodine,[15] sulphur[16] or selenium.[17]. In the last decades, oxynitrides have attracted special attention due to their significant applications as pigments, electronic materials, phosphors, and photocatalysts.[18]

Nitrides are less stable than oxides for two main reasons. The bond energy of N_2 is higher than that of O_2 (945 kJ/mol and 498 kJ/mol respectively), and the electron affinity, the energy required for the anion formation, is higher for nitride than for oxide ($N \rightarrow N^{3-}$ and $O \rightarrow O^{2-}$ are 1736 and 601 kJ/mol respectively).[19] As a consequence, nitrides show larger free energies of formation than oxides, and have been less investigated because their synthetic methodologies are not straightforward. The presence of small concentrations of H_2O or O_2 (at the ppm level) around the sample should be avoided as nitrides may decompose at high temperatures leading to the formation of more stable oxidic phases. Several factors need to be carefully considered in the synthesis of nitrides, including the choice of reactants, gas, flow rate, reaction time, maximum temperature, and the materials used for the

crucible and the reaction tube. In the following section, different methods of synthesis of nitrides are discussed.

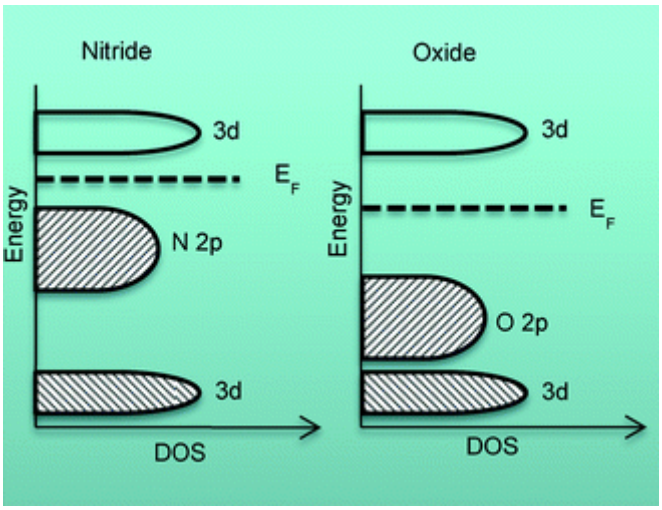

Figure 1.1. Schematic band structures in semiconducting late transition metal oxides and nitrides. Adapted from reference [18] with permission from the Royal Society of Chemistry.

In mixed anion compounds, an important factor that can affect the physical properties is the anion order. For instance, N/O order can change the crystal structure of a oxynitride from centrosymmetric to non-centrosymmetric, inducing properties such as pyroelectricity, ferroelectricity, and piezoelectricity.[20] The anionic distribution in oxynitrides and in other mixed oxyanion compounds such as oxyhalides can be predicted using the Pauling's second crystal rule. This principle states that "In a stable coordination structure the electric charge of each anion tends to compensate the strength of the electrostatic valence bonds reaching to it from the cations at the centres of the polyhedra of which it

forms a corner" [20], that is, for each anion, the charge q tends to be equal to the bond strength sum (b):

$$b = \sum_i \frac{z_i}{v_i}$$

Where z is the electric charge of the cations linked to a certain position of the anions and ν is its coordination number. In oxynitrides formed by two cations of different charges, nitrogen would preferentially occupy the anion sites with larger b values. [21, 22] A correlation plot between the b

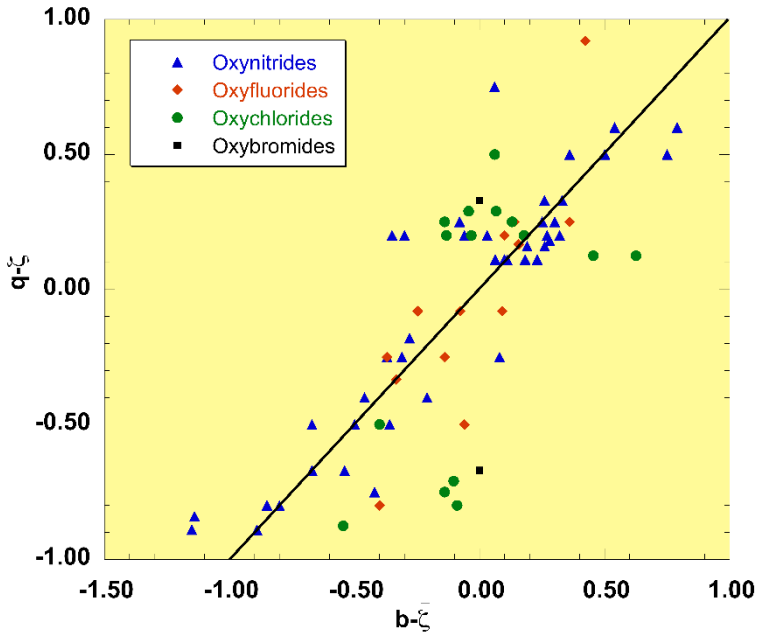

Figure 1.2. Correlation plot of the experimentally determined charge of the anion versus the bond strength sum both corrected for the average charge of anions, $\bar{\zeta}$, for oxynitrides and oxyhalides. Reproduced from ref [21] with permission of the American Chemical Society.

values and the electrical charge of each anion as observed experimentally from the determined crystal structure is shown in Figure 1.2.

1.2 Properties of Nitrides and Oxynitrides

1.2.1 Nitrides

The first studies of nitrides were conducted in the ‘20s and ‘30s and were further systematically investigated by Juza's group. Important review articles on nitrides are “Nitrides of metals of the first transition series” (1966) by R. Juza,[23] “Solid-state Chemistry with Nonmetal Nitrides” (1993) by Wolfgang Schnick[24] and “Structural families in nitride chemistry” (1998) by Ducan H. Gregory.[25]

Nitrides can be classified as metallic, ionic, and covalent. However, it is not always easy to determine the type of bond, especially in heteroatomic compounds when more than one type of bond can be present. Although the number of synthesized nitrides is limited compared to oxides, some of them show properties with important applications. Binary nitrides of Group III BN,[26] AlN,[27] GaN,[28] InN,[29] and TlN[30] have been investigated for several applications. Hexagonal boron nitride can be used in furnaces operating at high temperatures,[26] as dielectric material, sensor, luminescent material,[31] photon emitter, and catalyst. In addition to these properties, it is used in biomedicine[32] and in the makeup industry as a cosmetic.[32] AlN and GaN show applications as piezoelectric[33] and luminescent materials. GaN and $In_{1-x}Ga_xN$, [34] have been extensively studied as components of light-emitting diodes (LEDs). AlGaN is used as an emitter and detector of ultraviolet irradiation and for the fabrication of

UV-emitting LEDs at 275 nm with an efficiency of 20.3%.[35] InN is a semiconductor,[29] and TlN is a thermoelectric material.[36]

Si_3N_4 finds numerous applications in the ceramic industry, dental burs, and as a steel/ceramic material.[37] Its notable properties include high thermal conductivity[38] and hardness, corrosion resistance[39] and tensile strength.[40] P_3N_5 is a dielectric and optical material and it is used in nanoelectronics and protective coatings.[41, 42]

Ternary and higher nitrides of beryllium, silicon, aluminum, or phosphorus are important luminescent materials when excited with UV or visible light, emitting at long wavelengths. $MBe_{20}N_{14}:Eu^{2+}$ (M = Sr, Ba)[43] show emission bands centered up to 430 nm. Silicon-based nitrides $M_2Si_5N_8:Eu^{2+}$ (M = Ca, Sr, Ba)[44] and cerium-doped $CaSiN_2$ [45] emit at approximately 605 nm and 630 nm, respectively. $Ba[Mg_2Al_2N_4]$ doped with Eu^{2+} emits at 710 nm,[46] and $SrLiAl_3N_4:Eu^{2+}$ [47] and $CaAlSiN_3$ [48] emit at 650 nm. Phosphorus nitrides, such as $AEP_8N_{14}:Eu^{2+}$ (AE = Ca, Sr, Ba)[49] and GeP_2N_4,[50] also exhibit luminescent properties.

The binary transition metal nitrides TiN, ZrN, HfN, NbN, and TaN are metallic and show superconductivity at low temperatures, and are important refractory materials.[51] Hf_3N_4 and Zr_3N_4 find applications as hard and as semiconducting materials.[52] Titanium-containing nitrides are used to improve wear resistance and as barrier layers in silicon electronics. [53] TiN is applied to cutting tool surfaces to increase strength and prevent corrosion, and it is also used as a mechanical component. [54, 55]CrN shows antiferromagnetism, and Mn_4N, Fe_4N and Fe_2N are

ferromagnetic.[23] Mo_5N_6 [56] exhibits superconductivity below 12 K. Nitrides have also been studied in capacitors and batteries, and can operate at different temperatures.[57] For instance, VN exhibits a high capacitance value of 413 F g-1 when a current density of 1 A g-1 is applied.[58]

Transition metal nitrides are also applied as photocatalysts. For example, Mo_2N can be supported on activated carbon for photocatalytic applications in the hydrodeoxygenation of 2-methoxyphenol.[59] Many of these compounds are employed in the production of hydrogen and oxygen through electrochemical reactions or photocatalysis. An example is Fe_3N/Fe_4N, which is used for applications as anode catalyst of the oxygen evolution reaction.[60] Ni_3Mn nanosheets[61] and Ni_3N nanocrystals[62] are active in the oxygen evolution reaction (OER) and hydrogen evolution reaction (HER) processes. Cu_3N [63] and Co_4N are active in hydrogen evolution,[64] Zr_3N_4 [63] is active in oxygen evolution, and Ta_3N_5, AgN_3, Zn_3N_2 are active in both hydrogen and oxygen evolution.[63]

Ternary or higher transition metal nitrides show a variety of relevant properties. Polar perovskite $LaWN_3$ shows piezoelectric and ferroelectric properties, [65] and the spinel $MnTa_2N_4$ exhibits strong magnetic frustration.[66] TiNiN [67] is reported to have applications as a catalyst for the hydrogenolysis of aryl ethers. $NiMoN_x$,[68] $Co_{0.6}Mo_{1.4}N_2$,[69] and Co_3Mo_3N [70] have applications in HER as electrocatalysts. On the other hand, Ni_3FeN [70] nanoparticles supported on Co,N-CNF and Co_3Mo_3N [71]

have applications in OER and oxygen reduction reaction (ORR), while $Ti_{0.5}Nb_{0.5}N$ [72] is used solely in ORR.

1.2.2 Metal Oxynitrides

The synthesis of oxynitrides began around the same time as for nitrides. In the 80's Marchand's group performed a systematic investigation of oxynitrides, developing new synthetic approaches, mostly performed under gaseous ammonia.[73, 74] Metal oxynitrides have been reported with a variety of crystal structures including scheelite,[75] fluorite,[75] apatite,[76] perovskite,[77] pyrochlore,[78] and spinel,[79] and find applications in catalysis, electronics,[80] optics,[81] and as dielectric materials.

Lithium phosphorus oxynitride (LiPON) is used as a coating for lithium batteries to improve the stability of lithium ions due to its high ionic conductivity.[82] $CeO_{2-x}N_x$ is a photocatalyst for the decomposition of acetaldehyde under visible light.[83] TaON [84] and $TiO_{2-x}N_x$ [85-87] show photocatalytic activity under visible light for the production of hydrogen and oxygen through water splitting. Vanadium oxynitride is used in electrocatalysis for nitrogen reduction,[88, 89] and cobalt oxynitride ($CoO_{0.8}N_{0.2}$) is active in nitrogen reduction and hydrogen evolution reactions using this process.[90]

Perovskite oxynitrides have applications as electronic materials and as photocatalysts.[81, 91] For example, $BaTaO_2N$ has a high dielectric permittivity,[92] and $EuNbO_2N$ is ferromagnetic at low temperatures and shows colossal magnetoresistance.[93] $Ca_xLa_{1-x}TaO_{1+x}N_{2-x}$ is a non-toxic pigment with color tuned by the nitrogen content.[94] Perovskite

oxynitrides show small band gaps, making them suitable for applications as photocatalysts under visible light. Notable examples are $LaTiO_2N$,[95] $CaTaO_2N$, $SrTaO_2N$, $BaTaO_2N$,[96] and $LaTaON_2$.[97, 98, 99]

Oxynitridosilicates show important luminescent properties. $(Mg,Y)_5Si_3(O,N)_{13}:Ce^{3+}$, Mn^{2+} [100] shows whole visible light emission from 370 to 750 nm, and $Ca_4Y_3Si_7O_{15}N_5:Eu^{2+}$[101] is a green light emission phosphor that can also be used as a pressure sensor. $A_3Si_2O_4N_2$ (A = Sr, Ca)[102, 103] show emission bands centered up to 600 nm when excited with UV-blue light; $Ba_3Si_6O_{12}N_2:Eu^{2+}$,[104] emits at 527 nm under excitation at 450 nm, and (Sr, Ca, Ba)$Si_2O_2N_2$ [105] shows emission in the range of 492 to 563 nm after being irradiated with UV-blue light. $LaMSiO_3N$ (M = Sr, Ba)[106] can be activated with Ce^{3+} or Eu^{2+} and emits light from 650 to 700 nm when excited at 405 nm. Silicon aluminum oxynitrides (SiAlON) possess important properties including high chemical and thermal stability, transparency to visible light, small band gaps, and greater hardness than fused silica glass.[107] Ce^{3+}-doped $Y_3Al_{4.75}Si_{0.25}O_{11.75}N_{0.25}$ and $Al_9O_3N_7:Eu^{2+}$ [108] have applications as a luminescent materials.[109]

Synthetic approaches of metal oxynitrides

Ammonolysis of oxides

The reaction between oxides or of mixtures of oxides and salts under gaseous NH_3 at high temperature is one of the most commonly used methods for the synthesis of oxynitrides. Ammonia is a Lewis base and a weak Liebig acid, so it can reduce or oxidize metals.[110]At temperatures higher than 500 °C, it dissociates into N_2 and H_2 (Figure 1.3(a))[18]

therefore it is important to control the gas flow and temperature, as the percentages of NH_3, N_2, and H_2 in the reaction depend on these

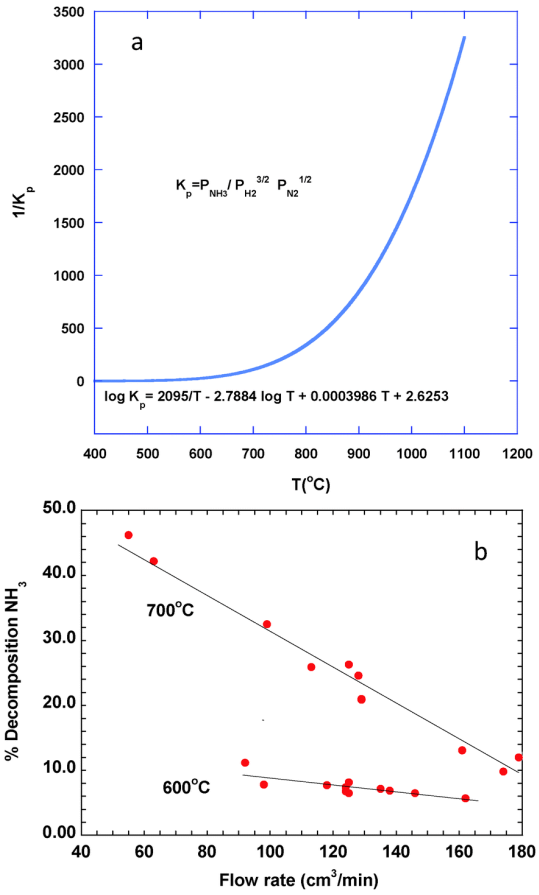

Figure 1.3 (a) Equilibrium constant of dissociation of NH_3 as a function of temperature using the equation $\log K_p = 2095/T - 2.7884 \log T + 0.0003986T + 2.6253$ where K_p is the equilibrium constant of the formation of NH_3, and **(b)** % of decomposition of NH_3 as a function of flow rate at different temperatures. Adapted from reference[18] with permission from the Royal Society of Chemistry

parameters. Hydrogen can reduce the transition metals leading to a decomposition of the oxynitride and giving rise to unwanted impurities. A high flow of NH_3 should be used at high temperatures to prevent and minimize its dissociation. Ammonolysis reactions are typically carried out at temperatures between 400 °C and 1100 °C, with reaction times varying from hours to days and flow rates from 50 to 1000 cm³/min. The obtained oxidation states of the cations depend on temperature, ammonia flow rate, and reaction times, which determine the O/N ratio in the oxynitride.

$Nb_{0.82}N_{0.81}O_{0.19}$ [111] was one of the first examples of oxynitrides prepared by this method in 1960. Later, Marchand's group reported the synthesis of several compounds. In 1983, $NaPO_2N_{0.67}$ and $KPO_{3-3x}N_{2x}$ [112] were prepared using an ammonia flow rate of 10 l/h at 700-750 °C. In 1988, $LnWO_xN_{3-x}$ (Ln = La and Nd)[113, 114] were prepared using their respective precursor oxide, $Ln_2W_2O_9$, at temperatures ranging from 700 to 900 °C. In 1989, the same group reported the synthesis of $LaVO_{3-x}N_x$.[115] TaON with baddeleyite structure can be prepared from Ta_2O_5 in NH_3 flow at 800 °C,[116] whereas γ-TaON with VO_2-type structure is formed from using a shorter treatment time at lower temperatures. [117, 18] Nitrogen doping of CeO_2 was performed using a flow rate of 270 cm³/min for 17 hours at temperatures between 550 and 900 °C. The amount of nitrogen increases rapidly from x = 0.015 to x = 0.09 with increasing temperature from 600 to 690 °C, but it decreases to 0.02 at temperatures above 740 °C because of the competing reaction of reduction of Ce^{4+} to Ce^{3+}.[83] Nitrogen introduction into TiO_2 films was performed by treatment under ammonia for 4 hours at different temperatures. Up to 600 °C, the anatase

structure is stable with partial substitution of oxygen by nitrogen and at 700 °C, cubic NaCl-type TiO_xN_{1-x} is observed. At 900 °C, the percentage of nitrogen decreases, and the rutile crystalline phase is formed.[118] Zr_2ON_2 was prepared by ammonolysis using ZrO_2 as a precursor, with an NH_3 flow rate of 670 cm^3/min, a temperature of 1000 °C, and a reaction time of 24 hours.[119]

Ammonolysis reactions have been extensively used to prepare perovskite oxynitrides $ABO_{3-x}N_x$, where A is an alkaline earth or lanthanide and B = Mg, Ti, Zr, V, Nb, Ta, Cr, Mo, W, or Fe.[120] Perovskite thin films of oxynitrides consisting of niobium and tantalum ($ATaO_2N$, A = Eu, Sr, Ba, Ca; $SrNbO_2N$; $LaNbON_2$; and $LaTaON_2$) have been synthesized from the oxide precursor.[121] The transformation of scheelites (ABO_4) into perovskites ($AB(O,N)_3$) in ammonia has been studied using calorimetric techniques, showing that in some cases other oxynitride compounds are obtained instead of the perovskites.[122]

Solid state reactions under N_2

N_2 is less reactive than NH_3, hence in this synthetic approach the nitrogen content in the oxynitride is controlled by the anion stoichiometry in the mixture of reactants. Because of the lower reactivity of N_2, the synthesis temperatures are higher than in the ammonolysis reactions, typically in the range between 900 and 1750 °C, usually starting with nitrides in combination with oxides or salts.

Si_2N_2O was one of the first compounds prepared by this method in 1964 at 1450 °C.[123] In 1983, Li-Al-Si-O-N[124] and Ca-Al-Si-O-N [125] glasses were prepared under N_2 at temperatures between 1450-1465 °C and 1530-1750 °C, respectively. Later, Schnick and collaborators prepared a large diversity of silicon-based nitride compounds as hosts to produce luminescent materials, starting with different reactants. $Ce_{16}Si_{15}O_6N_{32}$[126] was obtained with a yield of 20% using Ce, SiO_2, and $Si(NH)_2$ as precursors at 1540 °C. $Sm_2Si_3O_3N_4$ and silicon aluminates such as $Ln_2Si_{2.5}Al_{0.5}O_{3.5}N_{3.5}$(Ln = Ce, Pr, Nd, Sm, Gd),[127] were synthesized using $Si(NH)_2$, AlN, $SrCO_3$, and the corresponding lanthanide metals as reactants. $SrCO_3$ decomposed at high temperatures into SrO and CO_2, proving to be a suitable oxygen source for the syntheses performed. These syntheses were conducted at temperatures between 1550 and 1650 °C. $SrSiAl_2O_3N_2$ was prepared using silicon diimide, aluminum nitride, and strontium carbonate as precursors, at 1550 °C for 3 hours.[128] $SrErSiAl_3O_3N_4$ [129] was synthesized treating $SrCO_3$, $Si(NH)_2$, AlN, and metallic erbium powder at 1670 °C for 3 hours, with a yield of 20%. $Nd_3Si_5AlON_{10}$ [130] was prepared starting with silicon diimide, aluminum nitride, aluminum oxide, and neodymium aluminum oxide at 1650 °C for 60 minutes, achieving a yield of 65%. $Sr_{10}Sm_6Si_{30}Al_6O_7N_{54}$ [131] was prepared using $SrCO_3$, $Si(NH)_2$, AlN, Sr, and Sm which were treated at 1600 °C for 30 minutes, with a reaction yield of 20%. The boron compound $Sr_3(B_3O_3N_3)$[132] was prepared using $B(NH)_x(NH_2)_y$ and strontium carbonate as precursors at 1450 °C for 1 hour. The yield of this synthesis was low, and the formation of single crystals was observed.

$LaMSiO_3N$ (M = Ba, Sr, Eu) with a β-K_2SO_4 structure were prepared at temperatures between 1350 and 1500 °C. [106] $Sr_{2-x}La_xSiO_{4-x}N_x$ ($0 \geq x \geq 1$) was prepared starting from La_2O_3, SiO_2 and Si_3N_4 at 1500 °C under N_2/H_2.[133] Eu^{2+} doped $YSiO_2N$ was prepared by solid-state reaction from a mixture of Y_2O_3, SiO_2, Si_3N_4 and Eu_2O_3 at 1600 °C with treatment time of 24 hours,[134] and $SrSi_2N_2O_2:Eu^{2+}$ compounds were prepared from $SrCO_3$, SiO_2, and Si_3N_4 in a flow of N_2 at 1450 °C for 2 hours.[135]

Reactions under N_2 have also been used to prepare perovskite oxynitrides For example, $SrTaO_2N$, $BaTaON_2$, Ba_2TaO_3N, Sr_2TaO_3N and Ruddlesden-Popper oxyntrides Sr_2TaO_3N and Ba_2TaO_3N were prepared by treating SrO or BaO and TaON at temperatures between 1200 and 1600 °C.[94] $SrTaON_2$ was also prepared starting with $SrCO_3$, amorphous Ta_2O_5, and urea that were treated at 900 °C during 2 hours. Using the same conditions, it was not possible to synthesize $SrTaON_2$ starting with crystalline Ta_2O_5.[136] $BaTaO_2N$ was prepared at 1200 °C, starting with $BaCO_3$ and TaN.[137] $RHfO_2N$ (R = La, Nd, and Sm) were prepared at 1500 °C from a mixture of R_2O_3 (R = La, Nd, and Sm) and Hf_2ON_2, whereas $LaZrO_2N$ was prepared starting with La_2O_3, ZrO_2 and ZrN.[138]

Topochemical reactions and low temperature methods

This method has been used to obtain oxynitrides from their respective isostructural oxides at low to moderate temperatures, in most cases where other synthetic approaches were not successful. Oxygen is partially substituted by nitrogen without perturbing the cationic network, and as the two anions show different charges, the cations oxidize in order to

compensate the increase of charge induced by nitriding. The reactions are performed usually under NH_3 at temperatures in the range of 400 to 900 °C. Alternative nitriding agents such as urea can also be used under N_2 flow.

The perovskite $SrVO_{2.2}N_{0.6}$ was prepared starting with $SrVO_3$ under NH_3 at 600 °C,[139] and the pyrochlore $Eu_2Mo_2O_5N_2$ was synthesized using the same gas, starting with $Eu_2Mo_2O_7$.[140] Topochemical reactions are also used to obtain double perovskite oxynitrides $A_2B'B''O_{6-x}N_x$ with a high ordering of the B cations starting with the double perovskite oxides. For example, Sr_2FeMoO_5N was prepared from Sr_2FeMoO_6 under NH_3 at 575 ^oC using a flow rate of 1000 cm^3/min[141] Sr_2FeWO_5N was prepared starting with Sr_2FeWO_6 under the same ammonia flow rate at 660 ^oC. [142] The Ruddlesden-Popper compound $K_2LaTa_2O_6N$ was prepared from $CsLaTa_2O_7$. This process involved two stages: first, the ionic exchange of Cs^+ for K^+, and second, the substitution of O^{2-} for N^{3-} and the insertion of the second K^+ ion.[143] The compound $K_2Ca_2Ta_3O_9N{\cdot}2H_2O$ was prepared from a stoichiometric mixture of $KCa_2Ta_3O_{10}$ and K_2CO_3 with an NH_3 flow rate of 100 cm^3/min, at a temperature of 1173 K for 3 hours.[144]

In some cases, it is not possible to use topochemical synthesis to obtain oxynitrides from the corresponding oxide. Instead, an oxyhydride precursor must be prepared as a previous step. Examples of success of this method include $BaTiO_{3-x}N_{2x/3,}$ which was prepared from hydride substitution by nitride in $BaTiO_{2.40}H_{0.60.}$[145] Another example is $EuTiO_2N$

that cannot be prepared by ammonolysis of $EuTiO_3$, but it is formed from $EuTiO_{2.82}H_{0.18}$ under a flow rate of 300 cm^3/min at 400 °C. [146]

Topochemical syntheses can be performed using urea as nitrogen source, under nitrogen flow. An example of such a synthesis is $Ti_{2.85}O_4N$, which was prepared from $Cs_{0.68}Ti_{1.83}O_4$ at temperatures between 500 and 800 °C.[147] $K_{1.35}LaTa_2O_{6.65}N_{0.35}$ and $K_{1.4}Ca_2Ta_3O_{9.6}N_{0.4}$ were prepared by reaction of $KLaTa_2O_7$ or $KCa_2Ta_3O_{10}$, K_2CO_3 and urea at temperatures ranging from 450 to 550 °C.[148, 149]

Ammonothermal and high-pressure synthesis

Gases under supercritical conditions exhibit properties of both liquids and gases simultaneously, such as high solubility, low surface tension, low viscosity, and high diffusivity. In ammonothermal synthesis an autoclave is used where the temperature and pressure of NH_3 are increased simultaneously. Synthesis of oxynitrides by this method have been reported at temperatures in the range of 350 to 1950 °C and pressures from 0.8 to 6000 MPa. Recently, single crystals of $Eu^{II}Eu^{III}{}_2Ta_2N_4O_3$ were synthesized using this method.[150] $ATaN_2$ nitrides (A = Na, K, Rb, and Cs) were obtained at different temperatures (from 623 to 1073 K), heating rates from 0.1 to 2.5 K/min, and reaction times from 20 to 96 hours, at a maximum pressure of 170 MPa.[151] Perovskites $SrNbO_2N$, $BaNbO_2N$, $SrTaO_2N$ and $BaTaO_2N$ were also prepared by amonothermal synthesis, using Sr and Ba, Ta, Nb, NaN_3, and NaOH as precursors. The maximum temperature and pressure used in these

syntheses were 900 K and 300 MPa, respectively, and the reaction time was 80 hours.[151]

High pressure synthesis has allowed to obtain oxynitrides such as perovskites, nitridosilicates and nitridophosphates. $RZrO_2N$ perovskites (R = Pr, Nd, and Sm) were prepared by direct solid-state reaction starting with Zr_2ON_2 and the respective lanthanide oxides R_2O_3 at high temperatures and pressures of 1200-1500 °C and 2-3 GPa.[152] Polar $MnTaON_2$ with $LiNbO_3$ type structure was prepared by mixing TaON and MnO at 1400 °C and 6 GPa.[153]The oxynitridophosphate Ba_2PO_3N was synthesized at 1070 K and 120 MPa. [154] $Ca_{1+x}Y_{1-x}SiN_{3-x}O_x$ ($x > 0$), isostructural to Ca_2PN_3 and Eu_2SiN_3, was prepared by mixing CaH_2, YSi and NaN_3 at 1070 K at 140 MPa.[155] Different samples with the stoichiometry $Al_9O_3N_7$, both undoped and doped with 0.005 mol Eu^{2+} were synthesized from AlN, Al_2O_3 and EuF_3 at temperatures between 1750 °C and 1950 °C and a nitrogen pressure of 0.8 MPa.[108]

1.3 Objectives

The main objective of this thesis is the exploration of synthetic methodologies of new metal oxynitrides with electronic properties (electrical, magnetic, optical). A high temperature synthetic approach under N_2 gas has been developed for the preparation of new perovskite-related oxynitride phases of rare earth and transition metal cations, using solid state reactions between metal oxides and nitrides at high temperatures (between 1200 and 1700 ^oC), and a similar method has been used to prepare new luminescent rare earth oxynitridosilicates.

The thesis is structured in three chapters describing the experimental results, discussion and conclusions of four publications, and three additional chapters on the experimental methods (chapter 2), discussion (Chapter 6) and conclusions (chapter 7). Chapter 3 is devoted to the synthesis and characterization of pseudocubic perovskite oxynitrides of tantalum and rare earth cations. By using the new high temperature synthesis route, we have obtained the compound $LaTaON_2$ that was previously prepared under NH_3 at lower temperatures. We have investigated the influence of the synthetic approach in the anion order and its dielectric properties. Results have been published in Inorganic Chemistry 2021, 60, 16484−16491 shown in section 3.1. We also report the high temperature synthesis of the europium compounds $EuTaO_{2.37}N_{0.63}$ and $Eu_3Ta_3O_{3.66}N_{5.34}$. The last compound is the first example of a triple perovskite oxynitride and both oxynitrides show ferromagnetism at low temperatures. These results have been published in Inorganic Chemistry 2023, 62, 17362−17370 shown in section 3.2. In chapter 4 we present the synthesis and characterization of the new family of compounds $R_2TaO_{4-x}N_x$ with R= La, Ce, Nd, Eu and $1.20 \leq x \leq 2.81$ that are the first examples of n = 1 rare earth tantalum Ruddlesden-Popper oxynitrides. These results have been published in Chemistry of Materials 2024, 36, 5160−5171. Finally, in chapter 5 we report the results on the synthesis and characterization of the oxynitridosilicates $NdSrSiO_3N$:Eu and $NdEuSiO_3N$ that show luminescence properties, published in Journal of Solid State Chemistry 316 (2022) 123571.

The following sections describe the fundaments and state of the art of the two groups of compounds discussed in the thesis: perovskite oxynitrides with several applications and luminescent oxynitridosilicates.

1.4 Transition metal perovskite oxynitrides

The mineral perovskite $CaTiO_3$ was discovered in 1839 by Gustav Rose, a German chemist and mineralogist, in the Ural Mountains of Russia, and was named in honour of Alexeievitch Perovsky, a Russian mineralogist. The aristotype with ideal composition ABX_3 shows the cubic space group *Pm-3m*. The A and X ions form a cubic structure with close packing, with the B ion occupying the octahedral voids. The A cation is coordinated to 12 anions and is surrounded by eight BX_6 octahedra, and the anions are surrounded by four A cations and two B cations. Many perovskites are described as ionic, but they actually exhibit a mixture of ionic and covalent bonding.

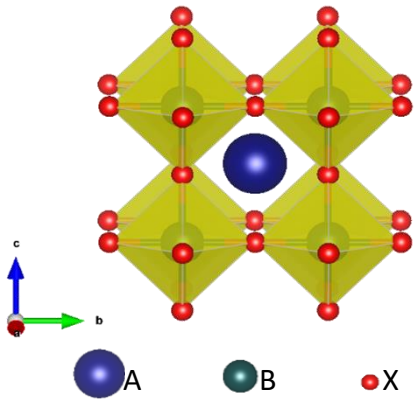

Figure 1.4. The cubic ABX_3 perovskite structure.

In 1926, Goldschmidt introduced the structural tolerance factor (t)[156] to predict the stability of perovskite structures. The crystal structure of a perovskite depends on this factor, which relates the A-X and B-X distances using the equation:

$$t = \frac{r_A + r_X}{[\sqrt{2}(r_B + r_X)]}$$

Where r_A, r_B are the ionic radii of A and B cations and r_X is the ionic radius of the anion. The volumes of AX_{12} and BX_6 polyhedra can change, and substitutions or vacancies can cause reordering of the atoms, allowing a wide range of elements from the periodic table to form the structure.[157] When the tolerance factor (t) is in the range of 0.89 to 1.0, the compound typically forms a cubic structure. Values below this range can result in symmetry lowering and distorted structures due to the octahedral tilting. Perovskites are among the most extensively studied materials worldwide. They show numerous physical properties including metallic conductivity, superconductivity, ferroelectricity, ferromagnetism, colossal magnetoresistance, piezoelectricity, and photoluminescence. Some important examples of electronic materials include superconducting $Ba_{1-x}K_xBiO_3$ [158] and ($YBa_2Cu_3O_7$),[159] colossal magnetoresistant $La_{1-x}M_xMnO_3$ (M= Ca, Sr), [160] piezoelectric $PbZr_{1-x}Ti_xO_3$, ionic conductors $La_{0.67-x}Li_{3x}TiO$ and $BaCeO_{3-x}$[161], ferromagnetic $SrRuO_3$ and ferroelectric $BaTiO_3$.[161]

There are few examples of nitrides with a perovskite structure. The first reported compound is $ThTaN_3$,[162] and more recently, $LaReN_3$,[163] and $LaWN_3$ [65] have been prepared either as powder or as thin films.

Perovskite oxynitrides with the formula $ABO_{3-x}N_x$ (A = alkaline earth or rare earth metal; B = transition metal) were first reported by Roger Marchand and coworkers.[120, 164] These materials have been more intensively investigated after 2000, when results on the non-toxic pigments $Ca_{1-x}La_xSrTaO_{2-x}N_{1+x}$ were published in Nature by Jansen and Letscher.[165] These materials exhibit significant properties as dielectrics, magnetic materials, and photocatalysts in various reactions.

Some examples of relevant materials are $SrTaO_2N$, [92] $BaTaO_2N$, [92] and $LaTiO_2N_x$ [166, 167] that show dielectric permittivities of 4900, 2900, and 1000, respectively, at room temperature. $SrTaO_2N$, in the form of an epitaxial thin film under compressive stress, is reported to show ferroelectricity.[168]

The perovskites $LaVO_{3-x}N_x$ [169] and $LnWO_{3-x}N_x$ (Ln = La, Nd) [114] are semiconducting. Some examples of oxynitride perovskites with magnetic properties include $EuTaO_2N$, $EuNbO_2N$, and $EuWO_{1+x}N_{2-x}$[170], which exhibit ferromagnetic properties due to the coupling of Eu^{2+} ions [171], and magnetoresistance at low temperatures. $NdVO_2N$[120] is paramagnetic, while $LnCrO_{3-x}N_x$ show antiferromagnetic order of Cr^{3+} spins.[172] The double perovskites $Sr_2FeMoO_{4.9}N_{1.1}$ [141] and Sr_2FeWO_5N [142] show ferromagnetic and antiferromagnetic order respectively at low temperatures.

These materials are also characterized by small band gap values compared to oxides due to the presence of nitrogen, which is less electronegative than oxygen. For example, the perovskites

$La(Mg,Ta)(O,N)_3$ and $Ba(Sc,Ta)(O,N)_3$, exhibit band gaps of 1.8 and 1.9 eV, respectively.[173] $PrHfO_2N$ [120] and $CeNbO_{1.49}N_{1.51}$[174] have band gaps of 3.40 and 1.79 eV, respectively. The lanthanide tantalum perovskites $LnTaON_2$ with Ln = La, Ce, Pr, Nd, Sm, Gd, [175] show band gaps of 1.8, 1.7, 1.9, 2.0, 2.0, and 1.8 eV, respectively.

Due to their low band gap values the following perovskite oxynitrides have been used as photocatalysts in several reactions: $LaTiO_2N$, $LaZrO_2N$ $LaNbON_2$ $LaTaON_2$, $CaNbO_2N$, $SrNbO_2N$, $BaNbO_2N$, $CaTaO_2N$, $SrTaO_2N$ and $BaTaO_2N$. [176] $LaTiO_2N$ and $NdTiO_2N$ exhibit comparable activity in water oxidation in the presence of a sacrificial agent. However, $PrTiO_2N$ and $CeTiO_2N$ display reduced activity, which may be attributed to the recombination of photoinduced electron-hole pairs.[120] Additionally $LaZrO_2N$, $SmHfO_2N$ [138] and $SrWO_2N$ [177] show activity in this process under visible light. $LaHfO_2N$ exhibits photocatalytic activity water splitting.[138]

Perovskite related layered Ruddlesden-Popper compounds[178] with the general formula $A_{n+1}B_nO_{3n+1}$ were first discovered in 1950 decade with the synthesis of Sr_2TiO_4 and $Sr_3Ti_2O_7$.[179, 180] The parameter "n" indicates the number of octahedral layers in the perovskite block which can have values of between 1 and ∞.[179, 180] The perovskite blocks are separated along the c direction by AO layers with rock salt-like structure.

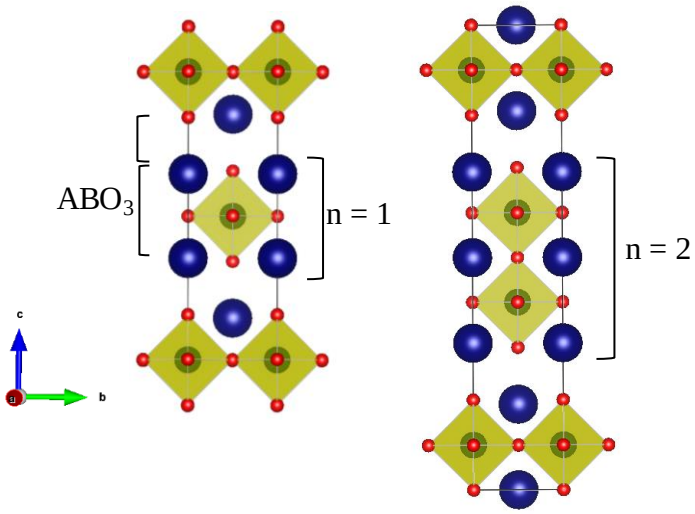

Figure 1.5. Crystal structures of Ruddlesden-Popper phases with n= 1 and 2.

The synthesis of the following Ruddlesden-Popper perovskite oxynitrides has been achieved: n=1 Sr_2TaO_3N, Ba_2TaO_3N, [181] Ln_2AlO_3N (Ln = Nd , Sm) [182]and Sr_2NbO_3N, and n=2 $Sr_3Nb_2O_5N_2$ and $Eu_3Ta_2N_4O_3$.[183]

Luminescent (Oxy)nitridosilicates

Approximately one fifth of the world's electricity consumption is attributed to lighting, making it crucial to develop alternatives to traditional incandescent and fluorescent lighting systems.[184] As part of the energy transition, solid-state lighting is expected to play a key role, with the scientific community aiming to achieve 50% energy savings by 2025.[184] In recent years, there have been significant advances in solid-state lighting, especially in applications such as light-emitting diodes (LEDs) and laser diodes (LDs).

Current research is focused on the development of thermally stable phosphors, which offer several advantages, including compact size, durability, and high luminous efficiency.[185] Solid phosphors doped with rare earths result in materials with excellent durability, thermal and chemical stability, and luminescence.[186, 187] Silicon-based materials offer several advantages, including easily tuneable colours and higher luminescence efficiency compared to other materials.[188] Si_3N_4, known for its thermal resistance, hardness, and elasticity, [188] forms the basis of oxynitridosilicates, similar to oxosilicates, which comprise a tetrahedral Si(O, N) lattice.[189] Some nitrides, formed from tetrahedral silicon nitride (SiN_4) or combinations of silicon and aluminium (Al, Si)N_4, emit visible light when excited with blue or near-ultraviolet LED light.[190]

In recent years, luminescent rare-earth-doped (oxy)nitrides have been reported, offering advantages such as broad emission bands, high efficiency and good thermal stability. Some phosphors can be excited with blue light, emitting yellow illumination, and can produce white light when irradiated with blue chips.[191] Examples of these compounds are $SrSi_2O_2N_2:Eu^{2+}$ and $Sr_2Si_5N_8:Eu^{2+}$, which emit green and red colors, respectively.[192] $Ba_2Si_5N_8:Eu^{2+}$,[193] and $CaSi_2O_2N_2:Eu^{2+}$,[194] when excited with radiation in the 445-480 nm range, emit light in the 555-605 nm range.[191] The emission of the compound $Sr_{0.98}Eu_{0.02}Si_2O_{(5-1.5x)}N_x$ (where x ranges from 1.33 to 2.66) has also been reported when exposed to visible light,[189] making it an excellent green phosphor.[189] These materials can also be doped with two or more lanthanides. For example, $CaSi_2O_2N_2$ improves its photoluminescent properties when doped with Eu^{2+}/Ce^{3+}.[195] Other nitridosilicates have been doped with cerium as $La_3Si_6N_{11}:Ce^{3+}$,[196]

or $CaMg_3SiN_4:Ce^{3+}$ [197] that under excitation in the 445-480 nm range, emit light in the 555-605 nm range.[191] $Y_6Si_3O_9N_4:Ce^{3+}$ produces green emissions with bands centered at 550 nm.[198] Other lanthanides are used to optimize the emission, such as $Ca_{2-x}Si_3O_2N_{4:}x\ Yb^{2+}$ or Dy^{3+}.[199] When this material is doped only with Yb^{2+}, it exhibits green emission at 545 nm, whereas if doped with Dy^{3+}, it emits blue and yellow colors with bands at 485 nm and 585 nm, respectively.[199]

Other researchers have explored modifications of the Si_3N_4 structure by substituting Si for Al and N for O to produce new hosts to dope with Eu^{2+}.[198, 199] Examples of luminescent materials include α-SiAlON:Eu^{2+},[200] which emits green color,[201] and β-SiAlON:Eu^{2+}.[202] M-α-SiAlON:Eu^{2+} (M = Ca, Sr) [192, 203, 204] or $BaAlSi_4O_3N_5:Eu^{2+}$,[205] $CaAlSiN_3:Eu^{2+}$,[48] $Ca_{0.99}Eu_{0.01}AlSi_4N_7$ emit white light with two main signals at 498 and 614 nm when excited at 400 nm.[190] The oxynitride $(Sr_{0.98}Eu_{0.02})(Al_{0.05}Si_{0.95})_6N_8$ emits at 448 nm when irradiated at 400 nm at room temperature, but the emission intensity decreases to 54% at 200°C. $Ba_{1-x}Al_2Si_3O_4N_4$ doped with Yb^{2+} exhibits yellow emission at a wavelength of 518 nm when excited at 254 nm.[206] Despite efforts in the previous years to improve the luminescent properties of silicates during synthesis, certain drawbacks hamper their use. For example, Eu^{2+} doped $MSi_2O_2N_2$ materials (M = Sr, Ba, Ca) lack homogeneity, which leads to a decrease in luminescence. Several synthesis methods have been tried to solve this problem, but the cost-benefit ratio remains unfavourable, and the product yield is low.[207]

1.7 References

(1) Hwang, J.; Feng, Z.; Charles, N.; Wang, X. R.; Lee, D.; Stoerzinger, K. A.; Muy, S.; Rao, R. R.; Lee, D.; Jacobs, R. Tuning perovskite oxides by strain: Electronic structure, properties, and functions in (electro) catalysis and ferroelectricity. *Materials Today* **2019**, *31*, 100-118.
(2) Muller, K.; Bednorz, J. The discovery of high temperature superconductivity. *Recherche (Paris)* **1988**, *195*.
(3) Haertling, G. H. Ferroelectric ceramics: history and technology. *Journal of the American Ceramic Society* **1999**, *82* (4), 797-818.
(4) Schirmer, O.; Thiemann, O.; Wöhlecke, M. Defects in $LiNbO_3$—I. experimental aspects. *Journal of Physics and Chemistry of Solids* **1991**, *52* (1), 185-200.
(5) Jin, S.; Tiefel, T. H.; McCormack, M.; Fastnacht, R.; Ramesh, R.; Chen, L. Thousandfold change in resistivity in magnetoresistive La-Ca-Mn-O films. *Science* **1994**, *264* (5157), 413-415.
(6) Tao, S.; Irvine, J. T. A Redox-stable efficient anode for solid-oxide fuel cells. *Nature Materials* **2003**, *2* (5), 320-323.
(7) Sczancoski, J.; Cavalcante, L.; Joya, M.; Varela, J. A.; Pizani, P.; Longo, E. $SrMoO_4$ powders processed in microwave-hydrothermal: Synthesis, characterization and optical properties. *Chemical Engineering Journal* **2008**, *140* (1-3), 632-637.
(8) Sczancoski, J.; Cavalcante, L.; Joya, M.; Espinosa, J.; Pizani, P.; Varela, J. A.; Longo, E. Synthesis, growth process and photoluminescence properties of $SrWO_4$ powders. *Journal of colloid and interface science* **2009**, *330* (1), 227-236.
(9) Thompson, T. L.; Yates, J. T. Surface science studies of the photoactivation of TiO_2 new photochemical processes. *Chemical reviews* **2006**, *106* (10), 4428-4453.
(10) Fuertes, A. Synthesis and properties of functional oxynitrides–from photocatalysts to CMR materials. *Dalton Transactions* **2010**, *39* (26), 5942-5948.
(11) Schouwink, P.; Ley, M. B.; Tissot, A.; Hagemann, H.; Jensen, T. R.; Smrčok, Ľ.; Černý, R. Structure and properties of complex hydride perovskite materials. *Nature communications* **2014**, *5* (1), 5706.
(12) Yang, C.; Tian, Y.; Pu, J.; Chi, B. Anion fluorine-doped $La_{0.6}Sr_{0.4}Fe_{0.8}Ni_{0.2}O_{3-\delta}$ perovskite cathodes with enhanced electrocatalytic activity for solid oxide electrolysis cell direct CO_2

electrolysis. *ACS Sustainable Chemistry & Engineering* **2022**, *10* (2), 1047-1058.
(13) Fan, L.; Ding, Y.; Luo, J.; Shi, B.; Yao, X.; Wei, C.; Zhang, D.; Wang, G.; Sheng, Y.; Chen, Y. Elucidating the role of chlorine in perovskite solar cells. *Journal of materials chemistry A* **2017**, *5* (16), 7423-7432.
(14) Dou, Y.; Cao, F.; Dudka, T.; Li, Y.; Wang, S.; Zhang, C.; Gao, Y.; Yang, X.; Rogach, A. L. Lattice distortion in mixed-anion lead halide perovskite nanorods leads to their high fluorescence anisotropy. *ACS Materials Letters* **2020**, *2* (7), 814-820.
(15) Chiba, T.; Hayashi, Y.; Ebe, H.; Hoshi, K.; Sato, J.; Sato, S.; Pu, Y.-J.; Ohisa, S.; Kido, J. Anion-exchange red perovskite quantum dots with ammonium iodine salts for highly efficient light-emitting devices. *Nature Photonics* **2018**, *12* (11), 681-687.
(16) Ishikawa, A.; Takata, T.; Kondo, J. N.; Hara, M.; Kobayashi, H.; Domen, K. Oxysulfide $Sm_2Ti_2S_2O_5$ as a stable photocatalyst for water oxidation and reduction under visible light irradiation ($\lambda \leq$ 650 nm). *Journal of the American Chemical Society* **2002**, *124* (45), 13547-13553.
(17) Todorov, T. K.; Tang, J.; Bag, S.; Gunawan, O.; Gokmen, T.; Zhu, Y.; Mitzi, D. B. Beyond 11% efficiency: characteristics of state-of-the-art Cu_2ZnSn (S, Se)$_4$ solar cells. *Advanced Energy Materials* **2013**, *3* (1), 34-38.
(18) Fuertes, A. Metal oxynitrides as emerging materials with photocatalytic and electronic properties. *Materials Horizons* **2015**, *2* (5), 453-461.
(19) Pearson, R. G. Negative electron affinities of nonmetallic elements. *Inorganic Chemistry* **1991**, *30* (14), 2856-2858.
(20) Oka, K.; Oh-ishi, K. Observation of Anion Order in $Pb_2Ti_4O_9F_2$. *Inorganic Chemistry* **2015**, *54* (21), 10239-10242.
(21) Fuertes, A. Prediction of Anion Distributions Using Pauling's Second Rule. *Inorganic Chemistry* **2006**, *45* (24), 9640-9642.
(22) Pauling, L. The principles determining the structure of complex ionic crystals. *Journal of the american chemical society* **1929**, *51* (4), 1010-1026.
(23) Juza, R. Nitrides of metals of the first transition series. In *Advances in Inorganic Chemistry and Radiochemistry*, Vol. 9; Elsevier, 1966; pp 81-131.

(24) Schnick, W. Solid-state chemistry with nonmetal nitrides. *Angewandte Chemie International Edition in English* **1993**, *32* (6), 806-818.
(25) Gregory, D. H. Structural families in nitride chemistry. *Journal of the Chemical Society, Dalton Transactions* **1999**, (3), 259-270.
(26) Eichler, J.; Lesniak, C. Boron nitride (BN) and BN composites for high-temperature applications. *Journal of the European Ceramic Society* **2008**, *28* (5), 1105-1109.
(27) Piazza, G.; Felmetsger, V.; Muralt, P.; Olsson III, R. H.; Ruby, R. Piezoelectric aluminum nitride thin films for microelectromechanical systems. *MRS bulletin* **2012**, *37* (11), 1051-1061.
(28) Liu, L.; Edgar, J. H. Substrates for gallium nitride epitaxy. *Materials Science and Engineering: R: Reports* **2002**, *37* (3), 61-127.
(29) Bhuiyan, A. G.; Hashimoto, A.; Yamamoto, A. Indium nitride (InN): A review on growth, characterization, and properties. *Journal of applied physics* **2003**, *94* (5), 2779-2808.
(30) Shaginyan, L. Synthesis and properties of thallium nitride films. *Materials Chemistry and Physics* **2019**, *227*, 157-162.
(31) Li, L. H.; Chen, Y. Atomically thin boron nitride: unique properties and applications. *Advanced Functional Materials* **2016**, *26* (16), 2594-2608.
(32) Roy, S.; Zhang, X.; Puthirath, A. B.; Meiyazhagan, A.; Bhattacharyya, S.; Rahman, M. M.; Babu, G.; Susarla, S.; Saju, S. K.; Tran, M. K. Structure, properties and applications of two-dimensional hexagonal boron nitride. *Advanced Materials* **2021**, *33* (44), 2101589.
(33) Lueng, C.; Chan, H. L.; Surya, C.; Choy, C. Piezoelectric coefficient of aluminum nitride and gallium nitride. *Journal of applied physics* **2000**, *88* (9), 5360-5363.
(34) Jain, S.; Willander, M.; Narayan, J.; Overstraeten, R. V. III–nitrides: Growth, characterization, and properties. *Journal of Applied Physics* **2000**, *87* (3), 965-1006.
(35) Li, D.; Jiang, K.; Sun, X.; Guo, C. AlGaN photonics: recent advances in materials and ultraviolet devices. *Advances in Optics and Photonics* **2018**, *10* (1), 43-110.
(36) Shah, E. V.; Roy, D. R. Density functional investigation on hexagonal nanosheets and bulk thallium nitrides for possible thermoelectric applications. *Applied Nanoscience* **2019**, *9*, 33-42.

(37) Wang, L.; Snidle, R. W.; Gu, L. Rolling contact silicon nitride bearing technology: a review of recent research. *Wear* **2000**, *246* (1), 159-173.
(38) Zhou, H.; Feng, T. Theoretical upper limits of the thermal conductivity of Si3N4. *Applied Physics Letters* **2023**, *122* (18).
(39) Manghnani, S.; Shekhawat, D.; Goswami, C.; Patnaik, T. K.; Singh, T. Mechanical and tribological characteristics of Si_3N_4 reinforced aluminium matrix composites: A short review. *Materials Today: Proceedings* **2021**, *44*, 4059-4064.
(40) Mohanavel, V.; Ashraff Ali, K. S.; Prasath, S.; Sathish, T.; Ravichandran, M. Microstructural and tribological characteristics of AA6351/Si_3N_4 composites manufactured by stir casting. *Journal of Materials Research and Technology* **2020**, *9* (6), 14662-14672.
(41) Veprek, S.; Roos, J. Dielectric properties of phosphorus nitride films. *Journal of Physics and Chemistry of Solids* **1976**, *37* (5), 554-554.
(42) Tolhurst, T. M.; Braun, C.; Boyko, T. D.; Schnick, W.; Moewes, A. Experiment-Driven Modeling of Crystalline Phosphorus Nitride P_3N_5: Wide-Ranging Implications from a Unique Structure. *Chemistry–A European Journal* **2016**, *22* (30), 10475-10483.
(43) Elzer, E.; Niklaus, R.; Strobel, P. J.; Weiler, V.; Schmidt, P. J.; Schnick, W. $MBe_{20}N_{14}:Eu^{2+}$ (M= Sr, Ba): Highly condensed nitridoberyllates with exceptional highly energetic Eu2+ luminescence. *Chemistry of Materials* **2019**, *31* (9), 3174-3182.
(44) Tolhurst, T. M.; Braun, C.; Schnick, W.; Moewes, A. Comprehensive band gap and electronic structure investigations of the prominent phosphors $M_2Si_5N_8$: Eu^{2+} (M= Ca, Sr, Ba) determined using soft X-ray spectroscopy and density functional theory. *The Journal of Physical Chemistry C* **2021**, *125* (46), 25799-25806.
(45) Le Toquin, R.; Cheetham, A. Red-emitting cerium-based phosphor materials for solid-state lighting applications. *Chemical Physics Letters* **2006**, *423* (4-6), 352-356.
(46) Ueda, J.; Leaño, J. L.; Richard, C.; Asami, K.; Tanabe, S.; Liu, R.-S. Broadband near-infrared persistent luminescence of $Ba[Mg_2Al_2N_4]$ with Eu^{2+} and Tm^{3+} after red light charging. *Journal of Materials Chemistry C* **2019**, *7* (6), 1705-1712..
(47) Pust, P.; Weiler, V.; Hecht, C.; Tücks, A.; Wochnik, A. S.; Henß, A.-K.; Wiechert, D.; Scheu, C.; Schmidt, P. J.; Schnick, W. Narrow-band red-emitting Sr $[LiAl_3N_4]$: Eu^{2+} as a next-generation LED-phosphor material. *Nature Materials* **2014**, *13* (9), 891-896.

(48) Uheda, K.; Hirosaki, N.; Yamamoto, Y.; Naito, A.; Nakajima, T.; Yamamoto, H. Luminescence properties of a red phosphor, $CaAlSiN_3$: Eu^{2+}, for white light-emitting diodes. *Electrochemical and Solid-State letters* **2006**, *9* (4), H22.
(49) Wendl, S.; Eisenburger, L.; Strobel, P.; Günther, D.; Wright, J. P.; Schmidt, P. J.; Oeckler, O.; Schnick, W. Nitridophosphate-based ultra-narrow-band blue-emitters: luminescence properties of AEP_8N_{14}: Eu^{2+} (AE= Ca, Sr, Ba). *Chemistry–A European Journal* **2020**, *26* (32), 7292-7298.
(50) Ambach, S. J.; Somers, C.; de Boer, T.; Eisenburger, L.; Moewes, A.; Schnick, W. Structural influence of lone pairs in GeP_2N_4, a Germanium (II) Nitridophosphate. *Angewandte Chemie International Edition* **2023**, *62* (3), e202215393.
(51) Gillan, E. G.; Kaner, R. B. Rapid solid-state synthesis of refractory nitrides. *Inorganic chemistry* **1994**, *33* (25), 5693-5700.
(52) Zerr, A.; Miehe, G.; Riedel, R. Synthesis of cubic zirconium and hafnium nitride having Th_3P_4 structure. *Nature Materials* **2003**, *2* (3), 185-189.
(53) Hyett, G.; Green, M. A.; Parkin, I. P. The use of combinatorial chemical vapor deposition in the synthesis of $Ti_{3-\delta}O_4N$ with $0.06 < \delta < 0.25$: a titanium oxynitride phase isostructural to anosovite. *Journal of the American Chemical Society* **2007**, *129* (50), 15541-15548.
(54) Dearnley, P. A.; Trent, E. Wear mechanisms of coated carbide tools. *Metals Technology* **1982**, *9* (1), 60-75.
(55) Hultman, L. Thermal stability of nitride thin films. *Vacuum* **2000**, *57* (1), 1-30.
(56) Marchand, R.; Tessier, F.; DiSalvo, F. J. New routes to transition metal nitrides: and characterization of new phases. *Journal of Materials Chemistry* **1999**, *9* (1), 297-304.
(57) Theerthagiri, J.; Durai, G.; Karuppasamy, K.; Arunachalam, P.; Elakkiya, V.; Kuppusami, P.; Maiyalagan, T.; Kim, H.-S. Recent advances in 2-D nanostructured metal nitrides, carbides, and phosphides electrodes for electrochemical supercapacitors – A brief review. *Journal of Industrial and Engineering Chemistry* **2018**, *67*, 12-27.
(58) Shu, D.; Lv, C.; Cheng, F.; He, C.; Yang, K.; Nan, J.; Long, L. Enhanced capacitance and rate capability of nanocrystalline VN as electrode materials for supercapacitors. *Int. J. Electrochem. Sci* **2013**, *8* (1), 1209-1225.

(59) Sepúlveda, C.; Leiva, K.; García, R.; Radovic, L. R.; Ghampson, I. T.; DeSisto, W. J.; Fierro, J. L. G.; Escalona, N. Hydrodeoxygenation of 2-methoxyphenol over Mo_2N catalysts supported on activated carbons. *Catalysis Today* **2011**, *172* (1), 232-239.
(60) Yu, F.; Zhou, H.; Zhu, Z.; Sun, J.; He, R.; Bao, J.; Chen, S.; Ren, Z. Three-dimensional nanoporous iron nitride film as an efficient electrocatalyst for water oxidation. *ACS Catalysis* **2017**, *7* (3), 2052-2057.
(61) Guo, H.-P.; Ruan, B.-Y.; Luo, W.-B.; Deng, J.; Wang, J.-Z.; Liu, H.-K.; Dou, S.-X. Ultrathin and edge-enriched holey nitride nanosheets as bifunctional electrocatalysts for the oxygen and hydrogen evolution reactions. *ACS Catalysis* **2018**, *8* (10), 9686-9696.
(62) Shanker, G. S.; Ogale, S. Faceted colloidal metallic Ni_3N nanocrystals: size-controlled solution-phase synthesis and electrochemical overall water splitting. *ACS Applied Energy Materials* **2021**, *4* (3), 2165-2173.
(63) Cheng, Z.; Qi, W.; Pang, C. H.; Thomas, T.; Wu, T.; Liu, S.; Yang, M. Recent advances in transition metal nitride-based materials for photocatalytic applications. *Advanced Functional Materials* **2021**, *31* (26), 2100553.
(64) Han, D.; Cai, J.; Xie, Y.; Wu, Y.; Niu, S.; Zang, Y.; Pan, H.; Qu, W.; Wang, G.; Qian, Y. Constructing complementary catalytic components on Co_4N nanowires to achieve efficient hydrogen evolution catalysis. *Advanced Energy and Sustainability Research* **2022**, *3* (6), 2100219.
(65) Talley, K. R.; Perkins, C. L.; Diercks, D. R.; Brennecka, G. L.; Zakutayev, A. Synthesis of $LaWN_3$ nitride perovskite with polar symmetry. *Science* **2021**, *374* (6574), 1488-1491.
(66) Trócoli, R.; Frontera, C.; Oró-Solé, J.; Ritter, C.; Alemany, P.; Canadell, E.; Palacín, M. R.; Fontcuberta, J.; Fuertes, A. $MnTa_2N_4$: a ternary nitride spinel with a strong magnetic frustration. *Chemistry of Materials* **2022**, *34* (13), 6098-6107.
(67) Molinari, V.; Giordano, C.; Antonietti, M.; Esposito, D. Titanium nitride-nickel nanocomposite as heterogeneous catalyst for the hydrogenolysis of aryl ethers. *Journal of the American Chemical Society* **2014**, *136* (5), 1758-1761.
(68) Chen, W. F.; Sasaki, K.; Ma, C.; Frenkel, A. I.; Marinkovic, N.; Muckerman, J. T.; Zhu, Y.; Adzic, R. R. Hydrogen-evolution catalysts

based on non-noble metal nickel–molybdenum nitride nanosheets. *Angewandte Chemie International Edition* **2012**, *51* (25), 6131-6135.
(69) Cao, B.; Veith, G. M.; Neuefeind, J. C.; Adzic, R. R.; Khalifah, P. G. Mixed close-packed cobalt molybdenum nitrides as non-noble metal electrocatalysts for the hydrogen evolution reaction. *Journal of the American Chemical Society* **2013**, *135* (51), 19186-19192.
(70) Wang, Q.; Shang, L.; Shi, R.; Zhang, X.; Waterhouse, G. I. N.; Wu, L.-Z.; Tung, C.-H.; Zhang, T. 3D carbon nanoframe scaffold-immobilized Ni_3FeN nanoparticle electrocatalysts for rechargeable zinc-air batteries' cathodes. *Nano Energy* **2017**, *40*, 382-389.
(71) Yuan, Y.; Adimi, S.; Thomas, T.; Wang, J.; Guo, H.; Chen, J.; Attfield, J. P.; DiSalvo, F. J.; Yang, M. Co_3Mo_3N-An efficient multifunctional electrocatalyst. *The Innovation* **2021**, *2* (2).
(72) Cui, Z.; Burns, R. G.; DiSalvo, F. J. Mesoporous $Ti_{0.5}Nb_{0.5}N$ ternary nitride as a novel noncarbon support for oxygen reduction reaction in acid and alkaline electrolytes. *Chemistry of Materials* **2013**, *25* (19), 3782-3784.
(73) Marchand, R.; Laurent, Y.; Guyader, J.; L'Haridon, P.; Verdier, P. Nitrides and oxynitrides: Preparation, crystal chemistry and properties. *Journal of the European Ceramic Society* **1991**, *8* (4), 197-213.
(74) Pors, F.; Marchand, R.; Laurent, Y. Une nouvelle famille de pyrochlores: les oxynitrures $Ln_2Ta_2O_5N_2$. Préparation et étude cristallochimique. *Journal of Solid State Chemistry* **1993**, *107* (1), 39-42.
(75) Malik, V.; Bhardwaj, N.; Uma, S. Transformation of scheelite M_2MoTiO_8 (M= Eu, Gd, Dy, Y) and zircon MVO_4 (M= Ce, Sm, Gd, Dy) oxides to fluorite oxynitrides and perovskite oxides under mild ammonolysis conditions. *Solid State Sciences* **2019**, *89*, 114-120.
(76) Kawahara, T.; Murata, T.; Tokuhara, Y.; Tezuka, K.; Shan, Y. J. Preparation of new apatite-type oxynitrides $Pr_xSi_3O_{(3x-\ 3y+\ 12)/2}N_y$(x= 4.4 to 4.8 and y= 0.8 to 1.1) in sealed silica tubes. *Journal of Solid State Chemistry* **2020**, *288*, 121406.
(77) Wang, H.-C.; Schmidt, J.; Botti, S.; Marques, M. A. A high-throughput study of oxynitride, oxyfluoride and nitrofluoride perovskites. *Journal of Materials Chemistry A* **2021**, *9* (13), 8501-8513.
(78) Veith, G.; Greenblatt, M.; Croft, M.; Goodenough, J. Synthesis and characterization of the oxynitride pyrochlore-$Sm_2Mo_2O_{3.83}N_{3.17}$. *Materials Research Bulletin* **2001**, *36* (7-8), 1521-1530.
(79) Bhat, S.; Wiehl, L.; Haseen, S.; Kroll, P.; Glazyrin, K.; Gollé-Leidreiter, P.; Kolb, U.; Farla, R.; Tseng, J. C.; Ionescu, E. A novel high-

pressure tin oxynitride Sn_2N_2O. *Chemistry–A European Journal* **2020**, *26* (10), 2187-2194.
(80) Kuriki, R.; Ichibha, T.; Hongo, K.; Lu, D.; Maezono, R.; Kageyama, H.; Ishitani, O.; Oka, K.; Maeda, K. A stable, narrow-gap oxyfluoride photocatalyst for visible-light hydrogen evolution and carbon dioxide reduction. *Journal of the American Chemical Society* **2018**, *140* (21), 6648-6655.
(81) Yang, M.; Oró-Solé, J.; Kusmartseva, A.; Fuertes, A.; Attfield, J. P. Electronic tuning of two metals and colossal magnetoresistances in $EuWO_{1+x}N_{2-x}$ Perovskites. *Journal of the American Chemical Society* **2010**, *132* (13), 4822-4829.
(82) LaCoste, J. D.; Zakutayev, A.; Fei, L. A Review on Lithium Phosphorus Oxynitride. *The Journal of Physical Chemistry C* **2021**, *125* (7), 3651-3667.
(83) Jorge, A. B.; Fraxedas, J.; Cantarero, A.; Williams, A. J.; Rodgers, J.; Attfield, J. P.; Fuertes, A. Nitrogen Doping of Ceria. *Chemistry of Materials* **2008**, *20* (5), 1682-1684.
(84) Hitoki, G.; Takata, T.; Kondo, J. N.; Hara, M.; Kobayashi, H.; Domen, K. An oxynitride, TaON, as an efficient water oxidation photocatalyst under visible light irradiation ($\lambda \leq$ 500 nm). *Chemical Communications* **2002**, (16), 1698-1699.
(85) Asahi, R.; Morikawa, T.; Ohwaki, T.; Aoki, K.; Taga, Y. Visible-light photocatalysis in nitrogen-doped titanium oxides. *Science* **2001**, *293* (5528), 269-271.
(86) Ni, M.; Leung, M. K. H.; Leung, D. Y. C.; Sumathy, K. A review and recent developments in photocatalytic water-splitting using TiO_2 for hydrogen production. *Renewable and Sustainable Energy Reviews* **2007**, *11* (3), 401-425.
(87) Boddy, P. Oxygen evolution on semiconducting TiO_2. *Journal of The Electrochemical Society* **1968**, *115* (2), 199.
(88) Balogun, K.; Ganesan, A.; Chukwunenye, P.; Gharaee, M.; Adesope, Q.; Nemsak, S.; Bagus, P.; Cundari, T.; D'Souza, F.; Kelber, J. Vanadium oxide, vanadium oxynitride, and cobalt oxynitride as electrocatalysts for the nitrogen reduction reaction: a review of recent developments. *Journal of Physics: Condensed Matter* **2023**.
(89) Osonkie, A.; Ganesan, A.; Chukwunenye, P.; Anwar, F.; Balogun, K.; Gharaee, M.; Rashed, I.; Cundari, T. R.; D'Souza, F.; Kelber, J. A. Electrocatalytic reduction of nitrogen to ammonia: the roles of lattice o

and n in reduction at vanadium oxynitride surfaces. *ACS Applied Materials & Interfaces* **2022**, *14* (1), 531-542.
(90) Chukwunenye, P.; Ganesan, A.; Gharaee, M.; Balogun, K.; Anwar, F.; Adesope, Q.; Cundari, T. R.; D'Souza, F.; Kelber, J. A. Electrocatalytic selectivity for nitrogen reduction vs. hydrogen evolution: a comparison of vanadium and cobalt oxynitrides at different pH values. *Journal of Materials Chemistry A* **2022**, *10* (40), 21401-21415.
(91) Camp, P. J.; Fuertes, A.; Attfield, J. P. Subextensive entropies and open order in perovskite oxynitrides. *Journal of the American Chemical Society* **2012**, *134* (15), 6762-6766.
(92) Kim, Y.-I.; Woodward, P. M.; Baba-Kishi, K. Z.; Tai, C. W. Characterization of the structural, optical, and dielectric properties of oxynitride perovskites AMO_2N (A= Ba, Sr, Ca; M= Ta, Nb). *Chemistry of Materials* **2004**, *16* (7), 1267-1276.
(93) Jorge, A. B.; Oró-Solé, J.; Bea, A. M.; Mufti, N.; Palstra, T. T. M.; Rodgers, J. A.; Attfield, J. P.; Fuertes, A. Large coupled magnetoresponses in $EuNbO_2N$. *Journal of the American Chemical Society* **2008**, *130* (38), 12572-12573.
(94) Clarke, S. J.; Hardstone, K. A.; Michie, C. W.; Rosseinsky, M. J. High-temperature synthesis and structures of perovskite and n = 1 ruddlesden−popper tantalum oxynitrides. *Chemistry of Materials* **2002**, *14* (6), 2664-2669.
(95) Kasahara, A.; Nukumizu, K.; Hitoki, G.; Takata, T.; Kondo, J. N.; Hara, M.; Kobayashi, H.; Domen, K. Photoreactions on $LaTiO_2N$ under visible light irradiation. *The Journal of Physical Chemistry A* **2002**, *106* (29), 6750-6753.
(96) Ida, S.; Okamoto, Y.; Matsuka, M.; Hagiwara, H.; Ishihara, T. Preparation of tantalum-based oxynitride nanosheets by exfoliation of a layered oxynitride, $CsCa_2Ta_3O_{10-x}N_y$, and their photocatalytic activity. *Journal of the American Chemical Society* **2012**, *134* (38), 15773-15782.
(97) Kitano, M.; Hara, M. Heterogeneous photocatalytic cleavage of water. *Journal of Materials Chemistry* **2010**, *20* (4), 627-641.
(98) Oehler, F.; Ebbinghaus, S. G. Photocatalytic properties of CoO_x-loaded nano-crystalline perovskite oxynitrides ABO_2N (A = Ca, Sr, Ba, La; B = Nb, Ta). *Solid State Sciences* **2016**, *54*, 43-48.
(99) Wang, Y.; Kang, Y.; Zhu, H.; Liu, G.; Irvine, J. T.; Xu, X. Perovskite oxynitride solid solutions of $LaTaON_2$-$CaTaO_2N$ with greatly enhanced photogenerated charge separation for solar-driven overall water splitting. *Advanced Science* **2021**, *8* (2), 2003343.

(100) Wu, Y.; Li, W.; Zheng, Y.; Xu, Y.; Wen, D.; Molokeev, M. S.; Pan, Z. Apatite oxynitride phosphor $(Mg,Y)_5Si_3(O,N)_{13}:Ce^{3+}$, Mn^{2+}: A single-phased host with solar-like and efficient emission. *Journal of the American Ceramic Society* **2023**, *106* (5), 2985-2996.
(101) Zheng, B.; Song, Y.; Zheng, Z.; Zhao, Y.; Yang, Q.; Shi, Z.; Zou, B.; Zou, H. Eu^{2+}-Doped $Ca_4Y_3Si_7O_{15}N_5$ phosphor with high thermal stability and pressure sensitivity for dual-functional applications in w-leds and pressure sensors. *Inorganic Chemistry* **2023**, *62* (10), 4361-4372.
(102) Wang, X.-M.; Wang, C.-H.; Kuang, X.-J.; Zou, R.-Q.; Wang, Y.-X.; Jing, X.-P. Promising oxonitridosilicate phosphor host $Sr_3Si_2O_4N_2$: Synthesis, structure, and luminescence properties activated by Eu^{2+} and Ce^{3+}/Li^{+} for pc-LEDs. *Inorganic Chemistry* **2012**, *51* (6), 3540-3547.
(103) Chiu, Y.-C.; Huang, C.-H.; Lee, T.-J.; Liu, W.-R.; Yeh, Y.-T.; Jang, S.-M.; Liu, R.-S. Eu^{2+}-activated silicon-oxynitride $Ca_3Si_2O_4N_2$: a green-emitting phosphor for white LEDs. *Optics Express* **2011**, *19* (103), A331-A339.
(104) Braun, C.; Seibald, M.; Boerger, S. L.; Oeckler, O.; Boyko, T. D.; Moewes, A.; Miehe, G.; Tücks, A.; Schnick, W. Material properties and structural characterization of $M_3Si_6O_{12}N_2$: Eu^{2+} (M= Ba, Sr)-a comprehensive study on a promising green phosphor for pc-LEDs. *Chemistry–A European Journal* **2010**, *16* (31), 9646-9657.
(105) Li, Y.; Delsing, A.; De With, G.; Hintzen, H. Luminescence properties of Eu^{2+}-activated alkaline-earth silicon-oxynitride $MSi_2O_{2-\delta}N_{2+2/3\delta}$ (M= Ca, Sr, Ba): a promising class of novel LED conversion phosphors. *Chemistry of materials* **2005**, *17* (12), 3242-3248.
(106) Black, A. P.; Denault, K. A.; Oró-Solé, J.; Goñi, A. R.; Fuertes, A. Red luminescence and ferromagnetism in europium oxynitridosilicates with a β-K_2 SO_4 structure. *Chemical Communications* **2015**, *51* (11), 2166-2169.
(107) Jack, K.; Wilson, W. Ceramics based on the Si-Al-ON and related systems. *Nature Physical Science* **1972**, *238* (80), 28-29.
(108) Ding, J.; Wei, Y.; Liu, W.; Li, Y.; Wu, Q.; Zhou, J. Highly efficient and thermally stable narrow-band cyan-emitting aluminum oxynitride phosphor for WLEDs and FEDs. *Chemical Engineering Journal* **2021**, *403*, 126382.
(109) Asami, K.; Shiraiwa, M.; Ueda, J.; Fujii, K.; Hongo, K.; Maezono, R.; Brik, M. G.; Yashima, M.; Tanabe, S. Crystal structure analysis and evidence of mixed anion coordination at the Ce^{3+} site in

$Y_3Al_2(Al,Si)_3(O,N)_{12}$ oxynitride garnet phosphor. *Journal of Materials Chemistry C* **2019**, *7* (5), 1330-1336.
(110) Meyer, G. The oxidation of metals with Liebig acids. *Zeitschrift für Anorganische und Allgemeine Chemie* **2008**, *634* (2), 201-222.
(111) Brauer, G. Nitrides, carbonitrides and oxynitrides of niobium. *Journal of the Less Common Metals* **1960**, *2* (2), 131-137.
(112) Marchand, R. Nitrogen-containing phosphate glasses. *Journal of Non-Crystalline Solids* **1983**, *56* (1), 173-178.
(113) Bacher, P.; Antoine, P.; Marchand, R.; L'Haridon, P.; Laurent, Y.; Roult, G. Time-of-flight neutron diffraction study of the structure of the perovskite-type oxynitride $LaWO_{0.6}N_{2.4}$. *Journal of Solid State Chemistry* **1988**, *77* (1), 67-71.
(114) Antoine, P.; Marchand, R.; Laurent, Y.; Michel, C.; Raveau, B. On the electrical properties of the perovskites $LnWO_xN_{3-x}$. *Materials Research Bulletin* **1988**, *23* (7), 953-957.
(115) Antoine, P.; Assabaa, R.; L'Haridon, P.; Marchand, R.; Laurent, Y.; Michel, C.; Raveau, B. Transport properties of the new perovskite-type $LaVO_3 \Leftrightarrow xN_x$ Oxynitrides. *Materials Science and Engineering: B* **1989**, *5* (1), 43-46.
(116) Orhan, E.; Tessier, F.; Marchand, R. Synthesis and energetics of yellow TaON. *Solid State Sciences* **2002**, *4* (8), 1071-1076.
(117) Schillinga, H.; Irrana, E.; Wolffb, H.; Bredowc, T.; Dronskowskib, R.; Lercha, M. γ-TaON: A New Metastable Polymorph of Tantalum Oxynitride. *Zeitschrift für Anorganische und Allgemeine Chemie*, **2006**, *632* (12-13), 2136-2136
(118) Martínez-Ferrero, E.; Sakatani, Y.; Boissière, C.; Grosso, D.; Fuertes, A.; Fraxedas, J.; Sanchez, C. Nanostructured titanium oxynitride porous thin films as efficient visible-active photocatalysts. *Advanced Functional Materials* **2007**, *17* (16), 3348-3354.
(119) Gilles, J. *Preparation by solid state reaction and structures of zirconium oxynitrides*; CNRS, Vitry-sur Seine, France, 1962.
(120) Fuertes, A. Nitride tuning of transition metal perovskites. *APL Materials* **2020**, *8* (2).
(121) Iborra-Torres, A.; Kulak, A. N.; Palgrave, R. G.; Hyett, G. Demonstration of visible light-activated photocatalytic self-cleaning by thin films of perovskite tantalum and niobium oxynitrides. *ACS Applied Materials & Interfaces* **2020**, *12* (30), 33603-33612.
(122) Li, W.; Li, D.; Gao, X.; Gurlo, A.; Zander, S.; Jones, P.; Navrotsky, A.; Shen, Z.; Riedel, R.; Ionescu, E. A study on the thermal

conversion of scheelite-type ABO_4 into perovskite-type AB $(O, N)_3$. *Dalton Transactions* **2015**, *44* (17), 8238-8246.
(123) Brosset, C.; Idrestedt, I. Crystal structure of silicon oxynitride, Si_2N_2O. *Nature* **1964**, *201* (4925), 1211-1211.
(124) Yao, L.; Fang, Q.; Hu, G.; Li, J. Z. Preparation and properties of some Li-Al-Si-ON glasses. *Journal of Non-Crystalline Solids* **1983**, *56* (1-3), 167-172.
(125) Sakka, S.; Kamiya, K.; Yoko, T. Preparation and properties of CaAlSiON oxynitride glasses. *Journal of Non-Crystalline Solids* **1983**, *56* (1-3), 147-152.
(126) Köllisch, K.; Schnick, W. $Ce_{16}Si_{15}O_6N_{32}$–ein Oxonitridosilicat mit Silicium in oktaedrischer Stickstoff-Koordination. *Angewandte Chemie* **1999**, *111* (3), 368-370.
(127) Lauterbach, R.; Schnick, W. $Sm_2Si_3O_3N_4$ und $Ln_2Si_{2,5}Al_{0,5}O_{3,5}N_{3,5}$ (Ln= Ce, Pr, Nd, Sm, Gd)–neuer synthetischer zugang zu n-haltigen melilith-phasen und deren einkristall-röntgenstrukturanalyse. *Zeitschrift für Anorganische und Allgemeine Chemie* **1999**, *625* (3), 429-434.
(128) Lauterbach, R.; Schnick, W. Synthese, kristallstruktur und eigenschaften eines neuen Sialons–$SrSiAl_2O_3N_2$. *Zeitschrift für Anorganische und Allgemeine Chemie* **1998**, *624* (7), 1154-1158.
(129) Schnick, W.; Huppertz, H.; Lauterbach, R. High Temperature Syntheses of Novel Nitrido-And Oxonitrido-Silicates and SiAlONS Using Rf Furnaces. *Journal of Materials Chemistry* **1999**, *9* (1), 289-296.
(130) Lauterbach, R.; Schnick, W. $Nd_3Si_5AlON_{10}$–synthese, kristallstruktur und eigenschaften eines SiAlONS im $La_3Si_6N_{11}$-Strukturtyp. *Zeitschrift für Anorganische und Allgemeine Chemie* **2000**, *626* (1), 56-61.
(131) Lauterbach, R.; Schnick, W. High-temperature synthesis and single-crystal X-ray structure determination of $Sr_{10}Sm_6Si_{30}Al_6O_7N_{54}$ — a layered SiAlON with an ordered distribution of Si, Al, O, and N. *Solid State Sciences* **2000**, *2* (4), 463-472.
(132) Schmid, S.; Schnick, W. Synthese und kristallstruktur des ersten oxonitridoborates—$Sr_3[B_3O_3N_3]$. *Zeitschrift für Anorganische und Allgemeine Chemie* **2002**, *628* (5), 1192-1195.
(133) Black, A. P.; Denault, K. A.; Frontera, C.; Seshadri, R.; Goñi, A. R.; Fuertes, A. Emission colour tuning through coupled N/La introduction in $Sr_2SiO_4:Eu^{2+}$. *Journal of Materials Chemistry C* **2015**, *3* (43), 11471-11477.

(134) Kitagawa, Y.; Ueda, J.; Fujii, K.; Yashima, M.; Funahashi, S.; Nakanishi, T.; Takeda, T.; Hirosaki, N.; Hongo, K.; Maezono, R.; et al. Site-Selective Eu^{3+} Luminescence in the Monoclinic Phase of $YSiO_2N$. *Chemistry of Materials* **2021**, *33* (22), 8873-8885.
(135) Barzowska, J.; Majewska, N.; Jankowski, D.; Grzegorczyk, M.; Mahlik, S.; Michalik, D.; Sopicka-Lizer, M.; Aleshkevych, P.; Zhydachevskyy, Y.; Suchocki, A. Mechanism of the luminescence enhancement of $SrSi_2N_2O_2:Eu^{2+}$ phosphor via manganese addition. *The Journal of Physical Chemistry C* **2022**, *126* (11), 5292-5301.
(136) Sakata, T.; Yoshiyuki, R.; Okada, R.; Urushidani, S.; Tarutani, N.; Katagiri, K.; Inumaru, K.; Koyama, K.; Masubuchi, Y. Environmentally benign synthesis and color tuning of strontium–tantalum perovskite oxynitride and its solid solutions. *Inorganic Chemistry* **2021**, *60* (7), 4852-4859.
(137) Niu, W.-B.; Sun, S.-K.; Guo, W.-M.; Chen, S.-L.; Lv, M.; Lin, H.-T.; Wang, C.-Y. Synthesis of perovskite $BaTaO_2N$ and $SrNbO_2N$ using TaN/NbN as the nitrogen source. *Ceramics International* **2018**, *44* (18), 23324-23328.
(138) Black, A. P.; Suzuki, H.; Higashi, M.; Frontera, C.; Ritter, C.; De, C.; Sundaresan, A.; Abe, R.; Fuertes, A. New rare earth hafnium oxynitride perovskites with photocatalytic activity in water oxidation and reduction. *Chemical Communications* **2018**, *54* (12), 1525-1528.
(139) Yamamoto, T.; Chikamatsu, A.; Kitagawa, S.; Izumo, N.; Yamashita, S.; Takatsu, H.; Ochi, M.; Maruyama, T.; Namba, M.; Sun, W. Strain-induced creation and switching of anion vacancy layers in perovskite oxynitrides. *Nature Communications* **2020**, *11* (1), 5923.
(140) Yang, M.; Oró-Solé, J.; Fuertes, A.; Attfield, J. P. Topochemical synthesis of europium molybdenum oxynitride pyrochlores. *Chemistry of Materials* **2010**, *22* (14), 4132-4134.
(141) Ceravola, R.; Frontera, C.; Oró-Solé, J.; Black, A. P.; Ritter, C.; Mata, I.; Molins, E.; Fontcuberta, J.; Fuertes, A. Topochemical nitridation of Sr_2FeMoO 6. *Chemical Communications* **2019**, *55* (21), 3105-3108.
(142) Ceravola, R.; Oró-Solé, J.; Black, A. P.; Ritter, C.; Orench, I. P.; Mata, I.; Molins, E.; Frontera, C.; Fuertes, A. Topochemical synthesis of cation ordered double perovskite oxynitrides. *Dalton Transactions* **2017**, *46* (16), 5128-5132.
(143) Mogi, H.; Kato, K.; Yasuda, S.; Kanazawa, T.; Miyoshi, A.; Nishioka, S.; Oshima, T.; Tang, Y.; Yokoi, T.; Nozawa, S.; et al. Control

of the photocatalytic activity of metastable layered oxynitride $K_2LaTa_2O_6N$ through topochemical transformation of tuned oxide precursors. *Chemistry of Materials* **2021**, *33* (16), 6443-6452.
(144) Tang, Y.; Kato, K.; Oshima, T.; Mogi, H.; Miyoshi, A.; Fujii, K.; Yanagisawa, K.-i.; Kimoto, K.; Yamakata, A.; Yashima, M.; et al. Synthesis of three-layer perovskite Oxynitride $K_2Ca_2Ta_3O_9N{\cdot}2H_2O$ and photocatalytic activity for h_2 evolution under visible light. *Inorganic Chemistry* **2020**, *59* (15), 11122-11128.
(145) Yajima, T.; Takeiri, F.; Aidzu, K.; Akamatsu, H.; Fujita, K.; Yoshimune, W.; Ohkura, M.; Lei, S.; Gopalan, V.; Tanaka, K. A labile hydride strategy for the synthesis of heavily nitridized $BaTiO_3$. *Nature Chemistry* **2015**, *7* (12), 1017-1023.
(146) Mikita, R.; Aharen, T.; Yamamoto, T.; Takeiri, F.; Ya, T.; Yoshimune, W.; Fujita, K.; Yoshida, S.; Tanaka, K.; Batuk, D.; et al. Topochemical nitridation with anion vacancy-assisted N^{3-}/O^{2-} exchange. *Journal of the American Chemical Society* **2016**, *138* (9), 3211-3217.
(147) Chen, W.; Li, J.; Wang, Z.; Wang, H.; Li, Y.; Tang, L. Synthesis of TiO_xN_y oxynitrides with a tunable nitrogen content. *Dalton Transactions* **2024**, *53* (3), 1265-1273,
(148) Tian, F.; Xu, Q.; Chen, W.; Liu, X.; Tang, L. Layered oxide precursor strategy for the synthesizing of titanium oxynitrides. *Journal of Solid State Chemistry* **2024**, *331*, 124551.
(149) Chen, W.; Wang, Z.; Wang, P.; Li, J.; Wang, J.; Tang, L. Cost-effective preparation of layered tantalum oxynitrides for visible light-driven photocatalysis. *Dalton Transactions* **2023**, *52* (10), 3127-3136.
(150) Cordes, N.; Nentwig, M.; Eisenburger, L.; Oeckler, O.; Schnick, W. Ammonothermal synthesis of the mixed-valence nitrogen-rich europium tantalum Ruddlesden-Popper phase $Eu^{II}Eu^{III}{}_2Ta_2N_4O_3$. *European Journal of Inorganic Chemistry* **2019**, *2019* (17), 2304-2311.
(151) Cordes, N.; Niklaus, R.; Schnick, W. Ammonothermal crystal growth of $ATaN_2$ with A = Na, K, Rb, and Cs and their optical and electronic properties. *Crystal Growth & Design* **2019**, *19* (6), 3484-3490.
(152) Yang, M.; Rodgers, J. A.; Middler, L. C.; Oró-Solé, J.; Jorge, A. B.; Fuertes, A.; Attfield, J. P. Direct solid-state synthesis at high pressures of new mixed-metal oxynitrides: $RZrO_2N$ (R = Pr, Nd, and Sm). *Inorganic Chemistry* **2009**, *48* (24), 11498-11500.
(153) Tassel, C.; Kuno, Y.; Goto, Y.; Yamamoto, T.; Brown, C. M.; Hester, J.; Fujita, K.; Higashi, M.; Abe, R.; Tanaka, K. $MnTaO_2N$: polar

$LiNbO_3$-type oxynitride with a helical spin order. *Angewandte Chemie* **2015**, *127* (2), 526-531.
(154) Wendl, S.; Mallmann, M.; Strobel, P.; Schmidt, P. J.; Schnick, W. Ammonothermal synthesis of Ba_2PO_3N–an oxonitridophosphate with non-condensed PO_3N tetrahedra. *European Journal of Inorganic Chemistry* **2020**, *2020* (10), 841-846.
(155) Mallmann, M.; Maak, C.; Schnick, W. Ammonothermal synthesis and crystal growth of the chain-type oxonitridosilicate $Ca_{1+x}Y_{1-x}SiN_{3-x}O_x$ (x> 0). *Zeitschrift für Anorganische und Allgemeine Chemie* **2020**, *646* (18), 1539-1544.
(156) Goldschmidt, V. M. Die gesetze der krystallochemie. *Naturwissenschaften* **1926**, *14* (21), 477-485.
(157) Vasala, S.; Karppinen, M. $A_2B'B''O_6$ perovskites: A review. *Progress in Solid State Chemistry* **2015**, *43* (1), 1-36.
(158) Schneemeyer, L.; Thomas, J.; Siegrist, T.; Batlogg, B.; Rupp, L.; Opila, R.; Cava, R.; Murphy, D. Growth and structural characterization of superconducting $Ba_{1-x}K_xBiO_3$ single crystals. *Nature* **1988**, *335* (6189), 421-423.
(159) Wu, M.-K.; Ashburn, J. R.; Torng, C.; Hor, P.-H.; Meng, R. L.; Gao, L.; Huang, Z. J.; Wang, Y.; Chu, a. Superconductivity at 93 K in a new mixed-phase Y-Ba-Cu-O compound system at ambient pressure. *Physical Review Letters* **1987**, *58* (9), 908.
(160) Moritomo, Y.; Asamitsu, A.; Kuwahara, H.; Tokura, Y. Giant magnetoresistance of manganese oxides with a layered perovskite structure. *Nature* **1996**, *380*, 141-144.
(161) King, G.; Woodward, P. M. Cation ordering in perovskites. *Journal of Materials Chemistry* **2010**, *20* (28), 5785-5796.
(162) Brese, N. E.; DiSalvo, F. Synthesis of the first thorium-containing nitride perovskite, $TaThN_3$. *Journal of Solid State Chemistry* **1995**, *120* (2), 378-380.
(163) Kloß, S. D.; Weidemann, M. L.; Attfield, J. P. Preparation of bulk-phase nitride perovskite $LaReN_3$ and topotactic reduction to $LaNiO_2$-type $LaReN_2$. *Angewandte Chemie International Edition* **2021**, *60* (41), 22260-22264.
(164) Marchand, R.; Pors, F.; Laurent, Y. Préparation et caractérisation de nouveaux oxynitrures à structure perovskite. *Revue Internationale des Hautes Températures et des Réfractaires* **1986**, *23* (1), 11-15.
(165) Jansen, M.; Letschert, H.-P. Inorganic yellow-red pigments without toxic metals. *Nature* **2000**, *404* (6781), 980-982.

(166) Ziani, A.; Le Paven-Thivet, C.; Le Gendre, L.; Fasquelle, D.; Carru, J.-C.; Tessier, F.; Pinel, J. Structural and dielectric properties of oxynitride perovskite $LaTiO_xN_y$ thin films. *Thin Solid Films* **2008**, *517* (2), 544-549.
(167) Ebbinghaus, S. G.; Abicht, H.-P.; Dronskowski, R.; Müller, T.; Reller, A.; Weidenkaff, A. Perovskite-related oxynitrides–Recent developments in synthesis, characterisation and investigations of physical properties. *Progress in Solid State Chemistry* **2009**, *37* (2-3), 173-205.
(168) Zhu, W.; Kamisaka, H.; Oka, D.; Hirose, Y.; Leto, A.; Hasegawa, T.; Pezzotti, G. Stress stabilization of a new ferroelectric phase incorporated into $SrTaO_2N$ thin films. *Journal of Applied Physics* **2014**, *116* (5), 053505.
(169) Sano, M.; Hirose, Y.; Nakao, S.; Hasegawa, T. Strong carrier localization in 3d transition metal oxynitride $LaVO_{3-X}N_X$ epitaxial thin films. *Journal of Materials Chemistry C* **2017**, *5* (7), 1798-1802.
(170) Yang, M.; Oro-Sole, J.; Kusmartseva, A.; Fuertes, A.; Attfield, J. P. Electronic tuning of two metals and colossal magnetoresistances in $EuWO_{1+x}$ N_{2-x} perovskites. *Journal of the American Chemical Society* **2010**, *132* (13), 4822-4829.
(171) Jorge, A. B.; Oro-Sole, J.; Bea, A. M.; Mufti, N.; Palstra, T. T.; Rodgers, J. A.; Attfield, J. P.; Fuertes, A. Large coupled magnetoresponses in $EuNbO_2N$. *Journal of the American Chemical Society* **2008**, *130* (38), 12572-12573.
(172) Hornreich, R. Magnetic interactions and weak ferromagnetism in the rare-earth orthochromites. *Journal of Magnetism and Magnetic Materials* **1978**, *7* (1-4), 280-285.
(173) Kim, Y.-I.; Woodward, P. M. Syntheses and characterizations of complex perovskite oxynitrides $LaMg_{1/3}Ta_{2/3}O_2N$, $LaMg_{1/2}Ta_{1/2}O_{5/2}N_{1/2}$, and $BaSc_{0.05}Ta_{0.95}O_{2.1}N_{0.9}$. *Journal of Solid State Chemistry* **2007**, *180* (11), 3224-3233.
(174) Shen, Z.; Wu, J.; Shorvon, M. W.; Cazaux, G.; Parker, S. C.; Skinner, S. J. Partially Anion-ordered cerium niobium oxynitride perovskite phase with a small band gap. *Chemistry of Materials* **2021**, *33* (11), 4045-4056.
(175) Cordes, N.; Schnick, W. Ammonothermal synthesis of crystalline oxonitride perovskites $LnTaON_2$ (Ln= La, Ce, Pr, Nd, Sm, Gd). *Chemistry–A European Journal* **2017**, *23* (47), 11410-11415.
(176) Kitano, M.; Kujirai, J.; Ogasawara, K.; Matsuishi, S.; Tada, T.; Abe, H.; Niwa, Y.; Hosono, H. Low-temperature synthesis of perovskite

oxynitride-hydrides as ammonia synthesis catalysts. *Journal of the American Chemical Society* **2019**, *141* (51), 20344-20353.
(177) Kawashima, K.; Hojamberdiev, M.; Wagata, H.; Zahedi, E.; Yubuta, K.; Domen, K.; Teshima, K. Two-step synthesis and visible-light-driven photocatalytic water oxidation activity of $AW(O,N)_3$ (A=Sr, La, Pr, Nd and Eu) perovskites. *Journal of Catalysis* **2016**, *344*, 29-37.
(178) Chen, Y.; Sun, Y.; Peng, J.; Tang, J.; Zheng, K.; Liang, Z. 2D Ruddlesden–Popper perovskites for optoelectronics. *Advanced Materials* **2018**, *30* (2), 1703487.
(179) Greenblatt, M. Ruddlesden-Popper $Ln_{n+1}NinO_{3n+1}$ nickelates: structure and properties. *Current Opinion in Solid State and Materials Science* **1997**, *2* (2), 174-183.
(180) Hungría, T.; Lisoni, J. G.; Castro, A. $Sr_3Ti_2O_7$ Ruddlesden−Popper phase synthesis by milling routes. *Chemistry of Materials* **2002**, *14* (4), 1747-1754.
(181) Pors, F.; Marchand, R.; Laurent, Y. Nouveaux oxynitrures A_2TaO_3N (A= alcalinoterreux) de type structural K_2NiF_4. In *Annales de Chimie (Paris. 1914)*, 1991; Vol. 16, pp 547-551.
(182) Marchand, R. Oxynitrures à Structure K_2NiF_4. Les composés Ln_2AlO_3N (Ln= La, Nd, Sm). **1976**.
(183) Cordes, N. Ammonothermal synthesis of functional nitride oxides and ternary nitrides. lmu, 2019.
(184) Huang, X.; Sun, Q.; Devakumar, B. Facile low-temperature solid-state synthesis of efficient blue-emitting $Cs_3Cu_2I_5$ powder phosphors for solid-state lighting. *Materials Today Chemistry* **2020**, *17*, 100288.
(185) He, M.; Jia, J.; Zhao, J.; Qiao, X.; Du, J.; Fan, X. Glass-ceramic phosphors for solid state lighting: A review. *Ceramics International* **2021**, *47* (3), 2963-2980.
(186) Krishnapriya, T.; Jose, A.; Jose, T. A.; Saritha, A. C.; Joseph, C.; Biju, P. R. Investigation of the structural and photoluminescence properties of Eu^{3+} doped $Na_6CaP_2O_9$ phosphors for solid state lighting. *Materials Research Bulletin* **2021**, *139*, 111259.
(187) Haque, M. M.; Lee, H.-I.; Kim, D.-K. Luminescent properties of Eu^{3+}-activated molybdate-based novel red-emitting phosphors for LEDs. *Journal of Alloys and Compounds* **2009**, *481* (1), 792-796.
(188) Ge, W.; Yin, H.; Lu, C.; Zhang, X.; Song, P.; Ma, M.; Liu, Z.; Tian, Y. Excellent yellow emission of Si_3N_4:Eu nanorods derived from waster silicon with better thermal stability for white LEDs. *Ceramics International* **2023**, *49* (1), 1328-1335.

(189) Mahlik, S.; Barzowska, J.; Szczodrowski, K.; Majewska, N.; Grinberg, M.; Michalik, D.; Adamczyk, B. J.; Pawlik, T.; Rzychoń, T.; Adamczyk, A.; et al. Enhancement of $SrSi_2O_2N_2:Eu^{2+}$ phosphor by means of oxygen to nitrogen control. *Journal of Alloys and Compounds* **2021**, *884*, 161047.
(190) Yoshimura, F.; Yamane, H.; Yamada, T. Synthesis, crystal structure, and luminescence properties of a white-light-emitting nitride phosphor, $Ca_{0.99}Eu_{0.01}AlSi_4N_7$. *Inorganic Chemistry* **2020**, *59* (1), 367-375.
(191) Deng, Y.; Xu, H.; Cheng, X.; Zhang, Y.; Sun, J.; Yu, X.; Bao, S. Polymer-derived preparations of the blue-excited greenish-yellow-emitting calcium-containing β-Si_3N_4:Eu-like phosphors. *Ceramics International* **2021**, *47* (11), 15415-15423.
(192) Lin, J.-D.; Liu, Y.-C. The preparation of $SrSi_2O_2N_2:Eu^{2+}$ and $Sr_2Si_5N_8:Eu^{2+}$ phosphors by a direct silicon nitridation process and $Sr(NO_3)_2$ as strontium and oxygen sources. *Materials Chemistry and Physics* **2023**, *297*, 127317.
(193) Li, H. L.; Xie, R. J.; Hirosaki, N.; Takeda, T.; Zhou, G. H. Synthesis and luminescence properties of orange–red-emitting $M_2Si_5N_8:Eu^{2+}$ (M= Ca, Sr, Ba) light-emitting diode conversion phosphors by a simple nitridation of MSi_2. *International Journal of Applied Ceramic Technology* **2009**, *6* (4), 459-464.
(194) Gu, Y.; Zhang, Q.; Li, Y.; Wang, H.; Xie, R.-J. Enhanced emission from $CaSi_2O_2N_2:Eu^{2+}$ phosphors by doping with Y^{3+} ions. *Materials Letters* **2009**, *63* (16), 1448-1450.
(195) Zou, Y.; Yu, L.; Gao, Z.; Zhong, J.; Guo, Q.; Liu, Z. Synthesis, crystal structure, and photoluminescence of Eu^{2+}, Ce^{3+}, Mn^{2+} doped oxynitride phosphors. *Optical Materials* **2019**, *92*, 411-417.
(196) Kijima, N.; Seto, T.; Hirosaki, N. A new yellow phosphor $La_3Si_6N_{11}:Ce^{3+}$ for white LEDs. *ECS Transactions* **2009**, *25* (9), 247.
(197) Schmiechen, S.; Schneider, H.; Wagatha, P.; Hecht, C.; Schmidt, P. J.; Schnick, W. Toward new phosphors for application in illumination-grade white pc-LEDs: the nitridomagnesosilicates Ca $[Mg_3SiN_4]: Ce^{3+}$, Sr $[Mg_3SiN_4]: Eu^{2+}$, and Eu $[Mg_3SiN_4]$. *Chemistry of Materials* **2014**, *26* (8), 2712-2719.
(198) Lü, W.; Wang, H.; Jia, C.; Kang, X. Generating green and yellow lines in $Y_6Si_3O_9N_4:Ce^{3+},Tb^{3+}/Dy^{3+}$ oxynitrides phosphor. *Journal of Luminescence* **2019**, *213*, 297-303.

(199) Zou, Y.; Yu, L.; Wu, Y.; Wu, Y.; Gao, Z. Synthesis and photoluminescence of Yb^{2+}/Dy^{3+} doped $Ca_2Si_3O_2N_4$ oxynitride phosphors. *Journal of Luminescence* **2019**, *215*, 116643.
(200) Shioi, K.; Hirosaki, N.; Xie, R. J.; Takeda, T.; Li, Y. Q.; Matsushita, Y. Synthesis, crystal structure, and photoluminescence of Sr-α-SiAlON: Eu^{2+}. *Journal of the American Ceramic Society* **2010**, *93* (2), 465-469.
(201) Xie, R.-J.; Hirosaki, N.; Li, H.-L.; Li, Y.; Mitomo, M. Synthesis and Photoluminescence Properties of β-sialon: $Eu^{2+}(Si_{6-Z}Al_ZO_ZN_{8-Z}:Eu^{2+})$: A promising green oxynitride phosphor for white light-emitting diodes. *Journal of the Electrochemical Society* **2007**, *154* (10), J314.
(202) Zhang, C.; Uchikoshi, T.; Xie, R.-J.; Liu, L.; Sakka, Y.; Hirosaki, N. Photoluminescence efficiency significantly enhanced by surface modification of SiO_2 coating on β-sialon:Eu^{2+} phosphor particle. *Journal of Alloys and Compounds* **2018**, *741*, 454-458.
(203) Wang, Y.; Zhu, G.; Xin, S.; Wang, Q.; Li, Y.; Wu, Q.; Wang, C.; Wang, X.; Ding, X.; Geng, W. Recent development in rare earth doped phosphors for white light emitting diodes. *Journal of Rare Earths* **2015**, *33* (1), 1-12.
(204) Xie, R. J.; Hintzen, H. T. Optical properties of (oxy) nitride materials: a review. *Journal of the American Ceramic Society* **2013**, *96* (3), 665-687.
(205) Park, W. B.; Singh, S. P.; Sohn, K.-S. Discovery of a phosphor for light emitting diode applications and its structural determination, $Ba(Si,Al)_5(O,N)_8:Eu^{2+}$. *Journal of the American Chemical Society* **2014**, *136* (6), 2363-2373.
(206) Lou, L.; Hua, Y.; Chu, S.; Zheng, J.; Qiao, P.; Tao, S.; Ping, Y.; Ma, H. Synthesis and phosphorescence mechanism of yellow-emissive long-afterglow phosphor $BaAl_2Si_3O_4N_4$: Yb^{2+}. *Ceramics International* **2021**, *47* (19), 26620-26626.
(207) Wang, H.; Zhu, Z.; Ma, B.; Wei, L.; Li, L. Improved thermal stability and luminescence properties of $SrSi_2O_2N_2:Eu^{2+}$ green phosphor by a heterogeneous precipitation protocol for solid-state lighting applications. *Ceramics International* **2021**, *47* (17), 24163-24169.

Chapter II

Methods

2.1 Synthesis of metal (oxy)nitrides

2.1.1 Thermal Ammonolysis

This method was used to prepare the reactants TaON and Ta_3N_5 used in high temperature synthesis under N_2 of some oxynitrides described in chapters 3 and 4. As indicated in the previous chapter, NH_3 decomposes into N_2 and H_2 above 500 ^oC and the percentage of its decomposition increases with rising temperature, as shown in figure 2.1 for a flow rate of 125 cm^3/min.

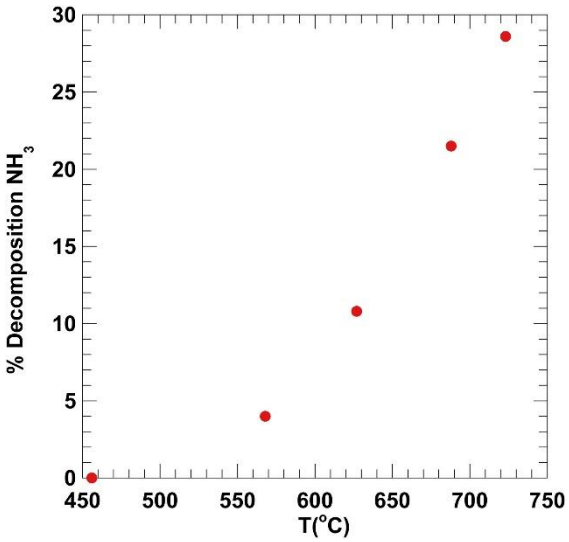

Figure 2.1. % of decomposition of ammonia as a function of temperature for a flow rate of 125 cm^3/min. Reproduced from Reference [1] with permission from Elsevier.

The kinetics of the dissociation is slow and its extent can be controlled by the flow rate (see figure 1.3.b). For high temperatures it is necessary to

use high flow rates in order to minimize the presence of H_2 in the system. Typical flow rates are between 180 and 1000 cm^3/min.[1]

The reactions were carried out in alumina boats in the sandwich type tubular furnace depicted in Figure 2.2 using a silica glass tube. Ammonia is toxic and flammable when is in contact with air. For example, if the air concentration is in the range of 16 to 27%, the autoignition temperature is 651°C. For this reason the system is purged with N_2 previously to introduce the ammonia in the reaction tube.The entire reaction system is located inside a fume hood, and accidental leaking is controlled by a sensor that stops the gas flow for NH_3 concentrations in the laboratory above 3 ppm. Once the gas has passed through the system and interacted with the sample, it is neutralized with an acetic acid trap (0.1 M).

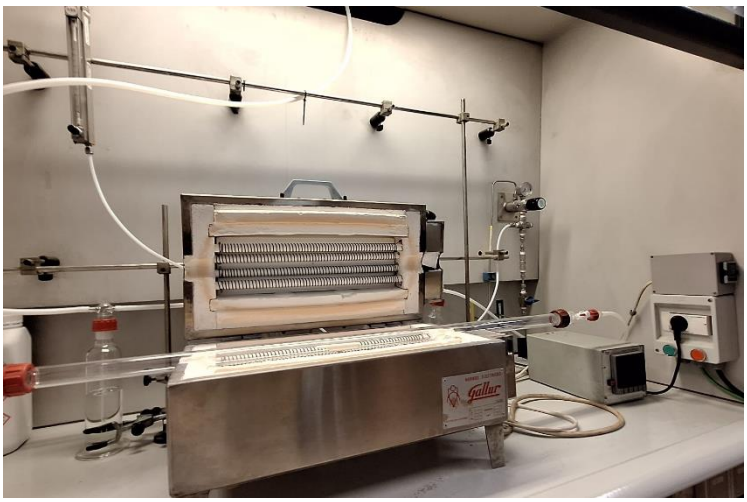

Figure 2.2. Ammonolysis furnace at the solid state chemistry laboratory of ICMAB.

The ammonolysis reactions were carried out at 850 ^{o}C starting from Ta_2O_5, using NH_3 flow rates of 600 cm³/min and 40 cm³/min for the synthesis of Ta_3N_5 and TaON, respectively. Ta_3N_5 was prepared using two 15-hour treatments, while TaON required only one 2-hour treatment.

2.1.2 High temperature solid state synthesis

This method is used for the preparation of all the oxynitrides reported in the present work, and proceeds under N_2 or N_2/H_2 gas at temperatures between 1200 and 1700 ^{o}C starting with mixtures of oxides and (oxy)nitrides. Two different tubular furnaces were used, with SiC resistances for reactions up to 1500 ^{o}C (Figure 2.4) and Si_2Mo resistances for temperatures up to 1700 ^{o}C. The gases used are N_2 (99.999% Air Liquide) and N_2/H_2 (95%/5%, V/V, Air Liquide 99.999%) with traces of water and oxygen below 0.5 ppm and 0.1 ppm, respectively. To avoid the presence of water around the sample, mixing and pelletizing of the reactants was conducted in a glovebox under recirculating argon. The rare earth oxide reactants were dried at 1000°C for 12 hours for dehydration. The reactants were weighed and mixed for a minimum of 30 minutes and pelletized under a pressure of 10 or 2 bars for 10 minutes. The pellet was then placed inside a molybdenum crucible covered with zirconium, which was moved into the furnace using a Schlenk flask. Sacrificial zirconium foil was positioned close to the sample inside the reaction tube in order to scavenge water and oxygen impurities from the gas (see Figure 2.3).

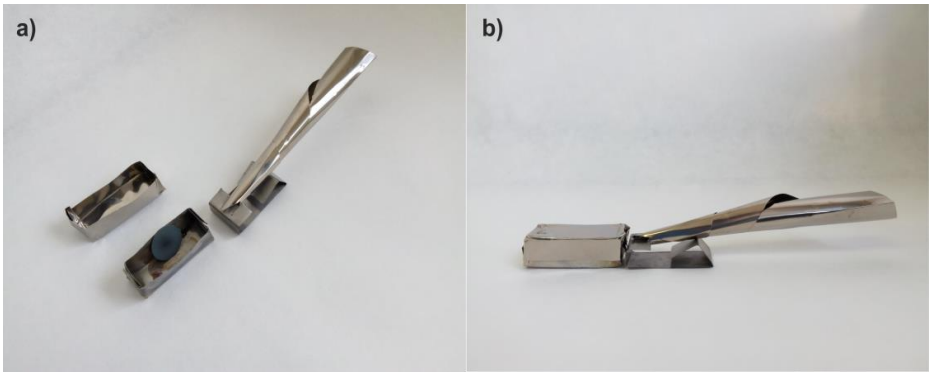

Figure 2.3. Molybdenum boat and sacrificial zirconium (right panel) used in the syntheses at high temperature.

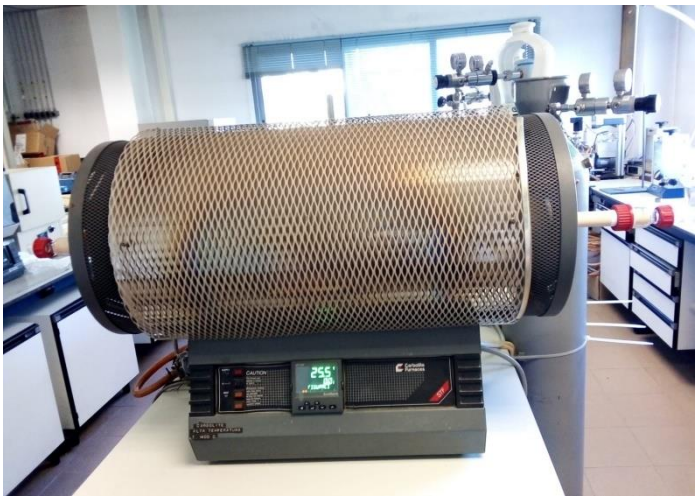

Figure 2.4. CSi high temperature tubular furnace of the solid state chemistry laboratory at ICMAB..

Three purges with the gas used in the reaction were performed at a vacuum of 0.4 mbar to remove oxygen from the tube. These precautions are essential to prevent the formation of unwanted oxides due to oxygen presence during various stages of the process. The sample was heated at

300°C/h up to the maximum temperature that was held typically 3 hours and after that the furnace was cooled naturally to room temperature.

2.2 Determination of the cationic and anionic stoichiometry

2.2.1 Combustion analysis

This technique was employed to determine the nitrogen content of the sample. The analysis was conducted using a Thermo Fisher Scientific instrument through combustion. Approximately 1000 μg of the sample was burned in an oxygen atmosphere at 1060°C. MgO, WO_3, and Sn in powder form were used as additives, and atropine served as the reference standard. The nitrogen produced in this reaction was transported by a helium flow to the thermal conductivity detector for detection.

2.2.2 Thermal analysis

The thermal analysis of the samples was conducted using a NETZSCH STA 449 F1 Jupiter instrument to check the thermal stability and oxidation behavior of some oxynitrides.. For these measurements, 10 mg of samples were placed in an alumina crucible and heated to a temperature of 1400°C under flowing oxygen. The heating rate was $5°C/min^{-1}$ and the O_2 flow rate was 70 cm^3/min^{-1}.

2.2.3 Energy dispersive X-ray spectroscopy

Energy dispersive spectroscopy (EDS) analyses of cation contents were conducted in a FEI Quanta 200 FEG scanning electron microscope equipped with an EDAX detector with an energy resolution of 132 eV.

2.3 Structural characterization

2.3.1 Laboratory X-ray powder diffraction

Powder X-ray diffraction was generally conducted in an A25 D8 Discover diffractometer and a Panalytical X'Pert Pro MPD diffractometer using Cuk_{α} radiation with λ= 1.5418 Å. For air unstable samples the X-ray powder diffraction data were acquired on borosilicate capillaries of 0.3 mm diameter as sample holders, which were filled in a glovebox under recirculating argon, using a Bruker D8 Advance A25 diffractometer in a Debye-Scherrer configuration equipped with a Johansson monochromatorand Mo $K\alpha_1$ radiation source (λ= 0.7093 Å).

2.3.2 Synchrotron X-ray powder diffraction

High-resolution synchrotron X-ray powder diffraction data were obtained using a 0.3 mm diameter capillary, which was rotated during data collection in the angular range of $3.0° \leq 2\theta \leq 50.0°$ at the MSPD (Materials Science And Powder Diffraction) beamline [2] of the ALBA Synchrotron in Cerdanyola del Vallès, Spain. A double Si (111) crystal monochromator was employed, and a short wavelength was selected and calibrated with Si NIST. Rietveld analysis was performed using the Fullprof program.[3]

2.3.3 Neutron powder diffraction

Neutron powder diffraction measurements were conducted at the Institut Laue-Langevin (ILL) in Grenoble, France, using the D20 diffractometer.

The high contrast against neutrons between oxygen and nitrogen allow to investigate the anion order and tilting superstructures.

2.3.4 Electron diffraction

Electron diffraction micrographs were obtained using a JEOL 1210 transmission electron microscope operating at 120 kV, equipped with a side-entry 60°/30° double tilt GATAN 646 specimen holder. The samples were deposited on a carbon film supported on a copper grid. The reconstruction of the reciprocal lattice was performed from different diffraction planes in order to determine the space group. Figure 2.5 depicts the projection of crystallographic planes from 3D to 2D, where each observed spot in the micrograph corresponds to a diffraction plane.

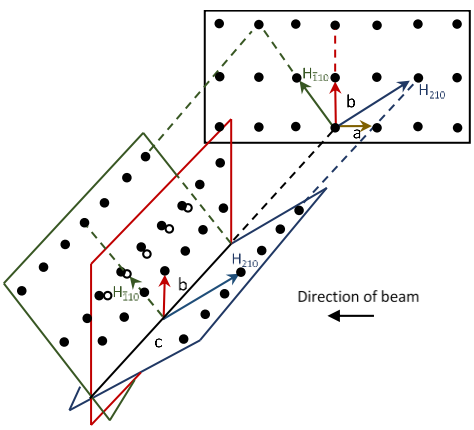

Figure 2.5. Schematic representation of the rotation method used to reconstruct the reciprocal lattice by electron diffraction. c* is the common axis for all patterns.

2.4 Optical characterization

2.4.1 Diffuse reflectance

Diffuse reflectance spectra were recorded at room temperature using a JASCO V-770 UV-visible/NIR spectrophotometer, with an operational range of λ=200-1200 nm. A Diffuse Reflectance Sphere DRA-2500 accessory was utilized.

The band gap values for the analyzed samples were calculated using the Kubelka-Munk function, F(R∞),[4, 5] which relates the material's diffuse reflectance (R) to the absorption (k) and scattering (σ) coefficients:

$$F(R\infty) = \frac{(1-R\infty)^2}{2R\infty} \propto \frac{k}{\sigma} \quad [6, 7]$$

By plotting the function $(F(R)*h\nu)^2$ versus UV-Vis radiation energy, extrapolation of the linear portion to an absorbance equal to zero provides an estimate of the band gap energy value.

2.4.2 Photoluminescence measurements

Luminescent emission measurements of the samples $NdSr_{1-x}Eu_xSiO_3N$ (x = 0, 0.5 and 1), were conducted at room temperature using a 405 nm laser for sample excitation. Data were collected on a LabRam HR800 spectrometer equipped with a charge-coupled device (CCD) detector. Photoluminescence (PL) spectra were corrected for the spectral response of the spectrometer by normalizing each spectrum using the detector and

grating characteristics. The intensity of the incident irradiations was 1 W/cm².

2.5 Electrical and magnetic properties characterization

The magnetic measurements were carried out in a Quantum Design SQUID magnetometer between 2 and 300 K at magnetic fields between 50 Oe an 8 T. Electrical measurements were performed using a Physical Properties Measurement System (PPMS, Quantum Design, USA) with a custom-made multifunctional probe. The electrical resistivity was measured using a Keithley 6517A Electrometer/High Resistance Meter, and the dielectric properties were measured on an Agilent (E4980A) Precision LCR meter. Electrical contacts with the sample were established using silver paste and copper wire. Data were recorded while the sample was heated.

2.6 References

(1) Fuertes, A. Metal oxynitrides as emerging materials with photocatalytic and electronic properties. *Materials Horizons* **2015**, *2* (5), 453-461.
(2) Fauth, F.; Peral, I.; Popescu, C.; Knapp, M. The new material science powder diffraction beamline at ALBA synchrotron. *Powder Diffraction* **2013**, *28* (S2), S360-S370.
(3) Rodríguez-Carvajal, J. Recent advances in magnetic structure determination by neutron powder diffraction. *Physica B: Condensed Matter* **1993**, *192* (1), 55-69.
(4) Kubelka, P. Ein Beitrag zur Optik der Farbanstriche (Contribution to the optic of paint). *Zeitschrift fur technische Physik* **1931**, *12*, 593-601.
(5) Kubelka, P.; Munk, F. An article on optics of paint layers. *Z. Tech. Phys* **1931**, *12* (593-601), 259-274.
(6) Landi, S.; Segundo, I. R.; Freitas, E.; Vasilevskiy, M.; Carneiro, J.; Tavares, C. J. Use and misuse of the Kubelka-Munk function to obtain

the band gap energy from diffuse reflectance measurements. *Solid State Communications* **2022**, *341*, 114573.
(7) Christy, A. A.; Kvalheim, O. M.; Velapoldi, R. A. Quantitative analysis in diffuse reflectance spectrometry: A modified Kubelka-Munk equation. *Vibrational Spectroscopy* **1995**, *9* (1), 19-27.

Chapter III

Perovskite Tantalum Oxynitrides Derived from the Pm-3m Aristotype

3.1 High Temperature Synthesis and Dielectric Properties of $LaTaON_2$

Published in: *Inorganic Chemistry*, **2021,** 60, 16484-16491.

Authors: Augustin Castets,[§] Ignasi Fina,[§] Jhonatan R. Guarín,[§] Judith Oró-Solé,[§] Carlos Frontera, [§] Clemens Ritter,[‡] Josep Fontcuberta[§,*] and Amparo Fuertes[§,*]

§ Institut de Ciència de Materials de Barcelona (ICMAB-CSIC), Campus UAB, 08193 Bellaterra(Spain).

‡ Institut Laue-Langevin, 71 Av. de Martyrs, Grenoble 38000(France)

https://doi.org/10.1021/acs.inorgchem.1c02325

Keywords: perovskite oxynitrides, synthesis of oxynitrides, $LaTaON_2$, dielectric properties

A new fast synthetic approach of $LaTaON_2$ at high temperature under N_2 is reported using two alternative reactions that produce ceramic samples with high crystallinity and sintering. The observed N/O anion distribution in this perovskite determined by neutron diffraction is different from previous studies on samples prepared under NH_3 at lower temperatures, indicating that the synthesis conditions have an influence on the anion order. The dielectric permittivity $\varepsilon_r \approx 200$, reported for the first time for a highly nitrided pseudocubic perovskite, is found to be similar to that observed in perovskites with one nitrogen per formula.

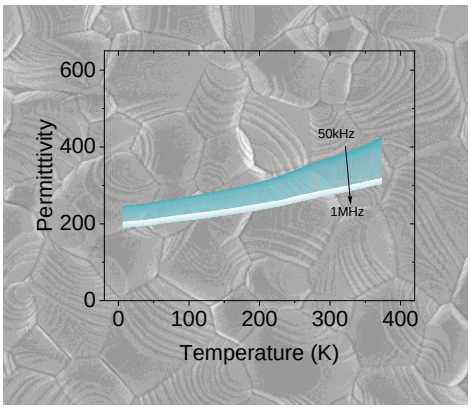

Abstract: The development of new synthetic methodologies of perovskite oxynitrides is challenging, but necessary for the search of new compounds and the investigation of new properties. Here we report a new method of preparation of the perovskite $LaTaON_2$ that has been investigated as pigment and as photocatalyst for water splitting. The synthesis proceeds through the solid state reactions under N_2 at 1500 ^oC between La_2O_3, LaN and Ta_3N_5 or between LaN and TaON, that are completed after 3 hours and lead to sintered, highly crystalline samples with particle sizes up to 1 μm. Nitrogen deficient samples $LaTaO_{1+x}N_{2-x}$ with $x \leq 0.35$ are prepared by changing the N/O ratio in the mixture of reactants. Electron diffraction, synchrotron diffraction and neutron diffraction studies on stochiometric and nitrogen deficient compounds indicate that they crystallize in the monoclinic space group *I2/m* with lattice parameters for $LaTaON_2$ of a= 5.71458(7), b= 8.05987(10), c=5.74772(6) Å, β=89.982(3). The three anion sites of the *I2/m* structure are partially occupied by oxygen and nitrogen, with a preference of nitride for two positions with occupancies of 77% and 88%. This anion distribution is different from that reported in previous studies of samples prepared by ammonolysis at lower temperatures, suggesting that the synthesis conditions affect the anion order of this perovskite. Optical measurements indicate a band gap of about 1.9 eV, which is close to that observed in samples prepared by other methods. The determined dielectric permittivity for $LaTaON_2$ $\varepsilon_r \approx 200$, reported for the first time for a highly nitrided pseudocubic perovskite, is similar to that observed in perovskites with one nitrogen per formula.

3.1.1 Introduction

Transition metal oxide perovskites ABO_3 show a large diversity of properties and technological applications. The substitution of the anion oxide (O^{2-}) by nitride (N^{3-}) with higher charge expands the possibilities of combining different oxidation states of A and B cations, resulting in totally new compounds $ABO_{3-x}N_x$ with nitrogen contents up to 2.4,[1] where A is an alkaline earth metal or a rare earth metal and B is an early transition metal in a high oxidation state. The differences in electronegativity and electronic polarizability between nitrogen and oxygen induce changes in the electronic structure and bonding -which is more covalent for nitride-, modifying the physical and chemical properties. Nitrogen decreases the band gap because its lower electronegativity compared to oxygen, and the majority of perovskite oxynitrides, with E_g values from 1.7 to 3.35 eV, absorb light in the visible range allowing remarkable applications as visible light active photocatalysts [2] and non-toxic inorganic pigments.[3] The higher charge of N^{3-} increases the ionic polarizability, which is further enhanced by bonding with highly charged cations and with anion order. The order of N^{3-} and O^{2-} may lead to the existence of long range ordered electric dipoles as in the non-centrosymmetric hexagonal perovskite $BaWON_2$.[4] Dielectric permittivity (ε_r) in centrosymmetric pseudocubic perovskites has been reported for a limited number of compounds, with values ranging from 16 for $NdHfO_2N$[5] to 4900 for $SrTaO_2N$.[6] The large permittivity values were early interpreted by the presence of local B-X (X= O, N) dipoles induced by partial anion order,[7,8,9] however it has been recently emphasized that some of the reported gigantic ε_r values may not

be intrinsic, but resulting from spurious effects due to poor sintering of the measured samples and leakage contributions.[10]

The synthesis of perovskite oxynitrides has been mostly performed under NH_3(g) at temperatures of 900-1000 ^oC.[11] The starting compounds are either ternary oxides or a mixture of oxides and carbonates. Under NH_3 at these temperatures, the rare earth oxides do not react with the transition metal oxides unless alkaline or alkaline earth chlorides are added to the reactants mixture as fluxes to increase the cation mobility. The ammonolysis reaction is usually very slow, and several cycles of 24 hours may be required to obtain single phase samples of the targeted oxynitride. The synthesis under N_2 of perovskite oxynitrides has been much less explored than ammonolysis. Higher temperatures are required, between 1200 ^oC and 1500 ^oC, but it has the great advantage of using a non-toxic gas. Moreover, the reaction times are generally short, typically of few hours, and normally one single thermal treatment is enough to obtain samples with high purity and crystallinity. The high temperatures also favor grain growth and sintering, which is necessary to perform electrical measurements. Initial examples of this approach were the syntheses of $SrTaO_2N$ or $BaTaO_2N$ starting with TaON and SrO or BaO respectively.[12] The same compounds have been more recently prepared by reacting Ta_3N_5 with the alkaline earth carbonate,[13] and $RHfO_2N$ perovskites with R= La, Nd, Sm were prepared using R_2O_3 and Hf_2ON_2 .[5] As the highly stable N_2 molecule does not react with oxides under these conditions, the main difficulty in this synthetic approach is to access the necessary nitrided reactants that will provide the desired molar ratio between N, O and the cations in the final product.

$LaTaON_2$, with a band gap of 1.9 eV, shows intense absorption up to 650 nm. It was initially investigated as red pigment,[3] and more recently it has attracted significant attention as a photocatalyst for water reduction under visible light.[14] It has been prepared following several synthetic approaches. The first synthesis of $LaTaON_2$ was reported by Marchand and colleagues, using the treatment in NH_3 at 950 ^oC of $LaTaO_4$.[15] The direct synthesis through a solid state reaction between La_2O_3 and Ta_2O_5 can be performed under NH_3 at 850-950 ^oC by using fluxes of $CaCl_2$, KCl or NaCl. [3, 16]Ammonothermal synthesis at temperatures as low as 600 ^oC has been used starting from La, Ta and $NaNH_2$ [17] or NaN_3,[18] and produce samples with large crystal sizes.

Here we report a new synthetic approach for $LaTaON_2$ by solid state reaction at 1500 ^oC using LaN, La_2O_3 and Ta_3N_5 or LaN and TaON as reactants, that represents the first high temperature synthesis under N_2 of a highly nitrided perovskite oxynitride. The samples are obtained after 3 hours of treatment at the maximum temperature, and show high crystallinity. Nitrogen stoichiometry can be adjusted from 1.65 to 2.0 by increasing the N/O ratio in the mixture of reactants or by post-synthesis annealing in NH_3. The crystal structures of stoichiometric $LaTaON_2$ and nitrogen deficient $LaTaO_{1.12}N_{1.88}$ are investigated by electron diffraction, neutron powder diffraction and synchrotron X-ray powder diffraction. They show the monoclinic *I2/m* space group, where three anion sites are partially occupied by N^{3-} and O^{2-} that display some preferential occupancy but without long range order. The observed anion distribution shows differences with those reported in previous neutron diffraction studies of $LaTaON_2$ prepared by ammonolysis.[16,19,20] The optical bandgap

determined by diffuse reflectance spectroscopy is 1.9 eV, in agreement with previous reports from several groups. High temperature sintering allows accurate determination of the dielectric permittivity (ε_r) that is remarkably larger ($\varepsilon_r \approx 200$ at 5 K) than for related oxidic compounds, although comparable to $SrTaO_2N$ which stress the tuneability of the dielectric properties in these perovskites.

3.1.2 Experimental

Synthesis of $LaTaO_{1+x}N_{2-x}$ ($0 \leq x \leq 0.35$)

The synthesis of $LaTaO_{1+x}N_{2-x}$ samples with $0 \leq x \leq 0.35$ was performed at 1500 ^oC in flowing N_2 (Air Liquide, 99.9999 %) using two different reactions, starting either with La_2O_3 (Aldrich 99.999%), LaN (Alfa Aesar 99.9%) and Ta_3N_5 (route (1)), or with LaN and TaON (route (2)). La_2O_3 was dried under dynamic vacuum of 10^{-3} torr at 900 ^oC during 12 hours. TaON was prepared by treatment of Ta_2O_5 (Aldrich 99.99%) in NH_3 (Carburos Metálicos, 99.9%) using two cycles of 3 hours at 850 ^oC under a flow rate of 40 cm^3/min. Ta_3N_5 was prepared by treatment of Ta_2O_5 (Aldrich 99.99%) in NH_3 using several cycles of 15 hours at 850 ^oC under a flow rate of 600 cm^3/min. Handling of the reactants and pelletizing were carried out in a glove box under recirculating argon atmosphere. Mixtures of the reactants in stoichiometric ratios lead to nitrogen deficient samples. Using an excess of nitrogen by increasing the LaN/La_2O_3 ratio in route (1) lead to stoichiometric $LaTaON_2$. The powders were thoroughly mixed in an agate mortar for 30 min, pressed

into a pellet and placed in a molybdenum crucible. Zirconium foil was used as a cover of the crucible and close to it in the reaction tube to scavenge oxygen and water from N_2. The mixtures were treated at the maximum temperature during one single cycle of 3 hours with heating and cooling rates of 300 °C/h. In order to decrease the amount of reduced species, the surface of the pellets was sanded and separated from the sample used for further characterization. Post treatment under NH_3 of a nitrogen deficient sample prepared by route (1) was performed at 1000 ^oC under a flow rate of 600 cm^3/min. We also prepared a sample of $LaTaON_2$ by ammonolysis of $LaTaO_4$ that was used to compare grain sizes and sintering with those of samples prepared at high temperature. $LaTaO_4$ was treated at 950 ^oC under NH_3 flow rate of 300 cm^3/min during two cycles of 40 h as reported in reference 19.

N contents were determined by combustion analysis in a Thermo Fisher Scientific instrument, heating the samples in oxygen up to 1060 ^oC and using MgO, WO_3 and Sn as additives and atropine as a reference standard. Scanning electron microscopy (SEM) images were obtained in a Thermo Fisher XHRSEM Magellan 400L microscope, and EDX analyses of cation contents were performed in a FEI Quanta 200 FEG microscope equipped with an EDAX detector with an energy resolution of 132 eV.

Structural characterization

Laboratory X-ray powder diffraction data were collected on a Panalytical X'Pert Pro MPD diffractometer using Cu Kα radiation (λ= 1.5418 Å). High resolution synchrotron X-ray powder diffraction (SXRD) data were

measured at room temperature from capillary (0.3 mm diameter) samples in the angular range $4.0^o \leq 2\theta \leq 46.5^o$ at the MSPD beamline[21] of the ALBA Synchrotron (Cerdanyola del Vallès, Spain). Using a double Si (111) and Si (220) crystal monochromator, a short wavelength was selected and calibrated with Si NIST (λ = 0.41322 Å), and collected using the multi-analyzer detector. Rietveld analysis was carried out using the program Fullprof.[22] Background refinement was performed by linear interpolation and an appropriate absorption correction was used. Neutron powder diffraction data were collected at room temperature on the D20 diffractometer at the Institut Laue-Langevin (ILL), Grenoble, using a vanadium can as sample holder and a wavelength of 1.865 Å. Rietveld analysis was carried out using the program Fullprof.[22]

Electron diffraction micrographs were obtained in a JEOL 1210 transmission electron microscope operating at 120 kV, equipped with a side-entry $60^o/30^o$ double tilt GATAN 646 specimen holder. The samples were prepared by dispersing the powders in hexane and depositing a droplet of this suspension on a holey carbon film supported on a copper grid.

Physical properties characterization

Diffuse reflectance spectra were registered at room temperature on a JASCO V-780 UV-visible/NIR spectrophotometer, with operational ranges of λ=200-1200 nm. Electrical resistance measurements were performed between 20 and 400 K on sintered pellets using silver past contacts by the four probe and Van der Pauw methods. Dielectric

measurements were performed using a capacitor geometry with silver paint circular electrodes covering about 80% of the surface of the pellet. Effective areas of tested samples varied between 0.5 and 3 mm^2. Their density was determined by measuring the volume and the weight of the pellets, resulting in relative values between 50.4% and 52.2%.

Capacitance (C(f,T)) was measured using excitations signals of 0.1 V at various frequencies (f = 1 kHz-1 MHz) as a function of temperature (T) between 10 K and 300 K, using an impedance analyzer and a Quantum Design Physical Property Measurement System for temperature control. Dielectric permittivity was determined from the capacitance data using the nominal capacitor geometry (area and thickness).

3.1.3 Results and Discussion

High temperature synthesis of $LaTaO_{1+x}N_{2-x}$

The reaction of formation of $LaTaON_2$ at 1500 ^oC under N_2 proceeds by using one of the following synthetic approaches:

(1) $La_2O_3 + LaN + Ta_3N_5 \longrightarrow 3\ LaTaON_2$

(2) $LaN + TaON \longrightarrow LaTaON_2$

In both cases the reaction is very fast, and samples with high crystallinity are obtained after 3 hours of treatment as shown in Figure 1 by the synchrotron X-ray powder diffraction pattern of a sample prepared with method (1). They showed high sintering degree and particle sizes up to 1 μm as shown in the scanning electron microscopy images of Figures 2a

and 2b. In spite of the excellent grain sintering, a SEM image at smaller magnification allowed to observe a larger fraction of the sample surface and to appreciate a relatively reduced density (see Figure S1 at Supplementary Information). A SEM image of the $LaTaON_2$ sample prepared by ammonolysis of $LaTaO_4$ at 950 ^oC is shown in figure 2c with the same magnification than in figure 2b, and evidences the dramatic improvement of grain connectivity and increase in particle sizes achieved by the high temperature synthesis under N_2.

In the X-ray diffraction patterns of some samples prepared by routes (1) and (2), hexagonal (*P6/mmm*) TaN and La_2O_3 were detected as impurities in variable small amounts below c.a. 2 % (w/w), resulting either from incomplete reactions or presence of adventitious H_2O and O_2. Figure S2 in Supplementary information shows the X-ray diffraction pattern of a sample prepared by route (1) that contained both impurity phases. In contrast with reaction (2) which has a fixed N:O ratio in the reactants, reaction (1) provides the possibility to increase the nitrogen content in the initial mixture by changing the proportion of La_2O_3 and LaN while keeping constant the La/Ta ratio. Combustion analyses indicated that the samples prepared with the stoichiometric ratios of the reactants using both (1) and (2) showed nitrogen deficiency, with contents between 1.65 and 1.9 atoms per formula. Nitrogen loss at 1500 ^oC has been previously observed during the treatment of the perovskite $SrTaO_2N$ in N_2 leading to similar deficiencies of up to 0.3 atoms per formula.[23] This is due to a decomposition reaction analogous to that shown by transition metal oxides at high temperatures that lead to reduced oxides together with O_2,[24] and in this case produces N_2 and partial reduction of Ta^{5+} to Ta^{4+}.

According to the presence of tantalum in a mixed oxidation state, the nitrogen deficient samples were black colored or dark brown -in contrast to red colored samples obtained by ammonolysis,[3,19] and showed an enhanced electrical conductivity (see below).

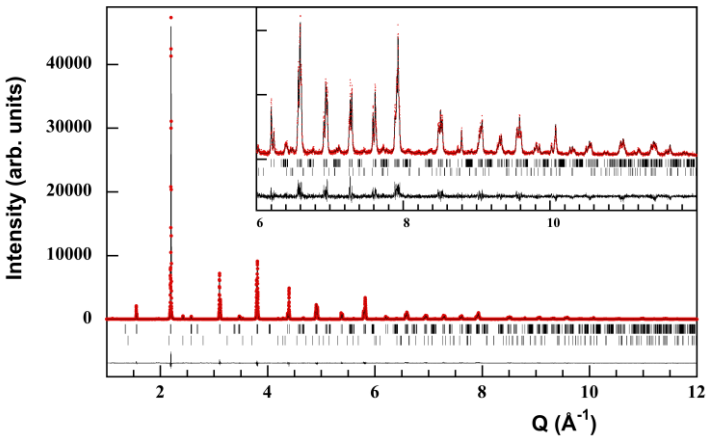

Figure 1. Observed and calculated synchrotron X-ray powder diffraction patterns of $LaTaON_2$ prepared at 1500 ^{o}C by route (1). Upper and lower reflection markers are respectively for $LaTaON_2$ and hexagonal (*P6/mmm*) TaN. The inset shows the high Q region enlarged.

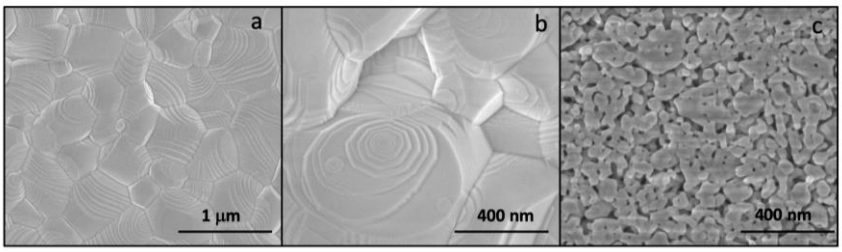

Figure 2. Scanning electron microscopy images of $LaTaON_2$ samples: (a) and (b) prepared at 1500 ^{o}C with reaction (1); (c) prepared by ammonolysis of $LaTaO_4$ at 950 ^{o}C.

In order to obtain highly insulating samples required for the study of the dielectric properties, it was necessary to minimize the presence of Ta^{4+}. The nitrogen content was increased up to two atoms per formula by using reaction (1), but starting with an excess of nitrogen in the mixture of LaN, La_2O_3 and Ta_3N_5, with molar ratio 1.36:0.82:1 instead of 1:1:1 to compensate the nitrogen loss in the decomposition process. The color of the $LaTaON_2$ sample was brown, but lighter than for the nitrogen deficient samples. Another approach to increase the nitrogen content was the post treatment under NH_3 of the pellets. By using this method, the nitrogen content of a sample prepared using reaction (1) with 1.7 atoms per formula was increased to 1.9 atoms per formula, thus leading to a residual nitrogen deficiency of 0.1. As-prepared samples following method (1) with compositions $LaTaON_2$, $LaTaO_{1.12}N_{1.88}$, $LaTaO_{1.18}N_{1.82}$ and $LaTaO_{1.27}N_{1.73}$ were selected for further structural and physical properties characterization. EDX analyses of these samples performed for several crystals gave La:Ta ratios between 1.07 and 1.21 which agree with the nominal compositions within the standard deviations.

Diffraction study

In Figure 3(a-c) we show electron diffraction patterns of a crystal of $LaTaON_2$ obtained by rotating around the a_0 axis, where the subindex 0 refers to the cubic *Pm-3m* perovskite subcell. Reconstruction of the reciprocal lattice from these and other electron diffraction patterns lead to a superstructure $\sqrt{2}a_0 \times 2a_0 \times \sqrt{2}a_0$ with parameters a = 5.80 Å, b = 8.17 Å and c = 5.84 Å, and reflection conditions compatible with the space

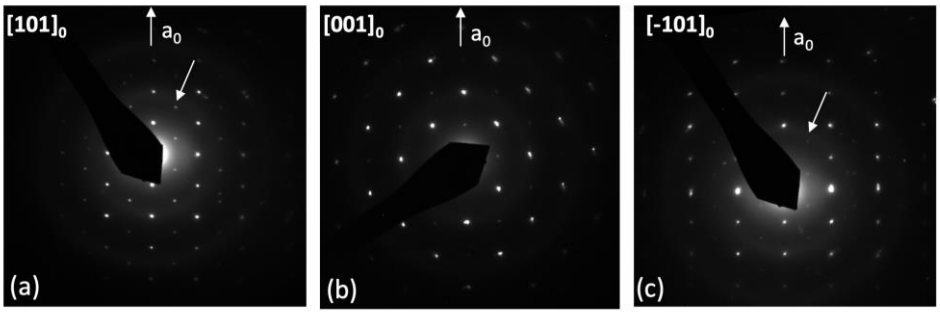

Figure 3. Electron diffraction patterns of (a, c) $\langle 101 \rangle_0$ and (b) $[001]_0$ planes of $LaTaON_2$ obtained by tilting around a_0 axis. In [101] (a) and [-101] (c) planes the small arrows indicate the superstructure reflections.

group *I2/m* (N^o 12). Similar results were obtained for the non-stochiometric compound $LaTaO_{1.12}N_{1.88}$.

The crystal structure of $LaTaON_2$ has been described in the space groups *Imma*[16] and *I2/m*,[19] which is equivalent to *C2/m*[20] but with a different orientation and dimensions of the unit cell. These groups correspond to the antiphase tilt systems $a^0b^-b^-$ and $a^0b^-c^-$ respectively.[25,26] The observation of superstructure reflections by electron diffraction in $\langle 110 \rangle_0$ zone-axis patterns (ZADPs) can help to infer the tilt system, following the method suggested by Woodward and Reaney.[27] Both *I2/m* and *Imma* space groups show $[110]_0$ planes with superstructure reflections, but whereas for *I2/m* these are present in all twelve $\langle 110 \rangle_0$ variants, for *Imma* there are two of these planes that do not show the extra spots. We performed the reconstruction of the reciprocal lattice by electron diffraction selecting 8 crystals for $LaTaON_2$ or $LaTaO_{1.12}N_{1.88}$, observing

superstructure reflections in all $\langle 110 \rangle_0$ planes. In consequence, the *I2/m* space group was chosen as statistically more probable.

In figures 1 and 4 we show the Rietveld fits for $LaTaON_2$ to synchrotron X-ray and neutron powder diffraction data respectively, and figures S3 and S4 show the corresponding refinements for $LaTaO_{1.12}N_{1.88}$. In both samples the secondary phase TaN was visible in the synchrotron X-ray diffraction patterns, as two small peaks at Q values of 2.42 and 2.57 $Å^{-1}$. The refined weight fraction of TaN was 2.06(4) % (molar fraction 0.04) in $LaTaON_2$ sample and 0.71(2) % (molar fraction 0.013) in $LaTaO_{1.12}N_{1.88}$. The presence of such small amounts of TaN does not change the anion stoichiometry determined by combustion analysis as it affects the %N content in a maximum value of +0.01 % (w/w) which is within the standard deviation of analysis results.

Tables 1 and 2 show the crystallographic data for $LaTaON_2$ and Tables S1 and S2 show those of $LaTaO_{1.12}N_{1.88}$. The initial model for neutron diffraction refinements was taken from our previous study on $LaTaON_2$ prepared by ammonolysis of $LaTaO_4$,[19] using the same *I2/m* space group, which resulted from symmetry lowering of orthorhombic *Imma* as a consequence of anion order. This splits the *8g* sites of *Imma* (Y2 positions) into two inequivalent positions *4g* and *4h* in *I2/m* (Y21 and Y22 sites). The O/N occupancies in the three anion sites Y1, Y21 and Y22 were refined independently starting with a random distribution 0.33/0.66. The refined nitrogen stoichiometries for $LaTaO_{1.12}N_{1.88}$ and $LaTaON_2$ were 1.79 and 2.04, respectively. These values are very close to the analyzed contents that were used as constraints in subsequent

refinements. In the refinements of synchrotron X-ray powder diffraction patterns the anion occupancies were fixed to those obtained from neutron diffraction. The resulting O/N occupancies for the three anion sites in $LaTaON_2$ Y1 (0.230(7)/0.770), Y21 (0.112(14)/0.888) and Y22 (0.658(14)/0.342), showed a marked preference of nitrogen for Y1 and Y21 sites (Figure 5a) and are different for Y21 and Y22 sites, accounting for the symmetry lowering from *Imma* to *I2/m*. The observed anion distribution in the nitrogen deficient sample $LaTaO_{1.12}N_{1.88}$ was similar to that found for $LaTaON_2$, with O/N occupancies of 0.296(6)/0.704, 0.164(11)/0.836 and 0.662(12)/0.338 for Y1, Y21 and Y22 sites respectively. The refined cell volume of $LaTaO_{1.12}N_{1.88}$, 264.545(4) $Å^3$ (from neutron diffraction data), was found smaller than for $LaTaON_2$, 264.733(5) $Å^3$, according with the larger ionic radius of N^{3-} (1.46 Å, CN=IV) compared to O^{2-}(1.38 Å, CN=IV) which over compensates the difference between the ionic radii of Ta^{5+} (0.65 Å, CN=VI) and Ta^{4+} (0.68 Å, CN=VI).[28] The differences in ionic radii of both anions affect the observed bond distances, which are larger for the stoichiometric compound (Tables 1 and S2). Bond valence calculations [29,30] for Ta, La, O and N ions lead to 4.954, 2.892, -2.079 and -2.959 valence units respectively in $LaTaO_{1.12}N_{1.88}$ and 4.966, 2.984, -2.079 and -2.959 valence units in $LaTaON_2$, which are both in close agreement with the ideal valences of 5, 3, -2, and -3.

The observed anion distribution in Y1, Y21 and Y22 sites is different from our previous results for $LaTaON_2$ prepared by ammonolysis (Figure 5b), where Y21 position was 100% occupied by nitride, whereas the other anion sites (Y1 and Y22) showed O/N occupancies close to 50%

(0.41(2)/0.59 for Y1 and 0.59/0.41 for Y22).[19] This anion distribution was interpreted as resulting from a *cis* configuration of nitrides in TaO_2N_4 octahedra induced by covalency, and the formation of zigzag M-anion chains that disorder in planes then leading to c.a. 50% of oxygen

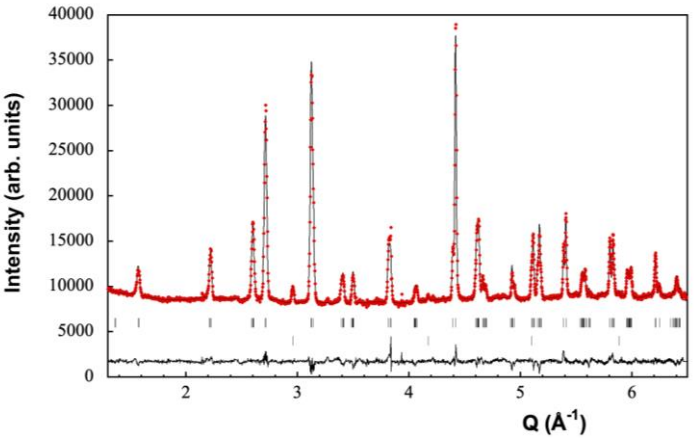

Figure 4. Observed and calculated neutron powder diffraction patterns of $LaTaON_2$. Upper and lower reflection markers are respectively for $LaTaON_2$ and vanadium from the sample environment.

and nitrogen in two sites. The observed occupancies in $LaTaON_2$ prepared at high temperature indicate a preference of nitrogen for Y21 and Y1 sites, but the three positions are partially occupied by the two anions which are more disordered than in the compound prepared by ammonolysis. The anion occupancies of the present study also differ from the distribution reported by Jansen and coworkers[20] for a sample of $LaTaON_2$ prepared in NH_3 at 850 ^oC from La_2O_3 and Ta_2O_5 using a

Table 1. Summary of the *I2/m* model for $LaTaON_2$ refined against room temperature neutron powder diffraction data using λ= 1.865 Å. Cell parameters: *a*= 5.71458(7), *b*= 8.05987(10), *c*=5.74772(6) Å, *β*=89.982(3)º. R_{Bragg}= 4.8 %, R_{wp}= 2.10 %, χ^2=4.34.[a]

atom	site	*x*	*y*	*z*	occupancy (O/N)
La	4i	0.7515(18)	0	0.2473(5)	
Ta	4e	3/4	1/4	3/4	
Y1	4i	0.7343(13)	0	0.6791(3)	0.230(7)/0.770
Y21	4g	0	0.7784(4)	0	0.112(14)/0.888
Y22	4h	1/2	0.2029(4)	0	0.658(14)/0.342
bond	**distance (Å)**	**Bond**	**distance (Å)**	**bond**	**distance (Å)**
La-Y1	2.484(3)	La-Y21	2.687(3) x 2	La-Y22	2.599(3) x 2
	2.807(7)		23.035(3) x 2		23.141(3) x 2
	2.970(7)				
	3.267(3)				
Ta-Y1	2.0578(5) x 2	Ta-Y21	2.0396(4) x 2	Ta-Y22	2.0614(6) x 2
Bond Angles (º): Ta-Y1-Ta	156.59(13)	Ta-Y21-Ta	167.07(18)	Ta-Y22-Ta	158.73(18)

[a] Estimated standard deviations in parentheses are shown once for each independent variable. Isotropic thermal parameters were common for all sites and refined to 0.06(4) $Å^2$.

mixture of $CaCl_2$, KCl and NaCl, that showed total order of O atoms in *trans* positions of the TaO_2N_4 octahedra (Figure 5c). Woodward and coworkers[16] used a similar method of synthesis under NH_3 with NaCl/KCl flux but at higher temperature of 950 ^oC, and described the crystal structure in the *Imma* space group with total disorder of nitrogen and oxygen in two crystallographically independent anion sites (Figure *5d*). The observed anion distributions in neutron diffraction studies of $LaTaON_2$ obtained by different routes indicate an influence of the preparation method on the crystal structure of perovskite oxynitrides, which may depend on kinetic or thermodynamic factors affected by the temperature of synthesis, reaction time, heating and cooling rates, and the

presence of liquid phases increasing the mobility of cations and anions. Differences in the crystal structure have been also observed in $SrTaO_2N$ samples prepared by distinct methods of synthesis. This compound crystallizes in the space group *I4/mcm* when prepared at 950 ^oC under NH_3, whereas it shows the non-tilted *P4/mmm* structure in samples obtained at 1500 ^oC in N_2.[31] However, in contrast to $LaTaON_2$, the observed anion order in $SrTaO_2N$ is similar for samples prepared at high temperature and by ammonolysis at lower temperatures.[31,32]

Table 2. Summary of the *I2/m* model for $LaTaON_2$ refined against room temperature synchrotron X-ray powder diffraction data using λ= 0.41322 Å. Cell parameters: *a*= 5.71436(2), *b*= 8.06057(3), *c*= 5.74729(2) Å, β=90.0067(5)º. R_{Bragg}= 4.36 %, R_{wp}= 11.7 %, χ^2=1.62.[a] The O/N occupancies were fixed to the values obtained from neutron diffraction.

atom	site	*x*	*y*	*z*	*B* (Å^2)	occupancy (O/N)
La	4*i*	0.7541(4)	0	0.2482(4)	0.613(9)	
Ta	4*e*	3/4	1/4	3/4	0.553(7)	
Y1	4*i*	0.748(8)	0	0.679(2)	1.09(14)	0.230/0.770
Y21	4*g*	0	0.786(4)	0	1.09	0.112/0.888
Y22	4*h*	1/2	0.204(3)	0	1.09	0.658/0.342
La-Y1	2.476(12)	La-Y21	2.64(2) × 2	La-Y22	2.617(15) × 2	
	2.88(5)		3.09(2) × 2		3.124(19) × 2	
	2.90(5)					
	3.272(12)					
Ta-Y1	2.056(2) × 2	Ta-Y21	2.047(5) × 2	Ta-Y22	2.060(4) × 2	
Bond Angles (^{o}): Ta-Y1-Ta 157.10(9)		Ta-Y21-Ta 163.70(18)		Ta-Y22-Ta 159.26(17)		

[a] Estimated standard deviations in parentheses are shown once for each independent variable.

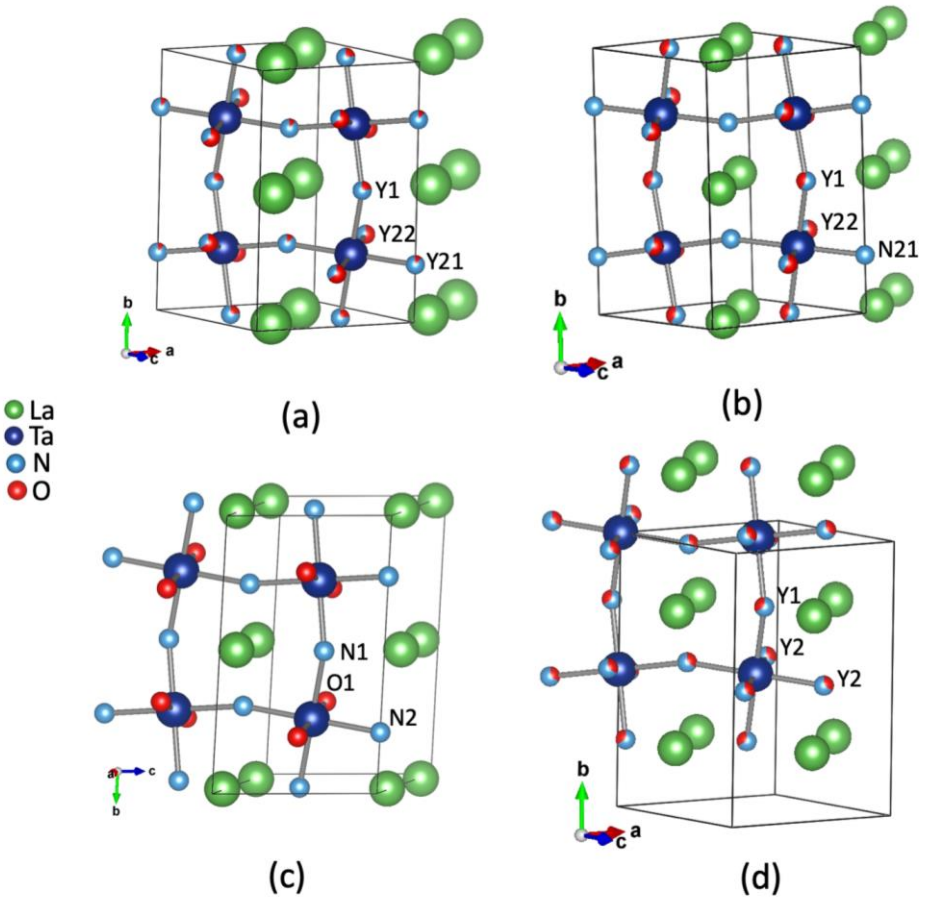

Figure 5. Anion order models for $LaTaON_2$: (a) This work; (b) *I2/m* structure corresponding to a sample prepared by ammonolysis of $LaTaO_4$;[19] (c) *C2/m* model for a sample prepared by ammonolysis of La_2O_3, Ta_2O_5 and an equimolecular mixture of $CaCl_2$, KCl and NaCl at 850 ^oC;[20] (d) *Imma* structure for a sample prepared by ammonolysis of La_2O_3, Ta_2O_5 and a mixture of NaCl and KCl at 950 ^oC.[16]

Electrical and optical properties

Figure 6a shows the electrical resistivity as a function of temperature of the stoichiometric $LaTaON_2$ compound. The room-temperature resistivity is of about 10^7 Ω·cm. It rapidly increases up to around $1x10^9$ Ω·cm at 50-60 K. By further cooling down, the resistivity increases moderately up to about $6x10^9$ Ω·cm at the lowest temperature (5 K). The large low temperature resistivity is consistent with the insulating character expected from the $5d^0$ nature of its conduction band. The room temperature resistivity is in fairly good agreement with that reported for high pressure sintered pellets of $SrTaO_2N$.[33] However, as emphasized by the Arrhenius plots in Figure 6a (top-right axes), it is clear that ρ(T) cannot be described by a single simple activated behavior. The increase of resistance observed at high temperature (> 60 K) could be compatible with an activated behavior, although with a relatively small activation energy (≈ 0.2 eV). In any event, the observed temperature dependence of the resistivity indicates that it is ruled by extrinsic defects.

Figure 6b shows the temperature dependence of the dielectric permittivity (ε_r) of $LaTaON_2$, recorded at various frequencies (50 kHz-1MHz). It can be noticed that ε_r decreases from ≈280 at room temperature to ≈ 200 at 5 K. The observed temperature and frequency dependences suggest a minor contribution from a Maxwell-Wagner effect[34] which typically occurs due to the finite conductivity of samples, and thus it is most noticeable at high temperature. The frequency dependent permittivity observed at room temperature is a fingerprint of

this effect. In contrast, the low-temperature data is rather insensitive to frequency. Therefore, the value obtained at the lowest temperature ($\varepsilon_r = 200$) is likely to be an accurate measure of the intrinsic permittivity of $LaTaON_2$. In principle, the measured permittivity could be corrected for density effects [35, 36] to extract the intrinsic permittivity of bulk $LaTaON_2$. However, this extraction is not free from uncertainties (See Figure S5 of Supplementary Information), and this correction is omitted here. The conductivity of N-deficient samples, such as $LaTaO_{1.12}N_{1.88}$ (Figure S6a), is found to be definitely larger than for the stoichiometric compound due to presence of N-vacancy donor levels and the subsequent electron doping of the conduction band. Consequently, the measured permittivity of nitrogen deficient samples is dominated by the Maxwell-Wagner contribution (Figure S6b), precluding extraction of reliable permittivity values. The temperature and frequency dependence of the dielectric losses of these samples are consistent with this view (See Figure S7 in Supplementary Information). UV-visible spectroscopy measurements of $LaTaON_2$ (Figure 6c) show an abrupt change of reflectance in the Kubelka-Munk function at about 600 nm. which is a fingerprint of the onset of optical absorption. However, a perceptible background is well visible at longer wavelengths. Similar absorbing tails have been observed in related compounds and have been attributed to the presence of reduced Ta^{m+} ($m<5$) species at the grains surface. The absorption edge is better appreciated in the Tauc plot shown in Figure 6d, that indicates a direct transition with bandgap energy of ≈ 1.9 eV.

Results reported above for the stoichiometric $LaTaON_2$ sample indicate a bandgap of about 1.9 eV and a permittivity of $\varepsilon_r \approx 200$ (10 K, 1MHz). As expected from the smaller electronegativity of nitrogen compared to oxygen, the band gap of $LaTaON_2$ is found to be narrower than in the related $SrTaO_2N$ (2.1 eV) and $KTaO_3$ (3.5 e V) oxides. On the other hand, the permittivity value is rather large as for other oxynitrides, but comparable to values reported for $SrTaO_2N$ ($\varepsilon_r \approx 66$-70)[37,38] or $BaTaO_2N$ (320)[39] films and high-pressure/high temperature sintered pellets of $SrTaO_2N$ ($\varepsilon_r \approx 200$).[33] We restrict the comparison to data reported for thin films and sintered samples, because, as stressed by Masubuchi, et al[10], the ammonolysis process used to prepare oxynitrides indefectibly leads to poorly sintered samples where the role of grain boundaries on impedance measurements can be overwhelming, precluding extraction of reliable data.

Permittivity values of about 200 in simple oxides are uncommon except when materials are close to polar distortions or contain (nano)polar regions. Whereas short range order of O^{-2} and N^{-3} ions in centrosymmetric perovskite oxynitride structures is claimed to give rise to local polar structures in strained thin films ($SrTaO_2N$) [40] or even in single crystals ($BaTaO_2N$),[41] long range order and the accompanying non-centrosymmetric and polar order has only been reported in the hexagonal perovskite $BaWON_2$.[4] In $LaTaON_2$, the octahedral coordination of Ta^{+5} ions involves 4 N and 2 O ions. The observed partially disordered anion distribution in our samples prepared at high temperature does not indicate the presence of ordered dipoles, but a local

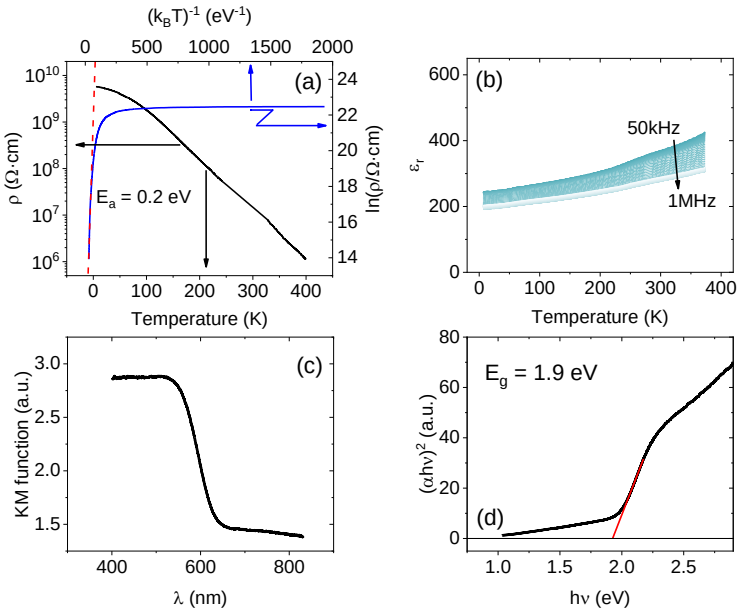

Figure 6. a) Electrical resistivity $\rho(T)$ (left axis) and ln $[\rho(T^{-1})]$ (right axis); b) permittivity $\varepsilon_r(T)$ recorded at various frequencies. Dashed line is the linear region used to evaluate the activation energy as indicated; c) Kubelka-Munk representation of the UV-Vis diffuse reflectance spectra of $LaTaON_2$; d) Optical absorption Tauc plots for direct transitions.

cis configuration of nitrides could still exist, similar to that suggested for cubic $BaTaO_2N$.[7] The competing Coulomb attraction between O^{-2} and N^{-3} anions and Ta^{+5} shall allow decentering of the metal, which it turn will give rise to a large permittivity, as observed. In the same vein, even in absence of any long or short range order of dipoles, a similar permittivity should be expected for $SrTaO_2N$ which is in agreement with observation.

3.1.4 Conclusions

Highly sintered ceramic samples of $LaTaON_2$ have been prepared in N_2 at 1500 ^oC following two approaches of solid state reaction between La_2O_3, LaN and Ta_3N_5 or between LaN and TaON. Partial decomposition leading to reduced $LaTaO_{1+x}N_{2-x}$ compounds with nitrogen deficiencies up to x=0.35 is observed, while the stoichiometric compound is obtained in the first reaction by increasing the LaN/La_2O_3 ratio in the initial mixture. The crystal structures of $LaTaON_2$ and $LaTaO_{1.12}N_{1.88}$ are described in the *I2/m* space group with nitride and oxide anions occupying three positions in different proportions, with preferred occupancy of nitride for two sites. This anion distribution contrasts with that observed in a previous study for $LaTaON_2$ prepared by ammonolysis at 950 ^oC, that showed one of the three anion sites totally occupied by nitride, and it also differs from results for samples of the same compound prepared by other groups under NH_3 at similar lower temperatures but using fluxes. Hence, the synthetic route of this highly nitrided compound has an impact on final anionic ordering. This is in contrast with the similar anion order schemes observed for the less nitrided perovskite $SrTaO_2N$ prepared by ammonolysis or under N_2 at high temperatures. However, the synthesis approach of $LaTaON_2$ does not have any perceptible impact on the optical gap, which is about 1.9 eV in all cases. The well sintered stoichiometric sample allows reliable determination of the dielectric permittivity which is about 200, similar to that reported for perovskites with one nitrogen per formula such as $SrTaO_2N$.

Associated Content

Supporting Information. Observed and calculated neutron powder diffraction, observed and calculated synchrotron X-ray powder diffraction patterns, crystallographic data and physical measurements of $LaTaO_{1.12}N_{1.88}$ and $LaTaON_2$.

Author Information

Corresponding Author

Amparo Fuertes- Institut de Ciència de Materials de Barcelona(ICMAB-CSIC), Campus UAB, 08193 Bellaterra (Spain). amparo.fuertes@icmab.es

Josep Fontcuberta- Institut de Ciència de Materials de Barcelona(ICMAB-CSIC), Campus UAB, 08193 Bellaterra (Spain). fontcuberta@icmab.cat

Author Contributions

The manuscript was written through contributions of all authors. All authors have given approval to the final version of the manuscript.

Funding Sources

Ministerio de Ciencia e Innovación, Spain (MAT2017-86616-R, MAT2017-85232-R and CEX2019-000917-S). Generalitat de Catalunya (2017SGR1377, 2017SGR581).

Acknowledgment

This work was supported by the Ministerio de Ciencia e Innovación, Spain (MAT2017-86616-R, MAT2017-85232-R, PID2019-107727RB-I00 (AEI/FEDER, EU) and CEX2019-000917-S), from Generalitat de Catalunya (2017SGR1377, 2017SGR581) and from CSIC through the i-LINK (LINKA20338) program. We thank Alba and ILL for beam time provision (experiments 2017092391 and 5-21-1113 respectively), Dr. François Fauth for assistance in data collection at Alba and Dr. Bernat Bozzo (ICMAB-CSIC) for performing electrical measurements. Project supported by a 2020 Leonardo Grant for Researchers and Cultural Creators, BBVA Foundation. IF acknowledges Ramón y Cajal contract RYC-2017-22531 and JRG acknowledges the AEAT predoctoral fellowship PRE2018-085204.

3.1.5 References

(1) Fuertes, A. Nitride tuning of transition metal perovskites. *APL Materials* **2020**, *8* (2), 020903.
(2) Kasahara, A.; Nukumizu, K.; Hitoki, G.; Takata, T.; Kondo, J. N.; Hara, M.; Kobayashi, H.; Domen, K. Photoreactions on $LaTiO_2N$ under visible light irradiation. *The Journal of Physical Chemistry A* **2002**, *106* (29), 6750-6753.
(3) Jansen, M.; Letschert, H.-P. Inorganic yellow-red pigments without toxic metals. *Nature* **2000**, *404* (6781), 980-982.
(4) Oró-Solé, J.; Fina, I.; Frontera, C.; Gàzquez, J.; Ritter, C.; Cunquero, M.; Loza-Alvarez, P.; Conejeros, S.; Alemany, P.; Canadell, E. Engineering polar oxynitrides: Hexagonal perovskite $BaWON_2$. *Angewandte Chemie International Edition* **2020**, *59* (42), 18395-18399.
(5) Black, A. P.; Suzuki, H.; Higashi, M.; Frontera, C.; Ritter, C.; De, C.; Sundaresan, A.; Abe, R.; Fuertes, A. New rare earth hafnium oxynitride

perovskites with photocatalytic activity in water oxidation and reduction. *Chemical Communications* **2018**, *54* (12), 1525-1528.
(6) Kim, Y.-I.; Woodward, P. M.; Baba-Kishi, K. Z.; Tai, C. W. Characterization of the structural, optical, and dielectric properties of oxynitride perovskites AMO_2N (A= Ba, Sr, Ca; M= Ta, Nb). *Chemistry of Materials* **2004**, *16* (7), 1267-1276.
(7) Page, K.; Stoltzfus, M. W.; Kim, Y.-I.; Proffen, T.; Woodward, P. M.; Cheetham, A. K.; Seshadri, R. Local atomic ordering in $BaTaO_2N$ studied by neutron pair distribution function analysis and density functional theory. *Chemistry of Materials* **2007**, *19* (16), 4037-4042.
(8) Kikkawa, S.; Sun, S.; Masubuchi, Y.; Nagamine, Y.; Shibahara, T. Ferroelectric response induced in cis-type anion ordered $SrTaO_2N$ oxynitride perovskite. *Chemistry of Materials* **2016**, *28* (5), 1312-1317.
(9) Yang, M.; Oró-Solé, J.; Rodgers, J. A.; Jorge, A. B.; Fuertes, A.; Attfield, J. P. Anion order in perovskite oxynitrides. *Nature Chemistry* **2011**, *3* (1), 47-52.
(10) Masubuchi, Y.; Sun, S.-K.; Kikkawa, S. Processing of dielectric oxynitride perovskites for powders, ceramics, compacts and thin films. *Dalton Transactions* **2015**, *44* (23), 10570-10581.
(11) Fuertes, A. Synthetic approaches in oxynitride chemistry. *Progress in Solid State Chemistry* **2018**, *51*, 63-70.
(12) Clarke, S. J.; Hardstone, K. A.; Michie, C. W.; Rosseinsky, M. J. High-temperature synthesis and structures of perovskite and n= 1 Ruddlesden− Popper tantalum oxynitrides. *Chemistry of Materials* **2002**, *14* (6), 2664-2669.
(13) Sun, S.-K.; Motohashi, T.; Masubuchi, Y.; Kikkawa, S. Direct synthesis of $SrTaO_2N$ from $SrCO_3/Ta_3N_5$ involving CO evolution. *Journal of the European Ceramic Society* **2014**, *34* (16), 4451-4455.
(14) Wang, X.; Hisatomi, T.; Wang, Z.; Song, J.; Qu, J.; Takata, T.; Domen, K. Core–shell-structured $LaTaON_2$ transformed from $LaKNaTaO_5$ plates for enhanced photocatalytic H_2 evolution. *Angewandte Chemie International Edition* **2019**, *131* (31), 10776-10780.
(15) Marchand, R.; Pors, F.; Laurent, Y. Nouvelles perovskites oxynitrures de stoechiometrie ABO_2N (A= lanthanide, B= Ti) et $ABON_2$ (A= lanthanide, B= Ta ou Nb). In *Annales de Chimie (Paris. 1914)*, 1991; Vol. 16, pp 553-560.
(16) Porter, S. H.; Huang, Z.; Woodward, P. M. Study of anion order/disorder in $RTaN_2O$ (R= La, Ce, Pr) perovskite nitride oxides. *Crystal Growth & Design* **2014**, *14* (1), 117-125.

(17) Watanabe, T.; Tajima, K.; Li, J.; Matsushita, N.; Yoshimura, M. Low-temperature ammonothermal synthesis of $LaTaON_2$. *Chemistry Letters* **2011**, *40* (10), 1101-1102.
(18) Cordes, N.; Schnick, W. Ammonothermal synthesis of crystalline oxonitride perovskites $LnTaON_2$ (Ln= La, Ce, Pr, Nd, Sm, Gd). *Chemistry–A European Journal* **2017**, *23* (47), 11410-11415.
(19) Clark, L.; Oró-Solé, J.; Knight, K. S.; Fuertes, A.; Attfield, J. P. Thermally robust anion-chain order in oxynitride perovskites. *Chemistry of Materials* **2013**, *25* (24), 5004-5011.
(20) Guenther, E.; Hagenmayer, R.; Jansen, M. Structural investigations on the oxidenitrides $SrTaO_2N$, $CaTaO_2N$, and $LaTaON_2$ by neutron and X-Ray powder diffraction. *ChemInform* **2000**, 626, 1519-1525.
(21) Fauth, F.; Peral, I.; Popescu, C.; Knapp, M. The new material science powder diffraction beamline at ALBA synchrotron. *Powder Diffraction* **2013**, *28* (S2), S360-S370.
(22) Rodríguez-Carvajal, J. Recent advances in magnetic structure determination by neutron powder diffraction. *Physica B: Condensed Matter* **1993**, *192* (1-2), 55-69.
(23) Chen, D.; Habu, D.; Masubuchi, Y.; Torii, S.; Kamiyama, T.; Kikkawa, S. Partial nitrogen loss in $SrTaO_2N$ and $LaTiO_2N$ oxynitride perovskites. *Solid State Sciences* **2016**, *54*, 2-6.
(24) Cox, P. A. Transition Metal Oxides: An Introduction to Their Electronic Structure and Properties; *Clarendon Press*, 1995.
(25) Glazer, A. M. The classification of tilted octahedra in perovskites. *Acta Crystallographica Section B: Structural Crystallography and Crystal Chemistry* **1972**, *28* (11), 3384-3392.
(26) Howard, C. J.; Stokes, H. T. Group-theoretical analysis of octahedral tilting in perovskites. *Acta Crystallographica Section B: Structural Science* **1998**, *54* (6), 782-789.
(27) Woodward, D. I.; Reaney, I. M. Electron diffraction of tilted perovskites. *Acta Crystallographica Section B: Structural Science* **2005**, *61* (4), 387-399.
(28) Shannon, R. D. Revised effective ionic radii and systematic studies of interatomic distances in halides and chalcogenides. *Foundations of Crystallography* **1976**, *32* (5), 751-767.
(29) Brown, I. D. The chemical bond in inorganic chemistry: the bond valence model; *Oxford University Press*, 2002.
(30) Brese, N.; O'keeffe, M. Bond-valence parameters for solids. *Acta Crystallographica Section B: Structural Science* **1991**, *47* (2), 192-197.

(31) Johnston, H.; Black, A. P.; Kayser, P.; Oró-Solé, J.; Keen, D. A.; Fuertes, A.; Attfield, J. P. Dimensional crossover of correlated anion disorder in oxynitride perovskites. *Chemical Communications* **2018**, *54* (41), 5245-5247.
(32) Zhang, Y.-R.; Motohashi, T.; Masubuchi, Y.; Kikkawa, S. Local anionic ordering and anisotropic displacement in dielectric perovskite $SrTaO_2N$. *Journal of the Ceramic Society of Japan* **2011**, *119* (1391), 581-586.
(33) Masubuchi, Y.; Kawamura, F.; Taniguchi, T.; Kikkawa, S. High pressure densification and dielectric properties of perovskite-type oxynitride $SrTaO_2N$. *Journal of the European Ceramic Society* **2015**, *35* (4), 1191-1197.
(34) Von Hippel, A. Dielectrics and waves, artech house. *Inc., Norwood, MA* **1995**.
(35) Wing, Z. N.; Wang, B.; Halloran, J. W. Permittivity of porous titanate dielectrics. *Journal of the American Ceramic Society* **2006**, *89* (12), 3696-3700.
(36) Markel, V. A. Introduction to the maxwell garnett approximation: tutorial. *JOSA A* **2016**, *33* (7), 1244-1256.
(37) Marlec, F.; Le Paven, C.; Le Gendre, L.; Benzerga, R.; Cheviré, F.; Tessier, F.; Gam, F.; Sharaiha, A. Deposition and dielectric study as function of thickness of perovskite oxynitride $SrTaO_2N$ thin films elaborated by reactive sputtering. *Surface and Coatings Technology* **2017**, *324*, 607-613.
(38) Ziani, A.; Le Paven, C.; Le Gendre, L.; Marlec, F.; Benzerga, R.; Tessier, F.; Cheviré, F.; Hedhili, M. N.; Garcia-Esparza, A. T.; Melissen, S. Photophysical properties of $SrTaO_2N$ thin films and influence of anion ordering: a joint theoretical and experimental investigation. *Chemistry of Materials* **2017**, *29* (9), 3989-3998.
(39) Kim, Y.-I.; Si, W.; Woodward, P. M.; Sutter, E.; Park, S.; Vogt, T. Epitaxial thin-film deposition and dielectric properties of the perovskite oxynitride $BaTaO_2N$. *Chemistry of Materials* **2007**, *19* (3), 618-623.
(40) Oka, D.; Hirose, Y.; Kamisaka, H.; Fukumura, T.; Sasa, K.; Ishii, S.; Matsuzaki, H.; Sato, Y.; Ikuhara, Y.; Hasegawa, T. Possible ferroelectricity in perovskite oxynitride $SrTaO_2N$ epitaxial thin films. *Scientific Reports* **2014**, *4* (1), 4987.
(41) Hosono, A.; Masubuchi, Y.; Yasui, S.; Takesada, M.; Endo, T.; Higuchi, M.; Itoh, M.; Kikkawa, S. Ferroelectric $BaTaO_2N$ crystals

grown in a BaCN2 flux. *Inorganic Chemistry* **2019**, *58* (24), 16752-16760.

3.2. High-Temperature Synthesis of Ferromagnetic $Eu_3Ta_3(O,N)_9$ with a Triple Perovskite Structure

Published in: *Inorganic Chemistry*. **2024**, *62*, 17362-17370.

Authors: Jhonatan R. Guarín,[§] Carlos Frontera,[§] Judith Oró-Solé,[§] Jaume Gàzquez,[§] Clemens Ritter,[‡] Josep Fontcuberta[§,*] and Amparo Fuertes[§,*]

§ Institut de Ciència de Materials de Barcelona (ICMAB-CSIC), Campus UAB, 08193 Bellaterra(Spain).

‡ Institut Laue-Langevin, 71 Av. de Martyrs, Grenoble 38000(France)

https://doi.org/10.1021/acs.inorgchem.3c02691

Keywords: Triple Perovskite, Perovskite oxynitrides, High temperature synthesis, Crystal Structure Elucidation, STEM.

Europium tantalum perovskite oxynitrides are prepared by a new solid-state synthesis approach under N_2 or N_2/H_2 at 1200 °C starting with metal nitrides and oxides. N/O tuning in the mixture of reactants allows to obtain the first triple perovskite oxynitride $Eu_3Ta_3O_{3.66}N_{5.34}$ where europium cations order in two A′ and A″ sites with ratio 2:1 occupied preferentially by Eu^{3+} and Eu^{2+}, respectively. The new compound is ferromagnetic with $T_c \approx 3$ K.

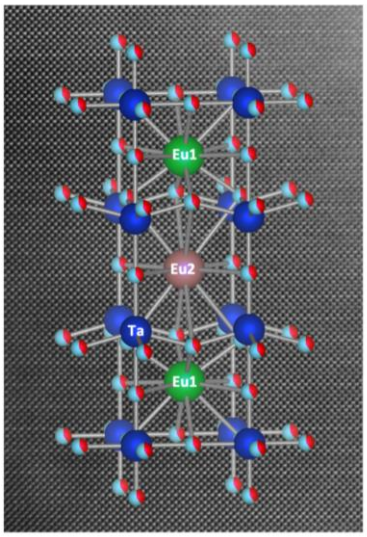

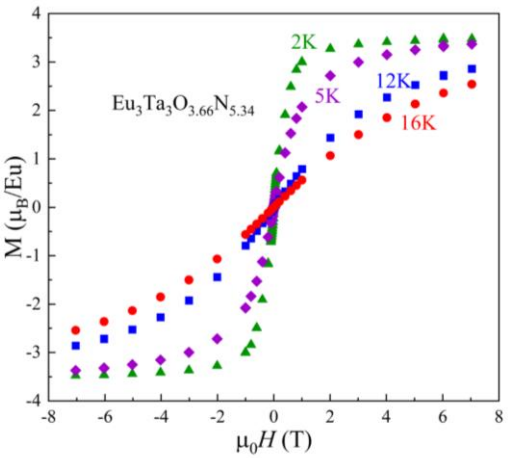

Abstract: Europium tantalum perovskite oxynitrides were prepared by a new high-temperature solid-state synthesis under N_2 or N_2/H_2 gas. The nitrogen stoichiometry was tuned from 0.63 to 1.78 atoms per Eu or Ta atom, starting with appropriate N/O ratios in the mixture of the reactants Eu_2O_3, EuN and Ta_3N_5, or Eu_2O_3 and TaON, which was treated at 1200 °C for 3 h. Two phases were isolated with compositions $EuTaO_{2.37}N_{0.63}$ and $Eu_3Ta_3O_{3.66}N_{5.34}$, showing different crystal structures and magnetic properties. Electron diffraction and Rietveld refinement of synchrotron radiation X-ray diffraction indicated that $EuTaO_{2.37}N_{0.63}$ is a simple perovskite with cubic *Pm*-3*m* structure and cell parameter a = 4.02043(1) Å, whereas the new compound $Eu_3Ta_3O_{3.66}N_{5.34}$ is the first example of a triple perovskite oxynitride and shows space group *P4*/*mmm* with crystal parameters a = 3.99610(2), c = 11.96238(9) Å. The tripling of the c-axis in this phase is a consequence of the partial ordering of europium atoms with different charges in two A sites of the perovskite structure with relative ratio 2:1, where the formal oxidation states +3 and +2 are respectively dominant. Magnetic data provide evidence of ferromagnetic ordering developing at low temperatures in both oxynitrides, with saturation magnetization of about 6 μ_B and 3 μ_B per Eu ion for $EuTaO_{2.37}N_{0.63}$ and the triple perovskite $Eu_3Ta_3O_{3.66}N_{5.34}$ respectively, and corresponding Curie temperatures of about 7 and 3 K, which is in agreement with the lower proportion of Eu^{2+} in the latter compound.

3.2.1 Introduction

Perovskite oxynitrides $AB(O,N)_3$ (A = alkaline earth or rare earth metal; B = transition) are important materials with electronic properties and photocatalytic activity of relevance in several reactions.[1] The majority of reported compounds show crystal structures derived from the *Pm*-3*m* aristotype, frequently showing lower symmetry space groups resulting from a combination of octahedral tilting and anion order.[2-4] Perovskite oxynitrides with more complex structures have been also reported, although the number of compounds is restricted to a few examples. Double perovskites with B-site order $A_2B'B''(O,N)_6$ have been reported for three compounds with the pairs of cations B'/B''= Fe^{3+}/W^{6+},[5] Fe^{3+}/Mo^{6+},[6] and Mn^{2+}/Ta^{5+}.[7] Layered Ruddlesden–Popper [8,9] ($A_{n+1}B_nO_{3n+1}$) phases with n = 1 ($A_2B(O,N)_4$) and n = 2 ($A_3B_2(O,N)_7$) have been reported for six compounds containing Nb,[10] Ta,[11−13] or Al, [14] and Dion-Jacobson structures [15,16] $A'[A''_{n-1}B_n(O,N)_{3n+1}]$ have been found for A′ = alkaline metal, A″ = La, Ca, and B = Ta, Nb.[17,18] In the group of hexagonal perovskite oxynitrides, the only known compound is $BaWON_2$ that shows the 6H polytype.[19]

Europium perovskite oxynitrides $EuB(O,N)_3$ (B = Ti, Nb, W, Ta) have been investigated for their electrical and magnetic properties, which are affected by the N/O balance that tunes the formal valence state of Eu and the B cations: Eu^{2+} to Eu^{3+}, and those of transition metals Nb^{4+}, Nb^{5+}, W^{5+}, and W^{6+}. For instance, $EuNbO_{2+x}N_{1-x}$ ($x \leq 0.14$) [20] and $EuWO_{1+x}N_{2-x}$ ($-0.16 \leq x \leq 0.46$) [21] show ferromagnetic ordering of Eu^{2+} S = 7/2 spins below 5.2 and 12 K, respectively. In $EuWO_{1+x}N_{2-x}$, the electrical

conductivity changes with the N/O ratio, and in both Nb and W compounds colossal magnetoresistance emerges below the Curie temperature, arising from the coupling between the localized Eu^{2+} spins and the transition metal (4,5)d carriers. $EuTiO_{3-x-y}N_x$ with nitrogen contents up to $x = 1$ has been also reported, [22] with the N/O ratio and the anion vacancies tuning the europium oxidation state and the electronic properties.

The europium tantalum oxynitride perovskite $EuTaO_2N$ was first prepared by Marchand et al. by the treatment of $EuTaO_4$ under NH_3 at 950 °C.[23] More recently, we prepared this oxynitride in similar conditions with a small nitrogen nonstoichiometry $EuTaO_{2-x}N_{1+x}$ ($0 \leq x \leq 0.2$), formally involving the presence of a low proportion of Eu^{3+} for $x > 0$, and ferromagnetism was observed below $T_c = 5.1$ K for a sample with $x = 0.05$. The laboratory X-ray diffraction pattern of the $EuTaO_2N$ sample could be indexed in a cubic cell with a =4.0217(2) Å, but synchrotron X-ray diffraction indicated a small tetragonal distortion with a =4.02054(2), c =4.03079(4) Å.[20] Electron diffraction of $EuTaO_2N$, $EuNbO_2N$, and $EuWO_2N$ shows a $\sqrt{2}a_0 \times \sqrt{2}a_0 \times 2a_0$ superstructure (where a_0 is the parameter of the perovskite cubic subcell) that was ascribed to octahedral tilting.[20,21] Disordered B-site perovskites with compositions $EuTi_{0.5}W_{0.5}O_{3-x}N_x$ and nitrogen contents between 0.87 and 1.63 show ferromagnetic and antiferromagnetic exchange interactions between the Eu^{2+} cations, and the magnetic properties are tuned by the equilibrium $Eu^{2+} + W^{6+} \leftrightarrow Eu^{3+} + W^{5+}$ which is shifted to the right for larger x values.[24]

The synthesis of all previously reported europium perovskite oxynitrides has been performed by ammonolysis of precursors at temperatures below 1000 °C. In this paper, we report the study of the crystal structure and magnetic properties of $EuTaO_{3-x}N_x$ compounds with a large range of N/O contents, prepared by a new synthetic approach that uses solid-state reactions between metal nitrides and oxides under N_2 or N_2/H_2 gas at relatively high temperature (1200 °C). Two phases have been isolated with $EuTaO_{2.37}N_{0.63}$ and $Eu_3Ta_3O_{3.66}N_{5.34}$ stoichiometries showing different perovskite structures, as determined from synchrotron X-ray diffraction and electron diffraction. $EuTaO_{2.37}N_{0.63}$ is a simple Eu^{2+} cubic perovskite similar to previously reported $EuTaO_2N$ but with a large proportion (37%) of reduced Ta^{4+}. The compound $Eu_3Ta_3O_{3.66}N_{5.34}$ represents the first example of an oxynitride with a triple perovskite structure, which is a consequence of the partial ordering of Eu^{2+} and Eu^{3+} ions in the A sites. The magnetic data are found to be fully consistent with this finding, with both oxynitrides displaying a ferromagnetic ordering at low temperatures, with Curie temperatures of about 7 K for $EuTaO_{2.37}N_{0.63}$ and somewhat lower (≈3 K) for $Eu_3Ta_3O_{3.66}N_{5.34}$ due to dilution effects of magnetic interactions in the latter compound.

3.2.2 Experimental Methods

Synthesis and Chemical Characterization

Samples of 130 mg with compositions $EuTaO_{3-x}N_x$ ($0.63 \leq x \leq 1.78$) were prepared using the reactants Eu_2O_3 (Sigma-Aldrich 99.9%), EuN (Materion, 99.9%), TaON, and Ta_3N_5. The N/O ratio in the initial mixture was the most determining factor in the final nitrogen content of the sample. This was changed by varying the proportion of the reactants while keeping constant the Eu/Ta ratio of 1:1. Eu_2O_3 was treated at 900 °C under a dynamic vacuum of 10^{-3} Torr for dehydration. Ta_3N_5 was prepared by the treatment of Ta_2O_5 (Sigma-Aldrich, 99.99%) at 850 °C under $NH_3(g)$ (Carburos Metálicos, 99.9%), at a flow rate of 600 cm^3/min, using several cycles of 15 h with intermediate regrinding. TaON was prepared by the treatment of Ta_2O_5 at the same temperature under NH_3(g) at a flow rate of 40 cm^3/min, using two cycles of 3 h with intermediate regrinding.[25] Handling of the reactants, mixing, and pelletizing were done in a glovebox under a recirculating Ar atmosphere. The pellets were placed in a molybdenum crucible covered by zirconium foil, which was also used for oxygen and water scavenging in a second crucible placed close to the sample in the furnace tube (Al_2O_3, Alsint 99.7%). The samples were heated at 300 °C/h up to 1200 °C under flowing N_2 (Air Liquide, 99.9999%) or N_2/H_2 (95%/5% v/v, Air Liquide, 99.9999%), treated for 3 h at 1200 °C, and cooled down to room temperature.

Nitrogen contents were determined by combustion analysis performed in a ThermoFisher Scientific instrument, heating the samples in oxygen up to 1060 °C and using MgO, WO_3, and Sn as additives and atropine as a reference standard. EDX analyses of cation contents were performed in a FEI Quanta 200 FEG microscope equipped with an EDAX detector with an energy resolution of 132 eV. The analyses were performed on 10–15 crystallites for each sample.

Structural Characterization

Laboratory X-ray powder diffraction data were acquired on a Panalytical X'Pert Pro MPD diffractometer using Cu Kα radiation (λ = 1.5418 Å). High-resolution synchrotron X-ray powder diffraction data were measured at room temperature from capillary samples (0.3 mm diameter) in the angular range $2.0° \leq 2\theta \leq 56.9°$ at the MSPD beamline [26] of the ALBA Synchrotron (Cerdanyola del Vallès, Spain). A short wavelength of 0.45872 Å calibrated with Si NIST was selected by using a double Si(111) and Si(220) crystal monochromator. Background refinement was performed by linear interpolation, and data were corrected from absorption.

Neutron powder diffraction data were collected for 12 h at room temperature on the high-intensity D20 diffractometer at the Institut Laue-Langevin (ILL), France. In order to reduce the absorption from Eu, a double wall vanadium can was used as a sample holder, and a short wavelength of 1.37 Å at the high 118° take-off angle giving high resolution was chosen. The step scanning mode where the detector was

moved in 61 steps of 0.05° was chosen in order to compensate for the nonperfect calibration of the more than 3000 detector cells. Rietveld analysis was carried out using the program Fullprof.[27]

Electron diffraction micrographs were obtained in a JEOL 1210 transmission electron microscope operating at 120 kV using a side entry double tilt ±60°/±30° specimen holder. The samples were prepared by dispersing the powders in hexane and depositing a droplet of the suspension on a copper grid coated with a holey carbon film. The local microstructure of the samples was analyzed by means of scanning transmission electron microscopy (STEM) on a ThermoFisher Spectra 300 operated at 300 kV. The high-angle annular dark field detector allows for recording incoherent *Z*-contrast images, in which the contrast of an atomic column is approximately proportional to the square of the average atomic number (*Z*). Accordingly, it is possible to distinguish between Ta and Eu. The experiments were performed in the Joint Electron Microscopy Center at ALBA (Cerdanyola del Vallès, Spain).

Magnetic Measurements

Magnetic measurements were performed at fields of 25 Oe and 10 kOe between 2 and 300 K using a Quantum Design SQUID magnetometer. Magnetization-field loops were measured between −70 and +70 kOe between 2 and 16 K.

3.2.3 Results and Discussion

Synthesis and Structural Study of $EuTaO_{2.37}N_{0.63}$ and $Eu_3Ta_3O_{3.66}N_{5.34}$

The synthesis of europium tantalum perovskite oxynitride samples is performed at high temperatures under N_2/H_2 (95%/5% v/v) or N_2 gas, using one of the following solid-state reactions with one single treatment of 3 h at 1200 °C

$$Eu_2O_3 + 2\ TaON \rightarrow 2\ EuTaO_{3-x}N_x \quad (1)$$

$$(3-y)/2\ Eu_2O_3 + y\ EuN + Ta_3N_5 \rightarrow 3\ EuTaO_{3-x}N_x \quad (2)$$

The reaction used, the proportions of the reactants, the selected gas, and the maximum synthesis temperature determined the average nitrogen content of the sample per Eu or Ta mol, which was tuned from $x = 0.63$ to 1.78, and the phase composition. We have recently reported a similar synthetic approach for the preparation of $LaTaON_2$ and slightly nitrogen-deficient $LaTaO_{1.12}N_{1.88}$ that we investigated for their dielectric properties. [28] Both compounds were prepared either from LaN and TaON or from La_2O_3, LaN, and Ta_3N_5 at 1500 °C. In the $EuTaO_{3-x}N_x$ samples, the syntheses performed at 1500 °C led to partial decomposition into TaN and Eu_3TaO_6 phases; hence, a lower temperature of 1200 °C was selected.

Two different perovskite phases were isolated, with stoichiometries $EuTaO_{2.37}N_{0.63}$ (phase I) and $Eu_3Ta_3O_{3.66}N_{5.34}$ (phase II) that showed black and brown colors, respectively. The Eu/Ta ratios using EDX analysis were 0.93(6) for phase I and 0.94(10) for phase II, whereas the

errors in the nitrogen contents obtained by combustion analysis were ±0.03 in both cases. The oxygen stoichiometry was calculated by difference, assuming that the total anion content was, respectively, three and six atoms per formula for phases I and II. $EuTaO_{2.37}N_{0.63}$ was prepared using reaction 1 in N_2/H_2 (95%/5% v/v) gas, which favored the reduction of the cations. The observed nitrogen content in this sample involved a decrease in the N/O ratio with respect to the initial composition (from 0.4 to 0.27). Considering the charge compensation, this stoichiometry is consistent with the presence of reduced Ta and Eu cations with the formal plausible composition $Eu^{2+}(Ta_{0.37}{}^{4+}Ta_{0.63}{}^{5+})O_{2.37}N_{0.63}$. The existence of 100% of europium in the divalent state agrees with the observed effective magnetic moment of this compound (see below), whereas the +4 oxidation state of tantalum has been suggested in other perovskite oxynitrides coexisting with the more stable Ta^{5+} cation.[28–30] The electron diffraction patterns of $EuTaO_{2.37}N_{0.63}$ indicated a cubic perovskite cell of $a \simeq 4.0$ Å with the space group of aristotype *Pm*-3*m* (Figure 1). This result differs from our previously reported electron diffraction study of $EuTaO_2N$ prepared by ammonolysis, which showed additional reflections indicative of a tilted *I2*/*m* superstructure with a, $b=\sqrt{2}\ a_0$ and $c = 2\ a_0$.[2,20] The perovskite $Eu_3Ta_3O_{3.66}N_{5.34}$ (phase II) was prepared with reaction 2 at the same temperature than $EuTaO_{2.37}N_{0.63}$, under N_2 with $y = 1.8$ (initial ratio N/O of 3.78). The electron diffraction patterns of this phase showed a $3 \times a_0$ superstructure along one of the axes of the perovskite subcell (Figure 2) The reconstruction of the reciprocal lattice leads to a tetragonal cell with parameters $a \simeq 4.04$, $c \simeq 12.08$ Å and reflection

conditions compatible with the space group *P4*/*mmm*. The study by electron diffraction of samples prepared using reaction 2 but starting with N/O ratios below 3.78 invariably led to the observation of a coexistence of two phases: the compound II and an additional perovskite phase, with symmetry *I2*/*m* and a, $b=\sqrt{2}a_0$ and $c=2a_0$, which is the same as previously reported for our $EuTaO_2N$ sample prepared by ammonolysis.[20] The biphasic nature of these samples was also clearly observed in the laboratory X-ray diffraction patterns.

Rietveld refinement of synchrotron X-ray diffraction data of $EuTaO_{2.37}N_{0.63}$ (Figure 3) was performed in the space group *Pm*-3*m* with a = 4.02044(1) Å (V = 64.986 $Å^3$), using a common temperature factor for all atoms B = 0.818(2) $Å^2$. The observed bond distances are d(Eu–O,N) = 2.843 Å and d(Ta–O,N) = 2.010 Å. The cell parameter is close to that shown by $EuTaO_2N$ (a = 4.0217(2) Å) prepared by ammonolysis,[20] indicating that the decrease in a caused by the lower nitrogen content ($r(N^{3-})$ = 1.46 Å vs $r(O^{2-})$=1.38 Å both for CN = IV) is compensated by the increase induced by the presence of Ta^{4+} ($r(Ta^{5+})$= 0.64 Å, $r(Ta^{4+})$= 0.68 Å, both for CN = VI).[31]

The synchrotron X-ray powder diffraction of $Eu_3Ta_3O_{3.66}N_{5.34}$ (Figure 4) did not show clearly visible superstructure peaks of the triple cell, but a tetragonal splitting is observed for several reflections even at low angles, as well as significant broadening in all peaks with respect to the cubic compound $EuTaO_{2.37}N_{0.63}$ (see Figure 5). A Rietveld refinement in a tetragonal subcell with parameters a = 3.98994(2), c = 3.9968(5) Å and

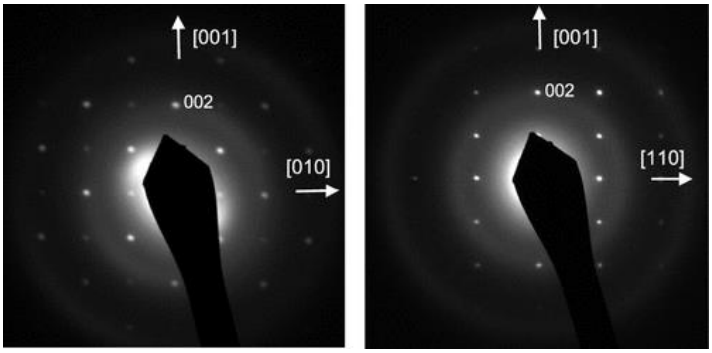

Figure 1. Electron diffraction patterns along the [100] and [1-10] axes of $EuTaO_{2.37}N_{0.63}$.

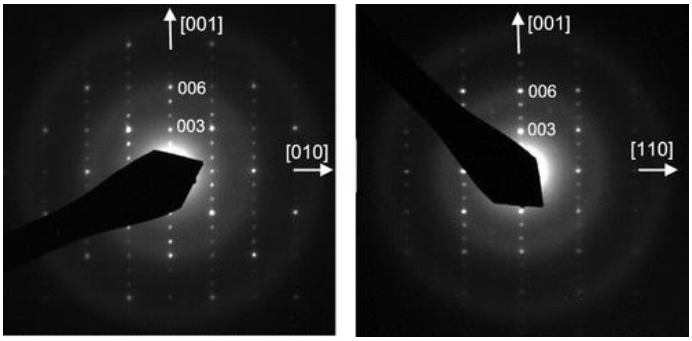

Figure 2. Electron diffraction patterns along the [100] and [1-10] axes of $Eu_3Ta_3O_{3.66}N_{5.34}$.

space group *P4*/*mmm* was performed with one position for Eu and Ta at sites *1d* and *1a* respectively, and two anion positions at 0, 1/2, 0 *(2f* site) and 0, 0, 1/2 (*1b* site). This led to poor agreement factors, with R_{Bragg} = 8.45%, R_{wp} = 7.97%, and χ^2 = 4.90. In contrast, the refinement performed using a triple perovskite structure model with parameters a = 3.99610(2), c = 11.96238(9) Å in the space group *P4*/*mmm* and two

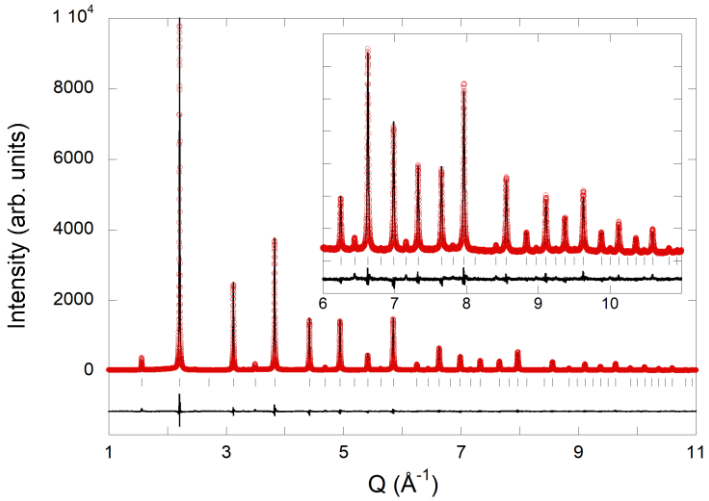

Figure 3. Rietveld fit to synchrotron X-ray powder diffraction pattern of $EuTaO_{2.37}N_{0.63}$ performed in space group *Pm*-3*m* with a = 4.02044(1) Å. The inset shows the high Q region enlarged (where $Q = (4\pi \sin\theta)/\lambda$). Agreement factors: R_{Bragg} = 3.73%, R_p = 4.76%, R_{wp} = 6.13%, χ^2 = 4.03.

crystallographically independent sites for both Eu and Ta atoms (Figures 4 and 6 and Table 1) showed significantly improved agreement factors, with R_{Bragg} = 5.64%, R_{wp} = 7.19%, and χ^2 = 3.74. For the nitrogen and oxygen atoms, we considered a statistical distribution in the four available sites, because the X-rays do not provide enough contrast between the two anions. In order to investigate the potential anion order, neutron diffraction data were acquired on a 380 mg sample prepared in the same conditions as $Eu_3Ta_3O_{3.66}N_{5.34}$, that showed close nitrogen content (1.91(3) atoms per perovskite unit), similar electron diffraction patterns, and refined parameters from X-ray diffraction a = 3.98919(2), c = 12.00107(11) Å. These data clearly showed

superstructure peaks that were indexed in the triple perovskite unit cell. However, the large absorption cross-section of europium and the small sample mass strongly limited the quality of the data and prevented the extraction of reliable structural data from the Rietveld refinement. A Le Bail fit performed using the Fullprof program without introducing any structural model returned the refined parameters a = 4.0262(2) and c = 12.0959(7) Å (Figure 7) The small deviations between the cell parameters obtained by neutron diffraction and X-ray diffraction for this sample are due to differences in the resolution and quality between the two sets of data, caused by the strong Eu absorption in neutron diffraction.

The structural data in Table 1 show that the observed average bond distance around the europium atom at the *1d* site (d(Eu2–O,N) = 3.090 Å) is significantly larger than for Eu1 at the *2h* site (2.711 Å). Considering charge compensation and the analyzed nitrogen stoichiometry of this sample (1.78 per Eu mol), phase II is formally mixed-valence $Eu_{2.34}^{3+}Eu_{0.66}^{2+}Ta_3O_{3.66}N_{5.34}$. According to the structural data and the differences in the ionic radii between Eu^{2+} and Eu^{3+} ($r\,Eu^{3+}$(CN IX) = 1.120 Å vs $r\,Eu^{2+}$(CN IX) = 1.30 Å),[31] the tripleperovskite structure is plausibly formed from two ordered A sites A1 and A2 with different charge and ratio 2:1, that show preferred occupancy by Eu^{3+} and Eu^{2+} respectively creating distinct anion environments. A recent example of mixed-valence europium tantalum oxynitride is the n = 2 Ruddlesden–Popper compound $Eu^{2+}Eu_2^{3+}Ta_2O_3N_4$ that shows, as $Eu_{2.34}^{3+}Eu_{0.66}^{2+}Ta_3O_{3.66}N_{5.34}$, a larger

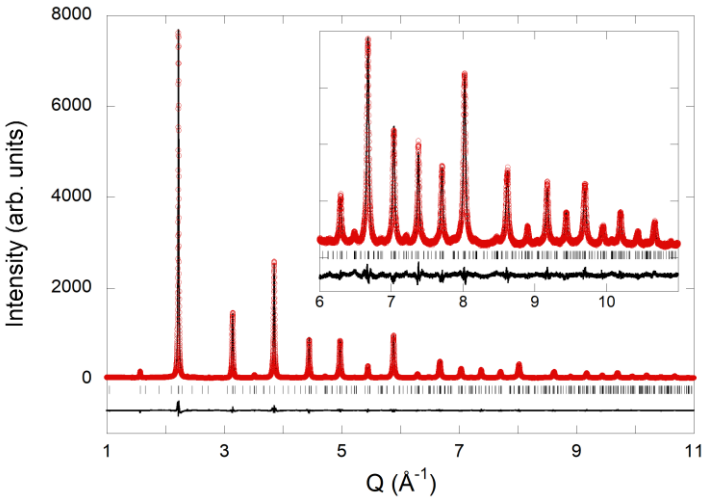

Figure 4. Rietveld fit to synchrotron X-ray powder diffraction pattern of $Eu_3Ta_3O_{3.66}N_{5.34}$ performed in the *P4/mmm* space group with parameters a = 3.99610(2), c = 11.96238(9) Å. The inset shows the high Q region enlarged.

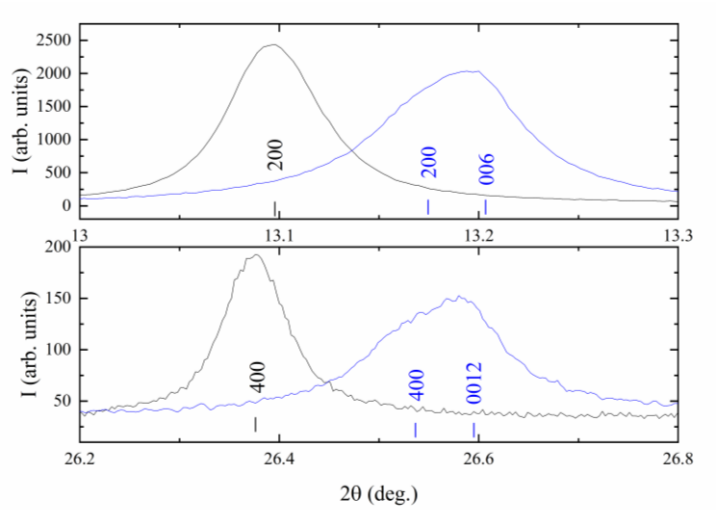

Figure 5. Synchrotron X-ray powder diffraction profiles in two 2θ regions of $EuTaO_{2.37}N_{0.63}$ and $Eu_3Ta_3O_{3.66}N_{5.34}$ are depicted in black and blue colors, respectively.

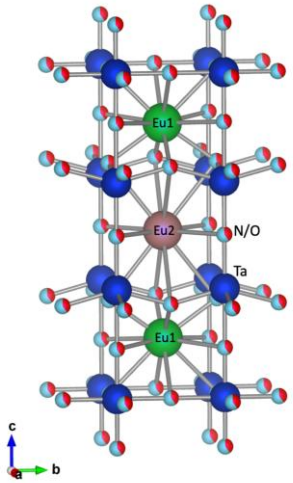

Figure 6. Structural model of the triple perovskite $Eu_3Ta_3O_{3.66}N_{5.34}$.

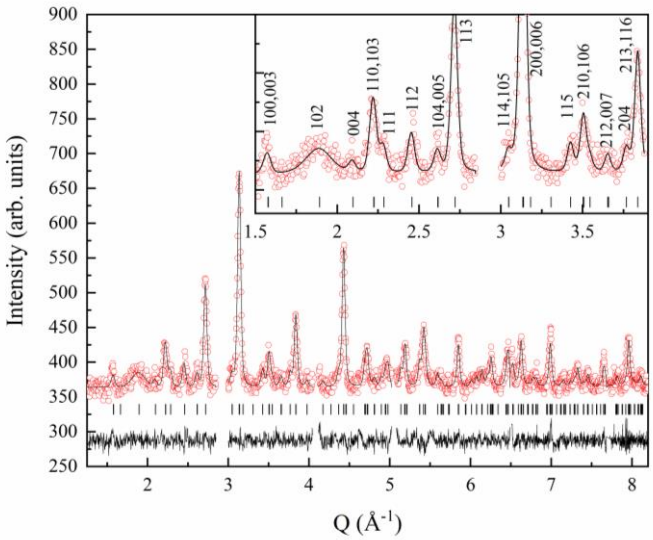

Figure 7. Le Bail fit of neutron diffraction data for phase II (λ = 1.37 Å) indexed (inset) in a *P4/mmm* unit cell with parameters *a* = 4.0265(2) and *c* = 12.0949(12) Å. Excluded regions correspond to peaks from the V sample holder.

proportion of Eu^{3+} related to Eu^{2+}. In $Eu^{2+}Eu_2{}^{3+}Ta_2O_3N_4$, the Eu^{2+} and Eu^{3+} cations order respectively in the rock-salt and in the perovskite-type positions of the Ruddlesden–Popper structure.[13] The unit-cell volumes of the two europium tantalum perovskites $EuTaO_{2.37}N_{0.63}$ and

Table 1. Summary of the *P4*/*mmm* Model for $Eu_3Ta_3O_{3.66}N_{5.34}$ Refined against Room Temperature Synchrotron X-ray Powder Diffraction Data Using λ= 0.45872 Å[a,b,c]

atom	site	*X*	*y*	*Z*	occupancy
Eu1	2h	0.5	0.5	0.1690(2)	1
Eu2	1d	0.5	0.5	0.5	1
Ta1	2g	0	0	0.33464(15)	1
Ta2	1a	0	0	0	1
O1/N1	2g	0	0	0.1522(13)	0.4/0.6
O2/N2	4i	0.5	0	0.2887(6)	0.4/0.6
O3/N3	1b	0	0	0.5	0.4/0.6
O4/N4	2f	0.5	0	0	0.4/0.6
bond	**distance (Å)**	**bond**	**distance (Å)**	**Bond**	**distance (Å)**
Eu1-O1,N1	2.833(1) x4	Eu1-O2,N2	2.458(4) x4	Eu1-(O4,N4)	2.842(2) x4
Eu2-O2,N2	3.222(6) x8	Eu2-O3,N3	2.826 x4		
Ta1-O1,N1	2.182(16)x 2	Ta1-O2,N2	2.072(2)x2	Ta1-O3,N3	1.978(2) x2
Ta2-O1,N1	1.821(16)x 2	Ta2-O4,N4	1.998x4		

[a] Cell parameters: a = 3.99610(2), c = 11.96238(9) Å. V = 191.025(2) Å^3. R_{Bragg} = 5.64%, R_{wp} = 7.19%, χ^2 = 3.74.

[b] Average bond distances (Å): Eu1–O,N 2.711; Eu2–O,N 3.090; Eu–O,N 2.90; Ta1–O,N 2.078; Ta2–O,N 1.939. Bond angles (deg): Ta1-(O2,N2)-Ta1 149.2(3).

[c] Estimated standard deviations in parentheses are shown once for each independent variable. Isotropic thermal parameters were refined to B = 0.657(3) Å^2 for all sites.

$Eu_3Ta_3O_{3.66}N_{5.34}$ are V_I = 64.986 Å^3 and V_{II} = 191.025(2) Å^3 respectively, which after normalizing to the cubic perovskite subcell (64.986 and 63.675 Å^3 respectively) show a decrease with increasing the nitriding degree. This is a consequence of the oxidation of the cations that

overcompensates the increase caused by the larger radius of N^{3-} compared to O^{2-}.

Figure 8a shows a high-resolution *Z*-contrast image of a $Eu_3Ta_3O_{3.66}N_{5.34}$ grain viewed along the [100] zone axis. The Fourier Transform (FT) of the image clearly shows the superstructure peaks of the triple cell (indicated by a red bracket). Figure 8b displays a higher-resolution *Z*-contrast image with a magnified view of the superstructure. Notice that every three planes of Ta one is more intense, which allows us to identify and pinpoint the triple perovskite (see yellow arrows in Figure 8b and the intensity profile along the *c*-axis shown in Figure 8c). This is due to the fact that this compound contains two types of Ta–O/N planes (see Figure 6), one with the anions perfectly aligned with Ta cations (Ta2 positions) and another with the anions slightly above or below the Ta plane (Ta1 sites), ensuing slightly dimmer Ta atomic columns compared with the former ones.

Magnetic Properties

In Figure 9a–d, we summarize the magnetic properties of $EuTaO_{2.37}N_{0.63}$ (phase I) and $Eu_3Ta_3O_{3.66}N_{5.34}$ (phase II). As previously stated, according to the stoichiometric ratios, the charge balance is expected to be (I) $Eu^{2+}Ta_{0.63}{}^{5+}Ta_{0.37}{}^{4+}O_{2.37}N_{0.63}$ and (II) $Eu_{2.34}{}^{3+}Eu_{0.66}{}^{2+}Ta_3{}^{5+}O_{3.66}N_{5.34}$.

The temperature-dependent magnetic susceptibility $\chi(T)$ of phase I is expected to display Curie–Weiss (CW) behavior governed by the presence of Eu^{2+} ($4f^7$ (^8S)) ions having localized $S = 7/2$ spin. The

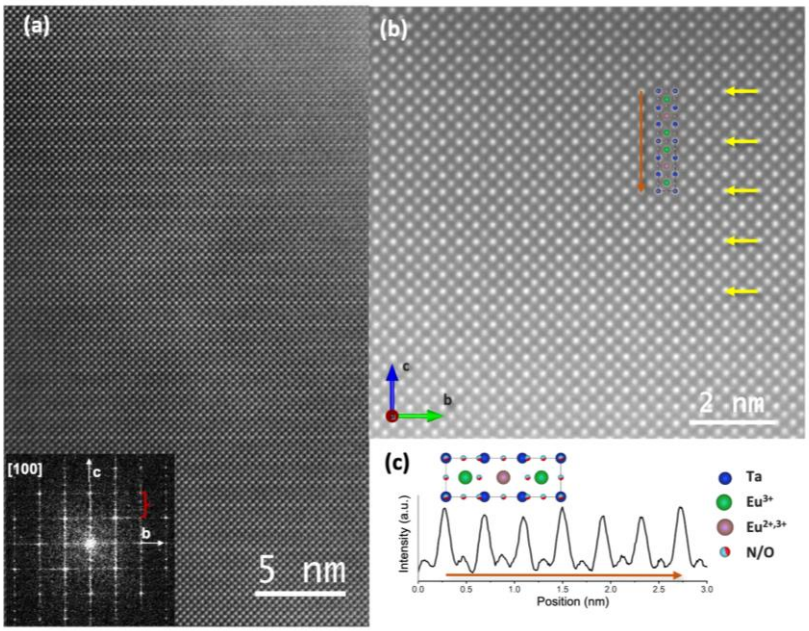

Figure 8. (a) High-resolution *Z*-contrast image of the $Eu_3Ta_3O_{3.66}N_{5.34}$ triple perovskite compound viewed along the [100] zone axis. The inset shows the Fourier Transform of the *Z*-contrast image, in which the extra Bragg stemming from the superstructure is indicated with a red bracket. (b) Atomic-resolution *Z*-contrast image of $Eu_3Ta_3O_{3.66}N_{5.34}$ phase viewed along the [100] zone axis. Yellow arrows point to the more intense Ta–O/N planes. The inset shows a sketch of the $Eu_3Ta_3O_{3.66}N_{5.34}$ triple perovskite structure along the [100] zone axis. (c) Two unit-cell-averaged intensity profiles along the direction of the orange arrow are shown in (b). Ta, Eu, O, and N atoms are represented with blue, green/pink, red, and blue circles, respectively.

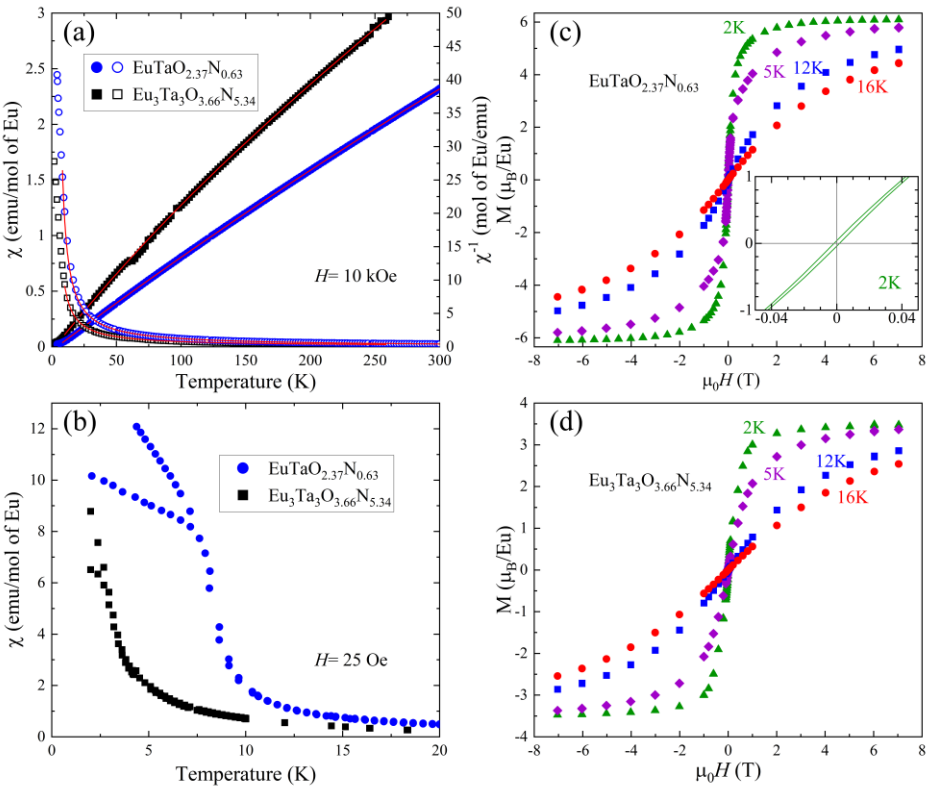

Figure 9. (a) Temperature dependence of the magnetic susceptibility recorded at 10 kOe (left axis) and the inverse susceptibility (right axis) of $EuTaO_{2.37}N_{0.63}$ and $Eu_3Ta_3O_{3.66}N_{5.34}$ together with the fitted values according to eqs 3 and 4, respectively. (b) Temperature dependence of the magnetic susceptibility recorded at a low magnetic field (25 Oe) after zero-field and field-cooling (ZFC-FC) for the same compounds. The corresponding magnetization loops collected between 2 and 16 K are shown in (c,d). Inset in (c) is a zoom of the magnetization loop at 2 K in the low field (<400 Oe) region.

presence of $5d^1$ electrons (Ta^{4+} ions) in a partially occupied broadband is expected to produce a marginal temperature-independent Pauli

paramagnetism that will add to any diamagnetic contribution. Accordingly, $\chi(T)$ is given by

$$\text{Phase I:} \qquad \chi(T) = \frac{C(Eu^{2+})}{(T-\theta_{CW})} + \chi_0 \qquad (3)$$

magnetic interactions between the spins, eventually ordered at low temperature. χ_0 contains temperature-independent paramagnetic and diamagnetic susceptibilities. If the $5d^1$ electrons are spin-polarized by the where $C(Eu^{2+})$ is the corresponding Curie constant and θ_{CW} is the extrapolated Curie temperature that give a measure of the strength of the magnetic moments of Eu^{2+} ions, a departure from the $\chi(T)$ dependence described by eq 3 is expected. This has been observed for instance in Sr_2FeMoO_6, [32] where localized moments of 3d-$Fe^{2+/3+}$ ions induce a spin polarization in the conduction band (4d-Mo^{4+}).

For $Eu_3Ta_3O_{3.66}N_{5.34}$ (phase II), the presence of localized moments at Eu^{2+} ions should produce a CW contribution to $\chi(T)$ as described above, of relative weight "$n_{Eu}{}^{2+}$" combined with the temperature-dependent van Vleck contribution of the magnetic moment of Eu^{3+}.[33, 34] Notice that although Eu^{3+} in its ground state is nonmagnetic ($^7F_0$), thermal excitation to higher lying states (for instance the first one ($^7F_1$) is only at about 46 meV [33] and shall produce a temperature-dependent magnetic susceptibility that will add to the Eu^{2+} contribution, of weight $(1 - n_{Eu}{}^{2+})$, and to any diamagnetic contribution). Accordingly, the magnetic susceptibility per Eu ion can be expressed as

$$\text{Phase II: } \chi(T) = n_{Eu^{2+}} \frac{C(Eu^{2+})}{(T-\theta_{CW})} + (1 - n_{Eu^{2+}})\chi_{Eu^{3+}}(T) + \chi_0 \qquad (4)$$

The magnetic susceptibility recorded at 10 kOe of these compounds displays roughly high-temperature CW behavior (Figure 9a, right axis), where some curvature can be readily appreciated more apparently for phase II than for phase I, as expected from eqs 3 and 4.

Equation 3 and 4 have been used to fit the data for $EuTaO_{2.37}N_{0.63}$ and $Eu_3Ta_3O_{3.66}N_{5.34}$, respectively. The van Vleck contribution to the susceptibility of Eu^{3+} was computed using an excitation energy of 46 meV as given in ref 33. Continuous lines through the data in Figure 9a are the results of fitting to the experimental $\chi(T)$ curves and the corresponding fitted parameters are listed in Table 2.

Table 2. Parameters obtained from fittings to magnetic susceptibility data of $EuTaO_{2.37}N_{0.63}$ using eq. [3], and for $Eu_3Ta_3O_{3.66}N_{5.34}$ using eq. [4] by fixing $\mu_{\text{eff}}^{Eu^{2+}} = 2\sqrt{\frac{7}{2}\frac{9}{2}}\mu_B = 7.94\ \mu_B$ and $\frac{\lambda_{Eu^{3+}}}{k_B} = 531.5\ K$.

	$n_{Eu^{2+}}$	μ_{eff} (μ_B)	θ_{CW} (K)	χ_0 (emu/mol)
$EuTaO_{2.37}N_{0.63}$	1	7.44	4.7	$2.5\cdot10^{-3}$
$Eu_3Ta_3O_{3.66}N_{5.34}$	0.49	7.94 (fixed)	2.4	$1.7\cdot10^{-3}$

Data in Table 2 reflect the dominating presence of Eu^{2+} ions in $EuTaO_{2.37}N_{0.63}$. The extracted effective moment ($\mu_{\text{eff}} \approx 7.44\ \mu_B$/f.u.) compares well with the expected one (7.94 μ_B/f.u.) for Eu^{2+} ($S = 7/2$) ions. The extracted θ_{CW} (≈4.7 K) implies that ferromagnetic order should be expected at around this temperature. Indeed, the magnetization data recorded under 25 Oe after zero-field and field-cooling processes (ZFC and FC), shown in Figure 9b, clearly display a hysteretic behavior,

developing around 7.5 K. The corresponding field-dependent magnetization loops measured at various temperatures are shown in Figure 9c. The shape of the $M(H)$ curves is consistent with a ferromagnetic ordering, with a saturation magnetization of about 6 μ_B, closely approaching the nominal 7 μ_B contribution from Eu^{2+} expected for $Eu^{2+}Ta_{0.63}{}^{5+}Ta_{0.37}{}^{4+}O_{2.37}N_{0.63}$, and coinciding with the effective moment extracted from susceptibility curves in Figure 9a. Detailed inspection of the low field range in the $M(H)$ data taken at 2 K (Figure 9c (inset)) shows the presence of a minor hysteresis, again consistent with the ferromagnetic character of the sample.

The magnetic data of the nitrogen-richer $Eu_3Ta_3O_{3.66}N_{5.34}$ sample reveals that the effective magnetic moment per Eu ion is largely suppressed and the Curie–Weiss temperature drops by about 50% down to ≈2.4 K. These observations are consistent with the larger fraction of the nonmagnetic Eu^{3+} ions as inferred from $n_{Eu}{}^{3+} \approx 0.51$ (Table 2). The corresponding ZFC-FC data (Figure 9b) confirm that ferromagnetic order develops only at lower temperatures (≈3 K). The $M(H)$ curves (Figure 9d) consistently reflect a dramatic reduction of the saturation magnetization (≈3.5 μ_B). The relative fraction of Eu^{2+} ions in the phase II sample deduced from susceptibility data in Figure 9a ($n_{Eu}{}^{2+} \approx 0.49$) is larger than expected from chemical analysis ($n_{Eu}{}^{2+} \approx 0.22$). This difference could originate from the possible existence of anion vacancies, which have not been considered and would increase the proportion of Eu^{2+}, as well as from the extreme simplification of eq 4. For instance, a concentration of oxygen vacancies of 4.7% (0.42 atoms) would lead to $n_{Eu}{}^{2+} = 0.5$, involving an

increase of the fraction of this cation in both A1 and A2 sites of the triple perovskite structure.

All in all, the magnetization data in Figure 9 allow us to conclude that by increasing the N/O ratio in europium tantalum perovskite oxynitrides, the magnetization reduces and the ferromagnetic ordering temperature lowers by the increasing contribution of the nonmagnetic Eu^{3+} in the structure, that dilutes magnetic interaction among Eu^{2+} ions.

3.2.4 Conclusions

A new high-temperature solid-state synthesis approach under N_2 or N_2/H_2 gas at 1200 °C is used to obtain europium perovskite tantalum oxynitrides with a large range of nitrogen contents, starting with mixtures of Eu_2O_3 and TaON or Eu_2O_3, EuN, and Ta_3N_5. $EuTaO_{2.37}N_{0.63}$ prepared from Eu_2O_3 and TaON under N_2/H_2 shows a simple cubic *Pm-3m* perovskite structure whereas the new, highly nitrided compound $Eu_3Ta_3O_{3.66}N_{5.34}$ is prepared from Eu_2O_3, EuN, and Ta_3N_5. $Eu_3Ta_3O_{3.66}N_{5.34}$ with formal stoichiometry $Eu_{2.34}^{3+}Eu_{0.66}^{2+}Ta_3O_{3.66}N_{5.34}$ is a mixed-valence Eu^{2+}/Eu^{3+} compound with long-range order of europium ions in two A sites with different average charge and ratio 2:1, occupied preferentially by Eu^{3+} and Eu^{2+} respectively, that generate well-differentiated coordination environments. This order leads to a triple perovskite structure crystallizing in the *P4*/*mmm* space group with parameters $a = a_0$, $c = 3a_0$, where a_0 is the parameter of the cubic perovskite subcell. The new perovskite is ferromagnetic with $T_c \approx 3$ K and saturation magnetization of

≈3 μ_B, which are lower than for $EuTaO_{2.37}N_{0.63}$ ($T_c \approx 8$ K, $M_s \approx 6$ μ_B) because of the presence of Eu^{3+}, which has a nonmagnetic ground state and dilutes the magnetic interactions between the Eu^{2+} cations. These findings increase the diversity of crystal structures in the field of perovskite oxynitrides and demonstrate that the synthesis from mixtures of binary nitrides and oxides is very effective in tuning their nitriding degree when cations in different oxidation states can be present by controlling the N/O ratio in the reactants. The same synthetic approach could be extended to other perovskite oxynitrides, potentially leading to new structures and physical properties by expanding the accessed anion compositions of the compounds prepared by ammonolysis.

Author Information

Corresponding Authors

Josep Fontcuberta - *Institut de Ciència de Materials de Barcelona (ICMAB-CSIC), Campus UAB, 08193 Bellaterra, Spain; Spain*;

Email: fontcuberta@icmab.cat

Amparo Fuertes - *Institut de Ciència de Materials de Barcelona (ICMAB-CSIC), Campus UAB, 08193 Bellaterra, Spain; https://orcid.org/0000-0001-5338-9724*

Email: amparo.fuertes@icmab.es

Authors

Jhonatan R. Guarín - *Institut de Ciència de Materials de Barcelona (ICMAB-CSIC), Campus UAB, 08193 Bellaterra, Spain*

Carlos Frontera - *Institut de Ciència de Materials de Barcelona (ICMAB-CSIC), Campus UAB, 08193 Bellaterra, Spain*; https://orcid.org/0000-0002-0091-4756

Judith Oró-Solé - *Institut de Ciència de Materials de Barcelona (ICMAB-CSIC), Campus UAB, 08193 Bellaterra, Spain*

Jaume Gàzquez - *Institut de Ciència de Materials de Barcelona (ICMAB-CSIC), Campus UAB, 08193 Bellaterra, Spain*; https://orcid.org/0000-0002-2561-328X

Clemens Ritter - *Institut Laue-Langevin, 71 Av. de Martyrs, Grenoble 38000, France*

Author Contributions

The manuscript was written with the contributions of all authors. All authors have given approval to the final version of the manuscript.

Funding

Ministerio de Ciencia e Innovación, Agencia Estatal de Investigación, Spain (PID2020-113805GB-I00, PID2020-118479RB-I00 (AEI/FEDER, EU), CEX2019-000917-S and PRE2018-085204) and Generalitat de Catalunya (2021SGR00439).

Notes

The authors declare no competing financial interest.

Acknowledgment

This work was supported by grants PID2020-113805GB-I00, PID2020-118479RB-I00, and CEX2019-000917-S funded by MCIN/AEI/10.13039/501100011033 (Ministerio de Ciencia e Innovación/Agencia Estatal de Investigación) and by "ERDF A way of making Europe" and European Union, and grant 2021SGR00439 funded by the Generalitat de Catalunya. It has been developed under the PhD program in Materials Science at the UAB. We thank ALBA synchrotron and Institut Laue-Langevin (experiment numbers AV-2021024982 and 5-23-748, respectively) for the provision of beam time; we also thank Dr. François Fauth (ALBA) for assistance during data collection and Dr. Bernat Bozzo (ICMAB-CSIC) for performing the magnetic measurements. JRG acknowledges AEAT predoctoral fellowship PRE2018-085204.

3.2.5 References

This article references 34 other publications.

(1) Fuertes, A. Nitride tuning of transition metal perovskites. *APL Materials* **2020**, *8* (2), 020903.
(2) Yang, M.; Oró-Solé, J.; Rodgers, J. A.; Jorge, A. B.; Fuertes, A.; Attfield, J. P. Anion order in perovskite oxynitrides. *Nature Chemistry* **2011**, *3* (1), 47-52.
(3) Porter, S. H.; Huang, Z.; Woodward, P. M. Study of anion order/disorder in $RTaN_2O$ (R= La, Ce, Pr) perovskite nitride oxides. *Crystal Growth & Design* **2014**, *14* (1), 117-125.
(4) Attfield, J. P. Principles and applications of anion order in solid oxynitrides. *Crystal Growth & Design* **2013**, *13* (10), 4623-4629.

(5) Ceravola, R.; Oró-Solé, J.; Black, A. P.; Ritter, C.; Orench, I. P.; Mata, I.; Molins, E.; Frontera, C.; Fuertes, A. Topochemical synthesis of cation ordered double perovskite oxynitrides. *Dalton Transactions* **2017**, *46* (16), 5128-5132.
(6) Ceravola, R.; Frontera, C.; Oró-Solé, J.; Black, A. P.; Ritter, C.; Mata, I.; Molins, E.; Fontcuberta, J.; Fuertes, A. Topochemical nitridation of Sr_2FeMoO_6. *Chemical Communications* **2019**, *55* (21), 3105-3108.
(7) Ishida, K.; Tassel, C.; Watabe, D.; Takatsu, H.; Brown, C. M.; Nilsen, G. J.; Kageyama, H. Spin frustration in double perovskite oxides and oxynitrides: enhanced frustration in La_2MnTaO_5N with a large octahedral rotation. *Inorganic Chemistry* **2021**, *60* (11), 8252-8258.
(8) Ruddlesden, S.; Popper, P. New compounds of the K_2NiF_4 type. *Acta Crystallographica* **1957**, *10* (8), 538-539.
(9) Ruddlesden, S.; Popper, P. The compound $Sr_3Ti_2O_7$ and its structure. *Acta Crystallographica* **1958**, *11* (1), 54-55.
(10) Tobías, G.; Oró-Solé, J.; Beltrán-Porter, D.; Fuertes, A. New family of Ruddlesden− Popper strontium niobium oxynitrides:$(SrO)(SrNbO_{2-x}N)_n$ (n= 1, 2). *Inorganic Chemistry* **2001**, *40* (27), 6867-6869.
(11) Pors, F.; Marchand, R.; Laurent, Y. Nouveaux oxynitrures A_2TaO_3N (A= alcalinoterreux) de type structural K_2NiF_4. In *Annales de Chimie (Paris. 1914)*, 1991; Vol. 16, pp 547-551.
(12) Clarke, S. J.; Hardstone, K. A.; Michie, C. W.; Rosseinsky, M. J. High-temperature synthesis and structures of perovskite and n= 1 Ruddlesden− Popper tantalum oxynitrides. *Chemistry of Materials* **2002**, *14* (6), 2664-2669.
(13) Cordes, N.; Nentwig, M.; Eisenburger, L.; Oeckler, O.; Schnick, W. Ammonothermal synthesis of the mixed-valence nitrogen-rich europium tantalum Ruddlesden-Popper phase $Eu^{II}Eu^{III}{}_2Ta_2N_4O_3$. *European Journal of Inorganic Chemistry* **2019**, *2019* (17), 2304-2311.
(14) Marchand, R. Oxynitrides with K_2NiF_4 structure-compounds Ln_2AlO_3N (Ln= La, Nd, Sm). *Comptes Rendus Hebdomadaires des Seances de l'Academie des Sciences Serie C* **1976**, *282* (7), 329-331.
(15) Dion, M.; Ganne, M.; Tournoux, M. Nouvelles familles de phases $M^IM^{II}{}_2Nb_3O_{10}$ a feuillets "perovskites". *Materials Research Bulletin* **1981**, *16* (11), 1429-1435.
(16) Jacobson, A.; Johnson, J. W.; Lewandowski, J. Interlayer chemistry between thick transition-metal oxide layers: synthesis and intercalation

reactions of $K[Ca_2Na_{n-3}Nb_nO_{3n+1}]$ *Inorganic Chemistry* **1985**, *24* (23), 3727-3729.
(17) Schottenfeld, J. A.; Benesi, A. J.; Stephens, P. W.; Chen, G.; Eklund, P. C.; Mallouk, T. E. Structural analysis and characterization of layer perovskite oxynitrides made from Dion–Jacobson oxide precursors. *Journal of Solid State Chemistry* **2005**, *178* (7), 2313-2321.
(18) Oshima, T.; Ichibha, T.; Oqmhula, K.; Hibino, K.; Mogi, H.; Yamashita, S.; Fujii, K.; Miseki, Y.; Hongo, K.; Lu, D. Two-dimensional perovskite oxynitride $K_2LaTa_2O_6N$ with an H^+/K^+ exchangeability in aqueous solution forming a stable photocatalyst for visible-light H_2 evolution. *Angewandte Chemie International Edition* **2020**, *59* (24), 9736-9743.
(19) Oró-Solé, J.; Fina, I.; Frontera, C.; Gàzquez, J.; Ritter, C.; Cunquero, M.; Loza-Alvarez, P.; Conejeros, S.; Alemany, P.; Canadell, E. Engineering polar oxynitrides: Hexagonal perovskite $BaWON_2$. *Angewandte Chemie International Edition* **2020**, *59* (42), 18395-18399.
(20) Jorge, A. B.; Oro-Sole, J.; Bea, A. M.; Mufti, N.; Palstra, T. T.; Rodgers, J. A.; Attfield, J. P.; Fuertes, A. Large coupled magnetoresponses in $EuNbO_2N$. *Journal of the American Chemical Society* **2008**, *130* (38), 12572-12573.
(21) Yang, M.; Oro-Sole, J.; Kusmartseva, A.; Fuertes, A.; Attfield, J. P. Electronic tuning of two metals and colossal magnetoresistances in $EuWO_{1+x}N_{2-x}$ perovskites. *Journal of the American Chemical Society* **2010**, *132* (13), 4822-4829.
(22) Mikita, R.; Aharen, T.; Yamamoto, T.; Takeiri, F.; Ya, T.; Yoshimune, W.; Fujita, K.; Yoshida, S.; Tanaka, K.; Batuk, D. Topochemical nitridation with anion vacancy-assisted N^{3-}/O^{2-}exchange. *Journal of the American Chemical Society* **2016**, *138* (9), 3211-3217.
(23) Marchand, R.; Pors, F.; Laurent, Y. Nouvelles perovskites oxynitrures de stoechiometrie ABO_2N (A= lanthanide, B= Ti) et $ABON_2$ (A= lanthanide, B= Ta ou Nb). In *Annales de Chimie (Paris. 1914)*, 1991; Vol. 16, pp 553-560.
(24) Oró-Solé, J.; Frontera, C.; Black, A. P.; Castets, A.; Velasquez-Mendez, K. L.; Fontcuberta, J.; Fuertes, A. Structural, magnetic and electronic properties of $EuTi_{0.5}W_{0.5}O_{3-x}N_x$ perovskite oxynitrides. *Journal of Solid State Chemistry* **2020**, *286*, 121274.
(25) Brauer, G.; Weidlein, J.; Strähle, J. Über das tantalnitrid Ta_3N_5 und das tantaloxidnitrid TaON. *Zeitschrift für Anorganische und Allgemeine Chemie* **1966**, *348* (5-6), 298-308.

(26) Fauth, F.; Peral, I.; Popescu, C.; Knapp, M. The new material science powder diffraction beamline at ALBA synchrotron. *Powder Diffraction* **2013**, *28* (S2), S360-S370.
(27) Rodríguez-Carvajal, J. Recent advances in magnetic structure determination by neutron powder diffraction. *Physica B: Condensed Matter* **1993**, *192* (1-2), 55-69.
(28) Castets, A.; Fina, I.; Guarín, J. R.; Oro-Sole, J.; Frontera, C.; Ritter, C.; Fontcuberta, J.; Fuertes, A. High-temperature synthesis and dielectric properties of $LaTaON_2$. *Inorganic Chemistry* **2021**, *60* (21), 16484-16491.
(29) Sakata, T.; Yoshiyuki, R.; Okada, R.; Urushidani, S.; Tarutani, N.; Katagiri, K.; Inumaru, K.; Koyama, K.; Masubuchi, Y. Environmentally benign synthesis and color tuning of strontium–tantalum perovskite oxynitride and its solid solutions. *Inorganic Chemistry* **2021**, *60* (7), 4852-4859.
(30) Bubeck, C.; Widenmeyer, M.; Richter, G.; Coduri, M.; Goering, E.; Yoon, S.; Weidenkaff, A. Tailoring of an unusual oxidation state in a lanthanum tantalum (IV) oxynitride via precursor microstructure design. *Communications Chemistry* **2019**, *2* (1), 134.
(31) Shannon, R. Revised effective ionic radii and systematic studies of interatomic distances in halides and chalcogenides. *Acta Crystallogr., Sect. A: Cryst. Phys., Diffr., Theor. Gen. Cryst.* **1976**, *32*, 751-767.
(32) Serrate, D.; De Teresa, J.; Algarabel, P.; Marquina, C.; Blasco, J.; Ibarra, M.; Galibert, J. Magnetoelastic coupling in $Sr_2(Fe_{1-x}Cr_x)ReO_6$ double perovskites. *Journal of Physics: Condensed Matter* **2007**, *19* (43), 436226.
(33) Andruh, M.; Bakalbassis, E.; Kahn, O.; Trombe, J. C.; Porcher, P. Structure, spectroscopic and magnetic properties of rare earth metal (III) derivatives with the 2-formyl-4-methyl-6-(N-(2-pyridylethyl) formimidoyl) phenol ligand. *Inorganic Chemistry* **1993**, *32* (9), 1616-1622.
(34) Zong, Y.; Fujita, K.; Akamatsu, H.; Murai, S.; Tanaka, K. Antiferromagnetism of perovskite $EuZrO_3$. *Journal of Solid State Chemistry* **2010**, *183* (1), 168-172.

Chapter IV

Anionic and Magnetic Ordering in Rare Earth Tantalum Oxynitrides with an n = 1 Ruddlesden–Popper Structure

Published in: *Chemistry of materials*. **2024**, 36, 5160-5171.

Authors: Jhonatan R. Guarín,[§] Carlos Frontera,[§] Judith Oró-Solé,[§] Bastian Colombel,[§] Clemens Ritter,[‡] François Fauth,[+] Josep Fontcuberta[§,*] and Amparo Fuertes[§,*]

§ Institut de Ciència de Materials de Barcelona (ICMAB-CSIC), Campus UAB, 08193 Bellaterra(Spain).

‡ Institut Laue-Langevin, 71 Av. de Martyrs, Grenoble 38000(France)

[+] CELLS-ALBA Synchrotron, Barcelona 08290, Spain

https://doi.org/10.1021/acs.chemmater.4c00533

Keywords: Oxynitrides, Ruddlesden Popper phases, High temperature synthesis

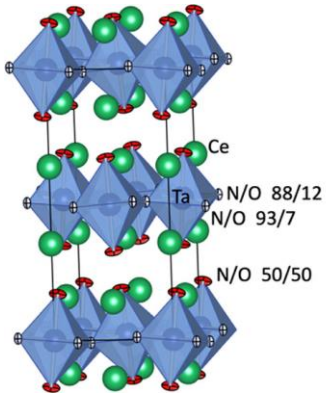
Ce
Ta
N/O 88/12
N/O 93/7
N/O 50/50

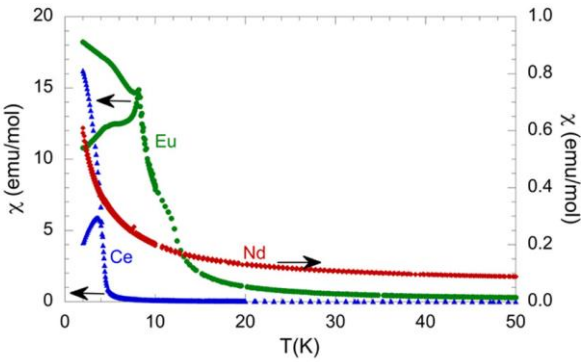
χ (emu/mol)
χ (emu/mol)
T(K)
Eu
Nd
Ce
0
5
10
15
20
0.0
0.2
0.4
0.6
0.8
1.0
0
10
20
30
40
50

Abstract: The new compounds $R_2TaO_{4-x}N_x$ with R = La, Ce, Nd, and Eu and $1.20 \leq x \leq 2.81$ have been obtained by a solid-state reaction between metal nitrides and oxides or oxynitrides under N_2 gas at temperatures between 1200 and 1700 °C. They are the first examples of rare earth transition metal oxynitrides with an $n = 1$ Ruddlesden–Popper structure and show different anion stoichiometries, crystal structures, and magnetic properties. Synchrotron X-ray powder diffraction and electron diffraction indicate that the lanthanum, cerium, and neodymium compounds crystallize in the orthorhombic space group *Pccn*, with cell parameters $a = 5.72949(2)$, $b = 5.73055(5)$, and $c = 12.77917(6)$ Å for $La_2TaO_{1.31}N_{2.69}$, $a = 5.70500(5)$, $b = 5.71182(4)$, and $c = 12.61280(7)$ Å for $Ce_2TaO_{1.19}N_{2.81}$, and $a = 5.70466(3)$, $b = 5.70476(5)$, and $c = 12.32365(5)$ Å for $Nd_2TaO_{1.46}N_{2.54}$. In contrast, $Eu_2TaO_{2.80}N_{1.20}$ shows a tetragonal $I4_1/acd$ superstructure doubling the *c* axis, with parameters $a = 5.71867(2)$ and $c = 25.00092(19)$ Å. Refinement of neutron powder diffraction data of $Ce_2TaO_{1.19}N_{2.81}$ indicated the nitrogen order in the two equatorial positions of the tantalum octahedron, with refined N/O occupancies of 0.930(7)/0.070 and 0.876(13)/0.124, and the axial position is occupied by 50% of each anion. This anion ordering agrees with the distribution predicted by Pauling's second crystal rule. Magnetization measurements show that the cerium and europium compounds are ordered magnetically at low temperatures, while the neodymium compound remains paramagnetic down to 2 K, as a consequence of suppression of the effective magnetic moment of the latter when reducing the temperature.

4.1 Introduction

Perovskite oxynitrides have been widely investigated in the last two decades because of their notable applications as electronic and photocatalytic materials. The strategy for finding new properties is based on the lower electronegativity of nitrogen compared to that of oxygen, which induces changes in the electronic structures and increases the covalency of bonds with the metals. Additionally, the larger electrical charge of the anion N^{3-} compared to O^{2-} allows the formation of phases with new combinations of cations that show oxidation states different than in the analogous oxides. The majority of known compounds are pseudocubic simple perovskites derived from the *Pm-3m* aristotype, of the general formula $ABO_{3-x}N_x$ with A = alkaline earth or rare earth metal and B = early transition metal, showing different crystal symmetries induced by octahedral tilting and the anion order.[1] Important examples of materials are nontoxic pigments $La_{1-x}Ca_xTaO_{1+x}N_{2-x}$,[2] $EuNbO_2N$ and $EuWO_{1+x}N_{2-x}$ with colossal magnetoresistance at low temperatures, [3,4] $BaTaO_2N$ and $SrTaO_2N$ with high dielectric constants,[5] and several tantalum perovskites with photocatalytic activity in water splitting.[6,7]

There are few reported perovskite oxynitrides with complex structures. Examples of double and triple perovskites are $Sr_2FeMoO_{4.9}N_{1.1}$,[8] Sr_2FeWO_5N,[9] La_2MnTaO_5N,[10] and $Eu_3Ta_3O_{3.66}N_{5.34}$, [11] all of them showing magnetic ordering at low temperatures. Polar $BaWON_2$ is the only known example of a hexagonal perovskite.[12] Layered, Ruddlesden–Popper[13] perovskite oxynitrides

$(AX)(ABX_3)_n$ (X = O, N) were first reported by R.Marchand and co-workers for the n = 1 members Sr_2TaO_3N, Ba_2TaO_3N,[14] and R_2AlO_3N (R = La, Nd, Sm).[15] We prepared the n = 1 and 2 members of the series $(SrO)(SrNbO_2N)_n$, with the compositions Sr_2NbO_3N and $Sr_3Nb_2O_5N_2$, respectively,[16] and the n = 2 compound $Eu_3Ta_2O_3N_4$ has been recently reported.[17]

Rare earth perovskite oxynitrides are known for the transition metals Cr, Ti, Zr, Hf, V, Nb, Ta, and W, and they have been mostly investigated for their electronic and photocatalytic properties. $RCrO_{3-x}N_x$ (R = La, Pr, and Nd) perovskites show antiferromagnetic coupling of Cr^{3+}/Cr^{4+} spins with Neel temperatures from 285 to 214 K.[18] Vanadium perovskites with R = La and Pr show spin freezing transitions at low temperatures.[19] $EuTaO_2N$, $EuNbO_2N$,[3] and $EuWO_{1+x}N_{2-x}$ [4] are ferromagnetic with T_c values between 5 and 12 K because of Eu^{2+} spin ordering. $LaTiO_2N$ [20] and $RHfO_2N$ [21] (R = La, Nd, Sm) compounds are visible light-active photocatalysts in water oxidation and reduction, whereas $LaTaON_2$, in addition to a photocatalyst for water splitting, [22] is a high-dielectric permittivity material.[23]

In this paper, we report the synthesis, crystal structures, and magnetic properties of the new compounds $R_2TaO_{4-x}N_x$ (R = La, Ce, Nd, and Eu) that are the first examples of transition metal n = 1 Ruddlesden–Popper oxynitrides with a rare earth cation at the A sites. These oxynitrides can be stabilized by using a high-temperature synthesis method under N_2, starting with a mixture of metal nitrides and oxides. The obtained anion stoichiometries indicate reduction of the cations during synthesis and are

determined by the stable oxidation states of tantalum (Ta^{4+}, Ta^{5+}) and the rare earth cations (La^{3+}, Ce^{3+}, Nd^{3+}, and Eu^{2+}/Eu^{3+}) under the preparative conditions. The anion distribution is investigated by neutron diffraction for $Ce_2TaO_{1.19}N_{2.81}$, showing the order of nitrides at the equatorial sites of the octahedra, whereas the axial positions are occupied by 50% of each anion. The cerium and europium compounds develop low-temperature (<10 K) magnetic ordering, while the Nd compound is paramagnetic down to 2 K. The striking differences between the magnetic behaviors of the Ce^{3+}, Nd^{3+}, and Eu^{2+}/Eu^{3+} compounds are rationalized in terms of the distinct role that crystal field effects and exchange interactions play in determining the singlet or triplet ground state of the rare earth cations.

4.2 Experimental Methods

Synthesis and Chemical Characterization

Samples of 100 to 200 mg of $R_2TaO_{4-x}N_x$ (R = La, Ce, Nd, Eu) compounds were prepared by a solid-state reaction under N_2 gas (Air Liquide, 99.9999%) at temperatures between 1200 and 1700 °C, starting from mixtures with different proportions of RN, R_2O_3, Ta_3N_5, and TaON, while keeping the stoichiometric ratio R/Ta of 2:1. $La_2TaO_{1.31}N_{2.69}$ was prepared starting with LaN and Ta_3N_5 (Alfa Aesar 99.9%) in a molar ratio of 6:1 at 1700 °C, $Ce_2TaO_{1.19}N_{2.81}$ was prepared from CeN, Ta_3N_5, and TaON in a molar ratio of 6:0.375:1.875 at 1500 °C, $Nd_2TaO_{1.46}N_{2.54}$ was prepared from Nd_2O_3(Aldrich 99.99%), NdN (Alfa Aesar 99.9%), and Ta_3N_5 at 1500 °C with a ratio of 0.05:1.9:0.33, and

$Eu_2TaO_{2.80}N_{1.20}$ was obtained from Eu_2O_3 (Sigma-Aldrich 99.9%), EuN (Materion, 99.9%), and Ta_3N_5 in a ratio of 0.85:0.30:0.33 at 1200 °C. The proportion of the reactants determining the O/N ratio in the initial mixture and the maximum synthesis temperature were optimized from several syntheses performed for each compound, until the sample was a single phase from laboratory X-ray diffraction. CeN was obtained by treatment under N_2 of Ce chips (Strem 99.9%) at 1000 °C. Ta_3N_5 was obtained from Ta_2O_5 (Sigma-Aldrich 99.99%) by treatment under NH_3 (Carburos Metálicos 99.9%) at 880 °C using a flow rate of 600 cm^3/min and several treatments of 15 h with intermediate regrinding. TaON was prepared by a similar procedure but using a flow rate of 40 cm^3/min and two treatments of 3 h with intermediate regrinding. Nd_2O_3 and Eu_2O_3 were treated at 900 °C under a dynamic vacuum of 1×10^{-3} Torr for dehydration. Handling, mixing, and pelletizing of the reactants were performed inside a glovebox under recirculating Ar. The samples were placed in molybdenum crucibles covered by Zr foil that was also placed in a second molybdenum crucible in order to scavenge oxygen and water from the N_2 gas. The reaction tube was evacuated to 10^{-3} Torr and purged several times with N_2 before starting the thermal cycle. This consisted of a single treatment of heating at 300 °C/h up to the maximum temperature that was kept for 3 h, with further natural cooling to room temperature.

Nitrogen contents were determined by combustion analysis performed in a Thermo Fisher Scientific instrument, heating the samples in oxygen up to 1060 °C and using MgO, WO_3, and Sn as additives and atropine as a reference standard. EDX analyses of cation contents were performed in a

FEI Quanta 200 FEG microscope equipped with an EDAX detector with an energy resolution of 132 eV. The analyses were performed on 10–15 crystallites for each sample.

Structural Characterization

Laboratory powder X-ray diffraction was used for controlling the purity of the samples during the synthesis. Data were acquired on a Panalytical X′Pert Pro MPD diffractometer using Cu Kα radiation (λ = 1.5418 Å) and on a Bruker D8 Advance A25 diffractometer in a Debye–Scherrer configuration with Mo $K\alpha_1$ radiation (λ = 0.7093 Å) using capillary samples (0.3 mm diameter). High-angular resolution synchrotron X-ray powder diffraction data were collected at room temperature from capillary samples in the angular range of $2.0° \leq 2\theta \leq 56.9°$ at the MSPD beamline [24] of the ALBA Synchrotron (Cerdanyola del Vallès, Spain), using 30 keV energy that resulted in exact wavelengths of 0.4137, 0.4139 and 0.4142 Å as determined by refining the SRM640d NIST Si standard. Neutron powder diffraction was used to determine the anion distribution in $Ce_2TaO_{1.19}N_{2.81}$. Data on a 80 mg sample were collected for 19 h at room temperature on the high-intensity D20 diffractometer at the Institut Laue-Langevin (ILL), France, using a vanadium can as a sample holder. The pattern was measured in scanning mode with a short wavelength of 1.37 Å created by using 118° takeoff angle, giving high resolution. Rietveld analysis was carried out using the program Fullprof.[25] Background refinement was performed by linear interpolation, and data were corrected from absorption.

Electron diffraction micrographs were obtained in a JEOL 1210 transmission electron microscope operating at 120 kV using a side entry double tilt ±60°/±30° specimen holder. The samples were prepared by depositing the powder on a copper grid coated with a holey carbon film.

Magnetic Measurements

Magnetic measurements were performed at fields of 25 and 10 kOe between 2 and 300 K using a Quantum Design SQUID magnetometer. Magnetization field loops were measured between −70 and +70 kOe between 2 and 16 K.

4.3 Results and Discussion

Synthesis and Crystal Structures of $R_2TaO_{4-x}N_x$ Compounds

The synthesis of new rare earth tantalum $n = 1$ Ruddlesden–Popper compounds was performed using the reactions at high temperature under N_2

$$(3-y)R_2O_3 + 2yRN + Ta_3N_5 \rightarrow 3\ R_2TaO_{4-x}N_x \text{ for R = La, Nd and Eu (1), and}$$

$$2RN + 1/8Ta_3N_5 + 5/8TaON \rightarrow R_2TaO_{4-x}N_x \text{ for R=Ce} \qquad (2)$$

The best samples of La, Nd, and Eu were obtained for $y = 3$, 2.85, and 0.45, respectively. In the case of cerium, we used TaON as an oxygen source because Ce_2O_3 is not easily available commercially. This synthetic route is similar to that used for the preparation of the rare earth perovskites $LaTaON_2$, [23] $EuTaO_{2.37}N_{0.63}$, and $Eu_3Ta_3O_{3.66}N_{5.34}$ [11] that we

have recently reported and produces samples of high crystallinity with short reaction times. The rare earth perovskite oxynitrides are commonly prepared under NH_3 at temperatures below 1000 °C, starting with oxide precursors such as scheelites because the rare earth binary oxides are poorly reactive in these conditions.[26] R_2O_3 reactants have been used for the synthesis of few compounds under NH_3 but in the presence of fused salts that increase the kinetics of the nitridation [27] or in high-pressure conditions.[28] The combination of rare earth nitrides, RN, with different proportions of oxides and nitrides allows one to change the nitrogen/oxygen ratio in the initial mixture up to avoiding or minimizing the impurity phases. These are frequently formed in the synthesis of nitrides at high temperatures because of the presence of oxygen or water around the sample.

The black-colored $R_2TaO_{4-x}N_x$ samples were prepared at different temperatures optimized in each case, from 1200 °C for R = Eu to 1700 °C for R = La, and showed analyzed nitrogen contents of 2.69(3), 2.81(3), 2.54(3), and 1.20(3) atoms per formula for R = La, Ce, Nd, and Eu, respectively. In all cases, these contents were below the nitrogen stoichiometry in the mixture of reactants (3, 3.25, 3.56, and 1.96 for La, Ce, Nd, and Eu samples, respectively), indicating the incorporation of extra oxygen in the samples during synthesis. Nitrogen loss at high temperatures has been observed in other tantalum perovskites such as $SrTaO_2N$ [29] and $LaTaON_2$ [23] and has been interpreted as a decomposition reaction releasing N_2 with partial reduction of Ta^{5+} to Ta^{4+}, analogous to the oxygen loss of transition metal oxides at high temperatures that produces reduced oxides together with O_2.[30] The corresponding cation

ratios determined by EDX were La/Ta = 1.82(17), Ce/Ta = 1.81(10), Nd/Ta = 1.77(17), and Eu/Ta = 1.89(15), which agree with the nominal compositions within the experimental error. The oxygen stoichiometries were calculated by difference, assuming that the total anion content was four atoms per formula, resulting in $La_2TaO_{1.31}N_{2.69}$, $Ce_2TaO_{1.19}N_{2.81}$, $Nd_2TaO_{1.46}N_{2.54}$, and $Eu_2TaO_{2.80}N_{1.20}$. Considering charge compensation and the trivalent oxidation state for the rare earth cations, the nitrogen deficiency with respect to the ideal R_2TaON_3 composition in the La, Ce, and Nd compounds would result in a proportion of Ta^{4+} of 31, 19, and 46%, respectively. Compared with the other rare earth compounds, the observed N content in $Eu_2TaO_{2.80}N_{1.20}$ indicates that europium is dominantly divalent, which is consistent with the observed structural data and the magnetic properties (see below). In the synchrotron X-ray powder diffraction patterns of lanthanum, neodymium, and europium samples, we detected the perovskite-phase $RTaON_2$ with the respective amounts of 6.6, 5.1, and 1.9% (w/w) as determined from Rietveld refinement.

The electron diffraction patterns of the compounds $La_2TaO_{1.31}N_{2.69}$, $Ce_2TaO_{1.19}N_{2.81}$, and $Nd_2TaO_{1.46}N_{2.54}$ showed additional reflections to those expected for the *I*4/*mmm* space group of the K_2NiF_4 aristotype (see Figures 1, S1, and S2) indicative of a tilted superstructure with parameters $\sqrt{2}a_0 \times \sqrt{2}a_0 \times c_0$ (where a_0 and c_0 are the parameters of the *I*4/*mmm* cell). The reconstruction of the reciprocal lattice led to an orthorhombic cell with parameters $a, b \simeq 5.7$ Å and the respective c axis of 12.89, 12.60, and 12.53 Å for R = La, Ce, and Nd, with the observed

reflection conditions consistent with the space group *Pccn* (No. 56) (*hk*0, *h*+*k* = 2*n*; *h*0*l*, *l* = 2*n*; 0*kl*, *l* = 2*n*; *h*00, *h* = 2*n*; 0*k*0, *k* = 2*n*; *00l*, *l* = 2*n*). This space group corresponds to a tilted $n = 1$ Ruddlesden–Popper structure with out-of-phase rotations around the a and *b* axis, notated as $\phi_1\ \phi_2\ 0$ for the first layer of octahedra and $\phi_2\ \phi_1\ 0$ for the second layer of octahedra at the origin and body center of the *I4*/*mmm* parent cell, and no rotation around the *c* axis.[31,32] In contrast, the compound $Eu_2TaO_{2.80}N_{1.20}$ showed an additional superstructure along the *c* axis doubling c_0, with cell parameters $a = 5.72$ Å and $c = 24.99$ Å(Figure 2). The electron diffraction planes indicated reflection conditions compatible with the space group $I4_1/acd$, which has been reported for K_2NiF_4 compounds including Sr_2IrO_4.[33] Weak additional reflections were also observed that could be indexed in a larger cell, with $a = 8.15$ Å and $c = 24.99$ Å. Rietveld refinement of synchrotron X-ray diffraction data was performed in the *Pccn* space group for the La, Ce, and Nd compounds (Figures 3, 4, and 5 and Tables 1, 2, and S1, respectively) and led the cell parameters $a = 5.72949(2)$, $b = 5.73055(5)$, and $c = 12.77917(6)$ Å for $La_2TaO_{1.31}N_{2.69}$, $a = 5.70500(5)$, $b = 5.71182(4)$, and $c = 12.61280(7)$ Å for $Ce_2TaO_{1.19}N_{2.81}$, and $a = 5.70466(3)$, $b = 5.70475(5)$, and $c = 12.32365(5)$ Å for $Nd_2TaO_{1.46}N_{2.54}$.

The refinement of the crystal structure of $Eu_2TaO_{2.80}N_{1.20}$ from synchrotron X-ray diffraction data was performed in the space group $I4_1/acd$ starting with the atomic coordinates of Sr_2IrO_4 [33] and led to

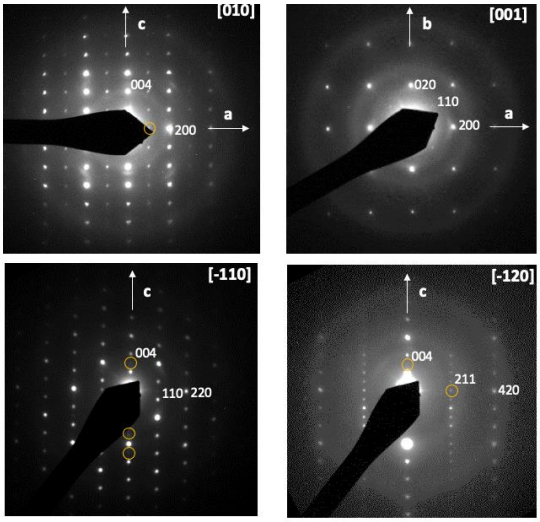

Figure 1. Selected electron diffraction patterns of $Ce_2TaO_{1.19}N_{2.81}$. Yellow circles indicate multiple diffraction reflections.

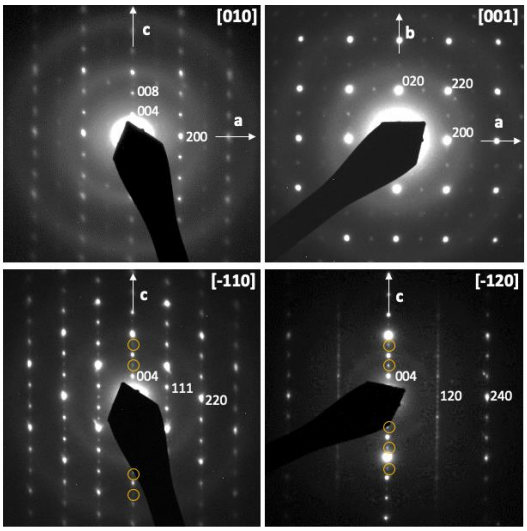

Figure 2. Selected electron diffraction patterns of $Eu_2TaO_{2.80}N_{1.20}$ with reflections indexed in the tetragonal cell with $a \simeq 5.7$ and $c \simeq 25$ Å. Yellow circles indicate multiple diffraction reflections.

the cell parameters a = 5.71867(2) and 25.00092(19) Å ($\sqrt{2}a_0 \times \sqrt{2}a_0 \times 2c_0$) (Figures 7 and 8, Table 3).

Table 1. Summary of the *Pccn* Model Refined against Room-Temperature Synchrotron Powder X-ray Diffraction Data for $La_2TaO_{1.31}N_{2.69}$ (λ = 0.4137 Å)[a,b]

atom	site	*x*	*y*	*z*	*B* (Å^2)	occupancy
La	*8e*	0.4965(7)	0.0043(6)	0.1419(5)	0.735(14)	1
Ta	*4a*	0	0	0	1.000(18)	1
O1/N1	*8e*	0.0185(13)	0.0600(6)	0.16527(18)	0.401(16)	0.33/0.67
O2/N2	4c	0.25	0.25	0.4761(5)	0.401	0.33/0.67
O3/N3	*4d*	0.25	0.75	–0.0065(4)	0.401	0.33/0.67

bond	distance (Å)	bond	distance (Å)	Bond	distance (Å)
Ta–O1,N1	2.142(2) × 2	Ta–O2,N2	2.049(1) × 2	Ta–O3,N3	2.0276(2) × 2
La–O1,N1	2.495(3)	La–O1,N1	2.516(5)	La–O1,N1	2.773(8)
La–O1,N1	3.023(8)	La–O1,N1	3.249(5)	La–O2,N2	2.551(5)
La–O2,N2	2.910(5)	La–O3,N3	2.662(4)	La–O3,N3	2.778(4)

[a]Refined cell parameters and agreement factors are a = 5.72949(2), b = 5.73055(5), and c = 12.77917(6) Å. V = 419.580(4) Å^3. R_{Bragg} = 3.46% and R_{wp} = 7.16%.

[b]The O/N occupancies were fixed to a statistical distribution considering the chemical analysis. The temperature factors were common for the three anions sites. Average bond distances: Ta–O,N 2.073 Å and La–O,N 2.773 Å.

Table 2. Summary of the *Pccn* Model Refined against Room-Temperature Synchrotron X-ray Powder Diffraction Data for $Nd_2TaO_{1.46}N_{2.54}$ (λ = 0.4139 Å)[a,b]

atom	site	*x*	*y*	*z*	B (Å2)	occupancy
Nd	8e	0.5118(4)	–0.00580(8)	0.14307(3)	0.868(2)	1
Ta	4a	0	0	0	1.039(10)	1
O1/N1	8e	–0.047(4)	–0.049(4)	0.1774(7)	1.41(13)	0.37/0.63
O2/N2	4c	0.25	0.25	0.5277(7)	1.41	0.37/0.63
O3/N3	4d	0.25	0.75	–0.013(3)	1.41	0.37/0.63

bond	distance (Å)	bond	distance (Å)	bond	distance (Å)
Ta–O1,N1	2.220(9) × 2	Ta–O2,N2	2.046(3) × 2	Ta–O3,N3	2.023(3)(×2)
Nd–O1,N1	2.259(10)	Nd–O1,N1	2.56(2)	Nd–O1,N1	2.58(2)
Nd–O1,N1	3.20(3)	Nd–O1,N1	3.23(3)	Nd–O2,N2	2.526(12)
Nd–O2,N2	2.866(15)	Nd–O3,N3	2.56(2)	Nd–O3,N3	2.81(3)

[a]Refined cell parameters and agreement factors: a = 5.70466(3), b = 5.70475(5), and c = 12.32365(5) Å. V = 401.056(4) $Å^3$. R_{Bragg} = 4.74% and R_{wp} = 9.19%.

[b]The O/N occupancies were fixed to a statistical distribution considering the chemical analysis. The temperature factors were common for the three anions sites. Average bond distances: Ta–O,N 2.096 Å and Nd–O,N 2.732 Å.

For the refinement of the La and Nd compounds, we fixed a statistical distribution of nitrogen and oxygen in the three available anion sites because the X-rays do not provide enough contrast between the two anions. For $Ce_2TaO_{1.19}N_{2.81}$, we used and fixed the occupancies obtained from the refinement of neutron diffraction data (see the next section). The structural model of this compound is shown in Figure 6.

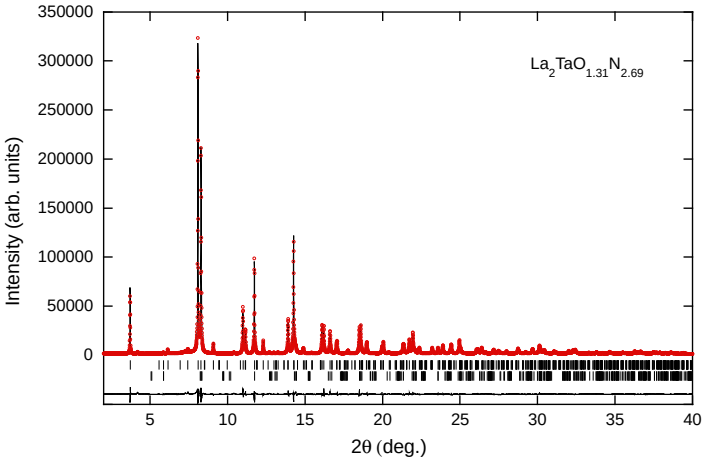

Figure 3. Rietveld fit to the synchrotron X-ray powder diffraction pattern of $La_2TaO_{1.31}N_{2.69}$ performed in the space group *Pccn* with parameters a = 5.72949(2), b = 5.73055(5), and c = 12.77917(6) Å. Upper and lower reflection markers are, respectively, for $La_2TaO_{1.31}N_{2.69}$ and $LaTaON_2$.[23]

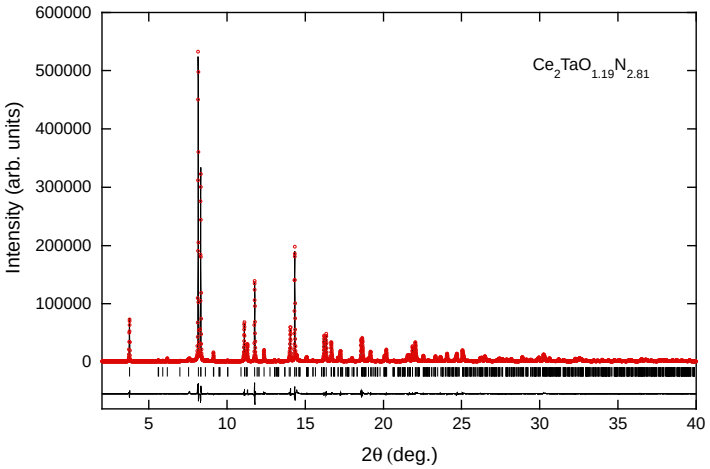

Figure 4. Rietveld fit to the synchrotron X-ray powder diffraction pattern of $Ce_2TaO_{1.19}N_{2.81}$ performed in the space group *Pccn* with cell parameters a = 5.70500(5), b = 5.71182(4), and c = 12.61280(7) Å.

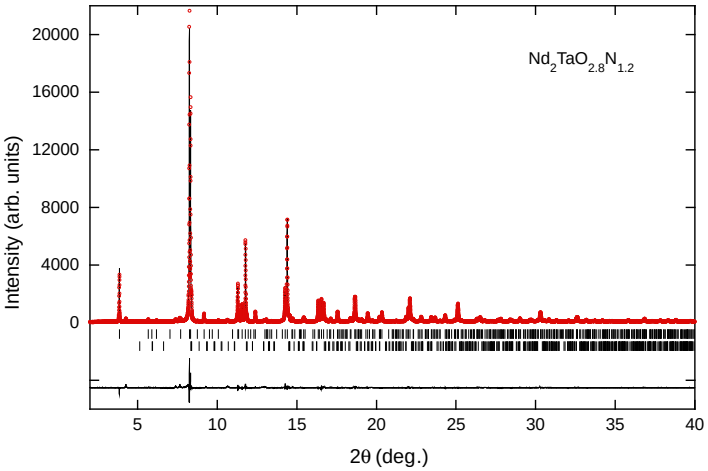

Figure 5. Rietveld fit to the synchrotron X-ray powder diffraction pattern of $Nd_2TaO_{1.46}N_{2.54}$ performed in the space group *Pccn* with cell parameters a = 5.70466(3), b = 5.70475(5), and c = 12.32366(5) Å. Upper and lower reflection markers are, respectively, for $Nd_2TaO_{1.46}N_{2.54}$ and $NdTaON_2$.

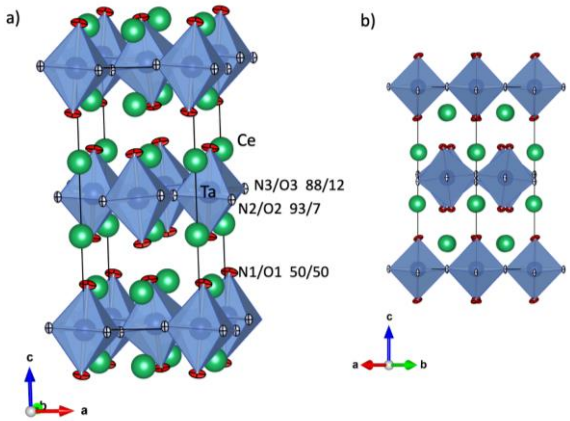

Figure 6. (a) Crystal structure of $Ce_2TaO_{1.19}N_{2.81}$ determined from neutron powder diffraction data. Thermal ellipsoids of the anions are shown at 50% probability. The refined N/O population (%) is indicated for each anion site. (b) Projection along 110 showing the tilting of the Ta octahedra.

As in the refinements of the La and Nd compounds, we fixed a statistical distribution of nitrogen and oxygen in the available anion sites because the X-rays do not provide enough contrast between the two anions. Attempts to refine a model with the larger cell of a = 8.15 and c = 24.99 Å observed by electron diffraction led to chemically inconsistent bond distances and angles. In the $I4_1/acd$ model, the doubling of the c_0 parameter results from a sequence of tilts along the c axis (θ tilts) that repeats every four layers of octahedra (Figure 8).[31] The cell volume of this compound normalized to a $\sqrt{2}a_0 \times \sqrt{2}a_0 \times c_0$ cell is 408.805 Å^3, that is larger than for $Nd_2TaO_{1.46}N_{2.54}$ (401.056(4) Å^3) as a consequence of the divalent state of Eu^{2+}, with a larger ionic radius than that of Nd^{3+} (for CN = IX, $r(Eu^{2+})$ = 1.30 Å and $r(Nd^{3+})$ = 1.163 Å).[34] The cell volumes of the La (419.580(4) Å^3) and Ce (411.000(5) Å^3) compounds are significantly larger than for the Nd phase, as expected from the ionic radii of R^{3+} cations.[34] The Goldschmidt tolerance factors (t) for the four phases have been calculated from the ionic radii considering the formal compositions $La_2^{3+}Ta_{0.31}^{4+}Ta_{0.69}^{5+}O_{1.31}N_{2.69}$, $Ce_2^{3+}Ta_{0.19}^{4+}Ta_{0.81}^{5+}O_{1.19}N_{2.81}$, $Nd_2^{3+}Ta_{0.46}^{4+}Ta_{0.54}^{5+}O_{1.46}N_{2.54}$, and $Eu_{1.80}^{2+}Eu_{0.20}^{3+}TaO_{2.80}N_{1.20}$, leading to the values of 0.904 (La), 0.896 (Ce), 0.886 (Nd), and 0.930 (Eu), respectively. The larger t of the europium compound, together with the lower nitride content of this phase and an expected distinct anion ordering (see the next section), may account for its different crystal symmetry compared with the other rare earth derivatives.

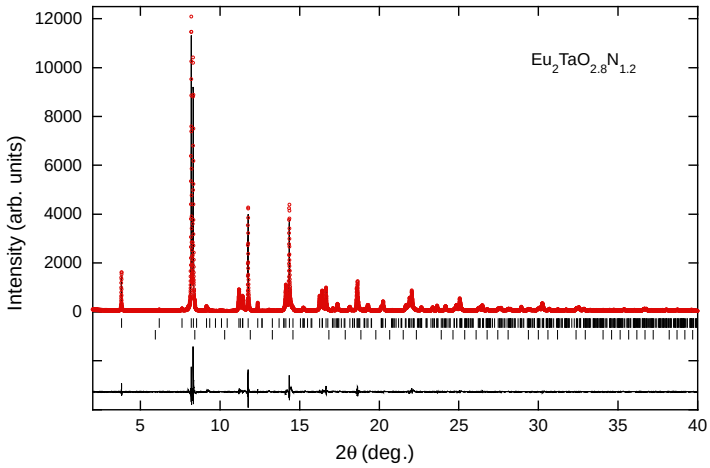

Figure 7. Rietveld fit to the synchrotron X-ray powder diffraction pattern of $Eu_2TaO_{2.80}N_{1.20}$ performed in the space group $I4_1/acd$ with cell parameters a = 5.71867(2) and c = 25.00092(19) Å. Upper and lower reflection markers are, respectively, for $Eu_2TaO_{2.80}N_{1.20}$ and $EuTaO_2N$.

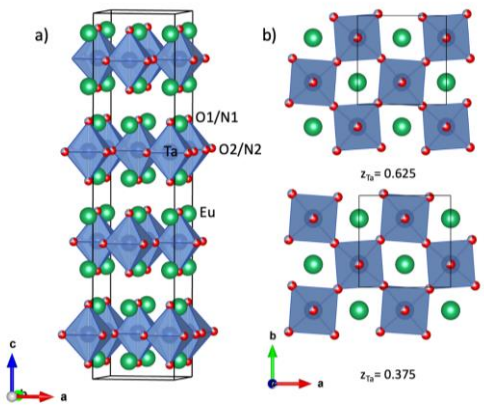

Figure 8. (a) Crystal structure of $Eu_2TaO_{2.80}N_{1.20}$ determined from synchrotron powder X-ray diffraction data. The nitride and oxide anions are depicted as gray and red spheres, respectively, and are distributed statistically in the X1 and X2 sites with proportions according to the chemical analysis. (b) Projection along c of the two central layers of the unit cell, showing the tilting of the Ta octahedra.

Table 3. Summary of the $I4_1/acd$ Model Refined against Room-Temperature Synchrotron X-ray Powder Diffraction Data for $Eu_2TaO_{2.80}N_{1.20}$ (λ= 0.4142 Å)[a,b]

atom	site	*x*	*y*	*z*	B (Å^2)	occupancy
Eu	16d	0	0.25	0.552190(18)	0.686(10)	1
Ta	8[a]	0	0.25	0.375	0.922(15)	1
O1/N1	16d	0	0.25	0.4564(3)	2.816	0.70/0.30
O2/N2	16f	0.232(2)	0.482(2)	0.125	2.816	0.70/0.30
bond		**distance (Å)**		**bond**	**distance (Å)**	
Ta–O1,N1		2.035(8) × 2		Ta–O2,N2	2.027(11) × 4	
Eu–O1,N1		2.395(8)		Eu–O1,N1	2.867(1) × 4	
Eu–O2,N2		2.830(9) × 2		Eu–O2,N2	2.614(8) × 2	

[a]Refined cell parameters and agreement factors are a = 5.71867(2) and c = 25.00092(19) Å. V = 817.609(8) Å^3. R_{Bragg} = 4.19% and R_{wp} = 10.5%.

[b]Isotropic thermal parameters of the anions were fixed to 2.816 Å^2. O/N occupancies were fixed to a statistical distribution considering the chemical analysis. Average bond distances: Ta–O,N 2.030 Å and Eu–O,N 2.750 Å.

Neutron Diffraction Study of $Ce_2TaO_{1.19}N_{2.81}$: Anion Order and the Prediction of Pauling's Second Crystal Rule in *n* = 1 Ruddlesden–Popper Oxynitrides

The refinement of neutron diffraction data of $Ce_2TaO_{1.19}N_{2.81}$ (Figure 9) was performed starting with a random distribution of nitrogen and oxygen in the three anion positions of the *Pccn* model, considering full occupancy in all sites and constraining the total content of each anion to the composition determined by chemical analysis. The refined N/O populations for the two equatorial sites were 93/7 (X2) and 88/12 (X3), whereas the obtained occupancies of the axial site X1 were 50% for each anion (Figure 6 and Table 4). This anion distribution shows a near-100% order of the nitride anions at the equatorial sites of the tantalum octahedra. The bond distances for these positions were significantly

shorter (*d*(Ta-X2) = 2.0504(3) Å, *d*(Ta-X3) = 2.0346(2) Å) than for the axial site (*d*(Ta-X1) = 2.1855(19) Å). The elongation of the octahedra along the c direction is an indication of the observed anion order, as the axial sites are occupied by 50% O/50% N, and the covalent character of metal–oxygen bonds is lower than for metal–nitrogen bonds. The large thermal parameter observed for the axial site is indicative of the O/N disorder in this position(see Figure 6). Shorter bond M–N distances compared to M–O bonds have been also observed in the hexagonal perovskite $BaWON_2$ [12] that shows the total order of N and O in corner-sharing positions and face-sharing positions of the W^{6+} octahedra. The observed anion order in $Ce_2TaO_{1.19}N_{2.81}$ is different from that previously reported in *n* = 1 Ruddlesden–Popper oxynitrides as a consequence of its larger nitrogen content and higher charge of the A cation. In the less nitrided alkaline earth compounds Sr_2TaO_3N,[35,36] Ba_2TaO_3N,[36] and Sr_2NbO_3N [37] crystallizing in the *I*4/*mmm* space group, the nitride anions also prefer the equatorial sites of the octahedra, but the N/O population for these positions is 50/50, whereas the axial sites are fully occupied by oxygen. These anion distributions agree with the prediction of Pauling's second crystal rule (PSCR),[38,39] which states that the electric charge of each anion (*q*) tends to compensate the strength of the electrostatic valence bonds from the cations, according to the equation $b = \sum_i \frac{z_i}{v_i}$, where z_i is the electric charge of each cation bonded to a given anionic position and v_i is its coordination number. The *b* values for the equatorial and axial positions in A_2BO_3N compounds (A = Sr^{2+}, Ba^{2+}; B = Nb^{5+}, Ta^{5+}) are 2.55 and 1.94, respectively, in close agreement with the charge of the anions occupying these sites ($q = -2.5$ and -2)[37,39] using the

determined distributions from neutron diffraction. For ideal R_2TaON_3 compounds, the trivalent rare earth cations increase the calculated sums for the equatorial and axial sites to 3 and 2.5, respectively. In $Ce_2TaO_{1.19}N_{2.81}$, considering 19% of Ta^{4+} and 81% of Ta^{5+}, the calculated sums are 2.94 and 2.47 for the equatorial and axial sites, respectively, and the observed anion distribution leads to $q = -2.93$, – 2.88, and −2.5 for X2, X3, and X1 positions, respectively, in excellent agreement with the prediction of PSCR. A similar anion ordering can be expected for the other trivalent rare earth derivatives reported in this work, $La_2TaO_{1.31}N_{2.69}$ and $Nd_2TaO_{1.46}N_{2.54}$. However, for $Eu_2TaO_{2.80}N_{1.20}$, the PSCR-predicted distribution is the same as for the alkaline earth oxynitrides because the europium in this compound is essentially divalent, as the alkaline earth cations. Hence, the expected anion populations at the axial sites would be 50/50 for $La_2TaO_{1.31}N_{2.69}$ and $Nd_2TaO_{1.46}N_{2.54}$, whereas for $Eu_2TaO_{2.80}N_{1.20}$, 100% O occupancy is expected for the same positions. For the analyzed anion compositions in each compound, the expected populations at the equatorial sites would be, respectively, O/N 15/85, 23/77, and 40/60 for the La, Nd, and Eu compounds. Future neutron diffraction experiments are planned to corroborate these predictions.

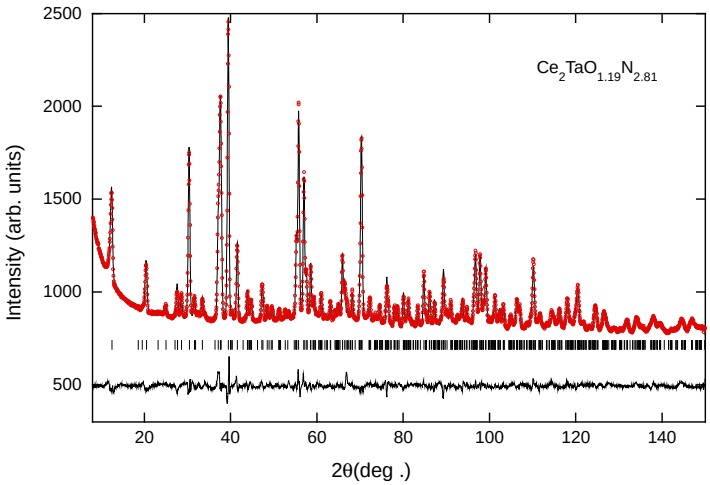

Figure 9. Rietveld fit to the neutron powder diffraction pattern of $Ce_2TaO_{1.19}N_{2.81}$ performed in the space group *Pccn* with cell parameters a = 5.75284(19), b = 5.75620(15), and c = 12.71338(18) Å.

Table 4. Summary of the *Pccn* Model Refined against Room-Temperature Neutron Diffraction Data for $Ce_2TaO_{1.19}N_{2.81}$ (λ = 1.37 Å)[a,b]

Atom	site	*x*	*y*	*z*	B (Å^2)	occupancy
Ce	8e	0.4997(17)	0.0115(8)	0.14118(15)	0.89(3)	1
Ta	4[a]	0	0	0	1.09(3)	1
O1/N1	8e	0.0309(11)	0.0401(5)	0.17037(13)	2.524	0.498(5)/0.502
O2/N2	4c	0.25	0.25	0.4800(2)	1.205	0.070(7)/0.930
O3/N3	4d	0.25	0.75	0.0011(11)	1.205	0.124(13)/0.876
Bond	**d (Å)**	**bond**	**d (Å)**	**bond**	**d (Å)**	
Ta-O1,N1	2.1855(19) × 2	Ta–O2,N2	2.0504(3) × 2	Ta–O3,N3	2.0346(2) × 2	
Ce–O1,N1	2.421(3)	Ce–O1,N1	2.614(5)	Ce–O1,N1	2.727(12)	
Ce–O1,N1	3.083(12)	Ce–O1,N1	3.202(5)	Ce–O2,N2	2.591(6)	

[a] Refined cell parameters and agreement factors are a = 5.75284(19), b = 5.75620(15), and c = 12.71338(18) Å. V = 420.997(19) Å^3. R_{Bragg} = 5.22% and R_{wp} = 1.34%.

[b] Estimated standard deviations in parentheses are shown once for each independent variable. The thermal parameters were refined anisotropically for the three anions; ellipsoids are shown on Figure 6. Average bond distances: Ta–O,N 2.090 Å and Ce–O,N 2.769 Å.

Magnetic Properties

The Ce, Nd, and Eu compounds display a Curie-like paramagnetic susceptibility at high temperature (T > 50 K) (Figure 10a), although deviations are clearly perceptible at least in $Nd_2TaO_{1.46}N_{2.54}$, as typically found in rare earth compounds. [40] $La_2TaO_{1.31}N_{2.69}$ shows an extremely small paramagnetic susceptibility, in accordance with the nonmagnetic nature of La^{3+} and plausibly associated with the presence of Ta^{4+} or to traces of magnetic impurity. A convenient way to identify deviations from the common Curie behavior and to get insights into their physical origin is to plot the effective paramagnetic moment (μ_{eff}), extracted from the measured susceptibility: $\chi_m = \mu_0 \frac{N_A \mu_B^2}{3k_B T} \mu_{\text{eff}}^2$. In Figure 10b, we show the μ_{eff} vs T plot, where μ_{eff} has been obtained through the thermal derivative of the inverse susceptibility:

$\frac{d\chi_m^{-1}}{dT} = \frac{3k_B T}{N_A \mu_B^2 \mu_0} \frac{1}{\mu_{\text{eff}}^2}$. It turns out that for Eu and Ce compounds, μ_{eff} is temperature-independent down to about 25K. The observed effective moments approach, although slightly smaller, to those expected for Eu^{2+} ions ($^8S_{7/2}$; g_J = 2) and Ce^{3+} ($^2F_{5/2}$, g_J = 6/7) (green and blue dashed lines in Figure 10b), which may indicate some overoxidation of Eu^{2+} and Ce^{3+}. In fact, from the susceptibility of $Ce_2TaO_{1.19}N_{2.81}$, we infer an effective paramagnetic moment of $\mu_{eff} \simeq 2.02\ \mu_B$/Ce, which could signal the partial appearance of Ce^{4+}(J = 0), estimated to be around 37%, together with an accompanying fraction of Ta^{4+} (J = 1/2) for charge compensation. The presence of Ce^{4+} may be induced by the existence of nitrogen-rich regions created by the anion disorder, that will be balanced

by oxide-rich regions where Ta^{5+} is reduced to Ta^{4+} according to the internal redox equilibrium $Ce^{3+} + Ta^{5+} \Leftrightarrow Ce^{4+} + Ta^{4+}$.[4] The observed effective paramagnetic moment of $Eu_2TaO_{2.80}N_{1.20}$ is $\mu_{eff} \simeq 7.63\ \mu_B$/Eu, which assuming a coexistence of Eu^{2+} and Eu^{3+} would correspond to a concentration of Eu^{3+} of about 10%, in excellent agreement with the chemical analysis. The small magnetic moment in the broad and rather delocalized $5d^1$ orbitals of Ta^{4+} ions should lead to a minor contribution to the measured small susceptibility. In contrast, the $Nd_2TaO_{1.46}N_{2.54}$ compound displays a conspicuous decrease of μ_{eff} on cooling below $T \simeq 100$ K. This is the common behavior of rare earths with an odd number of electrons in magnetically diluted systems, and it may result from crystal field effects or the presence of magnetic interactions, as discussed latter. For instance, the crystal field may break the degeneracy of the ground-state $^{2S+1}L_J$ of the rare earth into various site symmetry-dependent Kramers doublets, with electron occupancy, and thus, the magnetic susceptibility will evolve with temperature. The presence of magnetic interactions may also result in a reduction of magnetic susceptibility. It follows that the origin of the observed temperature dependence of $\mu_{eff}(T)$ cannot be, in general, univocally disentangled.[41] On the other hand, the observation that in the high-temperature limit, the measured μ_{eff} is larger than the free ion Nd^{3+} value ($^4I_{9/2}$; $J = 9/2$, $g_J = 8/11$) remains intriguing. It could be tentatively attributed to some spin polarization of neighboring Ta^{4+} ions, as in $Nd_2TaO_{1.46}N_{2.54}$, the proportion of this cation is the largest among the $R_2TaO_{4-x}N_x$ series presented here.

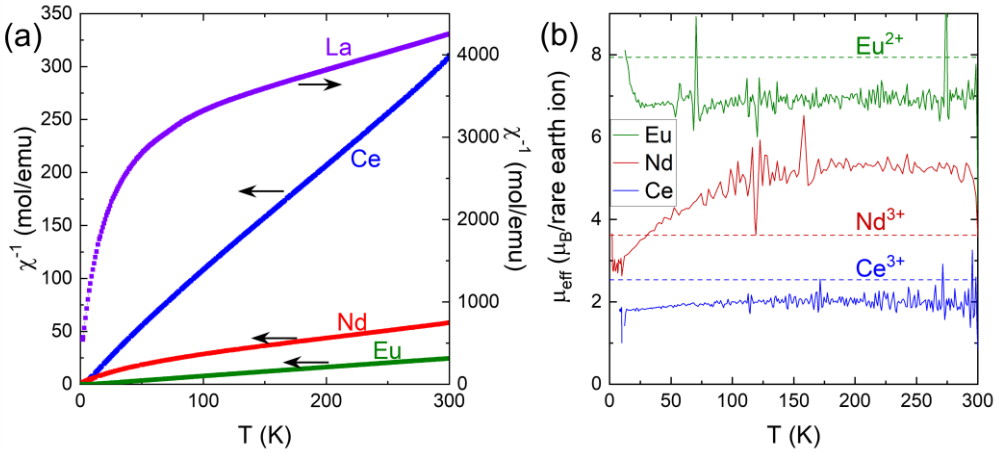

Figure 10. (a) Inverse susceptibility of $La_2TaO_{1.31}N_{2.69}$, $Ce_2TaO_{1.19}N_{2.81}$, $Nd_2TaO_{1.46}N_{2.54}$, and $Eu_2TaO_{2.80}N_{1.20}$, measured at 10 kOe (note the different scale, right axis, used for the La compound). (b) Temperature dependence of the effective paramagnetic moment obtained by the derivative of the inverse susceptibility as explained in the text.

To get a deeper insight into the low-temperature spontaneous magnetic behavior of these compounds, we explored the low-field magnetic susceptibility (χ). In Figure 11a, we show χ(*T*) measured on heating under 25 Oe magnetic field after a zero-field cooling (ZFC) and field cooling (FC). A well-pronounced peak followed by a low-temperature hysteresis shows up in the ZFC-FC at ~4K for $Ce_2TaO_{1.19}N_{2.81}$ and ~8K for $Eu_2TaO_{2.80}N_{1.20}$, indicating the appearance of magnetic order in these compounds. In contrast, $Nd_2TaO_{1.46}N_{2.54}$ does not display any hysteresis and thus no traces of magnetic order down to the lowest explored temperature (2K). To understand the origin of this hysteresis, we have

measured the field-dependent magnetization. The obtained *M*(*H*) curves are depicted in Figure 11b,c. Data show a rapid upturn of magnetic moment under a low magnetic field at low temperatures characteristic of magnetic order with a ferromagnetic component.

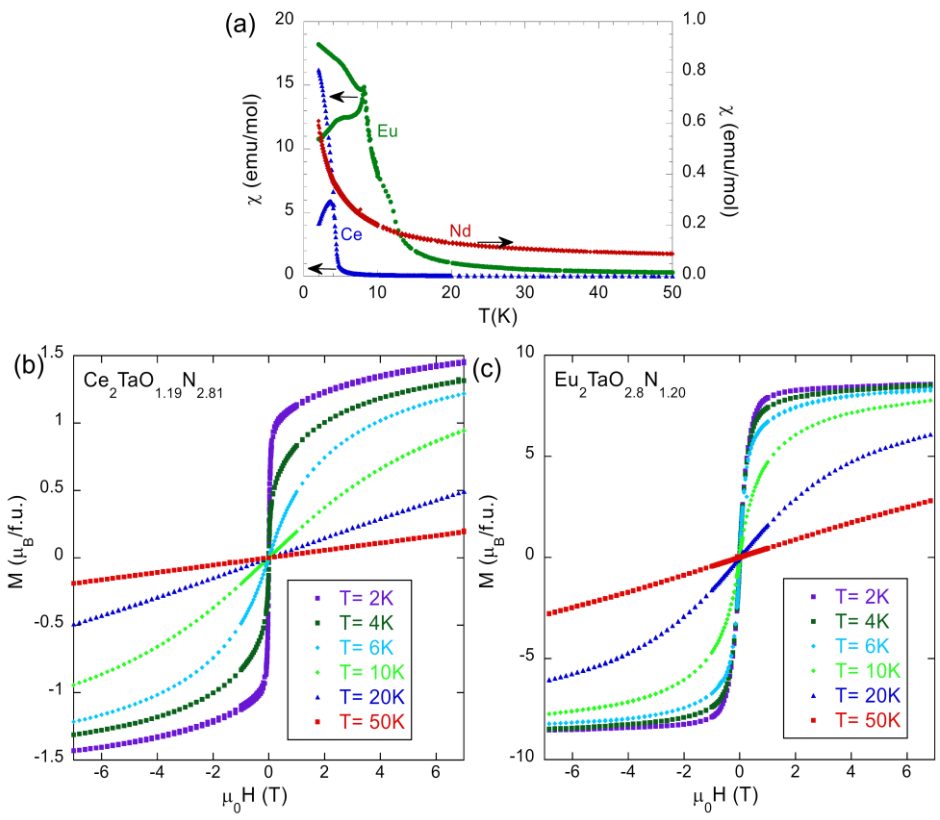

Figure 11. (a) Zero field-cooled/field-cooled magnetization vs temperature (measured under 25 Oe applied magnetic field) of $Nd_2TaO_{1.46}N_{2.54}$ (right axis) and $Ce_2TaO_{1.19}N_{2.81}$ and $Eu_2TaO_{2.80}N_{1.20}$ (left axis). (b, c) Magnetization vs magnetic field measured at different temperatures for $Ce_2TaO_{1.19}N_{2.81}$ and $Eu_2TaO_{2.80}N_{1.20}$, respectively.

We have discarded that this upturn corresponds to a paramagnet at low enough temperature by plotting the magnetization vs H/T and checked that the $M(H/T)$ curves at the lowest temperature ($T < 15$ K) do not scale (see Figure S3). Data collected at the lowest temperature reflect a lack of saturation, suggesting the coexistence of the remaining fraction of disordered spins in the samples.

The saturation magnetization (M_S) inferred from data collected at the lowest temperature (2K) and largest field (7 T) indicates $M_S(Ce_2TaO_{1.19}N_{2.81}) \sim 0.7\ \mu_B$/Ce and $M_S(Eu_2TaO_{2.80}N_{1.20}) \sim 4.3\ \mu_B$/Eu. Both values are significantly smaller than those expected for fully collinear ferromagnetic orders: 2.14 μ_B/Ce for Ce^{3+} and 1.35 μ_B/Ce for the aforementioned 37% of Ce^{4+}; 7 μ_B/Eu for full Eu^{2+}, and 6.3 μ_B/Eu for 10% of Eu^{3+} (according to chemical analysis). This discrepancy between the expected (or the maximal) and observed values of the saturation magnetization indicates that a more complex ordering pattern could be at work or that the disorder in the system drives to magnetic frustration and to an only partially ordered magnetic structure.

At first sight, the lack of magnetic ordering in $Nd_2TaO_{1.46}N_{2.54}$ may seem surprising as structural differences between the Nd, Ce, and Eu compounds are rather small. For the rare earth cations in the K_2NiF_4-type structure, there are eight superexchange pathways corresponding to the next nearest neighbors (NNN), four from the same NaCl-type layer (J_{21}) and four from a neighbor layer (J_{22}) (see Figure 12a–c). [42] In these pathways, the changes of bond distances across the series are extremely moderate (≈1%), and the R–X–R bond angles change monotonically by

≈3% (171.41° for the Eu compound, 167.7° for $Ce_2TaO_{1.19}N_{2.81}$ and 160.7° for $Nd_2TaO_{1.46}N_{2.54}$) (Figure 13). On the other hand, any superexchange R–X–R magnetic interaction is expected to be stronger when increasing the covalency of bonds by reducing the electronegativity of the anions,[43] and thus, a larger N/O ratio will reinforce the superexchange interactions. As illustrated in Figure 12, the N/O occupancy in the R–X–R pathways for $Nd_2TaO_{1.46}N_{2.54}$ is similar to that of the Ce compound and larger than in the Eu compound, and still no magnetic order is observed in the Nd compound. From these two sets of data, we conclude that superexchange interactions do not appear to play a major role in the magnetic ordering of the rare earth ions in these compounds, which thus appear to be governed by direct R–R exchange interactions depicted in Figure 12d. In exchange-coupled Nd^{3+}-Nd^{3+} units, crystal field and exchange interactions conspicuously combine to produce a singlet ground state, which is in sharp contrast with Ce^{3+}-Ce^{3+} and Eu^{2+}-Eu^{2+}units where the ground state can be a triplet (see, for instance, Figures 31, 26, and 22, pages 64–69 in ref [(40)]). It follows that the effective magnetic moment of Nd^{3+} decreases when decreasing temperature, and no magnetic order develops in $Nd_2TaO_{1.46}N_{2.54}$, which is completely different than the behavior of $Ce_2TaO_{1.19}N_{2.81}$ and $Eu_2TaO_{2.80}N_{1.20}$ compounds in agreement with our experimental observations.

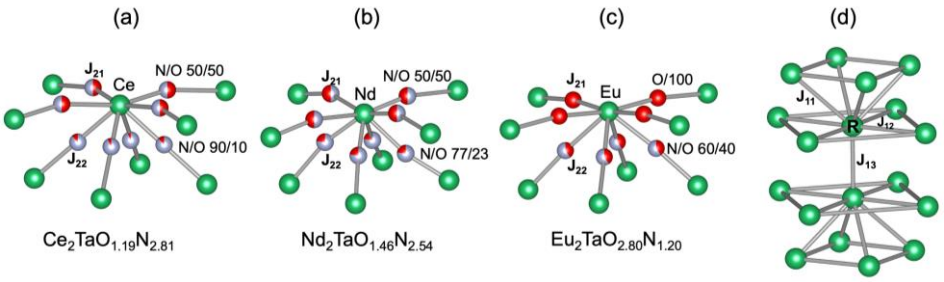

Figure 12. (a–c) Superexchange (J_{21}, J_{22}) and (d) direct exchange (J_{11}, J_{12}, J_{13}) magnetic interactions in $R_2TaO_{3-x}N_x$ compounds (R = Ce, Nd, Eu). Anion occupancies correspond to those determined from neutron diffraction for $Ce_2TaO_{1.19}N_{2.81}$. For $Nd_2TaO_{1.46}N_{2.54}$ and $Eu_2TaO_{2.80}N_{1.20}$, the anion populations are those expected using PSCR (see the precedent section).

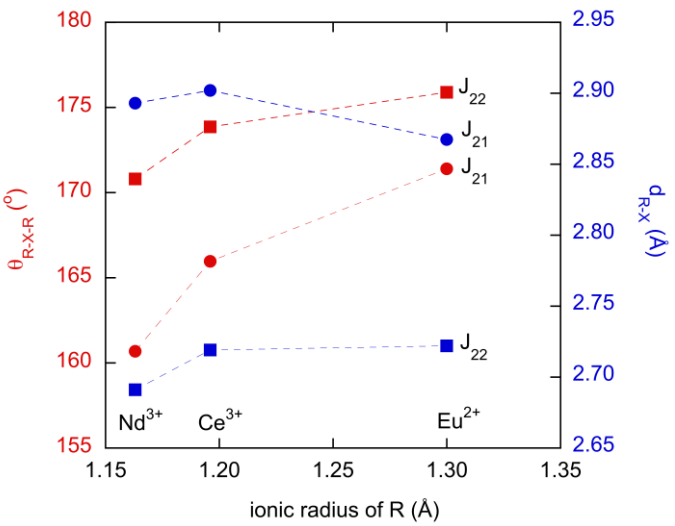

Figure 13. Average R–X–R angles and R–X (X = O,N) bond distances for superexchange interactions in $Ce_2TaO_{1.19}N_{2.81}$ (from neutron diffraction data), $Nd_2TaO_{1.46}N_{2.54}$, and $Eu_2TaO_{2.80}N_{1.20}$ plotted against the ionic radii of Ce^{3+}, Nd^{3+}, and Eu^{2+}, respectively, for CN = IX.[34]

4.4 Conclusions

The new $n = 1$ Ruddlesden–Popper rare earth tantalum oxynitrides $R_2TaO_{4-x}N_x$ (R = La, Ce, Nd, and Eu) are prepared using a solid-state reaction under N_2 at temperatures between 1200 and 1700 °C starting with mixtures of R_2O_3, RN, Ta_3N_5, and TaON. This is a versatile synthetic approach that allows to control the initial N/O ratio, a determining factor to stabilize the oxynitrides, by using different proportions of the four reactants while keeping the R/Ta = 2 stoichiometric ratio. The chemical analyses of the obtained oxynitrides $La_2TaO_{1.31}N_{2.69}$, $Ce_2TaO_{1.19}N_{2.81}$, $Nd_2TaO_{1.46}N_{2.54}$, and $Eu_2TaO_{2.80}N_{1.20}$ indicate a decrease of the N/O ratio during the synthesis that leads to an excess of oxygen with respect to the ideal stoichiometry R_2TaON_3, corresponding to the oxidation states of the cations R^{3+} and Ta^{5+}. The lower nitrogen content is formally charge-compensated by the reduction of europium to the divalent state or of Ta^{5+} to Ta^{4+}.

The La, Ce, and Nd compounds show a tilted superstructure with cell parameters $\sqrt{2}a_0 \times \sqrt{2}a_0 \times c_0$ (where a_0 and c_0 are the parameters of the *I4/mmm* K_2NiF_4 aristotype) with the *Pccn* space group. In contrast, the europium compound shows additional doubling of the *c* axis, with parameters $\sqrt{2}a_0 \times \sqrt{2}a_0 \times 2c_0$, and crystallizes in the $I4_1/acd$ space group. The observed different crystal chemistry in the europium compound is a consequence of the near total reduction of this rare earth to Eu^{2+}. The neutron diffraction study of $Ce_2TaO_{1.19}N_{2.81}$ shows that the equatorial sites of the tantalum octahedra have an occupancy of nearly 100% nitrogen, whereas the axial sites are occupied by 50% of each anion. This

anion distribution is in excellent agreement with the prediction of Pauling's second crystal rule that leads to the bond strength sums of 2.94 and 2.47 for the equatorial and axial sites, respectively. According to this prediction, a similar anion order is expected for the trivalent rare earth $n = 1$ Ruddlesden–Popper oxynitrides of La and Nd. For the Eu^{2+} compound, the corresponding calculated sums are 2.55 and 1.94; hence, a population of 50/50 O/N in the equatorial sites and 100% O in the axial sites is predicted. The Ce and Eu compounds display some magnetic order at low temperatures with a ferromagnetic component**.** In contrast, the Nd oxynitride does not show any fingerprint of magnetic order but remains paramagnetic down to the lowest temperature explored (2 K), consistent with the temperature-independent effective magnetic moment observed in the former and a low-temperature suppression in the latter, which we attribute to the combined effect of a temperature-dependent change of electron occupancy in the crystal-field split Kramers doublets and exchange interactions producing a singlet ground state. The new $n = 1$ Ruddlesden–Popper compounds reported in this paper expand the structural diversity of the family of perovskite oxynitrides opening avenues to search new materials in this group of solids. Post-treatments of the $R_2TaO_{4-x}N_x$ samples in strongly nitriding atmospheres such as NH_3 would plausibly increase the nitrogen contents with concomitant oxidation of the cations Eu^{2+} and Ta^{4+}, and new applications as dielectric materials or as visible light photocatalysts in different reactions may emerge.

Author Information

Corresponding Authors

Josep Fontcuberta - *Institut de Ciència de Materials de Barcelona (ICMAB-CSIC), Campus UAB, 08193 Bellaterra, Spain;* Email: fontcuberta@icmab.cat

Amparo Fuertes - *Institut de Ciència de Materials de Barcelona (ICMAB-CSIC), Campus UAB, 08193 Bellaterra, Spain;* https://orcid.org/0000-0001-5338-9724;

Email: amparo.fuertes@icmab.es

Authors

Jhonatan R. Guarín - *Institut de Ciència de Materials de Barcelona (ICMAB-CSIC), Campus UAB, 08193 Bellaterra, Spain*

Carlos Frontera - *Institut de Ciència de Materials de Barcelona (ICMAB-CSIC), Campus UAB, 08193 Bellaterra, Spain;* https://orcid.org/0000-0002-0091-4756

Judith Oró-Solé - *Institut de Ciència de Materials de Barcelona (ICMAB-CSIC), Campus UAB, 08193 Bellaterra, Spain*

Bastian Colombel - *Institut de Ciència de Materials de Barcelona (ICMAB-CSIC), Campus UAB, 08193 Bellaterra, Spain*

Clemens Ritter - *Institut Laue-Langevin, 71 Av. de Martyrs, BP 156, F-38042 Grenoble Cedex 9, France*

François Fauth - *CELLS-ALBA Synchrotron, Barcelona 08290, Spain*; https://orcid.org/0000-0001-9465-3106

Author Contributions

The article was written through contributions of all authors. All authors have given approval to the final version of the article.

Funding

Ministerio de Ciencia e Innovación, Agencia Estatal de Investigación, Spain (PID2020-113805GB-I00, PID2020-118479RB-I00 (AEI/FEDER, EU), CEX2019-000917-S and PRE2018-085204) and Generalitat de Catalunya (2021SGR00439).

Notes

The authors declare no competing financial interest.

Acknowledgments

This work was supported by grants PID2020-113805GB-I00, PID2020-118479RB-I00, and CEX2019-000917-S funded by MCIN/AEI/10.13039/501100011033 (Ministerio de Ciencia e Innovación/Agencia Estatal de Investigación) and by “ERDF A way of making Europe” and European Union and grant 2021SGR00439 funded

by the Generalitat de Catalunya. It has been developed under the PhD program in Materials Science of the UAB. The authors thank ALBA synchrotron and Institut Laue Langevin (Experiments numbers AV-2022097011 and EASY1232 respectively) for the provision of beam time; the authors also thank Dr. Bernat Bozzo (ICMAB-CSIC) for performing the magnetic measurements. J.R.G. acknowledges the AEAT predoctoral fellowship PRE2018-085204. The authors acknowledge the assistance of ICMAB Scientific and Technological services: Laboratory of Low Temperature and Magnetism and Electron Microscopy.

4.5 References

(1) Fuertes, A. Nitride tuning of transition metal perovskites. *APL Materials* **2020**, 8, 020903.
(2) Jansen, M; Letschert, H.P. Inorganic yellow-red pigments without toxic metals. *Nature* **2000**, 404, 980-982.
(3) Jorge, A. B.; Oró-Solé, J.; Bea, A. M.; Mufti, N.; Palstra, T. T. M.; Rodgers, J. A.; Attfield, J. P.; Fuertes, A. Large coupled magnetoresponses in $EuNbO_2N$. *Journal of the American Chemical Society* **2008**, 130, 12572-12573.
(4) Yang, M.; Oró-Solé, J.; Kusmartseva, A.; Fuertes, A.; Attfield, J.P. Electronic tuning of two metals and colossal magnetoresistances in $EuWO_{1+x}N_{2-x}$ perovskites. *Journal of the American Chemical Society* **2010**, 132, 4822-4829.
(5) Kim, Y.; Woodward, P.M.; Baba-Kishi, K.Z.; Tai, C.W. Characterization of the structural, optical, and dielectric properties of oxynitride perovskites AMO_2N (A = Ba, Sr, Ca; M = Ta, Nb). *Chemistry of Materials* **2004**, 16, 1267-1276.
(6) Wang, Q.; Domen, K. Particulate photocatalysts for light-driven water splitting: Mechanisms, challenges, and design strategies. *Chemical Reviews* **2020**, 120, 919-985.
(7) Chen,K.; Xiao, J.; Vequizo, J.M.; Hisatomi, T.; Ma, Y.; Nakabayashi, M.; Takata, T.; Yamakata, A.; Shibata, N.; Domen, K. Overall water splitting by a $SrTaO_2N$-based photocatalyst decorated with

an Ir-promoted Ru-based cocatalyst. *Journal of the American Chemical Society* **2023**, 145, 3839−3843.
(8) Ceravola, R.; Frontera, C.; Oró-Solé, J.; Black, A.P.; Ritter, C.; Mata, I.; Molins, E.; Fontcuberta, J.; Fuertes, A. Topochemical nitridation of Sr_2FeMoO_6. *Chemical Communications* **2019**, 55, 3105-3108.
(9) Ceravola, R.; Oró-Solé, J.; Black, A.P.; Ritter, C.; Puente Orench, I.; Mata, I.; Molins, E.; Frontera, C.; Fuertes, A. Topochemical synthesis of cation ordered double perovskite oxynitrides. *Dalton Transaction* **2017**, 46, 5128-52131.
(10) Ishida, K.; Tassel, C.; Watabe, D.; Takatsu, H.; Brown, C.M.; Nilsen, G.J.; Kageyama, H. Spin frustration in double perovskite oxides and oxynitrides: Enhanced frustration in La_2MnTaO_5N with a large octahedral rotation. *Inorganic Chemistry* **2021**, 60, 8252-8258.
(11) Guarín, J.R.; Frontera, C.; Oró-Solé, J.; Gàzquez, J.; Ritter, C.; Fontcuberta, J.; Fuertes. High-temperature synthesis of ferromagnetic $Eu_3Ta_3(O,N)_9$ with a triple perovskite structure. *Inorganic Chemistry* **2023**, 62, 17362-17370.
(12) Oró-Solé, J.; Fina, I.; Frontera, C.; Gàzquez, J.; Ritter, C.; Cunquero, M.; Loza-Alvarez, P.; Conejeros, S.; Alemany, P.; Canadell, E.; Fontcuberta, J.; Fuertes, A. Engineering polar oxynitrides: hexagonal perovskite $BaWON_2$. *Angewandte Chemie International Edition* **2020**, 59, 18395-18399.
(13) Ruddlesden, S. N.; Popper, P. New compounds of the K_2NiF_4 type. *Acta Crystallographica* **1957**, 10, 538-539.
(14) Pors, F.; Marchand, R.; Laurent, Y. Nouveaux oxynitrures A_2TaO_3N (A=Alcalinoterreux) de type structural K_2NiF_4. *Annales de Chimie* **1991**, 16, 547-551.
(15) Marchand, R. Oxynitrures à structure K_2NiF_4. Les composés Ln_2AlO_3N (Ln= La, Nd, Sm). *Comptes Rendus de l'Académie des Science* **1976**, 282, 329-331.
(16) Tobías, G.; Oró-Solé, J.; Beltrán-Porter, D.; Fuertes, A. New family of Ruddlesden-Popper strontium niobium oxynitrides: $(SrO)(SrNbO_{2-x}N)_n$ (n =1, 2). *Inorganic Chemistry* **2001**, 40, 6867-6869.
(17) Cordes, N.; Nentwig, M.; Eisenburger, L.; Oeckler, O.; Schnick, W. Ammonothermal synthesis of the mixed-valence nitrogen-rich europium tantalum Ruddlesden-Popper phase $Eu^{II}Eu^{III}{}_2Ta_2N_4O_3$. *European Journal of Inorganic Chemistry* **2019**, 2304-2311.

(18) Black, A.P.; Johnston, H.E.; Oró-Solé, J.; Bozzo, B.; Ritter, C.; Frontera, C.; Attfield, J.P.; Fuertes, A. Nitride tuning of lanthanide chromites. *Chemical Communications* **2016**, 52, 4317-4320.
(19) Oró-Solé, J.; Clark, L.; Kumar, N.; Bonin, W.; Sundaresan, A.; Attfield, J.P.; Rao, C.N.R.; Fuertes, A. Synthesis, Anion order and magnetic properties of $RVO_{3-x}N_x$ perovskites (R = La, Pr, Nd; $0 \leq x \leq 1$). *Journal of Materials Chemistry* **2014**, C2, 2212-2220.
(20) Kasahara, A.; Nukumizu, K.; Hitoki, G.; Takata, T.; Kondo, J. N.; Hara, M.; Kobayashi, H.; Domen, K. Photoreactions on $LaTiO_2N$ under visible light irradiation. *Journal of Physical Chemistry A* **2022**, 106, 6750-6753.
(21) Black, A.P.; Suzuki, H.; Higashi, M.; Frontera, C.; Ritter, C.; De, C.; Sundaresan, A.; Abe, R.; Fuertes, A. New rare earth hafnium oxynitride perovskites with photocatalytic activity in water oxidation and reduction. *Chemical Communications* **2018,** 54, 1525-1528.
(22) Wang, X.; Hisatomi, T.; Wang, Z.; Song, J.; Qu, J.; Takata, T.; Domen, K. Core–shell-structured $LaTaON_2$ transformed from $LaKNaTaO_5$ plates for enhanced photocatalytic H_2 evolution. *Angewandte Chemie International Edition* **2019**, 58, 10666-1070.
(23) Castets, A.; Fina, I.; Guarín, J.R.; Oró-Solé, J.; Frontera, C.; Ritter, C.; Fontcuberta, J.; Fuertes, A. High-temperature synthesis and dielectric properties of $LaTaON_2$. *Inorganic Chemistry* **2021**, 60, 6484−16491.
(24) Fauth, F.; Peral, I.; Popescu, C.; Knapp, M. The new material science powder diffraction beamline at ALBA synchrotron. *Powder Diffraction* **2013**, 28, S360−S370.
(25) Rodríguez-Carvajal, J. Recent advances in magnetic structure determination by neutron powder diffraction. *Physica B: Condensed Matter*, **1993**, 192, 55-69.
(26) Fuertes, A. Synthetic approaches in oxynitride chemistry. *Progress in Solid State Chemistry* **2018**, 51, 63-70.
(27) Kawashima, K; Hojamberdiev, M; Wagata, H; Yubuta, K; Vequizo, JJM; Yamakata A, et al. NH_3-assisted flux-mediated direct growth of $LaTiO_2N$ crystallites for visible light-induced water splitting. *Journal of Physical Chemistry C* **2015**, 119, 15896–904.
(28) Yang, M; Rodgers, J.A.; Middler, L.C.; Oró-Solé, J; Jorge, A.B,; Fuertes, A, Attfield, J.P. Direct solid state synthesis at high pressures of new mixed-metal oxynitrides: $RZrO_2N$ (R= Pr, Nd and Sm). *Inorganic Chemistry.* **2009**, 48, 11498–500.

(29) Chen, D.; Habu, D.; Masubuchi, Y.; Torii, S.; Kamiyama, T.; Kikkawa, S. Partial nitrogen loss in $SrTaO_2N$ and $LaTiO_2N$ oxynitride perovskites. *Solid State Sciences* **2016**, 54, 2−6.
(30) Cox, P. A. Transition Metal Oxides: An Introduction to Their Electronic Structure and Properties; Clarendon Press: Oxford, 1995.
(31) Liu, T.; Holzapfel, N.P.; Woodward, P.M. Understanding structural distortions in hybrid layered perovskites with the n = 1 Ruddlesden–Popper structure. *International Union of Crystallography* **2023**, 10, 385-396.
(32) Aleksandrov, K. S.; Beznosikov, B.V.; Misyul, S.V. Successive structure phase-transitions in crystals of K_2MgF_4-type structure. *physica status solidi* **1987**, 104, 529-543.
(33) Shimura, T.; Inaguma, Y.; Nakamura, T.; Itoh, M. Morii, Y. Structure and magnetic properties of $Sr_{2-x}A_xIrO_4$ (A= Ca, Ba). *Physical Review B* **1995**, 52, 9143-9146.
(34) Shannon, R. D. Revised effective ionic radii and systematic studies of interatomic distances in halides and chalcogenides. *Acta Crystallographica. A* **1976**, 32, 751−767.
(35) Diot, N.; Marchand, R.; Haines, J.; Léger, J. M.; Macaudière, P.; Hull, S. Crystal structure determination of the oxynitride Sr_2TaO_3N. *Journal of Solid State Chemistry* **1999**, 146, 390-393.
(36) Clarke, S; Hardstone, K.A.; Michie, C.W.; Rosseinsky, M.J. High-temperature synthesis and structures of perovskite and n = 1 Ruddlesden−Popper tantalum oxynitrides. Chemistry *of Materials* **2002**, 14, 2664-2669.
(37) Tobías, G.; Beltrán-Porter, D.; Lebedev, O.; Van Tendeloo, G.; Rodríguez-Carvajal, J.; Fuertes, A. Anion ordering and defect structure in Ruddlesden-Popper strontium niobium oxynitrides. *Inorganic Chemistry* **2004**, 43, 8010-8017.
(38) Pauling, L. The principles determining the structure of complex ionic crystals. *Journal of the American Chemical Sociey* **1929**, 51, 1010-1026.
(39) Fuertes, A. Prediction of Anion Distributions Using Pauling's Second Rule. *Inorganic Chem*istry **2006**, 45, 9640-9642.
(40) Lueken, H.; in "Course of lectures on magnetism of lanthanide ions under varying ligand and magnetic fields". *RWTH Aachen University* 2008.
(41) Kahn, M.L.; Sutter, J-P.; Golhen, S.; Guionneau, P.; Ouahab, L.; Kahn, O.; Chasseau, D. Systematic investigation of the nature of the

coupling between a Ln(III) Ion (Ln =Ce(III) to Dy(III)) and its aminoxyl radical ligands. Structural and magnetic characteristics of a series of {Ln(organic radical)$_2$} compounds and the related {Ln(Nitrone)$_2$} derivatives. *Journal of the American Chemical Society* **2000**, 122, 3413-3421.
(42) Chien, C-L; DeBenedetti, S.; Barros, F. D. S. Magnetic properties of $EuTiO_3$,, Eu_2TiO_4 and $Eu_3Ti_2O_7$. *Physical Review B* **1974**, 10, 3913-3922.
(43) Trócoli, R.; Frontera, C.; Oró-Solé, J.; Ritter, C.; Alemany, P.; Canadell, E.; Palacín, M.R.; Fontcuberta, J.; Fuertes, A. $MnTa_2N_4$: A ternary nitride spinel with a strong magnetic frustration. *Chemistry of Materials* **2022**, 34, 6098-6107.

Chapter V

Neodymium Europium Oxynitrido-Silicates of β-K_2SO_4 type: Structural, Magnetic and Red Luminescence Properties

Published in: *Journal of Solid State Chemistry*, **2022**, 316, 123571

Authors: Ashley P. Black,[§,1] Jhonatan R. Guarín,[§,1] Judith Oró-Solé,[§] Alejandro R. Goñi,[§,‡] , Carlos Frontera,[§] and Amparo Fuertes[§]*

[§]Institut de Ciència de Materials de Barcelona (ICMAB-CSIC), Campus UAB, 08193 Bellaterra, Spain

[‡]ICREA, Passeig Lluís Companys 23, 08010 Barcelona, Spain

*Author to whom correspondence should be addressed: amparo.fuertes@icmab.es

[1] These authors contributed equally to this work.

https://doi.org/10.1016/j.jssc.2022.123571

Keywords: oxynitridosilicates, β-K_2SO_4 type, ferromagnetism, red luminescence, Eu^{2+} luminescence β-K_2SO_4 type $NdEuSiO_3N$ and the

new oxynitridosilicate host $NdSrSiO_3N$ activated with Eu^{2+} show orange-red luminescence under excitation at 405 nm.

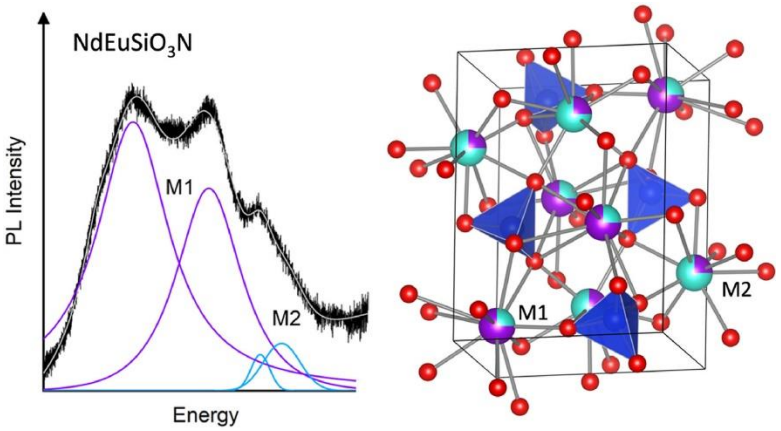

Abstract: Rare earth activated nitridosilicates have important applications as phosphor components in white light emitting diodes. (Oxy)nitridosilicates with β-K_2SO_4 structure doped with Eu^{2+} are luminescent materials with emission wavelengths ranging from green to red under excitation with blue-UV light. Here we report the synthesis of isostructural $NdEuSiO_3N$ and the new oxynitridosilicate $NdSrSiO_3N$ by solid state reaction between Nd_2O_3, NdN, Eu_2O_3 or SrO and Si_3N_4 under N_2/H_2 gas at temperatures of 1300 °C and 1500 °C respectively. These compounds are the limiting compositions of the solid solution $NdSr_{1-x}Eu_xO_3N$ crystallizing in the space group *Pmnb* with cell parameters a = 5.62293(1), b = 7.02285(1), c = 9.64784(2) Å for $NdEuSiO_3N$, and a = 5.63074(9), b = 7.01658(10), c = 9.65765(15) Å for $NdSrSiO_3N$. The $Nd^{3+}$and Eu^{2+} cations in $NdEuSiO_3N$ or Nd^{3+} and Sr^{2+} in $NdSrSiO_3N$ show partial order in the two available crystallographic sites of coordination numbers 10 (M1) and 9 (M2), with strongly preferred occupancy of the larger divalent cations Eu^{2+} (77%) and Sr^{2+} (78%) for the M1 site, whereas the M2 site is preferred by Nd^{3+}. Magnetic susceptibility measurements down to 2 K show that $NdEuSiO_3N$ is ferromagnetic with T_c = 3 K, in contrast to $NdSrSiO_3N$ that shows antiferromagnetic interactions at low temperatures. The band gaps of $NdEuSiO_3N$ and $NdSrSiO_3N$ determined from diffuse reflection spectroscopy are 2.37 and 3.72 eV respectively. $NdEuSiO_3N$ and the members of the solid solution $NdSr_{0.98}Eu_{0.02}SiO_3N$ and $NdSr_{0.5}Eu_{0.5}SiO_3N$ are orange-red light emitting luminescent materials, showing a broad emission band centered between 605 and 639 nm under excitation at 405 nm. These compounds are new phosphor materials with

emission wavelengths shifted to the red with respect to the isostructural oxysilicates, which is induced by the introduction of nitride.

5.1. Introduction

Oxynitridosilicates of rare earth and alkaline earth metals doped with Eu^{2+} or Ce^{3+} show broad emission bands when excited with UV-blue light. They show high thermal stability and colour tunability and are attractive as phosphor components in white light emitting diodes (LED's).[1,2] Compared to oxysilicates, the oxynitridosilicates show longer emission wavelengths as a consequence of several factors. The lower electronegativity of nitrogen increases the covalency of the bonds with the cations and the nephelauxetic effect, hence decreasing the energy of the d orbitals of the rare earth cations. Additionally, the higher charge and electronic polarizability of N^{3-} increases the crystal field splitting in these orbitals, resulting in a further decrease of the energies of $4f^{n-1}5d^1 \longrightarrow 4f^n$ transitions.[3,5]

The orthosilicate phosphor Sr_2SiO_4:Eu^{2+}shows a green emission with wavelength of 550 nm and high internal quantum efficiency.[6,9] The host compound Sr_2SiO_4 adopts a monoclinic structure (β phase) at room temperature with space group *P2₁/n*, that can be described as a distorted β-K_2SO_4 structure with two sites for the Sr atoms of coordination numbers 10 and 9 connected through $[SiO_4]^{4-}$ anions. At 85 °C it transforms into the orthorhombic α′ phase of β-K_2SO_4 type with *Pbnm* space group. In the α' phase the Sr atoms are placed at a mirror plane and are largely underbonded by the oxygen atoms.[10,11] In the more stable β phase the Sr atoms are shifted with respect to the mirror plane to improve their bonding, which induces the symmetry lowering to *P2₁/n*.

The concomitant substitution of Sr^{2+} by La^{3+} and O^{2-} by N^{3-} in β-Sr_2SiO_4 leads to the solid solution $Sr_{2-x}La_xSiO_{4-x}N_x$ [12] and induces a structural transition to the α', β-K_2SO_4 type phase for $x \geq 0.2$. The stabilization of this polymorph at room temperature is most likely a consequence of the increase in bond valence of the cations promoted by the introduction of the more charged anion N^{3-}. The doped compounds of these oxynitrides $Sr_{2-x}La_xSiO_{4-x}N_x$:$0.02Eu^{2+}$ show a red shift of the emission colours (λ_{exc} = 405 nm) with respect to Sr_2SiO_4:Eu^{2+}, from yellow for x = 0.2 (λ_{em} = 564 nm) to orange red (λ_{em} = 650 nm) for x = 1, the latter corresponding to the stoichiometric oxynitride $LaEuSiO_3N$.[13] A co-substitution at doping level in Sr_2SiO_4 of Sr^{2+} and O^{2-} by Lu^{3+} and N^{3-}, has been reported with a maximum Lu or N content of 0.005.[14] The resulting phosphors $Lu_xSr_{2-x}SiN_xO_{4-x}$:Eu^{2+} show the β-K_2SO_4 structure and the emission peaks are red shifted with respect to Sr_2SiO_4:Eu^{2+} up to a maximum wavelength of 595 nm. The β-K_2SO_4 type oxynitridophosphates Ca_2PO_3N [15] and Ba_2PO_3N [16] containing $[PO_3N]^{4-}$ anions have been investigated as hosts for luminescent materials. The Eu^{2+} doped compound exhibits luminescence in the green range of the visible spectrum with λ_{em} = 525 nm under excitation at 400 nm.

The compounds $LnEuSiO_3N$ (Ln = La, Nd, Sm) were first prepared in a sealed nickel tube through a solid state reaction between the rare earth oxides and Si_3N_4 by R.Marchand, who reported also their cell parameters and the X-ray powder diffraction patterns.[17] We have recently reported the synthesis and crystal structures of the isostructural alkaline earth derivatives $LaSrSiO_3N$ and $LaBaSiO_3N$, together with the luminescence properties and ferromagnetism of their europium doped

compounds and $LaEuSiO_3N$.[13] These oxynitridosilicates crystallize in the β-K_2SO_4 structure (Figure 1), where the cationic sites with coordination numbers 10 (site M1) and 9 (site M2) are occupied by both La^{3+}or the divalent (Eu^{2+}, Sr^{2+}, Ba^{2+}) cations. The two polyhedra are connected through $[SiO_3N]^{5-}$ anions with a strong preferred occupancy close to 80% of the larger alkaline earth or Eu^{2+} cations for the M1 site. The investigation of novel $LnMSiO_3N$ host compounds (M = alkaline earth metal; Ln = rare earth) and their corresponding Eu^{2+} doped derivatives, is relevant to study the effect of the rare earth on the luminescent properties and to find new phosphor materials. Here we report the synthesis under N_2/H_2 gas at 1350–1500 °C and the crystal structures of the new oxynitridosilicate host $NdSrSiO_3N$ and $NdEuSiO_3N$, which correspond to the end members of the solid solution $NdSr_{1-x}Eu_xSiO_3N$ with x = 0 and x = 1 respectively. These compounds show the β-K_2SO_4 structure where the M1 and M2 coordination sites are linked by $[SiO_3N]^{5-}$, with relative occupancies Nd:Eu and Nd:Sr of 0.23:0.77 and 0.22:0.78 respectively at site M1 and corresponding occupancies 0.77:0.23 and 0.78:0.22 at site M2. The europium compounds with x = 0.02, 0.5 and 1.0 show red-orange luminescence upon activation at 405 nm, and $NdEuSiO_3N$ is ferromagnetic below 3 K, in contrast to $NdSrSiO_3N$ which shows antiferromagnetic interactions between the Nd^{3+} cations at low temperature.

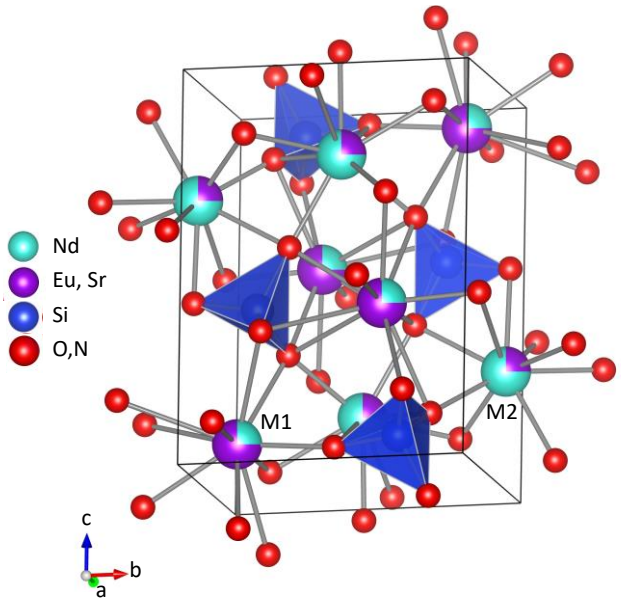

Figure 1. Crystal structures of Nd(Eu,Sr)SiO_3N compounds showing the 10 and 9- coordinated M1 and M2 sites respectively, connected by the [SiO_3N] tetrahedra.

5.2. Experimental

Polycrystalline samples of 250 mg of $NdSrSiO_3N$ were prepared by solid state reaction in N_2/H_2 (95%/5% V/V, Air liquide, 99.999%) between Nd_2O_3 (Aldrich, 99.99%), SrO and Si_3N_4 (α-phase, Alfa Aesar, 99.9%) in stoichiometric 0.5:1:1/3 ratio. $NdEuSiO_3N$ was prepared using the same gas, starting with Nd_2O_3, Si_3N_4 and Eu_2O_3 (Aldrich 99.99%). To minimize the proportion of oxidic impurities in $NdEuSiO_3N$ samples, we used either 7 mg of graphitic C (Alfa Aesar 99.9995%) or a mixture of Nd_2O_3 and NdN (Alfa Aesar 99.9%) as Nd source in the reactants (0.45 Nd_2O_3: 0.1 NdN). The samples $NdSr_{0.98}Eu_{0.02}SiO_3N$ and $NdSr_{0.5}Eu_{0.5}SiO_3N$ were prepared by the same method than $NdSrSiO_3N$,

starting with stoichiometric amounts of Nd_2O_3, SrO, Eu_2O_3 and Si_3N_4. Nd_2O_3 and Eu_2O_3 were previously treated at 950 °C under a dynamic vacuum of $5x10^{-2}$ mbar during 12 h. SrO was prepared by overnight decomposition of $SrCO_3$ (Alfa Aesar, 99.994%) at 1000 °C under dynamic vacuum of $5x10^{-2}$ mbar. Handling of the reactants was carried out in a Glovebox under recirculating argon atmosphere. The powders were thoroughly mixed in an agate mortar for 30 min, pressed into a pellet, placed in a molybdenum crucible and covered with a zirconium foil that was used as oxygen/water scavenger. The mixtures were fired during 3 h, at 1350 °C for $NdEuSiO_3N$ and at 1500 °C for $NdSrSiO_3N$, $NdSr_{0.98}Eu_{0.02}SiO_3N$ and $NdSr_{0.5}Eu_{0.5}SiO_3N$, with heating and cooling rates of 300 °C/h.

N contents were determined by combustion analysis in a Thermo Fisher Scientific instrument, heating the samples in oxygen up to 1060 °C and using MgO, WO_3 and Sn as additives and atropine as a reference standard. Thermogravimetric analysis in pure oxygen were performed to study the thermal oxidation stability of the samples, using a NETZSCH - STA 449 F1 Jupiter instrument. The samples were heated at 5 °C min^{-1} up to 1400 °C under O_2 flow rate of 70 cm^3 min^{-1}. Energy dispersive spectroscopy (EDS) analyses of cation contents were performed in a FEI Quanta 200 FEG scanning electron microscope equipped with an EDAX detector with an energy resolution of 132 eV.

X-ray powder diffraction data were collected on a Bruker D8 Advance A25 diffractometer in a Debye Scherrer configuration equipped with a Johansson monochromator, using Mo $K\alpha_1$ radiation source (λ = 0.7093

Å). High resolution synchrotron X-ray powder diffraction data were measured for a $NdEuSiO_3N$ sample using a capillary of 0.5 mm diameter, rotated during the data collection, in the angular range $3.0° \leq 2\theta \leq 50.0°$, at the MSPD (Materials Science And Powder Diffraction) beamline [18] of the ALBA Synchrotron (Cerdanyola del Vallès, Spain). Using a double Si (111) crystal monochromator, a short wavelength was selected and calibrated with Si NIST (λ = 0.635560 Å). Rietveld analysis was carried out using the program Fullprof.[19] Background refinement was performed by linear interpolation and the data were corrected for absorption.

Electron diffraction micrographs were obtained in a JEOL 1210 transmission electron microscope operating at 120 kV, equipped with a side-entry 60°/30° double tilt GATAN 646 specimen holder. The samples were prepared by deposition of the powder on a carbon film supported on a copper grid.

Diffuse reflectance spectra were registered at room temperature on a JASCO V-780 UV–visible/NIR spectrophotometer, with operational range of λ = 200–1200 nm. Photoluminescence (PL) spectra were measured at room temperature using the 405 nm line of a solid-state laser for excitation and collected using a LabRam HR800 spectrometer equipped with a charge-coupled device detector. PL spectra were corrected for the spectral response of the spectrometer by normalizing each spectrum employing the detector and grating characteristics. The incident light power density was about 1 W/cm^2.

Magnetic measurements were performed at fields of 50 Oe and 5 kOe between 2 and 300 K using a Quantum Design SQUID magnetometer. Magnetization-field loops were measured between −70 kOe and +70 kOe at 2 K.

5.3. Results and Discussion

Synthesis and Crystal Structure of $NdEuSiO_3N$ and $NdSrSiO_3N$

The synthesis of $NdSr_{1-x}Eu_xO_3N$ (x = 0, 0.02, 0.5, 1.0) was performed through a similar procedure than in our previous report on $LaMSiO_3N$ compounds (M = Sr, Ba, Eu)[13] under N_2/H_2 gas (95%/5% V/V), in contrast to the synthesis in sealed nickel tube reported for several $LnEuSiO_3N$ compounds (Ln = La, Nd, Sm).[17] The synthesis under a flowing gas is performed in an Al_2O_3 tube then allowing the use of higher temperatures, which are necessary to stabilize the neodymium strontium compounds. Whereas $NdEuSiO_3N$ was prepared at 1350 °C, the reaction of formation of $NdSrSiO_3N$ in these conditions was incomplete and it was necessary to raise the temperature up to 1500 °C. On the other hand, the use of H_2 in the gas mixture ensures the full reduction of europium to the divalent state, which is convenient for the ferromagnetic and luminescent properties induced by this cation. Samples with high crystallinity were obtained after short treatment times of typically 3 h at the maximum temperature. X-ray powder diffraction patterns for $NdEuSiO_3N$ and $NdSrSiO_3N$ are shown in Figures 2 and 3. The latter showed non-indexed peaks with low intensity at Q values of 1.98 and 2.31 $Å^{-1}$ that could not be assigned to any known phase in the

quaternary system. Nitrogen analyses gave values close to 1 atom per formula for all samples: 1.04 for $NdEuSiO_3N$, 0.96 for $NdSr_{0.5}Eu_{0.5}SiO_3N$ and 1.06 for $NdSrSiO_3N$, and the Nd/Eu and Nd/Sr ratios observed by EDS for 12 analyzed crystals of each sample were 0.94 for $NdEuSiO_3N$ and 0.97 for $NdSrSiO_3N$ respectively. For $NdSr_{0.5}Eu_{0.5}SiO_3N$ the analyzed ratios were Eu/Nd = 0.50 and Sr/Nd = 0.56. TGA experiments performed in O_2 up to 1400 °C show that $NdEuSiO_3N$ starts to decompose at 380 °C into the oxides, whereas the decomposition of $NdSrSiO_3N$ begins at 500 °C. The lower stability of the former compound is due to the presence of Eu^{2+} that oxidizes to Eu^{3+} at low temperatures.

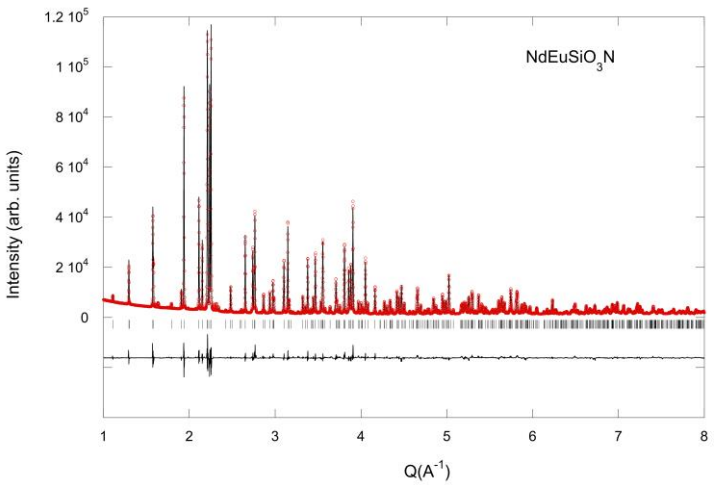

Figure 2. Rietveld fit to room temperature synchrotron X-ray diffraction pattern of $NdEuSiO_3N$ (λ = 0.63556 Å).

The reconstruction of the reciprocal lattice from electron diffraction patterns (Figure 4) showed the cell parameters *a* = 5.64, *b* =

7.02, *c* = 9.86 Å for $NdEuSiO_3N$ and *a* = 5.67, *b* = 7.05, *c* = 9.57 Å for $NdSrSiO_3N$, and the reflection conditions in both cases were: *h*0*l*, h + l =

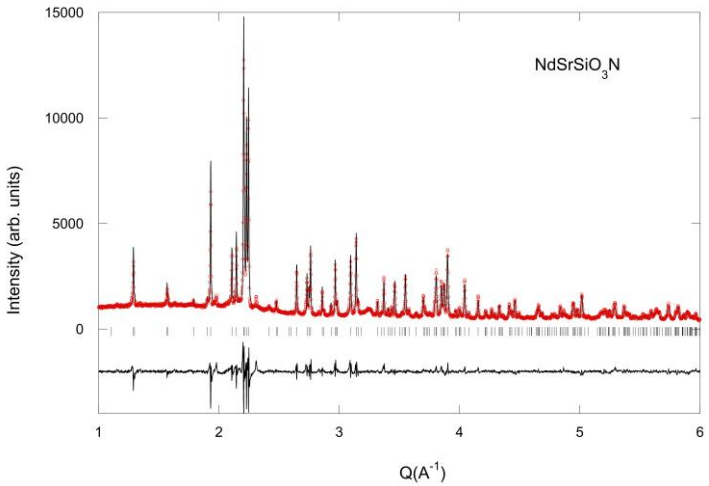

Figure 3. Rietveld fit to room temperature Mo $K\alpha_1$ X-ray diffraction pattern of $NdSrSiO_3N$ (λ = 0.7093 Å).

2n; *hk*0, k = 2n; *h*00, h = 2n; 0*k*0, k = 2n and 00*l*, l = 2n, which are compatible with the space group *Pmnb* (Nº 62) characteristic of the β-K_2SO_4 aristotype structure. An incommensurate superstructure along the *b* axis with wave vector q = 0.29*b*∗ is observed for $NdSrSiO_3N$ (Figure 4). The superstructure peaks are less intense in $NdEuSiO_3N$, that shows q = 0.27*b*∗, and in both compounds they are not detected in the X-ray diffraction patterns. Structural modulations along the *b* axis have been observed in compounds with β-K_2SO_4 type structures such as α′-Sr_2SiO_4,[20] $Ba_{2-x}Ca_xSiO_4$ and Ca_2SiO_4,[21] as well as in the oxynitrides $LaSrSiO_3N$ and $LaEuSiO_3N$.[13] The incommensurate superstructure in α' Sr_2SiO_4 has been found to be originated by a gradual

variation of metal-anion bond lengths that takes place to improve the bonding of Sr(1) atoms and leads to a tilting of the [SiO_4] tetrahedra.

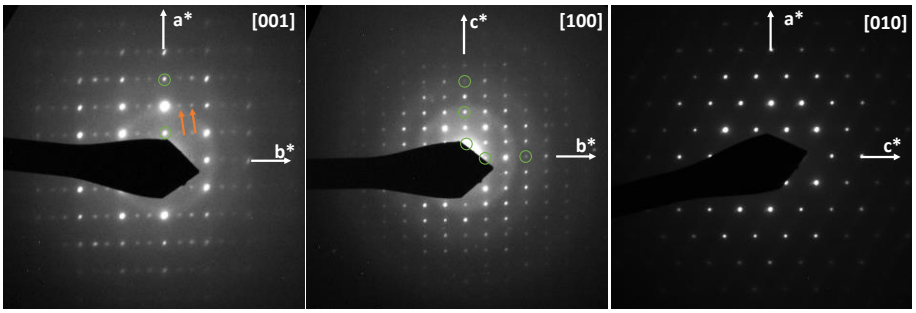

Figure 4. Electron diffraction patterns along the zone axes [001], [100] and [010] of $NdSrSiO_3N$. The structural modulation along $b*$ is visible in the [001] plane, where the superstructure reflections are indicated by arrows. Circles indicate multiple diffraction reflections.

The crystal structures of $NdEuSiO_3N$ and $NdSrSiO_3N$ have been determined by the Rietveld method from X-ray powder diffraction data using the space group *Pmnb* (Nº 62) and the coordinates of $LaEuSiO_3N$ [13] as initial structural model (Figures 2 and 3; Tables 1 and 2). The occupancies Nd:Eu and Nd:Sr at sites M1 and M2 were refined subjected to the ideal stoichiometry. On the other hand, as nitrogen and oxygen show small differences in the X-ray diffraction scattering lengths, their occupancies in the three anion sites X1, X2 and X3 were fixed to a statistical distribution with the constraint of the ideal stoichiometry. The refined cell parameters a = 5.62293(1), b = 7.02285(1), c = 9.64784(2) Å for $NdEuSiO_3N$ and a = 5.63074(9), b = 7.01658(10), c = 9.65765(15) Å for $NdSrSiO_3N$, are smaller than those of the analogous lanthanum compounds (a = 5.63246(14), b = 7.11675(18), c =

9.7998(2) Å for $LaEuSiO_3N$; *a* = 5.64362(14), *b* = 7.10719(17), *c* = 9.8062(2) Å for $LaSrSiO_3N$),[13] as expected from the differences in the ionic radii of La^{3+} and Nd^{3+}, 1.216 Å and 1.163 Å (CN=IX)[22] respectively. Despite the similar ionic radii of Eu^{2+} and Sr^{2+} (1.30 and 1.31 Å, respectively, for CN=IX) the cell is slightly contracted for the europium compound following the trend of the radii of the two cations (V = 380.984(1) $Å^3$ for $NdEuSiO_3N$ *vs* 381.560(10) $Å^3$ for $NdSrSiO_3N$). This tendency was also observed comparing $LaSrSiO_3N$ (V = 393.329(16) $Å^3$) with $LaEuSiO_3N$ (V = 392.825(17) $Å^3$).[13] The cell parameters of $NdSr_{0.5}Eu_{0.5}SiO_3N$, obtained by Rietveld refinement of powder X-ray diffraction data (λ Mo $K\alpha_1$) are intermediate between those for $NdEuSiO_3N$ and $NdSrSiO_3N$: *a* = 5.62381(6), *b* = 7.01999(7), c = 9.65588(11) Å, V = 381.206(7) $Å^3$. The cell volumes of the three compounds show a linear variation with x in agreement with the existence of the solid solution $NdSr_{1-x}Eu_xSiO_3N$. The two cationic positions of the β-K_2SO_4 structure with coordination numbers 10 (M1) and 9 (M2) are occupied by the trivalent Nd^{3+} and the divalent cations, either Eu^{2+} or Sr^{2+}, in a disordered manner, but with a preference of the smaller cation Nd^{3+} for the 9th coordinated site in a similar way to that observed for $LaSrSiO_3N$, $LaEuSiO_3N$ and $LaBaSiO_3N$.[13] The refined occupancy factors Nd1/Sr1 and Nd2/Sr2 positions in $NdSrSiO_3N$ are 0.216(2):0.784 and 0.784:0.216 respectively, similar to those obtained for $NdEuSiO_3N$, Nd1/Eu1 = 0.228(7):0.772 and Nd2/Eu2 = 0.772:0.228. These cation distributions are close to those found for $LaSrSiO_3N$ (La1/Sr1 = 0.242(3):0.758; La2/Sr2 = 0.758:0.242) and $LaEuSiO_3N$ (La1/Eu1 = 0.188(18):0.812; La2/Eu2 = 0.812:0.188) indicating that they

are not significantly affected by the smaller ionic radius of Nd^{3+} compared to La^{3+}. The average bond lengths were: M1-X = 2.841 Å for $NdEuSiO_3N$ and 2.830 Å for $NdSrSiO_3N$; M2-X = 2.640 Å for $NdEuSiO_3N$ and 2.701 Å for $NdSrSiO_3N$, which are similar, although slightly smaller than those observed in $LaEuSiO_3N$ (M1-X = 2.869 Å, M2-X = 2.685 Å) and $LaSrSiO_3N$ (M1-X = 2.868 Å, M2-X = 2.687 Å).

Table 1. Fractional atomic coordinates in space group *Pmnb*, cation occupancies and isotropic temperature factors for $NdEuSiO_3N$ from the refinement to synchrotron diffraction data at 300 K using λ = 0.63556 Å. Cell parameters: *a* = 5.62293(1), *b* = 7.02285(1), *c* = 9.64784(2) Å. R_{Bragg} = 5.47% and R_{wp} = 5.53%. [a].

atom	site	*x*	*y*	*z*	B(Å^2)	occ. factor
Nd1/ Eu1	4c	0.25	0.65666(8)	0.57824(6)	0.81(12)	0.228(7)/0.772
Nd2/ Eu2	4c	0.25	0.00725(8)	0.30120(5)	0.53(11)	0.772/0.228
Si	4c	0.25	0.2212(3)	0.5846(3)	0.24(4)	1
O1/N1	4c	0.25	0.9965 (10)	0.5619(7)	1.60(7)	0.75/0.25
O2/N2	4c	0.25	0.3301(11)	0.4282(8)	1.60	0.75/0.25
O3/N3	8d	0.0109(8)	0.2822(6)	0.6701(6)	1.60	0.75/0.25

bond	distance(Å)	bond	distance (Å)	bond	distance (Å)
M1-X1	2.392(7)	M2-X1	2.515(7)	Si-X1	1.593(7)
M1-X2	2.712(8)	M2-X1(x2)	3.107(3)	Si-X2	1.692 (8)
M1-X2 (x2)	2.8137(3)	M2-X2	2.577(8)	Si-X3 (x2)	1.635(5)
M1-X3 (x2)	3.084(4)	M2-X2	2.539(8)		
M1-X3 (x2)	2.912(5)	M2-X3 (x2)	2.522(4)		
M1-X3 (x2)	2.842(5)	M2-X3 (x2)	2.437(5)		

[a] Estimated standard deviations in parentheses are shown once for each independent variable. Nd/Eu occupation factors were refined subject to the ideal stoichiometry. Anion occupancy factors were fixed to the ideal stoichiometry considering total disorder of nitrogen and oxygen atoms.

Table 2. Fractional atomic coordinates in space group *Pmnb*, cation occupancies and isotropic temperature factors for $NdSrSiO_3N$ from the refinement to Mo $K\alpha_1$ diffraction data at 300 K (λ = 0.7093 Å). Cell parameters: a = 5.63074(9), b = 7.01658(10), c = 9.65765(15) Å. R_{Bragg} = 6.73% and R_{wp} = 7.90%.[a]

atom	site	*x*	*y*	*z*	B(Å^2)	occ. factor
Nd1/ Sr1	4c	0.25	0.6599(5)	0.5762(4)	1.29(5)	0.216(2)/0.784
Nd2/ Sr2	4c	0.25	0.0082(4)	0.3017(2)	1.29	0.784/0.216
Si	4c	0.25	0.2170(13)	0.5922(13)	1.2(2)	1
O1/N1	4c	0.25	0.004(3)	0.567(2)	1.9(3)	0.75/0.25
O2/N2	4c	0.25	0.346(4)	0.437(3)	1.9	0.75/0.25
O3/N3	8d	0.034(3)	0.277(2)	0.665(2)	1.9	0.75/0.25
bond	**distance (Å)**	**bond**	**distance (Å)**		**bond**	**distance (Å)**
M1-X1	2.42(2)	M2-X1	2.562(19)		Si-X1	1.51(2)
M1-X2	2.58(3)	M2-X1(x2)	3.089(8)		Si-X2	1.75(3)
M1-X2 (x2)	2.819(14)	M2-X2	2.71(3)		Si-X3 (x2)	1.466(18)
M1-X3 (x2)	3.071(15)	M2-X2	2.57(3)			
M1-X3 (x2)	2.899(18)	M2-X3 (x2)	2.582(15)			
M1-X3 (x2)	2.860(18)	M2-X3 (x2)	2.564(16)			

[a] Estimated standard deviations in parentheses are shown once for each independent variable. Nd/Sr occupation factors were refined subject to the ideal stoichiometry. Anion occupancy factors were fixed to the ideal stoichiometry considering total disorder of nitrogen and oxygen atoms.

Magnetic properties

Figures 5a and 5b show the evolution with temperature of magnetic susceptibility of $NdEuSiO_3N$ and $NdSrSiO_3N$ respectively. The susceptibility of $NdEuSiO_3N$ can be well fitted above 10 K by a Curie-Weiss law with a positive θ_{CW} = 2.7 K and an effective paramagnetic moment of μ_{eff} = 8.21 μ_B/f.u. In $NdSrSiO_3N$ the Curie-Weiss parameters obtained from the fit between 100 and 300 K are μ_{eff} = 3.97 μ_B/f.u. and θ_{CW} = −30.3 K, corresponding to localized $4f^3$ Nd^{3+} moments (ideal value 3.62 μ_B) with antiferromagnetic interactions. The paramagnetic moment of $NdEuSiO_3N$ has the contribution of both Nd^{3+} and Eu^{2+} ions.

Assuming that the contribution of Nd^{3+} ions is the same that observed for $NdSrSiO_3N$, the effective magnetic moment of Eu in $NdEuSiO_3N$ is μ_{eff}^{Eu} = 7.14 μ_B/f.u (ideal value of Eu^{2+} 7.94 μ_B/f.u). $NdEuSiO_3N$ orders ferromagnetically below T_c = 3 K whereas $NdSrSiO_3N$ does not show any magnetic transition down to 2 K.

The magnetization field curve obtained at 2 K for $NdEuSiO_3N$ (Figure 6) shows a typical behavior of soft ferromagnets at low temperatures and the saturated magnetization at μ_0H = 7 T is 7.75 μ_B/f.u. The Curie temperature of $NdEuSiO_3N$ is similar to those observed in other ferromagnetic europium silicates such as Eu_2SiO_4, that has been reported to show two different Curie temperatures for the monoclinic β form stable at room temperature, with T_c = 7 K [23] and the orthorhombic β-K_2SO_4 polymorph stable at low temperatures with T_c = 5 K,[24] and the layered oxynitridosilicate $EuSi_2O_2N_2$ which is ferromagnetic below 4.5 K.[25]

Higher Curie temperatures have been reported for nitridosilicates with condensed Si–N networks, such as chain-type Eu_2SiN_3 (13 K) [26] and the framework compound $Eu_2Si_5N_8$ (24 K).[27] The isostructural β-K_2SO_4 compound $LaEuSiO_3N$ shows the same T_c = 3 K that $NdEuSiO_3N$,[13] as expected from the close similarities in the environments of magnetic Eu^{2+} cations for the two orthosilicates.

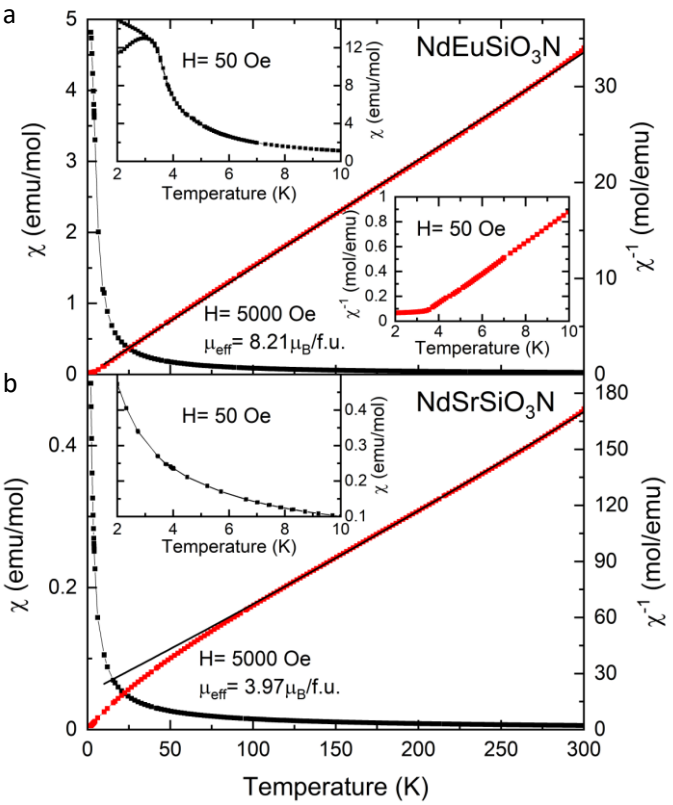

Figure 5. Dependence on temperature of (a) $NdEuSiO_3N$ and (b) $NdSrSiO_3N$ susceptibility (left axis) and its inverse (right axis) measured under a 5 KOe magnetic field. Inset: Magnetic susceptibility at low temperature and under 50 Oe of applied magnetic field.

Optical properties

The body color of $NdEuSiO_3N$ and $NdSr_{0.5}Eu_{0.5}SiO_3N$ is orange-brown, whereas $NdSrSiO_3N$ is pale blue and the $NdSr_{0.98}Eu_{0.02}SiO_3N$ sample showed a pale green color. The diffuse reflection spectrum of $NdSrSiO_3N$ sample shows sharp peaks corresponding to the transitions

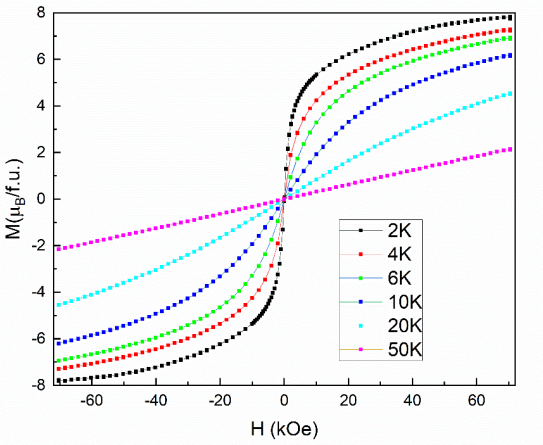

Figure 6. Magnetization curves of $NdEuSiO_3N$ measured between 2 K and 50 K up to 7 T.

between f states of Nd^{3+} as well as a drop in reflection that starts at ca. 400 nm (Figure 7a). The assigned levels of the observed f-f transitions,using the Dieke diagram and comparing the observed energies with those reported for other Nd^{3+} compounds are indicated on Figure 8 and Table 3.[28,30] The observed band gap in this compound, determined using the Kubelka-Munk function for a direct transition is 3.72 eV (Figure 7b). The linear regions in the Kubelka-Munk plots for an indirect band gap ($[F(R)h\nu]^{1/2}$ *vs* E) were less defined than for the direct band case. The compounds $NdEuSiO_3N$, $NdSr_{0.5}Eu_{0.5}O_3N$ and $NdSr_{0.98}Eu_{0.02}SiO_3N$ show Nd^{3+} f-f transitions at similar energies than those observed for $NdSrSiO_3N$ and smaller band gaps of 2.37 eV for the two samples with Eu contents x = 1 and 0.5 (Fig. 7a and b), and 3.64 eV for the sample with x = 0.02. The band gaps are similar to those observed

for the analogous lanthanum compounds, 3.83 and 2.35 eV for $LaSrSiO_3N$ and $LaEuSiO_3N$ respectively.[13]

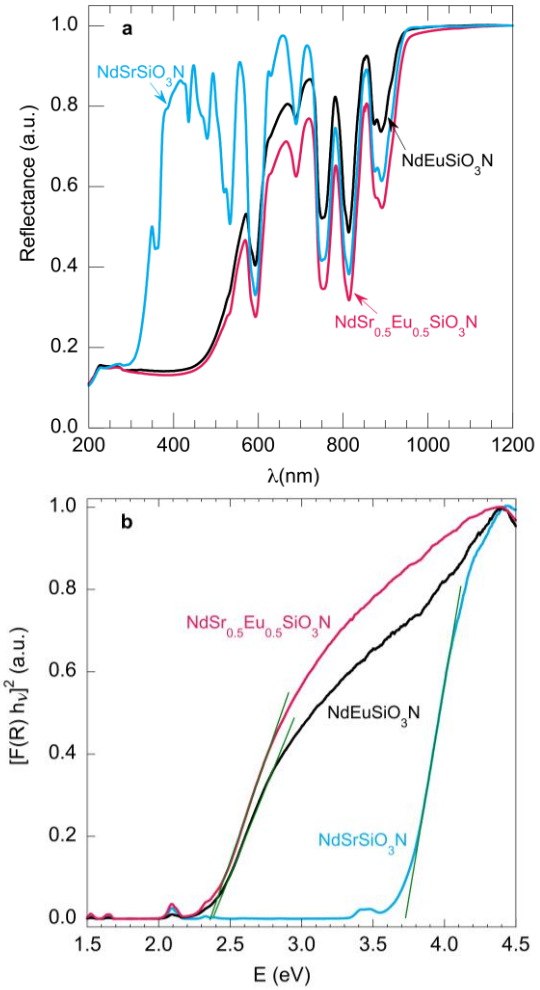

Figure. 7. (a) Diffuse reflection spectra and (b) Kubelka-Munk plots for a direct band gap transition in $NdEuSiO_3N$, $NdSr_{0.5}Eu_{0.5}SiO_3N$ and $NdSrSiO_3N$.

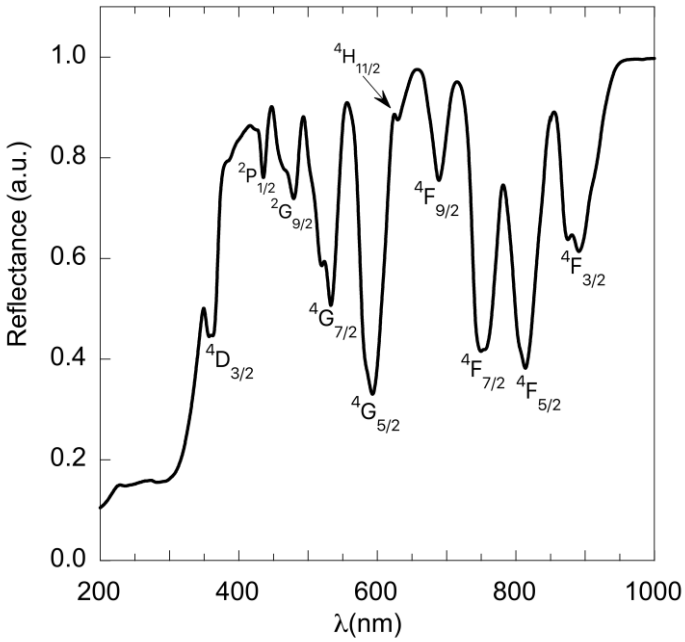

Figure. 8. Energy levels assignments for the transitions from the $^4I_{9/2}$ ground state of Nd^{3+} in $NdSrSiO_3N$.

Table 3. Energies of the transitions from the $^4I_{9/2}$ ground state of Nd^{3+} in $NdSrSiO_3N$.

Transition	E(cm^{-1})	Transition	E(cm^{-1})
$^4I_{9/2} \rightarrow {}^4F_{3/2}$	11278	$^4I_{9/2} \rightarrow {}^4G_{9/2}$	18929
$^4I_{9/2} \rightarrow {}^4F_{5/2}$	12330	$^4I_{9/2} \rightarrow {}^2G_{9/2}$	21128
$^4I_{9/2} \rightarrow {}^4F_{7/2}$	13303	$^4I_{9/2} \rightarrow {}^2P_{1/2}$	22957
$^4I_{9/2} \rightarrow {}^4F_{9/2}$	14493	$^4I_{9/2} \rightarrow ({}^2P, {}^2D)_{3/2}$	25900
$^4I_{9/2} \rightarrow {}^2H_{11/2}$	15845	$^4I_{9/2} \rightarrow {}^4D_{3/2}$	27778
$^4I_{9/2} \rightarrow {}^4G_{5/2}$	16855		

The emission spectra upon excitation at 405 nm of $NdSr_{1-x}Eu_xSiO_3N$ samples with x = 0.02, 0.5 a 1.0 (Figure 9) consist of a broad band centered between 1.94 eV (639 nm) for x = 1.0 and 2.05 eV (605 nm) for x = 0.02 with three main components of different relative intensities in the three compounds, at wavelengths of 675, 610 and 570 nm. The best

fits of the deconvolution of the spectra are obtained with an additional component centered at 551 nm. The number of components is the same that in the emission spectra obtained upon excitation at 405 nm of the isostructural, β-K_2SO_4 oxynitrides, $LaSr_{1-x}Eu_xSiO_3N$, $LaBa_{1-x}Eu_xSiO_3N$ and $Sr_{2-x}La_xSiO_{3+x}N_x$ that we reported previously.[12,13] As in these oxynitrides and in Sr_2SiO_4:Eu^{2+},[7] the two components at lower energy (black, dot-dashed curves) of $NdSr_{1-x}Eu_xSiO_3N$ compounds can be assigned to the M1 site that Eu^{2+} occupies preferentially in $NdEuSiO_3N$ (or together with Sr^{2+} in the x = 0.02 and 0.5 compounds).

The increase of the relative intensity shown by these bands as the europium concentration increases (Figure 9) is consistent with this assignment. The two components at higher energy (black, solid curves), are assigned to the 9-fold coordinated M2 site occupied by 75% Nd^{3+} and 25% of Sr^{+2}(Eu^{+2}). As in previously reported isostructural lanthanum compounds, the two emission wavelengths observed for each site are a result of the mixed occupation by cations of different charges, which lead to different environments in the crystal field of the activator. The position of the lower energy band of $NdEuSiO_3N$ (675 nm) is shifted to the blue with respect to that found for $LaEuSiO_3N$ (705 nm). The position of the bands observed for $LaSrSiO_3N$: Eu^{2+} and $LaBaSiO_3N$:Eu^{2+} were found to be similar, hence they are not affected by the differences in bond distances between the two hosts that are a consequence of the smaller ionic radius of Sr^{2+} compared to Ba^{2+}.[13]

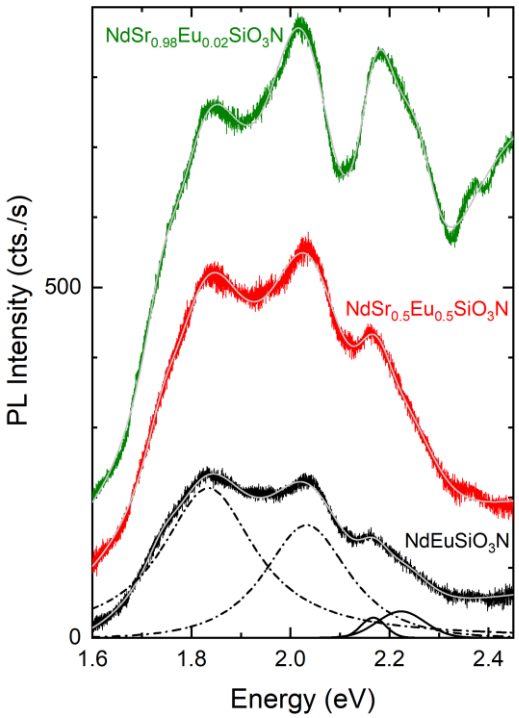

Figure. 9. Emission spectra of $NdSr_{0.98}Eu_{0.02}SiO_3N$, $NdSr_{0.5}Eu_{0.5}SiO_3N$ and $NdEuSiO_3N$ samples.

The origin of the blue shift of the emission band in the neodymium compounds with respect to the lanthanum compounds is not clear and deserves further attention. Future studies on these and other $LnMSiO_3N:Eu^{2+}$ derivatives (Ln = Lanthanide; M = alkaline earth cation) are planned to provide more clues for the understanding of the electronic structure and luminescence properties of this family of oxynitrides.

5.4. Conclusions

In summary, these results show a new synthetic approach under N_2/H_2 of the oxynitridosilicate $NdEuSiO_3N$ and the new compound $NdSrSiO_3N$ that crystallize in the β-K_2SO_4 structure type. The study of magnetic

properties of these compounds shows that the Eu^{2+} cations are ferromagnetically coupled with a T_c comparable to analogous europium silicates, whereas in $NdSrSiO_3N$ the Nd^{3+} cations show antiferromagnetic interactions at low temperatures. The study of the optical properties demonstrates the potential of $NdSrSiO_3N$ as host for luminescent materials analogous to the phosphors $M_2SiO_4:Eu^{2+}$ (M = Ca, Ba, Sr) but with longer emission wavelengths induced by the lower electronegativity of nitride anion compared to oxide. The europium samples in the solid solution $NdSr_{1-x}Eu_xSiO_3N$ with x = 0.02, 0.5 and 1.0 show a broad emission band upon activation at 405 nm, centered between 605 and 639 nm with several components assigned to the occupancy by Eu^{2+} of two different sites in the structure, with the band of longer wavelength showing maximum intensity at 670 nm (orange red) for $NdEuSiO_3N$. Further increase of emission color range in this family of compounds would be expected by substitution in $NdSrSiO_3N$ of Nd^{3+} by Ce^{3+}, that should produce luminescent materials with broad emission bands, or by doping with Eu^{2+} or Ce^{3+} other unexplored $LnSrSiO_3N$ hosts with β-K_2SO_4 structure.

CRediT authorship contribution statement

Ashley P. Black: Investigation. **Jhonatan R. Guarín:** Investigación. **Judith Oró-Solé:** Investigation, Formal analysis. **Alejandro R. Goñi:** Investigation, Formal analysis. **Carlos Frontera:** Investigation, Formal analysis. **Amparo Fuertes:** Conceptualization, Supervision, Writing – original draft.

Declaration of competing interest

The authors declare that they have no known competing financial interests or personal relationships that could have appeared to influence the work reported in this paper.

Acknowledgements

This work was supported by the Ministerio de Ciencia e Innovación, Spain (PID2020-113805 GB-I00 and CEX2019-000917-S), and it has been developed under the PhD program in Materials Science of the UAB. We thank Alba for beam time provision and Dr. François Fauth for assistance in data collection at Alba. We acknowledge assistance from ICMAB-CSIC Scientific & Technological Services: X-Ray Diffraction (Mr. Joan Esquius), Thermal Analysis (Ms. Roberta Ceravola), Spectroscopic Techniques (Dr. Vega Lloveras) and Low Temperatures and Magnetometry (Dr. Bernat Bozzo). JRG acknowledges the AEI predoctoral fellowship PRE2018-085204.

Data availability

The data that has been used is confidential.

5.5 References

(1) Zeuner, M.; Pagano, S.; Schnick, W. Nitridosilicates and oxonitridosilicates: from ceramic materials to structural and functional diversity. *Angewandte Chemie International Edition* **2011**, 50, 7754-7775.

(2) Wang, L.; Xie, R. J.; Suehiro, T.; Takeda, T.; Hirosaki, N. Down-conversion nitride materials for solid state lighting: Recent advances and perspectives. *Chemical Reviews* **2018**, 118, 1951-2009.
(3) Dorenbos, P. Energy of the first $4f^7 \rightarrow 4f^6 5d$ transition of Eu^{2+} in inorganic compounds. *Journal of Luminescence* **2003**, 104, 239-260.
(4) Fuertes, A. Metal oxynitrides as emerging materials with photocatalytic and electronic properties. *Materials Horizons* **2015**, 2, 453-461.
(5) McKittrick, J.; Shea-Rohwer, L. E. Review: Down conversion materials for solid state lighting. *Journal of the American Ceramic Society* **2014**, 97, 1327-1352.
(6) Barry, T. L. Fluorescence of Eu^{2+}-activated phases in binary alkaline earth orthosilicate systems. *Journal of The Electrochemical Society* **1968**, 115, 1181-1184.
(7) Poort, S. H. M.; Janssen, W.; Blasse, G. Optical properties of Eu^{2+}-activated orthosilicates and orthophosphates. *Journal of Alloys and Compounds* **1997**, 260, 93-97.
(8) Park, J. K.; Lim, M. A.; Kim, C. H.; Park, H. D.; Park, J. T.; Choi, S. Y. White light-emitting diodes of GaN-based Sr_2SiO_4:Eu and the luminescent properties. *Applied Physics Letters* **2003**, 82, 683-685.
(9) Denault, K.; Brgoch, J.; Gaultois, M.; Mikhailovsky, A.; Petry, R.; Winkler, H.; DenBaars, S.; Seshadri, R. Consequences of optimal bond valence on structural rigidity and improved luminescence properties in $Sr_xBa_{2-x}SiO_4$:Eu^{2+} orthosilicate phosphors. *Chemistry of Materials* **2014**, 26, 2275-2282.
(10) Catti, M.; Gazzoni, G.; Ivaldi, G. The β ↔ α' Phase transition of Sr_2SiO_4. I. Order–disorder in the structure of the α' Form at 383 K. *Acta, Crystallographica Section C: Structural Chemistry* **1983**, 39, 29-34.
(11) Catti, M.; Gazzoni, G.; Ivaldi, G.; Zanini, G. Structures of twinned β-Sr_2SiO_4 and of α'-$Sr_{1.9}Ba_{0.1}SiO_4$. *Acta Crytallographica* **1983**, B39, 674-679.
(12) Black, A. P.; Denault, K. A.; Frontera, C.; Seshadri, R.; Goñi, A. R.; Fuertes, A. Emission colour tuning through Coupled N/La introduction in Sr_2SiO_4:Eu^{2+}. *Journal of Materials Chemistry* C **2015**, 3, 11471-11477.
(13) Black, A. P.; Denault, K. A.; Oro-Sole, J.; Goni, A. R.; Fuertes, A. Red luminescence and ferromagnetism in europium oxynitridosilicates with a β-K_2SO_4 structure. *Chemical Communications* **2015**, 51, 2166-2169.

(14) Xia, Z. Miaom, S.; Molokeev, M. S.; Chen, M.; Liu, Q. Structure and luminescence properties of Eu^{2+} doped $Lu_xSr_{2-x}SiN_xO_{4-x}$ phosphors evolved from chemical unit cosubstitution. *Journal of Materials Chemistry C* **2016**, 4, 1336-1344.
(15) Marchuk, A.; Schultz, P.; Hoch, C.; Oeckler, O.; Schnick, W. M_2PO_3N (M=Ca, Sr): Ortho-oxonitridophosphates with β-K_2SO_4 structure type. *Inorganic Chemistry* **2016**, 55, 975-982.
(16) Wendl, S.; Mallmann, M.; Strobel, P.; Schmidt, P. J.; Schnick, W. Ammonothermal synthesis of Ba_2PO_3N– an oxonitridophosphate with non-condensed PO_3N tetrahedra. *European Journal of Inorganic Chemistry* **2020**, 10, 841–846.
(17) Marchand, R. Oxynitrures à structure β-K_2SO_4. Les composés $LnEuSiO_3N$ (Ln= La, Nd, Sm). *Comptes Rendus Hebdomadaires des Seances de l' Academie des Sciences Ser. C* **1976**, 283, 281-283.
(18) Fauth, F.; Peral, I.; Popescu, C.; Knapp, M. The new material science powder diffraction beamline at ALBA synchrotron. *Powder Diffraction* **2013**, 28, S360-S370.
(19) Rodríguez-Carvajal, J. Recent advances in magnetic structure determination by neutron powder diffraction. *Physica B: Condensed Matter* **1993**, 192, 55-69.
(20) Stenberg, L.; Sellar, J. R.; Hyde, B. G. Incommensurately modulated α′-Sr_2SiO_4. *Nature* **1986**, 320, 428-429.
(21) Withers, R. L.; Thompson, J. G.; Hyde, B. G. Modulated phases in the Ba_2SiO_4-Ca_2SiO_4 system of A_2BX_4, K_2SO_4-related structures. *Crystallography reviews* **1989**, 2, 27-61.
(22) Shannon, R. D. Revised effective ionic radii and systematic studies of interatomic distances in halides and chalcogenides. *Acta Crystallographica Section A* **1976**, 32, 751-767.
(23) Verreault, R. Crystallographic, Optical and magnetic properties of Eu_2SiO_4. *Journal of Physics: Condensed Matter* 1971, **14**, 37-54.
(24) Shafer, M. W.; McGuire, T. R.; Suits, J. C. Europium orthosilicate, a new transparent ferromagnet. *Physical Review Letters* **1963**, 11, 251-252.
(25) Stadler, F.; Oeckler, O.; Höppe, H. A.; Möller, M. H.; Pöttgen, R.; Mosel, B. D.; Schmidt, P.; Duppel, V.; Simon, A.; Schnick, W. Crystal structure, physical properties and HRTEM investigation of the new oxonitridosilicate $EuSi_2O_2N_2$. *Chemistry – A European Journal* **2006**, 12, 6984-6990.
(26) Zeuner, M.; Pagano, S.; Matthes, P.; Bichler, D.; Johrendt, D.; Harmening, T.; Pöttgen, R.; Schnick, W. Mixed valence europium

nitridosilicate Eu_2SiN_3. *Journal of the American Chemical Society* **2009**, 131, 11242–11248.
(27) Höppe, H.; Trill, H.; Mosel, B. D.; Eckert, H.; Kotzyba, G.; Pöttgen, R.; Schnick, W. Hyperphine interactions in the 13 K ferromagnet $Eu_2Si_5N_8$. *Journal of Physics and Chemistry of Solids* **2002**, 63, 853-859.
(28) Dieke, G. H. Spectra and energy levels of rare earth ions in crystals. *interscience, New York*, 1968.
(29) Carnall, W. T.; Fields, P. R.; Rajnak, K. Electronic energy levels in the trivalent lanthanide aquo Ions. I. Pr^{3+}, Nd^{3+}, Pm^{3+}, Sm^{3+}, Dy^{3+}, Ho^{3+}, Er^{3+}, and Tm^{3+}. *Journal of Chemical Physics* **1968**, 49, 4424-4442.
(30) Campvell, J. H.; Suratwala, T. I. Nd-doped phosphate glasses for high-energy/high-peak-power lasers. *Journal of Non-Crystalline Solids* **2000**, 263-264, 318-341.

VI. Discussion

In this work we have developed a synthetic approach of new perovskite oxynitrides at temperatures between 1200 and 1700 ^{o}C in N_2 or N_2/H_2 (95%/5% V/V) atmospheres, controlling the anion content by the starting stoichiometric ratios of metal nitrides, oxides and oxynitride reactants. New oxynitridosilicates of rare earth and alkaline earth cations have been also prepared, as host structures to produce luminescent materials.

The investigated oxynitrides with perovskite-type structures are formed by rare earth cations in the A positions and tantalum in the B sites. They exhibit different crystal symmetries according to the differences in size of the A and B cations and the oxidation state of the cations that are tuned by the stoichiometric ratio of oxygen and nitrogen. In the first part of Chapter 3, the synthesis, structural study and dielectric properties of $LaTaON_2$ are reported. In the second part of this chapter, the synthesis and study of the simple perovskite $EuTaO_{2.37}N_{0.63}$ and the new triple perovskite $Eu_3Ta_3O_{3.66}N_{5.34}$ are discussed. In Chapter 4, we discuss the synthesis and characterization of new oxynitrides with Ruddlesden-Popper $R_2TaO_{4-x}N_x$ (R = La, Ce, Eu, and Nd) structures. Finally, the synthesis and applications of oxynitride-type silicates $NdSr_{1-x}Eu_xO_3N$ are discussed on Chapter 5.

The syntheses of these oxynitrides are challenging because of several reasons. The lanthanide nitrides that are used as reactants are hygroscopic and decompose in ambient air with NH_3 evolution, and the prepared oxynitrides easily decompose into oxides at high temperatures in presence of small amounts of oxygen or water. For this reason, the handling of the reactants and the samples have to be performed in a glove

box under recirculating Ar, the transfer of the samples to the reaction tube has to be done using Schlenk flasks, and oxygen and water scavengers such as Zr foil should be placed around the sample. High purity 99.9999 % gases are used, with concentration of water and oxygen below 0.5 and 0.1 ppm respectively, and the system should be evacuated to 10^{-3} torr and purged several times before starting the heating. The main advantage of the synthetic approach is the possibility of optimization of the O/N ratio in the starting mixture of oxides, oxynitrides and nitrides, while keeping the cationic stoichiometry, up to the obtention of a single phase sample.

The perovskite $LaTaON_2$ had been previously prepared by ammonolysis of $LaTaO_4$, [1] or of mixtures of La_2O_3 and Ta_2O_5 (in presence of mineralizers),[2, 3] or by ammonothermal synthesis starting from La, Ta, and $NaNH_2$[4] or NaN_3[5], at temperatures up to 950 ^oC. In this work, we report a new synthetic method at 1500 °C in N_2 atmosphere that produces highly crystalline $LaTaON_2$ after a short treatment time of only three hours, starting either from LaN and TaON or by a mixture of La_2O_3, LaN, and Ta_3N_5. We determined that nitrogen is lost during the synthesis, resulting in a final product $LaTaO_{1+x}N_{2-x}$ with x values up to 0.35 atoms per formula, which involves the concomitant reduction of part of Ta^{5+} to Ta^{4+} for charge compensation. In the second reaction a stoichiometric $LaTaON_2$ (Ta^{5+}) compound was obtained by using an excess of nitrogen modifying the molar ratio between La_2O_3 and LaN. Electron diffraction indicated that this compound shows a distorted monoclinic structure with space group *I2/m*. Refinement of synchrotron X-ray powder diffraction led the cell parameters a = 4.71458(7), b = 8.05987(10), c = 5.74772(6)

Å, and β = 89.982(3)º. Refinement of neutron diffraction data revealed that the order of oxygen and nitrogen differs from that observed when this compound is synthesized by other methods. The anions are located in three different sites, with oxygen and nitrogen present in all of them, and nitrogen occupies preferentially two positions with populations of 77% and 88%. The new high-temperature synthesis method produced highly sintered samples as confirmed by scanning electron microscopy, in contrast with poorly sintered samples prepared by ammonolysis. Electrical measurements showed that the samples had a dielectric permittivity of 200, which is similar to that reported for perovskite oxynitrides with one nitrogen for formula such as Sr_2TaO_2N or $BaTaO_2N$. $LaTaON_2$ is brown colored and shows a band-gap of 1.9 eV, which is very close to the value obtained in samples produced by ammonolysis.

In the second part of Chapter 3, the synthesis of pseudocubic $EuTaO_{2.37}N_{0.63}$, and the new triple perovskite $Eu_3Ta_3O_{3.66}N_{5.34}$ are discussed. In previous reports $EuTaO_2N$ had been prepared by ammonolysis of $EuTaO_4$ at a temperature of 950°C.[1, 6] In this work, we used two different reactions at 1200 ^oC starting either with Eu_2O_3 and TaON, or with Eu_2O_3, EuN and Ta_3N_5, performed in N_2/H_2 (95%75% V/V) and N_2 respectively. The syntheses at temperatures above 1200 ^oC led to the formation of TaN, while lower temperatures prevented the completion of the reaction. In both cases the nitrogen content of the final sample is lower than in the initial mixture, involving the reduction of both cations: Eu^{3+} to Eu^{2+} and Ta^{5+} to Ta^{4+}. In the synthesis from Eu_2O_3 and TaON the, analyzed stoichiometry of the product was

$EuTaO_{2.37}N_{0.63}$, indicating 100 % of reduction of Eu^{3+} to Eu^{2+} and 37 % of reduction of Ta^{5+} to Ta^{4+} ($Eu^{2+}(Ta^{4+}_{0.37}Ta^{5+}_{0.63})O_{2.37}N_{0.63}$). The proportion of 100 % of Eu^{2+} in this sample was further confirmed by magnetic measurements. The large reduction of the cations in this case resulted from the presence of H_2 in the gas. The highly nitrided new perovskite $Eu_3Ta_3O_{3.66}N_{5.34}$ was prepared using the reaction:

$$(3\text{-}y)/2\ Eu_2O_3 + y\ EuN + Ta_3N_5 \longrightarrow 3\ EuTaO_{3-x}N_x$$

under N_2. As in previous reactions we also observed a nitrogen loss with respect to the initial N/O ratio, and an excess of nitrogen was optimized by changing the ratio Eu_2O_3/EuN up to obtaining a single phase sample. Electron diffraction revealed that $Eu^{2+}(Ta^{4+}_{0.37}Ta^{5+}_{0.63})O_{2.37}N_{0.63}$ is a simple cubic perovskite crystallizing in the *Pm-3m* space group with a = 4.02043(1) Å, as refined from synchrotron X-ray powder diffraction data. In contrast, $Eu_3Ta_3O_{3.66}N_{5.34,}$ which is formally mixed valence $Eu^{3+}_{2.34}Eu^{2+}_{0.66}Ta_3O_{3.66}N_{5.34,}$ is the first example of a triple perovskite oxynitride and crystallizes in the space group *P4/mmm* with cell parameters a = 3.99610(2) Å and c = 11.96238(9) Å. The tripling of the c axis is a consequence of the order of Eu^{2+} and Eu^{3+}, which have different occupancies at two sites of the tetragonal structure. The new perovskite was studied by neutron powder diffraction and scanning transmission electron microscopy (STEM) that confirmed the structural model refined from synchrotron X-ray powder diffraction. Both $EuTaO_{2.37}N_{0.63}$ and $Eu_3Ta_3O_{3.66}N_{5.34}$ are ferromagnetic with Curie temperatures of 7 K and 3 K, respectively.

We have also obtained new oxynitride perovskites that are the first examples of rare earth transition metal oxynitrides with n=1 Ruddlesden-Popper structure, and show different anion stoichiometries, crystal structures and magnetic properties. $R_2TaO_{4-x}N_x$ with R = La, Ce, Nd, and Eu were prepared using the following reactions at high temperature under N_2:

(1) (3-y) R_2O_3 + 2y RN + Ta_3N_5 ⟶ 3 $R_2TaO_{4-x}N_x$ for R= La, Nd and Eu

(2) 2 RN + 1/8 Ta_3N_5 + 5/8 TaON ⟶ $R_2TaO_{4-x}N_x$ for R=Ce.

at temperatures between 1200 ^oC (for R=Eu) to 1700 ^oC (for R=La), optimized in each case to minimize the presence of aside phases. As in the other syntheses performed in this thesis, the nitrogen content in the initial mixture was adjusted by varying the proportion of oxides and nitrides up to obtaining the targeted compound. In all cases the analyzed stoichiometries indicated a nitrogen deficiency with respect to that corresponding to the cations in maximum oxidation states R^{3+} and Ta^{5+}, R_2TaON_3: 2.69(3), 2.81(3), 2.54(3) and 1.20(3) atoms per formula for R=La, Ce, Nd and Eu respectively. Electron diffraction showed that the compounds of La, Ce and Nd crystallize in the *Pccn* space group with cell parameters a = 5.72949(2) Å, b = 5.73055(5) Å, and c = 12.77917(6) Å for $La_2TaO_{1.31}N_{2.69}$; a = 5.70500(5) Å, b = 5.71182(4) Å, and c = 12.61280(7) Å for $Ce_2TaO_{1.19}N_{2.81}$; and a = 5.70466(3) Å, b = 5.70476(5) Å, and c = 12.32365(5) Å for $Nd_2TaO_{1.46}N_{2.54}$, as refined from synchrotron X-ray powder diffraction data. $Eu_2TaO_{2.80}N_{1.20}$ showed a lower nitrogen content and a tetragonal structure with the *$I4_1/acd$* space

group. For $Ce_2TaO_{1.19}N_{2.81}$, neutron diffraction measurements revealed anion order with c.a. 100 % of occupancy of nitrogen at the equatorial sites of the Ta octahedron and 50% of each anion at the axial sites. The compounds $Ce_2TaO_{1.19}N_{2.81}$ and $Eu_2TaO_{2.80}N_{1.20}$ exhibit magnetic order at temperatures below 4 K and 8 K respectively, whereas the Nd compound remains paramagnetic down to 2 K.

The oxynitride-type silicates $NdSr_{1-x}Eu_xO_3N$ ($0 \leq x \leq 1$) have been synthesized at temperatures ranging between 1500 and 1350 °C under N_2/H_2 gas, starting with Nd_2O_3, SrO, EuN and Si_3N_4. These compounds have a β-K_2SO_4 type structure with space group *Pmnb*. Rietveld refinement of X-ray diffraction data lead the cell parameters a = 5.62293(1) Å, b = 7.02285(1) Å, and c = 9.64784(2) Å for $NdEuSiO_3N$ phase, and a = 5.63074(9) Å, b = 7.01658(10) Å, and c = 9.65765(15) Å for $NdSrSiO_3N$. The M1 position of the β-K_2SO_4 structure is predominantly occupied by 80% of europium or strontium, and 20% by neodymium, while the M2 position is mainly occupied by 80% of neodymium and 20% by the other cations. $NdEuSiO_3N$ exhibits ferromagnetism at temperatures below 3 K, while $NdSrSiO_3N$ shows antiferromagnetic interactions at low temperatures. The europium-containing materials $NdEuSiO_3N$, $NdSr_{0.5}Eu_{0.5}SiO_3N$, and $NdSr_{0.98}Eu_{0.02}SiO_3N$ are orange-brown colored, while $NdSrSiO_3N$ is pale blue. The determined band gaps from diffuse reflection spectroscopy are 2.37 eV for $NdEuSiO_3N$ and 3.72 eV for $NdSrSiO_3N$. Under excitation at 405 nm, the europium compounds show luminescence with broad emission bands centered in the range from 570 to 675 nm.

To summarize, the principal contribution of this thesis is the development of synthetic approaches for the preparation of new oxynitride materials containing rare earth metals with diverse applications. The main novelty in the synthesis is the control of the nitrogen stoichiometry by varying the initial N/O ratio, which provides a great flexibility for the obtention of new compositions with controlled degree of nitriding and highly crystalline samples. The method is simple and advantageous, and consists in heating mixtures of binary oxides and nitrides up to high temperatures under non-toxic N_2 or N_2/H_2 gases, using very short reaction times of typically three hours. The rare earth nitride reactants provide an important source of nitrogen that is crucial in the syntheses under N_2, as this gas is not as nitriding as NH_3 used in the standard ammonolysis reactions reported in previous works by different groups. The new synthetic approach has led to the discovery of several perovskite-related compounds that, in addition to the investigated electrical and magnetic properties, show potential interest in other fields, such as visible light photocatalysis for different reactions. The new oxynitridosilicates, prepared by a similar method are interesting luminescent materials; substitution of Nd^{3+}in the same hosts by other cations such as Ce^{3+} may increase the emission color range providing a way to explore new phosphors.

References

(1) Marchand, R.; Pors, F.; Laurent, Y. Nouvelles perovskites oxynitrures de stoechiometrie ABO_2N (A= lanthanide, B= Ti) et $ABON_2$ (A= lanthanide, B= Ta ou Nb). In *Annales de Chimie (Paris. 1914)*, 1991; Vol. 16, pp 553-560.

(2) Jansen, M.; Letschert, H.-P. Inorganic yellow-red pigments without toxic metals. *Nature* **2000**, *404* (6781), 980-982.
(3) Porter, S. H.; Huang, Z.; Woodward, P. M. Study of anion order/disorder in $RTaN_2O$ (R= La, Ce, Pr) perovskite nitride oxides. *Crystal Growth & Design* **2014**, *14* (1), 117-125.
(4) Watanabe, T.; Tajima, K.; Li, J.; Matsushita, N.; Yoshimura, M. Low-temperature ammonothermal synthesis of $LaTaON_2$. *Chemistry Letters* **2011**, *40* (10), 1101-1102.
(5) Cordes, N.; Schnick, W. Ammonothermal synthesis of crystalline oxonitride perovskites $LnTaON_2$ (Ln= La, Ce, Pr, Nd, Sm, Gd). *Chemistry–A European Journal* **2017**, *23* (47), 11410-11415.
(6) Jorge, A. B.; Oró-Solé, J.; Bea, A. M.; Mufti, N.; Palstra, T. T. M.; Rodgers, J. A.; Attfield, J. P.; Fuertes, A. Large coupled magnetoresponses in $EuNbO_2N$. *Journal of the American Chemical Society* **2008**, *130* (38), 12572-12573.

VII. Conclusions

This thesis has focused on the synthesis and study of new oxynitride materials with electronic properties. The main contributions can be summarized as follows:

We have developed a new synthesis approach for the perovskite $LaTaON_2$, that had been previously investigated as a visible light photocatalyst in water splitting. We used two solid state reactions at 1500 ^oC under N_2 gas, starting with mixtures of LaN and TaON or La_2O_3, LaN, and Ta_3N_5. The obtained samples with composition $LaTaO_{1+x}N_{2-x}$ showed some nitrogen deficiency, up to x=0.35 when TaON was used as reactant, implying the partial reduction of Ta^{5+} to Ta^{4+}. In the second reaction the stoichiometric compound $LaTaON_2$ was obtained increasing the proportion of nitrogen in the mixture of La_2O_3, LaN, and Ta_3N_5. It crystallizes in the *I2/m* space group, with unit cell parameters a = 5.71458(7) Å, b = 8.05987(10) Å, and c = 5.74772(6) Å. Neutron diffraction experiments showed that this new synthesis method results in a different anion distribution compared to $LaTaON_2$ prepared by ammonolysis of $LaTaO_4$ at 950 ^oC previously reported. The oxide and nitride anions occupy the three sites *4i*, *4g* and *4h* of the *I2/m* structure, but nitrogen preferentially occupies two of these sites (*4i* and *4g*). The samples show a high degree of sintering with particle sizes up to 1 μm, which are much larger than those obtained in the samples prepared by ammonolysis. The determined dielectric permittivity $\varepsilon_r \approx 200$, reported for the first time, is similar to the values reported for other perovskite oxynitrides with one nitrogen per formula.

We report the synthesis and study of new perovskite oxynitrides of europium and tantalum. $EuTaO_{2.37}N_{0.63}$ was synthesized with a reaction similar to that used for $LaTaON_2$, by treating a mixture of Eu_2O_3 and TaON at 1200 °C under N_2/H_2 (95%/5% V/V). The reaction between Eu_2O_3, EuN and Ta_3N_5 under N_2 at the same temperature led the new nitrogen rich compound $Eu_3Ta_3O_{3.66}N_{5.34}$. The first compound, with formal composition $Eu^{2+}Ta^{4+}_{0.37}Ta^{5+}_{0.63}O_{2.37}N_{0.63}$, adopts a simple cubic Pm-3m perovskite structure with parameter a=4.02043(1) Å, while the second phase, with composition $Eu_{2.34}^{3+}Eu_{0.66}^{2+}Ta_3O_{3.66}N_{5.34}$ crystallizes in a triple perovskite structure with the *P4/mmm* space group and unit cell parameters a = 3.99610(2) Å and c = 11.96238(9) Å. The superstructure that triples the c axis in $Eu_3Ta_3O_{3.66}N_{5.34}$ is a consequence of the order of Eu^{3+} and Eu^{2+} in two different positions of the P4/mmm structure. These perovskites exhibit ferromagnetism with Curie temperatures of 3 K and 8 K, respectively. The lower T_c for $Eu_3Ta_3O_{3.66}N_{5.34}$ is attributed to the presence of non-magnetic Eu^{3+}.

New perovskites with a n=1 Ruddlesden-Popper type structure and general formula $R_2TaO_{4-x}N_x$ (R = La, Ce, Nd, and Eu), were prepared at temperatures ranging from 1200 to 1700 °C in nitrogen flow. R_2O_3, Ta_3N_5, and the nitrides RN were used for the synthesis of La, Nd, and Eu compounds, whereas for the Ce compound, TaON was used as oxygen source, together with CeN. The La, Ce and Nd compounds crystallize in the *Pccn* space group, with a = 5.72949(2) Å, b = 5.73055(5) Å, and c = 12.77917(6) Å for $La_2TaO_{1.31}N_{2.69}$; a = 5.70500(5) Å, b = 5.71182(4) Å, and c = 12.61280(7) Å for $Ce_2TaO_{1.19}N_{2.81}$; and a = 5.70466(3) Å, b = 5.70476(5) Å, and c = 12.32365(5) Å for $Nd_2TaO_{1.46}N_{2.54}$.

$Eu_2TaO_{2.80}N_{1.20}$ was obtained by using a lower amount of nitrogen in the initial mixture and shows a tetragonal structure with *I4₁/acd* space group and cell parameters a = 5.71867(2) Å and c = 25.00092(19) Å. In the La, Ce and Nd oxynitrides the nitrogen deficiencies involve the partial reduction of Ta^{5+} to Ta^{4+}. Deviations from the cubic symmetry in these compounds are a consequence of octahedral tilting. The different crystal structure of $Eu_2TaO_{2.80}N_{1.20}$ is caused by the reduced oxidation state Eu^{2+}, with larger ionic radius than La^{3+}, Ce^{3+} and Nd^{3+}. According to the refinement of neutron diffraction data, $Ce_2TaO_{1.19}N_{2.81}$ shows anion order, with nitrogen located in the equatorial positions of the tantalum octahedron and nitrogen and oxygen (50/50) occupying the axial sites. The Ce and Eu compounds show magnetic order at low temperatures, while the Nd compound is paramagnetic down to low temperatures.

The new oxynitridosilicates $NdEuSiO_3N$ and $NdSrSiO_3N$ were prepared at 1350 °C and 1500 °C, respectively, under N_2/H_2 (95%/5% V/V), starting from mixtures of Nd_2O_3, Eu_2O_3, Si_3N_4, and SrO. These compounds adopt a β-K_2SO_4-type structure and crystallize in the space group *Pmnb*. They show the cell parameters a = 5.62293(1) Å, b = 7.02285(1) Å, and c = 9.64784(2) Å for $NdEuSiO_3N$, and a = 5.63074(9) Å, b = 7.01658(10) Å, and c = 9.65765(15) Å for $NdSrSiO_3N$. $NdEuSiO_3N$ is ferromagnetic with a T_c of approximately 3 K, while $NdSrSiO_3N$ shows antiferromagnetic interactions at low temperatures. The band gaps of the europium compounds $NdEuSiO_3N$ and $NdSr_{0.5}Eu_{0.5}SiO_3N$ are 2.37 eV, while the undoped compound $NdSrSiO_3N$ has a band gap value of 3.72 eV. $NdSr_{0.98}Eu_{0.02}SiO_3N$, $NdSr_{0.5}Eu_{0.5}SiO_3N$, and $NdEuSiO_3N$ show broad emission bands in the

605–639 nm range when activated under 405 nm blue light, with two main components due to Eu^{2+} occupying two different positions, M1 and M2, with different coordination numbers.

VIII. Appendix

8.1 Supporting Information for Chapter 3.1

High Temperature Synthesis and Dielectric Properties of $LaTaON_2$

Augustin Castets,[§] *Ignasi Fina,*[§] *Jhonatan R. Guarín,*[§] *Judith Oró-Solé,*[§] *Carlos Frontera,*[§] *Clemens Ritter,*[‡] *Josep Fontcuberta*[§,*] *and Amparo Fuertes*[§,*]

§ Institut de Ciència de Materials de Barcelona (ICMAB-CSIC), Campus UAB, 08193 Bellaterra(Spain).

‡ Institut Laue-Langevin, 71 Av. de Martyrs, Grenoble 38000(France)

Corresponding Author

Amparo Fuertes- Institut de Ciència de Materials de Barcelona(ICMAB-CSIC), Campus UAB, 08193 Bellaterra (Spain). amparo.fuertes@icmab.es

Josep Fontcuberta- Institut de Ciència de Materials de Barcelona (ICMAB-CSIC), Campus, UAB, 08193 Bellaterra (Spain). fontcuberta@icmab.cat

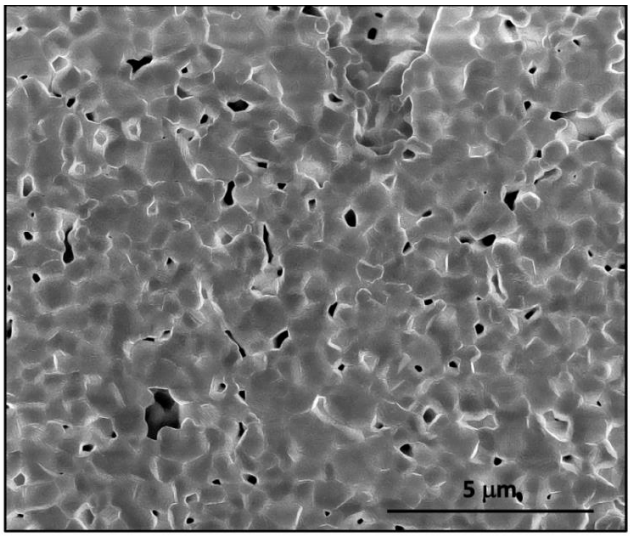

Figure S1. Low magnification scanning electron microscopy image of $LaTaON_2$ prepared at 1500 ^oC with reaction (1).

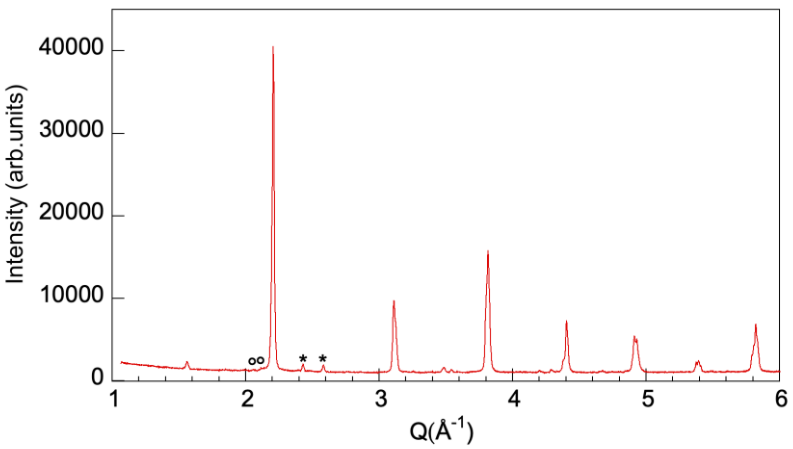

Figure S2. X-ray powder diffraction pattern (Cu k_α radiation) of a sample of $LaTaON_2$ prepared by route (1) showing TaN (*) and La_2O_3 (∘) impurity peaks.

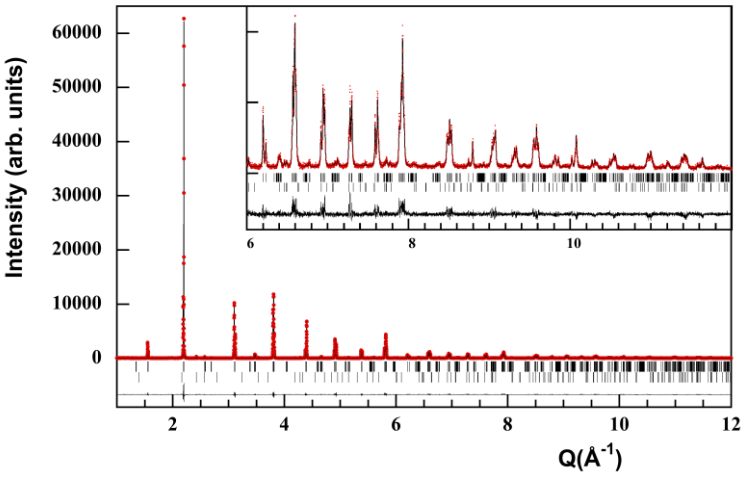

Figure S3. Observed and calculated synchrotron X-ray powder diffraction patterns of $LaTaO_{1.12}N_{1.88}$. Upper and lower reflection markers are respectively for $LaTaO_{1.12}N_{1.88}$ and hexagonal *P6/mmm* TaN. The inset shows the high Q region enlarged.

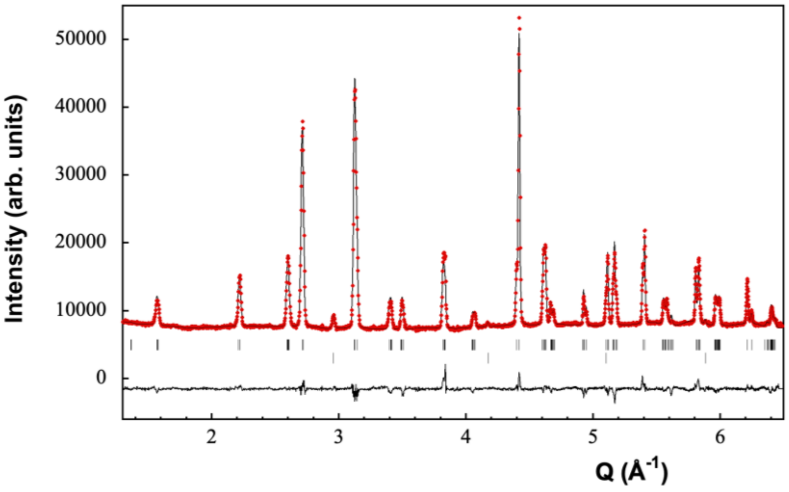

Figure S4. Observed and calculated neutron powder diffraction patterns of $LaTaO_{1.12}N_{1.88}$. Upper and lower reflection markers are respectively for $LaTaO_{1.12}N_{1.88}$ and vanadium from the sample environment.

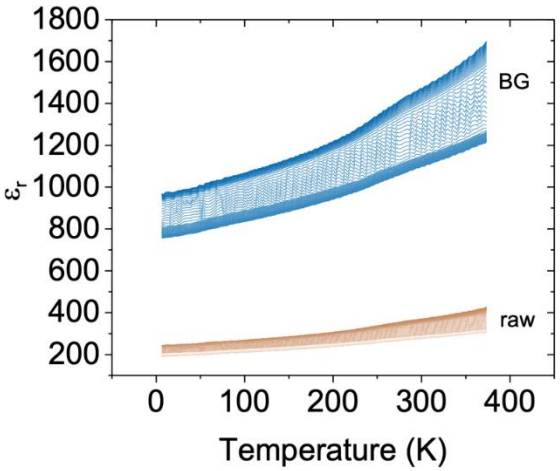

Figure S5. Dielectric permittivity of $LaTaON_2$. Raw data and data calculated using effective density of 50 % and the Bruggeman (BG) model.[1] It can be seen that the low temperature permittivity increases significantly from a measured value of c.a. 200 up to c.a.790 after correction by density. The BG correction is well stablished and its limitations are known; for instance, when pores are not isotropic the BG expression should be adapted ad-hoc. However, porosity not only affects the effective permittivity as described by the BG or related models, but it also affects the effective surface area of the electrodes which will reduce again the permittivity. Indeed, the effective surface can be significantly larger in presence of pores, particularly when conformal metallic coatings are used to prepare metallic electrodes. An increase of electrode surface due to porosity leads to a decrease of the effective permittivity that may counterbalance to some extent the increase caused by the correction by density. Accurate determination of both competing effects is beyond the scope of this manuscript. For these reasons, in the main paper we show the raw permittivity data.

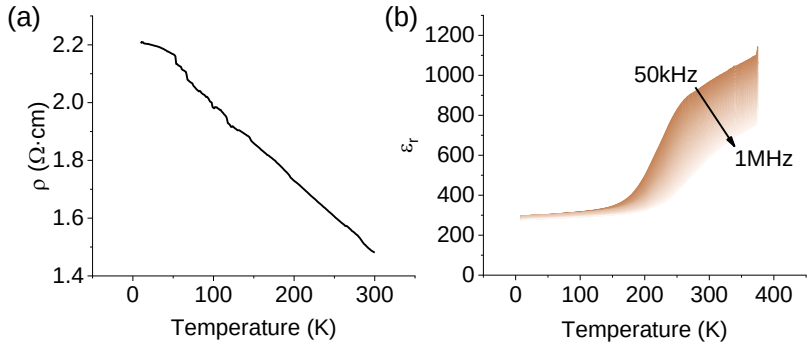

Figure S6. a) Electrical resistivity $\rho(T)$ for $LaTaO_{1.12}N_{1.88}$ and b) permittivity ε_r recorded at various frequencies for $LaTaO_{1.27}N_{1.73}$.

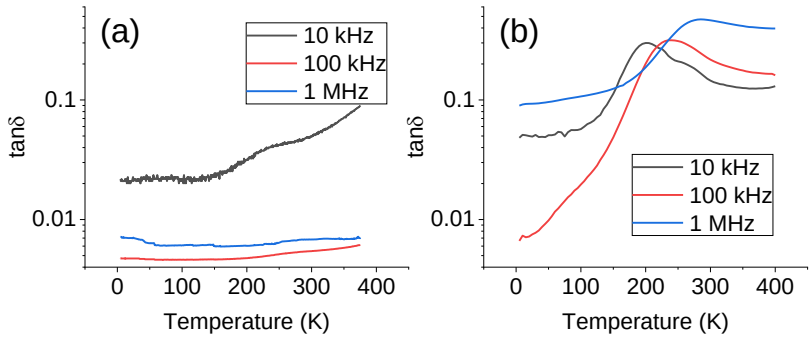

Figure S7. The dielectric tangent loss (tan δ) as a function of temperature for selected frequencies is shown for $LaTaON_2$ (a) and $LaTaO_{1.18}N_{1.82}$ (b) respectively. For $LaTaON_2$, tan δ is roughly constant for all frequencies, and it is larger at low frequency due to the contribution of small but sizeable electrical conductivity of the sample. For $LaTaO_{1.18}N_{1.82}$, tan δ evidences a frequency dependent peak at around 250K indicating Maxwell-Wagner relaxation process. The tan δ values are also greater in the latter case, because the sample shows larger conductivity.

Table S1. Summary of the *I2/m* model for $LaTaO_{1.12}N_{1.88}$ refined against room temperature synchrotron X-ray powder diffraction data using λ= 0.41322 Å. Cell parameters: a= 5.716527(14), b= 8.059731(16), c= 5.741623(11) Å, β=90.0036(3)º. R_{Bragg}= 3.74 %, R_{wp}= 11.2 %, χ^2=1.81. [a] The O/N occupancies were fixed to the values obtained from neutron diffraction.

Atom	**site**	***x***	***y***	***z***	**B(Å^2)**	**occupancy (O/N)**
La	4*i*	0.7511(7)	0	0.2465(2)	0.664(7)	
Ta	4*e*	3/4	1/4	3/4	0.525(5)	
Y1	4*i*	0.729(5)	0	0.6781(17)	1.07(11)	0.296/0.704
Y21	4*g*	0	0.781(4)	0	1.07	0.164/0.836
Y22	4*h*	1/2	0.208(3)	0	1.07	0.662/0.338
bond	**distance (Å)**		**bond**	**distance(Å)**	**bond**	**distance(Å)**
La-Y1	2.481(10)		La-Y21	2.67(2) x 2	La-Y22	2.622(16) x 2
	2.78(3)			3.05(2) x 2		3.111(18) x 2
	3.00(3)					
	3.266(10)					
Ta-Y1	2.060(3) x 2		Ta-Y21	2.041(4) x 2	Ta-Y22	2.054(4) x 2
La-Y1	2.481(10)		La-Y21	2.67(2) x 2	La-Y22	2.622(16) x 2
	2.78(3)			3.05(2) x 2		3.111(18) x 2
	3.00(3)					
	3.266(10)					
Ta-Y1	2.060(3) x 2		Ta-Y21	2.041(4) x 2	Ta-Y22	2.054(4) x 2
Bond Angles(º):	Ta-Y1-Ta	155.91(10)	Ta-Y21-Ta	165.94(16)	Ta-Y22-Ta	161.03(16)

[a] Estimated standard deviations in parentheses are shown once for each independent variable.

Table S2. Summary of the *I2/m* model for $LaTaO_{1.12}N_{1.88}$ refined against room temperature neutron powder diffraction data using λ= 1.86502 Å. Cell parameters: *a*= 5.71668(5), *b*= 8.05939(8), *c*= 5.74188(5) Å, β=89.982(3)º. R_{Bragg}= 4.34 %, R_{wp}= 2.56 %, χ^2=6.02. [a]

atom	site	*x*	*y*	*z*	occupancy (O/N)	Atom
La	4i	0.75178(14)	0	0.2477(4)		La
Ta	4e	3/4	1/4	3/4		Ta
Y1	4i	0.7338(12)	0	0.6817(3)	0.296(6)/0.704	Y1
Y21	4g	0	0.7764(3)	0	0.164(11)/0.836	Y21
Y22	4h	1/2	0.2041(4)	0	0.662(12)/0.338	Y22

bond	distance (Å)	Bond	distance (Å)	bond	distance (Å)
La-Y1	2.495(3)	La-Y21	2.699(2) x 2	La-Y22	2.608(2) x 2
	2.805(7)		3.022(2) x 2		3.131(2) x 2
	2.969(7)				
	3.251(3)				
Ta-Y1	2.0547(5) x 2	Ta-Y21	2.0371(3) x 2	Ta-Y22	2.0588(4) x 2

Bond Angles(º): Ta-Y1-Ta 157.410(18) Ta-Y21-Ta 168.009(12) Ta-Y22-Ta 159.298(18)

[a] Estimated standard deviations in parentheses are shown once for each independent variable. Isotropic thermal parameters were common for all sites and refined to 0.26(4) $Å^2$.

References

(1) Markel, V. A. Introduction to the Maxwell Garnett approximation: tutorial. *JOSA A* **2016**, *33* (7), 1244-1256.

8.2 Supporting Information for Chapter 4

Anionic and magnetic order in rare earth tantalum oxynitrides with n=1 Ruddlesden Popper structure

Jhonatan R. Guarín, Carlos Frontera, Judith Oró-Solé, Bastian Colombel, Clemens Ritter, François Fauth, Josep Fontcuberta and Amparo Fuertes**

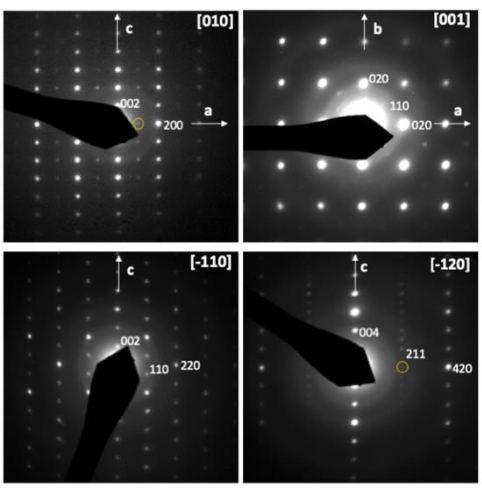

Figure S1. Electron diffraction patterns of $La_2TaO_{1.31}N_{2.69}$. Yellow circles indicate multiple diffraction reflections.

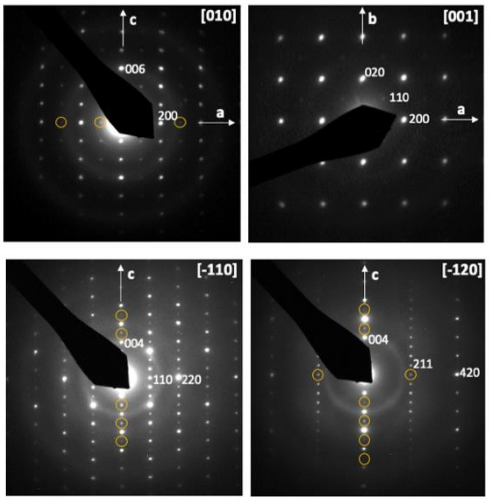

Figure S2. Electron diffraction patterns of $Nd_2TaO_{1.46}N_{2.54.}$ Yellow circles indicate multiple diffraction reflections.

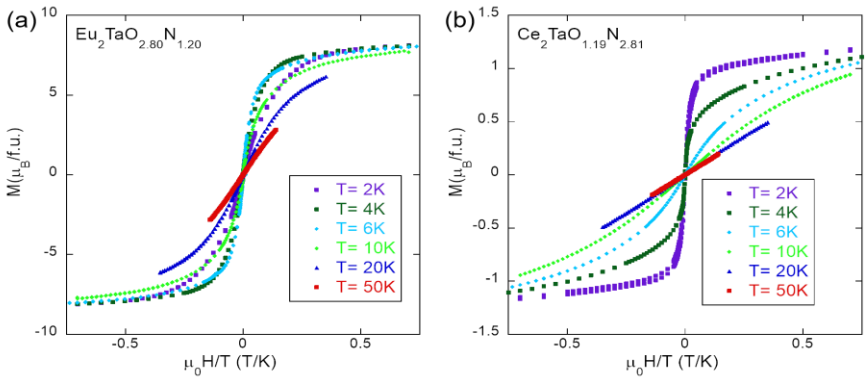

Figure S3. Magnetization plotted in front of μ_0H/T at different temperatures for a) $Eu_2TaO_{2.80}N_{1.20}$ and b) $Ce_2TaO_{1.19}N_{2.81}$. The lack of scaling of the curves proves that magnetization does not follow a Langevin nor a Brillouin function that describe paramagnetism.

Table S1. Summary of the *Pccn* model refined against room temperature synchrotron X-ray powder diffraction data for $Ce_2TaO_{1.19}N_{2.81}$ (λ=0.41784 Å). Refined cell parameters and agreement factors are: a=5.76215(5), b=5.76903(4), c=12.73914(7) Å. V= 423.475(5) $Å^3$. R_{Bragg}= 5.54%, R_{wp}= 9.68 %. [a]

Atom	***site***	**x**	**y**	**z**	**B($Å^2$)**	**occupancy**
Ce	*8e*	0.4958(4)	0.0089(4)	0.1428(4)	0. 565(9)	1
Ta	*4a*	0	0	0	0.996(16)	1
O1/N1	*8e*	0.03090	0.04010	0.17037	2.29(15)	0.498/ 0.502
O2/N2	4c	0.25	0.25	0.4800	2.29	0.070/ 0.930
O3/N3	*4d*	0.25	0.75	0.0011	2.29	0.124/0.876
Bond		**distance (Å)**	**bond**	**distance (Å)**	**bond**	**distance (Å)**
Ta-O1,N1		2.190x2	Ta-O2,N2	2.054x2	Ta-O3,N3	2.039x 2
Ce-O1,N1		2.405(1)	Ce-O1,N1	2.630(2)	Ce-O1,N1	2.708(2)
Ce-O1,N1		3.109(3)	Ce-O1,N1	3.190(3)	Ce-O2,N2	2.612(2
Ce-O2,N2		2.871(2))	Ce-O3,N3	2.728(2)	Ce-O3,N3	2.738(2)

[a] Estimated standard deviations in parentheses are shown once for each independent variable. The temperature factors were common for the three anions sites. Average bond distances: Ta-O,N 2.094 Å; Ce-O,N 2.777 Å.

IX. Publications

This thesis has led to the following publications:

- Augustin Castets, Ignasi Fina, Jhonatan R. Guarin, Judith Oró-Solé, Carlos Frontera, Clemens Ritter, and Amparo Fuertes, High-temperature synthesis and dielectric properties of $LaTaON_2$. *Inorganic Chemistry* ***2021***, 60, 16484-16491

- Ashley P. Black, Jhonatan R. Guarin, Judith Oró-Solé, Carlos Frontera, Alejandro Goñi and Amparo Fuertes. Neodymium europium oxynitridosilicates of β-K_2SO_4 type: Structural, magnetic and red luminescence properties. *Journal of Solid State Chemistry* ***2022***, 316, 123571

- Jhonatan R. Guarin, Carlos Frontera, Judith Oró-Solé, Jaume Gàzquez, Clemens Ritter, Josep Fontcuberta, and Amparo Fuertes. High temperature synthesis of ferromagnetic $Eu_3Ta_3(O,N)_9$ with a triple perovskite structure. *Inorganic Chemistry* ***2023***, 62, 42, 17362-17370.

- Jhonatan R Guarín, Carlos Frontera, Judith Oró-Solé, Bastian Colombel, Clemens Ritter, François Fauth, Josep Fontcuberta, Amparo Fuertes. Anionic and magnetic ordering in rare earth tantalum oxynitrides with an n = 1 Ruddlesden–Popper structure, *Chemistry of Materials*, **2024**, 36, 10, 5160-5171.